



HAL
open science

Investigation of the Optical Emission of Hall Effect Thrusters using a Collisional Radiative Model, Particle-In-Cell Simulations, and Machine Learning

Tarek Ben Slimane

► **To cite this version:**

Tarek Ben Slimane. Investigation of the Optical Emission of Hall Effect Thrusters using a Collisional Radiative Model, Particle-In-Cell Simulations, and Machine Learning. Plasmas. Institut Polytechnique de Paris, 2023. English. NNT : 2023IPPAX153 . tel-04572928

HAL Id: tel-04572928

<https://theses.hal.science/tel-04572928>

Submitted on 13 May 2024

HAL is a multi-disciplinary open access archive for the deposit and dissemination of scientific research documents, whether they are published or not. The documents may come from teaching and research institutions in France or abroad, or from public or private research centers.

L'archive ouverte pluridisciplinaire **HAL**, est destinée au dépôt et à la diffusion de documents scientifiques de niveau recherche, publiés ou non, émanant des établissements d'enseignement et de recherche français ou étrangers, des laboratoires publics ou privés.



INSTITUT
POLYTECHNIQUE
DE PARIS

NNT : 2023IPPAX153

Thèse de doctorat



Investigation of the Optical Emission of Hall Effect Thrusters using a Collisional Radiative Model, Particle-In-Cell Simulations, and Machine Learning

Thèse de doctorat de l'Institut Polytechnique de Paris
préparée à l'École polytechnique

École doctorale n°626 Ecole Doctorale de l'Institut Polytechnique de Paris (EDIPP)
Spécialité de doctorat : Optique, laser et plasma

Thèse présentée et soutenue à Palaiseau, le 19 Décembre 2023, par

TAREK BEN SLIMANE

Composition du Jury :

Erik Johnson Directeur de Recherche, Ecole polytechnique	Président
Sedina Tsikata Professeure associée, Georgia Tech	Rapporteur
Tsanko Tsankov Maître de conférences, Ruhr University Bochum	Rapporteur
Mark Cappelli Professor, Stanford University	Examineur
Olivier Duchemin Directeur Technique Adjoint, Safran Spacecraft Propulsion	Examineur
Victor Désangles Chargé de Recherche, ONERA	Examineur
Anne Bourdon Directrice de Recherche, Ecole polytechnique	Co-directrice de thèse
Pascal Chabert Directeur de Recherche, Ecole polytechnique	Co-directeur de thèse

INSTITUT POLYTECHNIQUE DE PAIRS
DOCTORAL SCHOOL IPP
DEPARTEMENT OF PHYSICS

PHD THESIS

to obtain the title of

PhD of Science

in Physics

Specialty : OPTICS, LASER AND PLASMAS

Defended by

Tarek BEN SLIMANE

Investigation of the Optical Emission of Hall Effect Thrusters using a Collisional Radiative Model, Particle-In-Cell Simulations, and Machine Learning

Thesis Advisors: Anne BOURDON & Pascal CHABERT

prepared at the Laboratoire de Physique des Plasmas, ECOLE
POLYTECHNIQUE

defended on December 19th, 2023

Jury :

<i>President:</i>	Erik JOHNSON	- Ecole polytechnique
<i>Reviewers:</i>	Sedina TSİKATA	- Georgia Tech
	Tsanko TSANKOV	- Ruhr University Bochum
<i>Examinators:</i>	Mark CAPPELLI	- Stanford University
	Olivier DUCHEMIN	- Safran Spacecraft Propulsion
	Victor DÉSANGLES	- ONERA
<i>Advisor:</i>	Anne BOURDON	- Ecole polytechnique
	Pascal CHABERT	- Ecole polytechnique

Étude de l'Émission Optique des Propulseurs à Effet Hall à l'aide d'un Modèle Collisionnel Radiatif, des Simulations PIC et du Machine Learning

Résumé : Ce travail cherche à analyser l'émission optique des propulseurs à effet Hall afin d'en extraire les paramètres plasma. Elle s'inscrit dans le contexte des micro-lanceurs réutilisables et des programmes de ride-share pour les satellites, qui ont considérablement réduit les coûts des opérations spatiales. Cette évolution a intensifié la demande d'équipements de satellites standardisés et miniaturisés, avec un accent particulier sur les propulseurs à effet Hall en raison de leur avantageux rapport poussée/puissance, de leur impulsion spécifique et de leur efficacité. La thèse s'appuie sur le développement du code LPPic Particle-In-Cell et explore la dynamique du plasma en couplant les résultats de la simulation avec des diagnostics virtuels. Le premier diagnostic virtuel mis en œuvre est la diffusion Thomson Collective, qui explore les fluctuations de la densité électronique dans le propulseur. Le deuxième diagnostic virtuel est la spectroscopie d'émission optique générée via un modèle collisionnel radiatif, permettant de caractériser la fonction de distribution d'énergie des électrons. Ces deux diagnostics permettent de valider les simulations de LPPic avec des expériences. En outre, la spectroscopie d'émission sert également d'outil prometteur pour évaluer les performances en orbite et caractériser les effets des installations au sol. La thèse est structurée en huit chapitres. Ceux-ci couvrent la mise en place du diagnostic virtuel de diffusion Thomson Collective, le développement et la validation de HETOD - un modèle collisionnel radiatif pour le xénon neutre - et la mise en place de la spectroscopie d'émission optique virtuelle. L'implémentation de ces méthodes a démontré l'importance de rendre compte des gradients spatiaux dans le propulseur pour l'extraction des paramètres du plasma à partir de l'émission optique ou du signal de diffusion. Elle a également mis en évidence la validité des hypothèses sur le transport des métastables et de l'utilisation d'une fonction de distribution maxwellienne dans les modèles collisionnels radiatifs des neutres dans la zone d'accélération et la plume, ainsi que les limitations de bandes passantes spécifiques à chaque raie d'émission pour étudier des instabilités à haute fréquence (≥ 1 MHz).

Ces observations ont été confrontées ensuite à des expériences où des spectres expérimentaux ont été utilisés pour extraire les paramètres du plasma à l'aide HETOD pour diverses conditions d'opération. Les recommandations issues du couplage virtuel ont été vérifiées démontrant ainsi l'adéquation de l'émission optique et des modèles collisionnels radiatifs pour suivre et contrôler les propulseurs à effet Hall. Ces expériences ont souligné les gradients des paramètres plasma (densité et température électronique) dans les trois directions. En particulier, le gradient de la température électronique dans le canal du propulseur, a été mesuré pour la première fois avec de l'émission optique, soulignant des températures électronique entre 20 et 30 eV et qui augmentent linéairement avec la tension d'opération du propulseur. Enfin, une amélioration du modèle d'émission optique et du modèle collisionnel radiatif est également présentée via l'intégration de réseaux de neurones. Cette méthode améliore considérablement l'efficacité et la portée du diagnostic, en accélérant le traitement de quelques minutes par spectre à quelques dizaines de millisecondes. La conséquence pratique de cette accélération est la réduction du hardware nécessaire en orbite et éventuellement le contrôle optique en temps réel des paramètres du propulseur.

Investigation of the Optical Emission of Hall Effect Thrusters using a Collisional Radiative Model, Particle-In-Cell Simulations, and Machine Learning

Abstract: This thesis provides an analysis of the optical emission of Hall Effect thrusters. The study is grounded in the context of micro-reusable launchers and ride-share satellite programs, which have substantially reduced space operation costs. This shift has intensified the demand for standardized and miniaturized satellite equipment, with a particular focus on Hall effect thrusters due to their advantageous thrust-to-power ratio, specific impulse, and efficiency. The thesis builds upon the development of the LPPic Particle-In-Cell code and explores the plasma dynamics by coupling the simulation results with the novel concept of virtual diagnostics. The first virtual diagnostic implemented is collective Thomson scattering, which explores the electron density fluctuations in the thruster. The second virtual diagnostic is optical emission spectroscopy coupled with a collisional radiative model, which characterizes the electron energy distribution function. Both are instrumental in validating LPPic simulations, with the latter also serving as a promising tool for assessing the performance in orbit and characterizing ground facility effects. The thesis is structured into eight chapters. These include the implementation of virtual collective Thomson scattering diagnostics, the development and validation of HET0D, a collisional-radiative model for neutral xenon, and the establishment of the virtual optical emission spectroscopy framework. These methods established the importance of considering spatial gradients in the plume of the thruster when extracting plasma parameters from optical emission or scattered emission. It also highlighted the validity of the transport and the Maxwellian energy distribution function assumptions in the collisional radiative models of neutral species in the acceleration zone and the plume and highlighted line-specific bandwidth limitations for the implementation of optical emission spectroscopy to study high-frequency instabilities (≥ 1 MHz).

These insights were confronted with experiments where actual spectra were used to extract plasma parameters using the collisional radiative model under various thruster conditions, thereby demonstrating the validity of the recommendations from the virtual diagnostic analysis and the adequacy of optical emission and collisional radiative models to monitor Hall Effect thrusters. These experiments put in evidence the gradient in the plasma parameters in the three directions. In particular, the gradient in the electron temperature in the thruster channel was measured for the first time using optical emission spectroscopy, highlighting temperatures between 20 and 30 eV, that increase linearly with the applied anode voltage. Finally, an innovative enhancement to optical emission and collisional radiative model through the integration of artificial neural networks is also presented, which significantly improves the efficiency and scope of the diagnostic, by speeding up the processing from 1min to 10ms, reducing the needed hardware in-orbit, and allowing the real-time optical control of the operating parameters of the thruster.

Acknowledgments

خُلِقَتْ ظَلِيقًا كَطَيْفِ النَّسِيمِ - وَحُرًّا كَنُورِ الضُّحَى فِي سَمَاءِهِ
تُعَرِّدُ كَالظَّيْرِ أَيْنَ انْدَفَعَتْ - وَتَشْدُو بِمَا شَاءَ وَحِي إِلَهُ
أبو القاسم الشابي

The three years swiftly flew and my PhD came to an end. As I stand up at the doorstep of the coming chapter and reflect upon the past time, gratitude nestles within me for the people who crossed my journey with their support and encouragement. Truth be told, the PhD started in a thorny COVID period, where everyone, including myself, was seeking for a guiding light in a sky of uncertainty. Yet, for me, that much-needed light was never to be found high in the sky but I found it rather in the warmth of the wonderful people around me who helped keeping me on the right track.

Foremost, my gratitude goes to my supervisors, Anne Bourdon and Pascal Chabert, who supported me throughout these three years. From our discussions, not only did I improve as a scientist but also I became more self-reliant and resilient. During the difficult moments, your counsel was golden, though perhaps it was sought in urgency (Sorry for that). Anne, I am profoundly grateful for your encouragement and faith. Thank you for always making me feel valued and deserving of my place, even when I struggled to see it myself. Your support has been a constant source of strength. You provided a shoulder to lean on and a listening ear, offering reassurance when I needed it most. Your impact cannot truly be overstated, and I will be forever grateful for that.

To Cyrille, I am immensely thankful for finding in you the mentor I needed. Your willingness to answer my questions without hesitation and to spend time with me on the problems I was facing has been invaluable to this work. Thank you from the bottom of my heart for your time and your expertise. Most importantly for, thank you for welcoming me with open arms, despite not being your formal student. Your patience and guidance, even as I was in a different field, have been an immense support. Thank you for giving meaning to my work and for imparting countless lessons along the way.

To Loic, I also extend my sincere thanks for your help and enthusiasm. Your leadership within the team has been for a short moment but was very impactful. Together, we spent countless hours conducting experiments, exploring new ideas and always pushing forward. Your kindred spirit has inspired me to pursue my own ideas with a lot of confidence. To Alexandre, I offer also my sincere gratitude for your support throughout the experiments til the last moment before the beginning of the writing. Truly, the solitude of the experiment room weighs heavily on a person, but your presence provided a nice company. To Alexis, I am deeply grateful for

your assistance in setting up the processing methods I desired. Your expertise was instrumental in speeding up my codes and always getting new and better Pythonic ways to do the tasks I wanted to implement.

To the members of the propulsion team – Thomas, Antoine, Florian, Federico, Nicolas, and Benjamin – I express my heartfelt appreciation. The bond, that was forged by our shared passion for space and science, was further strengthened by moments of camaraderie and laughter in conferences, travel and football. Federico my conference pal and running buddy, I am very lucky to have collaborated with you. Let us finally plan that marathon we always wanted to do.

To my comrades-in-arms, Edmond and Victor, I struggle to find the right words to express the extent of my gratitude. Honestly, gratitude itself does not even describe it in the slightest. As colleagues, confidants, and indeed brothers, your presence lightened up my every day in the lab. Your impact was far beyond academic work, teaching me the importance of balance, adventure, and authenticity. From skiing lessons to new experiences and cherished moments during a certain hike, you coloured my life in colours I did not know existed. To Edmond, my 8pm office mate, flatmate, and dear friend, your influence on me and contribution to this thesis is immeasurable. I will forever look up to you with a lot of admiration and inspiration.

To Carolina, my office mate and dear friend, I express my deepest thanks for the laughs, the discussions and the fun. We shared our common love for science, books, museums and tea. I will always remember the unexpected but much-appreciated morning croissant and obviously the delicious banana cake. Talking with you always lifted my spirit every single time. I am very lucky to have you! To Bayane, "Mon Comité de Convivialité", we've done a lot of foolishness, we've stirred things up: we've brought in a ping pong table, initiated many games, and many evenings. We've shared joys and sorrows, long work weekends in the lab, and small meals with instant noodles and chips (the best I have ever eaten, by the way). Thank you for your counsel when things were very chaotic. My partner-in-crime, and my friend forever.

To Nadj, an unexpected yet incredible encounter, whose influence extended far beyond plasmas. Thanks to you, I fell into the dark side of engineering and got hooked on CAD modelling, 3D printing and circuit design (just kidding). I enjoyed our spirited matches of Ping-pong and Badminton which helped me unwind. In times of uncertainty, you were also there and your wise counsel provided me with great clarity. Between our shared laughter and friendly competition, we became close friends. A special mention to the time you helped me not to miss my flight (It was close). To Marilyne and Cherifa, thank you for your small yet thoughtful gesture of having a non-empty candy jar for me every day at 5 pm. It was my source of comfort amidst the tremors of the writing period. Your smile, kindness and generosity brightened my days. And to Edouard, thank you for our playful banter, teasing each other all in good humour, of course.

During my PhD, I had the opportunity to work with many nice master's students, PhD students and post-docs: Paul, Julien, Romain, Etienne, Olivier, Tom, Timothé, Pierre, Sophie, Dihya, Anatole, Ambre, Anna, Benoit, Davide, Giulio, Gwendal,

Emanuele, Vincent, Tat Loon, Adii... and many more. Thanks for the good time and for everything I learned from you. Our time together was marked by countless moments of science, heated discussions and heartfelt laughter. Whether in the lab or during the breaks, your presence enriched my experience, creating memories that I will always cherish. Special thanks to Tom since I clearly lost the bet.

Then I would like to thank all the members of the jury: Erik Johnson, Victor Désangles, Marc Capelli, and Olivier Duchemin with a special mention to the rapporteurs Sedina Tsikata, Tsanko Tsankov and also my supervisors, to have agreed to read my thesis. Thank you for being kind with the questions for the good mood and the great atmosphere you created during the defence. A general thanks to everyone who participated in the "pot" on a day that was one of the happiest in my life.

To my students, Jad and Cristian, you grounded me during my Ph.D. You taught me more than you ever imagined on how to become a better teacher. Also to my colleagues and students from the Centre Spatial Etudiant, I express my tender affection. The projects were the highlight of my week, igniting my passion for rockets, aerodynamics, and prototyping. These discussions stimulated me to evolve as an engineer. A special mention to Alexandre Duran, Joseph Redaud, Luca Bucciantini, and Antoine Tavant. A sincere appreciation goes also to my dearest friends: Hervé, Fatou, Elyes, Najd, Romain, Khadija, Hiba, Matthieu, Yann, and Pierre. Your presence provided much-needed solace and a fresh perspective on life, far from the academic world. Our discussions allowed me to take my mind off work and talk about arts, music, politics, sustainability and board games. Thank you very much!

To my beloved family, you can't imagine how your presence in my defence was a source of strength. It was important for me to dedicate this final academic degree to all of you and that you were able to be there. Thank you very much for attending. It would have not been the same without you. To my parents, your endless love, encouragement, and sacrifices have been the bedrock of this adventure. Your faith in my abilities gave me the confidence to pursue my PhD til the end. Your wisdom, guidance, and support have shaped me into the person I am today. I love you so much. To my brothers and my little sister, your presence in my life has been a constant source of inspiration. Though distance may have kept us apart during this milestone moment, your love and support were felt deeply. I missed each of you dearly and wished for nothing more than to share this momentous occasion with you. To my extended family members, relatives, and loved ones, your encouragement from the other side of the Mediterranean has meant the world to me. Your words of encouragement, prayers, and well-wishes have uplifted my spirits. Thank you a lot!

Finally, to my departed grandmother, Dalinda, whose spirit infuses every page of this work, I dedicate this manuscript. I am sorry and I wish I knew. You were the cornerstone of my education and the driving force behind my pursuit of excellence. Your spirit has been and still is the wind beneath my wings. At the end of this journey, your memory shines upon the following path as the door opens for the new chapter.

Contents

List of Acronyms	xxxi
1 Introduction	1
1.1 Electric propulsion and Hall effect thrusters	1
1.2 Challenges	3
1.3 Thesis context, content and objectives	6
2 Analysis of Hall Effect Thruster Using Virtual Collective Thomson Scattering on Particle-In-Cell Simulations	9
2.1 Methods	11
2.1.1 Axial-azimuthal PIC simulation	11
2.1.2 Collective Thomson scattering analysis	15
2.1.3 Pre-processing of the PIC results	18
2.2 Results	18
2.2.1 Amplitude variation of the dominant modes	18
2.2.2 Dispersion relation	20
2.2.3 Electron density fluctuation rate	21
3 Optical Emission Spectroscopy and Collisional Radiative Modelling	25
3.1 Collisional and radiative data for xenon	28
3.1.1 Spectroscopic notations, electronic configuration, and main radiative emissions	28
3.1.2 Electron impact excitation cross sections	31
3.2 HET0D neutral xenon collisional radiative model	36
3.2.1 Model overview	37
3.2.2 Included kinetic processes	38
3.2.3 Balance equation	45
3.3 HET0D implementation	45
3.3.1 Code inputs	45
3.3.2 Module structure	47
3.3.3 Sampling, interpolation, extrapolation, and integration schemes	49
3.3.4 Example of calculations	50
3.4 HET0D verification and quantification of uncertainties	51
3.4.1 Verification of the model	51
3.4.2 Quantification of the uncertainties in HET0D	55

4	Parametric Study of Hall Effect Thruster 0D (HET0D)	61
4.1	Parametric study of HET0D	62
4.1.1	Reduction of the system	63
4.1.2	Parametric study over the collisional parameters	64
4.1.3	Parametric study over the radiative parameters	69
4.2	Dominant kinetic mechanism	70
4.2.1	Dominant kinetic region in the n_e - n_g space	71
4.2.2	Dominant kinetic mechanisms in HET	75
4.3	Validation against the KCD model	78
4.3.1	KCD model	78
4.3.2	Verification against KCD model	82
5	Coupling the CRM with PIC Simulations	89
5.1	PIC simulation and coupling methodology	90
5.1.1	Self-consistent axial-azimuthal PIC simulation	90
5.1.2	Description of the case results	92
5.2	Coupling methodology and assumptions	99
5.3	Insights into the dominant kinetic mechanisms along the thruster axis	102
5.4	Application of the line ratio method on synthetic spectra	103
5.5	Maxwellian EEDF and non Maxwellian EEDF comparison	110
5.6	Time analysis of the synthetic spectra	115
5.7	Discussion	117
6	Overview of the Experimental of HET0D	125
6.1	The main experimental setup	126
6.1.1	The Hall effect thruster	126
6.1.2	Electrical and magnetic configuration	128
6.1.3	Gas injection and vacuum configuration	129
6.1.4	Ignition sequence	130
6.1.5	Thruster characterization	130
6.2	Overview of the diagnostics and their calibration	132
6.2.1	Optical emission spectroscopy	132
6.2.2	Langmuir probe	135
7	Results Langmuir probes, Optical Emission Spectroscopy (OES) and HET0D	139
7.1	Langmuir probe results	140
7.1.1	Structure of the plume	141
7.1.2	Isentropic expansion	143
7.2	Emission spectra results	144
7.2.1	Lateral OES measurements results	144
7.2.2	Axial OES measurements results	145
7.2.3	Radial OES measurements results	149

7.3	Coupling the Collisional Radiative Model (CRM) with experimental spectra	152
7.3.1	Relating the spectral measurement to CRM output	153
7.3.2	Relating spectral measurements to CRM inputs	153
7.3.3	Relating Langmuir probes measurements to CRM predictions	155
7.3.4	Validating the CRM with Langmuir probe measurements	157
7.4	CRM results	159
7.4.1	Axial scan of the plume	159
7.4.2	Radial scan of the plume	160
7.5	Discussion	164
7.5.1	Impact of the optimization method	164
7.5.2	Gas density variation	165
7.5.3	Electron temperature dynamics	168
7.5.4	Preliminary insights from Particle-In-Cell (PIC) simulations vs. experimental results	168
8	Enhancing CRM Predictions using Machine Learning	173
8.1	Machine learning methodology	175
8.1.1	Presentation of Artificial Neural Network (ANN)s	175
8.1.2	The learning process	177
8.1.3	Hyperparameter tuning and cross validation	179
8.1.4	Practical workflow to developping ANN	180
8.2	Accelerating predictions with the collisional radiative model	182
8.2.1	Data collection and integration approach	182
8.2.2	Results	184
8.3	Learning macroscopic parameters	186
8.3.1	Experimental setup, data acquisition and cleaning	186
8.3.2	Model development	190
8.3.3	Results and insights	192
8.4	Machine learning control with PID	197
8.4.1	Control strategy and implementation of the Proportional-Integrator-Derivative controller (PID)	198
8.4.2	Control simulation results	199
8.4.3	Enhancing control and monitoring: PID and varied magnetic configurations	202
8.5	Chapter conclusions	203
9	Summary	205
9.1	General recommandations	205
9.2	Key findings	208
9.3	Future perspectives	210
9.4	In closing	211

Appendices	213
A Appendix Example	215
A.1 General Notes	215
B Racah and Paschen Notations	217
C Comparison Between Numerical and Experimental Cross Section	219
C.1 From the ground state to the $6s$	219
C.2 From the ground state to the $6p$	221
C.3 From the $6s$ to the $6p$	224
C.4 From $6s$ to $6s$	226
C.5 From $6p$ to $6p$	226
C.6 Energy levels and radiative data	228
D Estimation of Uncertainties for Rate Coefficients	231
E Kinetics Diagrams of Xenon Excited Species at Typical HET Conditions	233
F Line broadening	237
G Estimation of the Depth of Field of the Lens Setup	239
H ADAM Optimization	241
Bibliography	243

List of Figures

1.1	Schematic of the operating principle of a Hall-Effect Thruster (HET). Neutral xenon is injected from the anode. Electrons that are emitted from the cathode are trapped by the radial magnetic field, hence increasing the collision frequency with the neutral gas and leading to the production of electron-ion pairs. Ions are exhausted out of the channel under the effect of the electric field, creating thrust.	2
2.1	Schematic of a transversal cross-section of the thruster and the simulation domain adapted from [Charoy <i>et al.</i> 2019]. The x axis is the axial direction, and the y axis is the (periodic) azimuthal direction. The black dashed line at $x = 7.5$ mm corresponds to the position of the maximum radial magnetic field and the exit plane of the thruster. The green dashed line at $x = 24$ mm is the plane from which electrons are emitted.	12
2.2	Typical results from PIC simulations. This snapshot of the electron density is taken at $t = 12.5$ μ s. The dashed red line at $x = 7.5$ mm indicates the limit between the ionization zone and the acceleration zone which also corresponds to the position of the maximum radial magnetic field and the exit plane of the thruster	13
2.3	2D FFT of the electron density at $x = 3$ mm and $x = 20$ mm. Solid white line: ion-acoustic dispersion relation.	14
2.4	The axial variation of the electron density fluctuation rate in the simulation case from [Charoy <i>et al.</i> 2019]. The blue curve corresponds to the reference fluctuation rate from PIC results using Eq. 2.1. The red curves correspond to the synthetical fluctuation rate from the virtual Collective Thomson Scattering (CTS) at a waist $w = 0.1$ mm based on Eq. 2.7. The black dashed line at $x = 7.5$ mm corresponds to the position of the maximum radial magnetic field and the exit plane of the thruster.	15
2.5	2D configuration for the virtual CTS calculation. The scattering volume is a Gaussian profile with a waist $w = 3$ mm. The phase factor in the Fourier transform is directed along the scattering vector \mathbf{k} , here expressed in polar coordinates with $\alpha = 120^\circ$ and $k = 3$ rad.mm ⁻¹	16
2.6	2D polar maps of the intensity of the scattering signal at different axial positions	19

2.7	Variation of the dominant modes along the axial direction. The blue curves show the intensity of the scattering signal while, on the secondary axis, the dashed curves show the variation of the axial component k_x and the azimuthal component k_y . The dashed black curve indicates the thruster exit plane and the position of the maximum radial magnetic field.	20
2.8	Dynamic form factor for $k_y = 3 \text{ rad.mm}^{-1}$ and $k_y = 8 \text{ rad.mm}^{-1}$ at $x = 3 \text{ mm}$ and 20 mm . Blue curves correspond to $x = 3 \text{ mm}$ and an angle $\alpha = 110^\circ$ and the red curve correspond to $x = 20 \text{ mm}$ and an angle $\alpha = 90^\circ$	21
2.9	Dispersion relations derived from the virtual Thomson scattering experiment along the privileged observation angle relative to each zone: (a) corresponds to the ionization zone with $\alpha = 110^\circ$ while (b) corresponds to the acceleration zone with $\alpha = 90^\circ$. The dashed black lines correspond to the best linear fit	22
2.10	Axial profile of the electron density for different values of the laser waist: $w = 1$ and 3 mm in the CTS analysis and from the PIC simulations.	22
2.11	Axial profile of the electron fluctuation rate for different values of the laser waist: $w = 1$ and 3 mm in the CTS analysis and from the PIC simulations.	23
3.1	Xenon energy diagram [Raptor 2003]. The black circle indicates the ground state. The red circle indicate the $6s$ levels while the two green circles are the $6p$ levels split into $6p$ tier and $6p'$ tier.	30
3.2	Energy diagram for xenon levels included in the CRM	38
3.3	Electron energy distribution and probability function: (a) Maxwellian Electron Energy Distribution Function (EEDF) for different temperatures (b) Comparison between a Maxwellian Electron Energy Probability Function (EEDF) at 21 eV with a simulated EEDF from PIC simulation from [Petronio <i>et al.</i> 2023a] in the plume of a hall thruster	39
3.4	Shape of the generalized two parameters EEDF for different values of the parameter x	40
3.5	Comparison of the rate coefficient for electron impact excitation: (a) Maxwellian EEDF at 15 eV superposed to the excitation cross-section from the ground state to $2p5$ with respect to the electron energy to illustrate the integral expression of the rate coefficient. Note that the threshold region has the biggest contribution. (b) Comparison of the rate coefficient calculated with a Maxwellian EEDF and a generalized two parameters Maxwellian with $x = 2$. The energy here should be understood as the effective electron temperature expressed in electronvolts.	41
3.6	Escape factor as a function of the optical depth	44
3.7	Workflow of HET0D	46

3.8	Architecture of HET0D	48
3.9	Illustration of the impact of numerical extrapolation on the calculation of the rate coefficient. The energy here should be understood as the effective electron temperature expressed in electronvolts.	49
3.10	Sample calculation using HET0D. The inputs are $n_e = 1 \times 10^{17} \text{ m}^{-3}$, $T_e = 20 \text{ eV}$, $n_g = 1 \times 10^{20} \text{ m}^{-3}$, $T_g = 300 \text{ K}$, d is 15 cm, and the EEDF f_e follows a Maxwellian distribution. Initially, all xenon atoms are in the ground state. a) The time evolution of the ratio of the state densities to the initial density of the ground state b) Synthetic spectra generated from the excited species density distribution at steady state	51
3.11	Computed and analytical time evolution of the density of the ground state and the $1s_2$ levels. For this model, only electron impact excitations between the two levels are included. The solid lines correspond to the analytical solution, the triangles correspond to the numerical solution from HET0D. Parameters: xenon, $n_e=1 \times 10^{17} \text{ m}^{-3}$, $n_g = 1 \times 10^{20} \text{ m}^{-3}$, $T_g = 300 \text{ K}$, Maxwellian EEDF at 20 eV	53
3.12	Computed and analytical time evolution of the density of the two-state levels. For this model, electron impact excitations between the two levels and the radiative decay from the $1s_2$ level are included. The solid lines correspond to the analytical solution, the triangles correspond to the numerical solution from HET0D. Parameters: xenon, $n_e=1 \times 10^{17} \text{ m}^{-3}$, $n_g = 1 \times 10^{20} \text{ m}^{-3}$, $T_g = 300 \text{ K}$, Maxwellian EEDF at 20 eV	53
3.13	Time evolution of the population density to reach LTE. Parameters: xenon, $n_e=1 \times 10^{17} \text{ m}^{-3}$, $n_g = 1 \times 10^{20} \text{ m}^{-3}$, $T_g = 300 \text{ K}$, Maxwellian EEDF at $T_e^{low} = 5 \text{ eV}$, $T_e^{medium} = 20 \text{ eV}$, and $T_e^{high} = 40 \text{ eV}$	54
3.14	Ratio of state population at LTE. Parameters: $n_e=1 \times 10^{17} \text{ m}^{-3}$, $n_g = 1 \times 10^{20} \text{ m}^{-3}$, $T_g = 300 \text{ K}$, Maxwellian EEDF at T_e^{medium} at 20 eV.	55
3.15	The standard deviations across the species included in HET0D for three different xenon chemistries. Parameters: xenon, $n_e=1 \times 10^{17} \text{ m}^{-3}$, $n_g = 1 \times 10^{20} \text{ m}^{-3}$, $T_g = 300 \text{ K}$, Maxwellian EEDF at $T_e^L = 4 \text{ eV}$ and $T_e^H = 40 \text{ eV}$	57
3.16	Breakdown of the contribution to the total uncertainty between the radiative transitions and the electron collision processes.	58
4.1	Varying the dominant kinetic mechanism of the excited species of xenon in HET0D by changing the optical length d and consequently the escape factor Γ . This results in changing the contribution of radiative processes compared to collisional processes in the population of excited species which translates in return in different steady state distributions. (a) $d = 0$ and $\Gamma = 1$, (b) $d = 15 \text{ cm}$ and $\Gamma \neq 0$ and (c) $d = \infty$ and $\Gamma = 0$. Parameters: $T_e = 20 \text{ eV}$, $n_g = 1 \times 10^{20} \text{ m}^{-3}$, $T_g = 300 \text{ K}$ with the EEDF f_e following a Maxwellian distribution. The dashed line correspond to a Boltzmann equilibrium at 20 eV . .	62

-
- 4.2 Impact of electron density on excited species ratio x_p . Parameters: $T_e = 20$ eV, $n_g = 1 \times 10^{20} \text{ m}^{-3}$, $T_g = 300$ K, and $d = 15$ cm, with the EEDF f_e following a Maxwellian distribution. 64
- 4.3 Impact of electron temperature T_e on the excited species density ratio x_p . Parameters: $n_e = 1 \times 10^{17} \text{ m}^{-3}$, $n_g = 1 \times 10^{20} \text{ m}^{-3}$, $T_g = 300$ K, and $d = 15$ cm, with the EEDF f_e following a Maxwellian distribution. 65
- 4.4 The generalized twp-parameter EEPF for different shape parameters x and different effective electron temperatures T_{eff} . The gray shaded area is the range of energies greater than the xenon's first excitation energy, ie ≈ 8 eV. In (a), the generalized EEDF are computed for an effective temperature $T_e = 1.5$ eV. The tail is mainly within the threshold region. In (b), the generalized EEDF are computed for an effective temperature $T_e = 7$ eV. The bulk is mainly within the threshold region. 66
- 4.5 Impact of T_{eff} on the excited species population for different values of the shape parameter x : $x = 1.5$ (a depleted tail), $x = 1$ (Maxwellian), and $x = 0.5$ (an enhanced tail). Parameters $n_e = 1 \times 10^{17} \text{ m}^{-3}$, $n_g = 1 \times 10^{20} \text{ m}^{-3}$, $d = 15$ cm, and $T_g = 300$ K. (a) Density ratio of the ground state population to n_g (b) Density ratio of the total $1s$ population to n_g and (c) Density ratio of the total $2p$ population to n_g . 68
- 4.6 Impact of shape parameter x on the deviation from the steady-state distribution of the excited species under the Maxwellian assumption. If the density ratio of the steady state densities $\frac{n_p}{n_p^{MAXW}}$ is smaller than 1, then the excited species are less populated than at the steady state under the Maxwellian assumption and vice versa. 69
- 4.7 Impact of n_g and d on $1s5$ metastable density ratios: The density ratios of the metastable levels $1s5$ are depicted for different values of n_g and d , with $T_e = 20$ eV, $n_e = 1 \times 10^{17} \text{ m}^{-3}$, and $T_g = 300$ K. The EEDF was assumed Maxwellian. The dashed black lines correspond to constant κ values. 70
- 4.8 Effect of κ on excited species density ratios. The graph showcases the influence of the parameter κ on the density ratios of the excited species. 71
- 4.9 Example of a kinetic diagram for the ground state obtained for $n_e = 4 \times 10^{15} \text{ m}^{-3}$ and $n_g = 1 \text{ m}^{-3}$. The percentage on the arrows indicates the contribution to the population of the ground state if it is a population process or the contribution to the depopulation of the ground state if it is a depopulation process. For these plasma conditions, the kinetics is dominated by the electron impact collisions. Radiative processes though present contribute very marginally to the population and depopulation of the ground state. 72

4.10	Identification of kinetics regions based on the density ratio of the ground state and resonant levels $1s4$ densities to the total gas density at steady state in (n_e, n_g) space.	73
4.11	Zoom on the dominant kinetics in the Region II based on the density ratio of $1s5$, $2p8$ and $2p1$ at steady state in n_e - n_g space	74
4.12	Zoom on the dominant kinetics in the kinetic Region III based on the density ratio of $1s5$, $2p8$ and $2p1$ at steady state in n_e - n_g space . . .	75
4.13	Reduced kinetic diagram illustrating dominant mechanisms in the IIb and IIc subregions.	76
4.14	Simplified schematics of the Karabadzhak-Chiu-Dressler (KCD) model: (a) Diagram of the $2p$ levels included in the KCD model. The red arrows correspond to electron impact excitation, the yellow arrows correspond to radiative decay, (b) The $2p6$ level is shown as an example to highlight the stepwise excitation from the metastable to the $2p$ followed by radiative decay to $1s4$	79
4.15	Line intensity ratios as a function of T_e predicted for a HET with $V = 300$ V and $\alpha = 0.8$. In blue, the results from [Karabadzhak <i>et al.</i> 2006] and in green, the improved results from [Dressler <i>et al.</i> 2009]	82
4.16	Line ratio curves from the KCD model. A 20% error bar is used, based on the propagation of error from the previous Uncertainty Quantification (UQ) in Chapter 3.	84
4.17	Evolution of the calculated line intensity of Near Infra-Red (NIR) transitions with respect to T_e . In solid line is the output from HET0D and in dashed lines is the output from KCD	85
4.18	Comparison of line ratios in HET0D-KCD model with varying atomic data sets: blue (CS gs) changing the emission cross-section to apparent cross-section, green (Rad) including all the 22 xenon lines while keeping the emission cross-sections, dark red (CS gs + Rad) we made both changing the emission cross-section and including all 22 lines. The red curves are the ratios from the KCD model and the black curves are the ratios from HET0D	85
5.1	The simulation domain for the axial-azimuthal simulation coupled with the external circuit. (Courtesy to Federico Petronio)	91

5.2	Axial profiles averaged over 120 μs of plasma parameters: a) The normalized radial magnetic field B_z (in red), the ionization source term S_{iz} (in blue), and the axial electric field E_x (in green). The blue arrow delineates the ionization zone, while the green one defines the acceleration zone. b) Axial profiles (azimuthally and time-averaged over 120 μs) of the neutral density (in blue) and neutral axial velocity (in green). c) Axial profile of the electron density n_e . d) Axial profile of the mean kinetic electron temperature ($3T_e = T_{e,x} + T_{e,y} + T_{e,z}$). The vertical black dashed lines correspond to the position of the maximum magnetic field, which also represents the exit plane of the thruster.	93
5.3	Temporal evolution of normalised axial profiles of plasma parameters from 350 μs to 476 μs . a) The discharge current I_d b) The gas density n_g c) The electron density n_e and d) The mean kinetic electron temperature T_e . The black solid line represents the position of the maximum magnetic field, which also denotes the exit plane of the thruster. Dashed white lines help distinguish the increasing phase of the discharge current from its decreasing phase, and the dashed red line tracks the axial position of the maximum of T_e and n_e over time.	94
5.4	Evolution of the electron density during one Breathing Mode (BM) period from 380 μs to 440 μs . a) 2D map of n_e during the increasing phase of the BM. b) 2D map of n_e during the decreasing phase of the BM. c) Axial profiles of n_e at three different times of the increasing phase. d) Axial profiles of n_e at three different times of the decreasing phase. The black solid line represents the exit plane of the thruster. The dark gray stream field corresponds to the velocity field of the electrons.	95
5.5	Evolution of the mean kinetic electron temperature T_e during one BM period. a) 2D map of T_e during the increasing phase of the BM. b) 2D map of T_e during the decreasing phase of the BM. c) Axial profiles of T_e at three different times of the increasing phase. d) Axial profiles of T_e at three different times of the decreasing phase. The black solid line represents the exit plane of the thruster.	96
5.6	Axial evolution of the normalized EEDF during a) the increasing phase of the discharge current and b) its decreasing phase. The black solid line represents the exit plane of the thruster.	97
5.7	Isotropic EEDF from PIC (in blue) compared to the Maxwellian EEDF at the kinetic electron temperature T_e also from PIC for 5 axial positions (columns) and at 3 distinct times (rows) during the increasing phase of the discharge current.	98
5.8	Isotropic EEDF from PIC (in blue) compared to the Maxwellian EEDF at the kinetic electron temperature T_e also from PIC for 5 axial positions (columns) and at 3 distinct times (rows) during the decreasing phase of the discharge current.	98
5.9	Coupling methodology between CRM and PIC simulations	99

- 5.10 Validation of the time-scale compatibility between PIC and CRM. Figure a) shows the time required by the CRM to reach the steady state across the simulation domain for both Case I and Case II. It can be seen that it is well within the 80 ns of PIC time step, indicated here by the solid black line. Figure b) shows the distance traveled by the neutral particles based on their time-averaged axial neutral velocity, during the time required by the CRM to reach the steady state across the simulation domain for both Case I and Case II. It can be seen that it is well below the PIC 160 μm mesh size, indicated also by the solid black line. 100
- 5.11 Comparison of the rate of collisional depopulation of the metastables to the rate of convective transport of excited species. The blue line corresponds to the axial profile of the time-averaged, azimuthally-averaged deexcitation rate of the 1s3 metastable level. The green line corresponds to the axial profile of the time-averaged, azimuthally-averaged deexcitation rate of the 1s5 metastable level. The red line corresponds to the average convection loss rate calculated using the axial profile of the neutral velocity and density. 100
- 5.12 Synthetic spectra generated by the coupled CRM and PIC simulation: a) depicts the spectral profile during the BM growth, and subfigure and b) during the BM decay. Locations in the thruster channel and plume are indicated as $x = 18 \text{ mm}$ and $x = 36 \text{ mm}$, respectively. . . . 101
- 5.13 Evolution of the density of the excited species. The dashed black line in a) indicates the maximum in the excitation source term, while the solid black line in b) indicates the thruster's exit plane. The dashed white lines punctuate the phases of the BM. Finally, the red line in b) follows the position of the peak in the excited species densities in the thruster's channel. 103
- 5.14 Axial variation of the $\frac{I_{823}}{I_{828}}$ and $\frac{I_{835}}{I_{828}}$ line ratio for three different times of the PIC simulation. The blue curve is mid the growth phase of the BM the green curve is when the discharge current is maximum and the red curve is mid the decreasing phase of the BM. 104
- 5.15 Estimated electron temperature from the line ratios of the KCD model from Figure 4.15 based on the synthetic spectra generated from PIC results using HET0D: a) Reference T_e axial profiles from PIC simulations, b) Predicted T_e based on the $\frac{I_{823}}{I_{828}}$ line ratio and c) Predicted T_e based on the $\frac{I_{835}}{I_{828}}$ line ratio 105

5.16	Calibration abacuses generated from the complete chemistry model in HET0D. a) corresponds to the 823/828 – 835/828 abacus and b) corresponds to the 823/828 – 980/992 abacus. Both abacuses assume a constant $n_g = 1 \times 10^{19} \text{ m}^{-3}$ and $d = 10 \text{ cm}$. The 823/828 line ratio (in blue, panel a) and b)) shows mainly horizontal contour lines reflecting a sensitivity to T_e . This is the same for the 835/828 line ratio (in green panel a)). The 980/992 line ratio (in green, panel b)) show vertical contour lines reflecting on the contrary a sensitivity to n_e	106
5.17	Prediction of plasma parameters using the 823/828 – 980/992 abacus. In solid lines are the reference profiles from PIC and in dashed lines are the predictions from the abacus	107
5.18	Sensitivity analysis of T_e predictions to variations in n_g and d . In solid lines are the reference profiles from PIC and in dashed lines are the predictions from the abacus method	108
5.19	Comparison between azimuthally and time-averaged spectra profiles and plasma parameters.	109
5.20	Axial profiles of excited species density for Cases I with an isotropic EEDF (solid lines) and II with a Maxwellian EEDF (dashed lines). Panels a), b), and c) show the axial profile grouped by manifold. Panels d), e), and f) show the relative difference in density by level between Case I and Case II.	110
5.21	Time evolution of the total $6p$ manifold population for both Case I with an isotropic EEDF (solid lines) and Case II with a Maxwellian EEDF (dashed lines), emphasizing the temporal dynamics associated with the BM and the time evolution of the gap between the two cases	111
5.22	Comparison of the normalized synthetic spectra at five different positions and three times during the decay phase of the BM. Focusing on the mid-channel and ionization zone $x = 12 \text{ mm}$, 20 mm and 25 mm , the spectra reveal minimal differences, validating the use of a Maxwellian EEDF in these regions. Looking near the anode and in the far plume regions, $x = 4 \text{ mm}$ and 32 mm , some differences are observed, indicating the limitation of the Maxwellian approximation in these regions.	113
5.23	Comparison of the normalized synthetic spectra at five different positions and three times during the growth phase of the BM. Focusing on the mid-channel and ionization zone $x = 12 \text{ mm}$, 20 mm and 25 mm , the spectra reveal minimal differences, validating the use of a Maxwellian EEDF in these regions. Looking near the anode and in the far plume regions, $x = 4 \text{ mm}$ and 32 mm , some differences are observed, indicating the limitation of the Maxwellian approximation in these regions.	114

5.24	Density fluctuations of $2p8$ state during the growth and decay phases of the BM: The patterns observed here mirror the structures found in electron density and electron temperature maps.	115
5.25	Temporal evolution of the intensity of the 882 nm emission line from the side and the front views: b) Side view reveals the breathing mode oscillations, whereas c) the front view reveals small wavelengths structures.	116
5.26	Spectral analysis of the intensity of the 882 nm emission line. Dominant frequencies and their corresponding modes are highlighted. The side view spectrum notably shows the BM at 16 kHz but lacks evidence of the Ion-Transit Time Instability (ITTI). The front view notably features the Ion Acoustic Wave (IAW)/Electron Cyclotron Drift Instability (ECDI).	116
5.27	Normalized Frequency response of excited species densities. The temporal mean was subtracted to highlight the fluctuations in the excited species densities δn_p . The dark solid line corresponds to the oscillating part of the electron temperature perturbation. Here $T_{e,0} = 35$ eV, $f_{T_e} = 16$ kHz and $\delta T_e = 1\%$	118
5.28	Frequency response of the density of the excited species: Bode diagram for amplitude and phase shift. Here the input perturbation has $T_{e,0} = 15$ eV and 55 eV and $\delta T_e = 10\%$. The frequency was varied from 3 kHz to 1×10^4 kHz. Subfigure a) Bode diagram for $2p8$ level and subfigure b) for $2p1$ levels. The diagrams show the amplitude gain defined as the amplitude of the oscillation δn_p normalized by the mean value n_p times the temperature fluctuation rate δT_e	119
5.29	Spectral analysis of the density fluctuation of the $2p3$ level. Here the input perturbation has $T_{e,0} = 35$ eV and 60 eV and $\delta T_e = 1\% - 10\%$	120
5.30	Impact of collection area width on predicted axial electron temperature profiles. This graph illustrates how varying the width w of a cylindrical collection area influences the axial profiles of the electron temperature.	121
6.1	Schematic overview of the Hall-Effect Thruster experimental setup. The figure illustrates the four primary components involved: the vacuum system (colored in orange), the gas injection system (green), the electrical circuit (blue), and the thruster itself (red). Each component is color-coded for easy identification and will be discussed in detail in the following sections.	127
6.2	Front view (left) and lateral view (right) of the Propulseur à Plasma Stationnaire (PPS)X00-CHEAP Hall-Effect Thruster. The origin $(0,0,0)$ is defined at the intersection of the thruster's axis and its exit plane.	127

6.3	Axial and radial evolution of the radial component of the magnetic field. $z = 2.3$ cm corresponds to the mid-radius of the channel and measurements were made parallel to the thruster's axis. The position $x = -0.7$ cm corresponds to the axial position at which the radial magnetic field was maximum. Measurements were made inside the channel from the inner wall to the outer wall.	129
6.4	Relationship between the chamber pressure and xenon mass flow rate while the thruster is off.	130
6.5	Current-voltage characteristics of the PPSX00-Compact Hall Effect Advance Propulsion System (PPSX00-CHEAP). The transparent envelope corresponds to the standard deviation of the current signal. Solid lines are for a cathode flow of $q_c = 0.6$ mg.s ⁻¹ with for each color a different value of the anode flow rate. The dashed line is for an anode flow of 2.5 mg.s ⁻¹ and a cathode flow of $q_c = 0.4$ mg.s ⁻¹ . . .	131
6.6	Top view of the experimental setup consisting of a 500 W Hall effect thruster, a Langmuir probe placed at $z = 6$ cm from the exit plane of the thruster, a 50 cm-focal length lens in a $2f - 2f$ configuration, an Avantes Spectrometer, optical fiber and a collimator for visible and near-infrared wavelengths. The origin of the frame of reference is placed on the intersection between the axis of the thruster and its exit plane.	132
6.7	Background noise subtraction: The solid transparent blue corresponds to a typically measured spectrum. After filtering, we separate the random noise component (red) from the dark background (dark blue).	134
6.8	Relative intensity calibration. Left panel: Normalized irradiance of Configuration 1 (green) and Configuration 2 (red) from the Deuterium Halogen light bulb (blue). Right panel: Normalized spectral response of Configuration 1 R_1 and Configuration 2 R_2	135
6.9	Schematics of the Langmuir probe measurements geometry. The probe is placed at a fixed $x = 6$ cm and is able to move in the $y - z$ plane.	136
6.10	Comparison of the electron temperature and density before and after the correction at low electron energy of the EEPF. Compensating for the depletion of the EEPF at low energy results in increasing the electron density and reducing the electron temperature.	138
7.1	Front view (left) and lateral view (right) of the PPSX00-CHEAP Hall-Effect Thruster. The origin $(0, 0, 0)$ is defined at the intersection of the thruster's axis and its exit plane.	140
7.2	The measured EEDF at different radial positions z at $y = -1$ cm and $x = 6$ cm within the thruster's plume.	141

7.3	Radial profiles of electron temperature and density after the processing of the EEDF at three different lateral positions at $x = 6$ cm. Higher values are observed near the thruster axis, diminishing towards the plume's periphery. The dashed line represents the Gaussian fit to the data.	141
7.4	2D map depicting the spatial distribution of electron temperature and density derived from the Langmuir probe measurements at $x = 6$ cm. A hot core near the thruster axis that cools while advancing toward the chamber walls is shown. The 2D image was smoothed using a 2D Gaussian filter.	142
7.5	Plot of electron temperature as a function of electron density. The points are fitted to an isentropic expansion with an exponent $\gamma = 1.29$ (red dashed curve).	143
7.6	Evolution of line intensities in the lateral direction along the y axis (Configuration 1 of Figure 6.6).	145
7.7	Comparison of ionic and neutral emission lines at three distinct lateral positions: peripheral ($y = -5$ cm), plume center ($y = 0$ cm), and near the cathode ($y = 3$ cm) in Configuration 2 of Figure 6.6.	146
7.8	Spectra along the thruster's axial direction in Configuration 1 of Figure 6.6.	147
7.9	Spatial evolution of emission lines intensities along the axial direction.	148
7.10	Effect of the anode voltage on the intensity of selected emission lines.	148
7.11	Effect of the anode flow on the intensity of selected emission lines. .	148
7.12	Emission spectra at different radial positions. The zoomed axes correspond to the 540 nm to 750 nm range containing several Xe^+ lines.	150
7.13	Spatial gradient of several neutral lines along the radial direction. . .	150
7.14	Intensity evolution of neutral and ionic lines at different radial positions, concerning the anode voltage: a) at $z = -2.35$ cm (inside the channel) and b) at $z = 0$ cm (center of symmetry of the thruster). In green are the 597 nm and 604 nm ion lines and in blue are the 881 nm and 823 nm neutral lines.	151
7.15	Intensity evolution of neutral and ionic lines in the channel, concerning the anode flow injection. In green are the 597 nm and 604 nm ion lines and in blue are the 881 nm and 823 nm neutral lines. Note the change in the line ratio which reflects the sensitivity to T_e	152
7.16	Gaussian profile fit of the 882 nm line	153
7.17	Schematic representation of the optimization process relating the CRM to the plasma parameters.	155
7.18	Illustration of the Langmuir measurement comparison to the OES. Each measurement with OES corresponds to 15 measurements (yellow) with a Langmuir probe along the line of sight (green).	156

7.19	Lateral profiles of the electron temperature and density as determined by Langmuir probe measurements, alongside predictions from the CRM. In blue are the predictions of the CRM. In green are the line-of-sight plasma parameters derived from Langmuir probes using Eq. (7.7). In red is the arithmetic average along the line of sight. Note that in this graph, one spectra (blue data point) corresponds to the average of 15 Langmuir probe measurements (green or red points)	157
7.20	Lateral profiles of neutral gas density illustrating the comparison between CRM predictions and the pressure gauge reading (dashed horizontal line) converted into a density based on ideal gas law $P = nk_bT_g$: $P = 1.6 \times 10^{-3}$ mbar and $T_g = 640$ K (T_g is not measured on the setup and the value used here is the same used in the optimization for consistency).	158
7.21	Axial profiles of CRM-predicted electron temperature for different operational conditions.	160
7.22	Axial profiles of CRM-predicted electron densities for different operational conditions.	161
7.23	Axial profiles of CRM-predicted gas densities for different operational conditions.	161
7.24	Radial profiles of CRM-predicted electron temperature for different operational conditions.	162
7.25	Radial profiles of CRM-predicted electron densities for different operational conditions.	162
7.26	Radial profiles of CRM-predicted gas densities for different operational conditions.	162
7.27	Dependence on the anode voltage of T_e and n_g predicted from the CRM at $z = -2.35$ cm (the thruster channel) and $z = 0$ cm (the thruster center) for a flow rate at $2.5 \text{ mg}\cdot\text{s}^{-1}$.	163
7.28	Dependence on the rate flow of T_e and n_g predicted from the CRM at $z = -2.35$ cm (the thruster channel) and $z = 0$ cm (the thruster center) for a voltage at 105 V.	164
7.29	Comparison between a 3-variable and a 4-variable formulation of the CRM optimisation problem. The blue circles are superposed to the green squares on the left Figure a). On the right Figure b), we can see that the n_g prediction between the two formulations is very different. The 4-variable formulation exhibit a fluctuating profile compared to the smooth profile for the 3-variables formulation.	165
7.30	Axial profiles of CRM-predicted electron temperature for different operational conditions using the cost function from Eq. (7.8). The trends are similar to the results reported in Figure 7.21. However, the values are smaller.	166
7.31	Model-derived map of neutral density in the plume.	167
7.32	Normalized neutral density, illustrating optical length evolution in the plume.	167

7.33	Comparison between PIC simulations and CRM predictions at $U_a = 200$ V and $q_a = 2$ mg.s ⁻¹ for the experiment and $U_a^{PIC} = 300$ V and $q_a^{PIC} = 2$ mg.s ⁻¹ a) Comparative overview of CRM predicted and PIC T_e profiles b) Comparative overview of experimental, CRM-predicted, and PIC-resultant synthetic spectra at $x = 1$ cm.	170
8.1	Representation of the perceptron with n inputs x_i . Each is weighed with w_i before being summed with the summation operator Σ . A bias b is added to the result before passing the result to the activation function σ to yield the output y	175
8.2	Canonical illustration of the general architecture of an ANN. The ANN here consists of 2 hidden layers. The inputs are forward propagated from one layer to another. The resulting output is tested against the validation data during the Training stage. If the ANN prediction is not satisfactory, then the ANN is re-trained. Otherwise, the trained model is deployed on new data.	176
8.3	Example ANN with 2 hidden layers, an input layer, and an output layer. Each perceptron is indicated by u_i^j with j as the rank of the layer and i as the rank of the perceptron within the layer. The weights are indicated with $w_{i,k}^{(j)}$ representing the weight from the perceptron i to k at the input of the layer j . The activation function is not indicated here and is assumed constant across the ANN.	177
8.4	Typical workflow for developing ANNs	180
8.5	Schematic representation of the learning process for inverting the HET0D CRM. This figure illustrates the development of ANNs to predict the electron temperature T_e based on optical emission data.	182
8.6	Performance of the selected ANN model learning the CRM. a) shows the distribution of R^2 testing scores in cross-validation across the 1000 train-test pairing. b) shows the evolution of the R^2 score with the size of the training set. The testing set was unchanged and corresponded to a third of the dataset.	184
8.7	Comparison between the results from the CRM via a basin hopping least square optimization (fine solid lines) with the results from the ANN predictions (scatter plot with dashed lines). This comparison involves experimental spectra from the axial scans in Chapter 7.	185
8.8	Schematic representation of the learning process for macroscopic parameters in HET. This figure illustrates the development of ANNs to predict the anode voltage U_a , discharge current I_d , anode flow rate q_a , and coil current I_b based on optical emission data.	186
8.9	Experimental setup in PIVOINE 2G vacuum chamber. The collimated optical fiber is pointing at the thruster's exit plane perpendicular to the thruster's axis. The origin of the x axis is placed at the exit plane of the thruster.	187

8.10	Time evolution of the normalized values of the operation parameters during the acquisition of the spectra. For a given flow rate q_a , the coil current I_b was changed at increments of $\delta I_b = 0.2$ A and the anode voltage U_a described a ramp.	188
8.11	Histograms for the explored operation parameters before and after data cleaning. After the cleaning, the data is uniformly distributed. .	189
8.12	Spectral Line Selection for Target Parameters. The figure shows the histogram with the normalized scores of the 8 best-scoring features based on the F-Test (blue) and Mutual Information (MI) test (green). 191	191
8.13	Distribution of R^2 scores for the selected models for each operation parameter from cross-validation across 10000 models. Opaque colors correspond to test scores when evaluating the model on the test data and transparent color is the training score when evaluating the model on the training data.	193
8.14	Distribution of Mean Absolute Error (MAE) and the root of the Mean Squared Error (MSE) scores for the selected models for each operation parameter from cross-validation across 10000 models. Opaque colors correspond to test scores when evaluating the model on the test data and transparent color is the training score when evaluating the model on the training data.	194
8.15	predicted vs. target values for four parameters. The orange line corresponds to the line $y = x$. The predictions align around this line, illustrating the performance of the model. The uncertainty envelope is a 3σ envelope based on the root of the average MSE score.	195
8.16	Comparison of the performance of different learning models. Linear models have a competitive performance on q_a and I_d , while ANN outperforms these models for U_a and I_b	196
8.17	Impact of learning on a specific range of flow rate instead of training on random sampling.	197
8.18	Block diagram for the PID controller.	198
8.19	Control results from the first and second studies. Voltage and flow rate are controlled at a fixed flow rate and a fixed voltage respectively. 200	200
8.20	Control results from the third study. Voltage and rate flow are controlled simultaneously.	201
8.21	Impact of changing the magnetic configuration on the stability of the control. Oscillations appear at 12.5 s.	202
B.1	Illustration of the angular momentum coupling between the core and the optical electron relevant to Racah's coupling scheme	217
C.1	Excitation cross-section from the ground state to the 6s levels from the BSR dataset (solid line) and BIAGI dataset (dashed lines).	220

C.2	Comparison of the total excitation cross-section from the ground state to the $6s$ levels from the BSR dataset (solid line) and BIAGI dataset (dashed lines).	220
C.3	Comparison of the total excitation cross-section from the ground state to the $6p$ levels from BSR dataset (solid line) and BIAGI dataset (dashed lines), Fons & Lin measurements (dotted line).	222
C.4	Comparison apparent and direct section from the ground state to the $6p$ levels from Fons & Lin measurements.	223
C.5	Comparison of direct excitation cross-section from the $11s5$ to $6p$ from BSR dataset (solid line) and FONS dataset (dashed lines).	224
C.6	Comparison of direct excitation cross-section from the $6s$ to the $6p$ levels from BSR dataset (solid line) and Priti dataset (dashed lines).	225
C.7	Comparison of the direct excitation cross-section from the $6s$ levels to the $6s$ levels from the BSR dataset (solid line) and PRITI dataset (dashed lines) and the FONS dataset (dotted line).	226
C.8	Excitation cross section for the collisional mixing inside the $6p$ levels.	227
C.9	Difference in the energy of the excited species provided by the NIST to those BSR and those of PRITI. The light green region indicates an overall deviation that is less than 0.05 eV .	228
C.10	Ratio of the Einstein coefficients and oscillators strength provided by the NIST to those of BSR and those of PRITI. The light green region indicates a deviation that is less than a factor of 2.	229
E.1	Kinetic diagram for Xe ground state. The number on the line is the percentage contribution of the process to production or depopulation of the level. These contributions were estimated using HET0D with the following parameters: $T_e = 20\text{ eV}$, $n_e = 4 \times 10^{15}\text{ m}^{-3}$, $n_g 1 \times 10^{20}\text{ m}^{-3}$ and $T_g = 300\text{ K}$, $d = 15\text{ cm}$ and a Maxwellian EEDF.	233
E.2	Kinetic diagram for Xe($1s$) states.	234
E.3	Kinetic diagram for Xe($6p'$) states.	234
E.4	Kinetic diagram for Xe($6p$) states.	235

List of Tables

3.1	Xenon energy levels in Paschen and Racah notations	29
3.2	Radiative transitions from $6s$ and $6p$ levels. The Einstein coefficients are collected from National Institute of Standards and Technology (NIST) and are expressed in units of 10^6 s^{-1}	31
3.3	List of the databases investigated in this work in Appendix C	35
3.4	The collisional processes included in our model. The third column gives the references for the cross sections	42
4.1	Population rate ratio of $6p$ states from three groups of processes: (a) ground-state excitation by electrons and radiative decay from high-lying levels, (b) excitation or deexcitation by electrons from metastable or excited levels, and (c) self-absorption. The ratio of (c) is omitted when very small. This table was transcribed from the work of [Zhu <i>et al.</i> 2019]. The levels were conveniently renamed in Paschen's notation for the sake of consistency with this work. The ratio is reported as follows: Group (a): Group (b): Group (c). The last column reports the values found in HET0D in the region II d with $T_e = 20 \text{ eV}$, $n_e = 1 \times 10^{16} \text{ m}^{-3}$, $n_g = 1 \times 10^{20} \text{ m}^{-3}$ and $T_g = 300 \text{ K}$, $d = 15 \text{ cm}$ and a Maxwellian EEDF.	77
4.2	NIR xenon emission line from the $6p$ tier included in the KCD model. Only the intensities of the lines with the superscript "a" are calculated with the Eq. (4.6). The 895.2 and the 992.3 transitions are included to close the kinetic scheme on the $2p6$ and $2p9$ and create a realistic depopulation pathway	80
4.3	Parameters involved in the high energy extrapolation from [Chiu <i>et al.</i> 2006, Karabadzhak <i>et al.</i> 2006]	81
4.4	Highlight of the differences between KCD, HET0D-KCD and HET0D	83
5.1	Parametric space for the analysis of the CRM time response	118
6.1	Nominal Operating Parameters of the PPSX00-CHEAP Thruster	128
7.1	Operational parameters for axial scan analysis	145
7.2	Operational parameters for radial scan analysis	149
7.3	Simulation parameters for the PIC simulation used for the comparison with the CRM.	169
8.1	Range of plasmas parameters used to generate the synthetic spectra with the CRM	182
8.2	Range and distribution of the hyperparameters explored in the random grid search for tuning of the ANN	183

8.3	Hyperparameters of the best-performing model from the cross-validation results	184
8.4	Range of the explored operating conditions of the thruster during the acquisition of the spectra.	188
8.5	List of the four best scoring lines selected based on the F-scores and MI scores for each of the four target parameters. The ionic lines are put in bold	192
8.6	Range of hyperparameters explored in the random grid search for tuning the ANN predicting the operation parameters of the thruster.	192
8.7	Hyperparameters of the best models for each operation parameters obtained from the cross-validation results	193
8.8	Coefficients of the PID Controller	199
8.9	The target values for the third simulation	199
F.1	Radiative Rates [Rutten 2003]	237

List of Acronyms

ADAM Adaptive Moment	178
ANN Artificial Neural Network	6
ANN-PID Adaptive Neural Network PID	202
BM Breathing Mode	4
BSR B-Spline R-matrix cross sections	33
CHT Cylindrical Hall Thruster	4
CRM Collisional Radiative Model	5
PPSX00-CHEAP PPSX00-Compact Hall Effect Advance Propulsion System	131
CTS Collective Thomson Scattering	5
DLS Deep Learning Spectroscopy	174
ECDI Electron Cyclotron Drift Instability	5
EEDF Electron Energy Distribution Function	6
EEPF Electron Energy Probability Function	39
EVDF Electron Velocity Distribution Function	99
EP Electric Propulsion	1
FFT Fast Fourier Transform	115
HET0D Hall Effect Thruster 0D	7
HET Hall-Effect Thruster	2
IAW Ion Acoustic Wave	5
ITTI Ion-Transit Time Instability	4
KCD Karabadzhak-Chiu-Dressler	62
LPP Laboratoire de Physique de Plasmas	6
LTE Local Thermodynamic Equilibrium	26
LEO Low Earth Orbit	2
MC Monte Carlo	56

MI Mutual Information	190
ML Machine Learning.....	174
MAE Mean Absolute Error	179
MSE Mean Squared Error	179
NIST National Institute of Standards and Technology.....	31
NIR Near Infra-Red.....	37
ODE Ordinary Differential Equations	45
OES Optical Emission Spectroscopy	4
PID Proportional-Integrator-Derivative controller	173
PIC Particle-In-Cell.....	6
POSEIDON <i>future Plasma thrusters for lOw earth orbit SatEllite propulsiON systems</i>	6
PPS Propulseur à Plasma Stationnaire	4
PPU Power Processing Unit	92
RDW Relativistic Distorted Wave.....	34
ReLU Rectified Linear Unit.....	176
SPT Stationnary Plasma Thruster	36
UQ Uncertainty Quantification.....	55

Introduction

Light is therefore colour.

William Turner

Contents

1.1	Electric propulsion and Hall effect thrusters	1
1.2	Challenges	3
1.3	Thesis context, content and objectives	6

1.1 Electric propulsion and Hall effect thrusters

The emergence of micro reusable launchers and the increasing popularity of "ride-share" for satellites have led to significant cost reductions for space operators. This has not only opened doors for the deployment of commercial satellite constellations but has also expanded the horizons of space exploration. It has created a growing demand for standardized and miniaturized equipment for satellites, hence reducing the structural mass for the benefit of the payload. In the past, propulsion systems' robustness and reliability have been a major shortcoming for the satellite market. However, the situation has improved today with the availability of many capable propulsion systems as well as associated components, enabling control of attitude, changes in orbit, and other complex space maneuvers [Miller & Woellert 2020]. This has sparked the interest of the space industry for Electric Propulsion (EP) systems. Indeed, compared to traditional propulsion systems, EP can produce a wide range of exhaust velocities, from $1 \text{ km}\cdot\text{s}^{-1}$ to $100 \text{ km}\cdot\text{s}^{-1}$ [Choueiri 2009], which enables spacecraft to achieve higher velocities while consuming less propellant. Nevertheless, this comes at the expense of lower thrust density, hence a longer transfer time.

Broadly speaking, EP systems are elements of the spacecraft that harness the solar panel-generated electric power, converting it into kinetic energy delivered to the propellant through electromagnetic forces. The concept of EP dates back to as early as 1906, with pioneers Robert Goddard and Konstantin Tsiolkovsky. However, in-orbit demonstrations were not until the early 1980s when EP gained widespread recognition and adoption within the aerospace industry, owing to its versatility and robust designs. These systems can employ various field and current types, including steady, pulsed, or alternating configurations while offering flexibility in

magnetic field sources and a choice of solid or liquid propellants with diverse geometries and densities [Jahn & Choueiri 2003]. Today, electric propulsion stands as the standard propulsion solution for orbit maintenance across commercial, military, and scientific satellites in Earth’s orbit [O’Reilly *et al.* 2021]. Furthermore, the extended lifetime of the propellant utilization makes EP invaluable for space missions venturing beyond the Earth’s orbit, paving the way not only to scientific interplanetary missions, such as ESA’s BepiColombo [Clark *et al.* 2013] or NASA’s Psyche [Snyder *et al.* 2020] but also manned space travel.

Among the technologies meeting the rising demand in this sector, Hall-Effect Thruster (HET)s play a pivotal role. HETs distinguish themselves from other electric propulsion methods with their high thrust-to-power ratio, specific impulse, total efficiency, extended operational lifetime, and reduced mass. Consequently, they have witnessed a growing preference for a wide array of space missions and maneuvers requiring significant velocity increments. Today, HETs have a rich flight heritage [Mazouffre 2016], ranging from drag compensation and trajectory correction for Low Earth Orbit (LEO) satellites [Cornara *et al.* 2012] to full orbit transfer for deep space missions [Koppel *et al.* 2004, Jackson *et al.* 2018, Snyder *et al.* 2020].

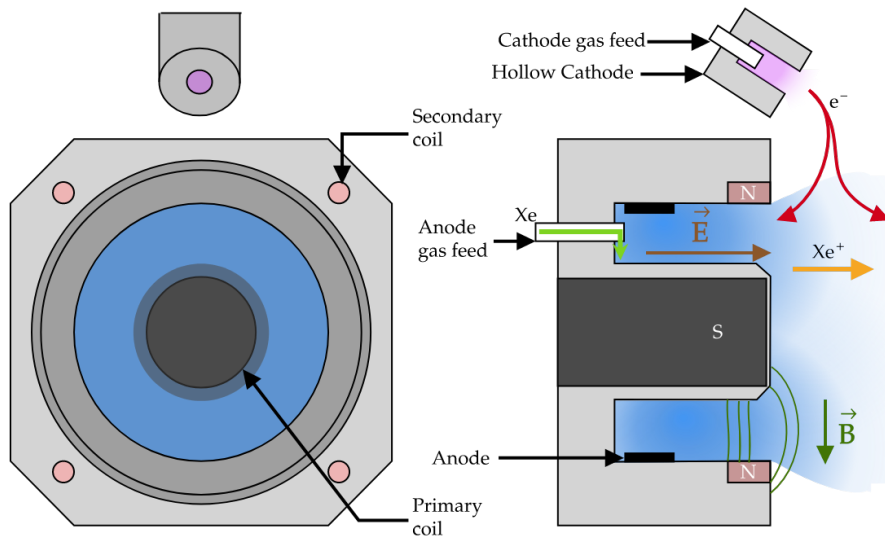


Figure 1.1: Schematic of the operating principle of a HET. Neutral xenon is injected from the anode. Electrons that are emitted from the cathode are trapped by the radial magnetic field, hence increasing the collision frequency with the neutral gas and leading to the production of electron-ion pairs. Ions are exhausted out of the channel under the effect of the electric field, creating thrust.

HET (Figure 1.1) consists typically of an axisymmetric discharge chamber housing an internal anode and an externally mounted cathode. The propellant is injected at a very low velocity at the anode. Then, a voltage drop is applied, which estab-

lishes an electric field along the symmetry axis. The electric field accelerates the electrons that are emitted by the cathode discharge toward the entrance of the discharge channel. When the electrons reach the latter, they are subject to a strong radial magnetic field, trapping them in an $\mathbf{E} \times \mathbf{B}$ drift. This drift reduces their mobility, hence, increasing the frequency of ionizing electron-neutral collisions and consequently the production of electron-ion pairs. The positively charged ions are un-magnetized and are accelerated out of the thruster by the axial electric field, while the electrons are re-trapped by the magnetic field promoting further ionization and thereby enhancing the thrust density. Additional electrons are emitted from the cathode and are supplied to the downstream discharge to keep the plume of the thruster quasi-neutral. The most commonly employed propellants in HETs are noble gases, xenon mainly because they are chemically inert, easily ionized, and safe to handle at standard conditions.

1.2 Challenges

Despite the maturity of the technology and the rich flight heritage, HET faces still several challenges that restrict its current performance. First, alternative propellants to noble gases are being actively explored, such as bismuth [Szabo *et al.* 2017], adamantane [A. Bretti 2022], molecular gas mixtures similar to the upper atmospheric conditions of Earth [Andreussi *et al.* 2022, Tejada & Knoll 2023], and halogen iodine [Szabo *et al.* 2013]. This is still a part of the current research and has become a recent economic priority given the soaring prices of noble gases and the inadequacy of the current production means to meet the increasing rate of demand. Along with the quest for alternative propellants, the current development activity on HET actively aims at expanding their capabilities and reducing their size [Levchenko *et al.* 2020]. Alongside efforts to enhance efficiency and thrust levels, there is a strong focus today on increasing the thruster's lifetime, widening its operational envelope, and simplifying the overall system. One significant challenge that affects the lifetime is the erosion of the electrodes. Recent advances in magnetically shielded thrusters [Garrigues *et al.* 2019, Grimaud & Mazouffre 2017] and the concept of wall-less HET [Mazouffre *et al.* 2014] have shown promising results in mitigating this issue, albeit with a slight reduction in efficiency at lower power levels. The magnetic field topology is also a key area of exploration. Researchers are investigating more sophisticated configurations to enhance the degree of ionization within the channel, including the implementation of a pre-ionization helicon stage [Shabshelowitz *et al.* 2014], an RF antenna [Bugrova *et al.* 2012] or the utilization of a two-peak magnetic field topology [Perez-Luna *et al.* 2007]. Finally increasing the power envelope of HETs is also a crucial aspect of current research and an effective candidate is using a nested configuration consisting of multiple thruster channels within a single system which allows the division of the power load and effectively achieves higher thrust regimes [Cusson *et al.* 2018].

Looking ahead, the miniaturization of HETs is expected to align with

the increasing demand for smaller, low-mass spacecraft. One potential candidate for miniature HET is the Cylindrical Hall Thruster (CHT) [Smirnov *et al.* 2002, Smirnov *et al.* 2006, Smirnov *et al.* 2007, Smirnov *et al.* 2008, Garrigues *et al.* 2008] which demonstrates an efficiency that is comparable to its traditional counterpart. Over the years, various scaling methodologies have been developed to explore the possibilities of scaling down the size of HETs [Khayms & Martinez-Sanchez 1996, Warner 2007, Dannenmayer & Mazouffre 2011, Andrenucci *et al.* 2005]. While there are established methods to overcome the challenges of scaling HETs to larger sizes, decreasing their sizes appears to have some fundamental limits. Indeed, as the size of the channel decreases, a higher magnetic field is required to maintain a decent mass utilization efficiency. However, the implementation of the magnetic field requirement is still technically challenging because the magnetic circuit in such a small space would leave no room for magnetic poles and heat shields, hence increasing ion and power losses, heating, and erosion. In addition, the ratio of surface-to-volume increases requiring a deeper characterization of plasma/wall interactions and the testing of new wall materials to limit erosion. Furthermore, the quest for miniaturization extends beyond the thrusters themselves to the diagnostics used to study and evaluate their performances. The reduction in the device scale inevitably poses difficulties and invasiveness when using direct measurement approaches. Consequently, there is a growing interest today in optical measurement techniques as a viable solution for diagnosing and monitoring miniaturized HETs, either in test facilities or in orbit, for instance via the use of Optical Emission Spectroscopy (OES). The development of such techniques is not only relevant to the study of small-scale HETs but also to the characterization of any type of EP system due to their noninvasive nature.

Second, the change of scale also brings up the question of its impact on plasma instabilities in HETs. Due to the presence of gradients in different directions, multiple instabilities can grow and interact together, covering a broad range of frequencies. The most prominent ones in HETs, such as the Propulseur à Plasma Stationnaire (PPS)-1350 of *Safran*, are:

- The low-frequency Breathing Mode (BM) which is an ionization wave characterized by kHz-level oscillations in the discharge current of HETs. These oscillations, which can reach amplitudes as high as 100% of the mean discharge current, pose operational challenges. The commonly adopted explanation is a predator-prey model between neutrals and plasma, involving ionization and neutral replenishment. However, the exact onset criteria for BM oscillations remain undefined and require further investigation.
- The intermediate-frequency Ion-Transit Time Instability (ITTI) which occurs in the range of hundreds of kHz. It is related to the transit time of ions within the acceleration region of HETs. The ITTI results in variations in plasma potential and ion velocity, causing oscillations in the discharge properties. The "wave-riding" mechanism, where ions gain or lose energy from the wave,

contributes to this instability. The precise criteria for its onset are still not well-defined, necessitating ongoing research.

- The high-frequency Electron Cyclotron Drift Instability (ECDI), typically in the MHz range, which arises from the coupling between electron Bernstein modes and ion acoustic modes. The ECDI exhibits short wavelengths and dominant propagation in the azimuthal direction. While the linear stage of the ECDI is well understood and translates usually into an Ion Acoustic Wave (IAW), the transition to the nonlinear regime and saturation mechanisms are areas of ongoing research.
- Other instabilities include azimuthally rotating modes like "rotating spokes" and "gradient-induced instabilities" with frequencies in the 10-100 kHz range. These instabilities are related to ionization inhomogeneities and gradients in density and magnetic field. While they have been observed and studied, they are generally less concerning for HET operation and do not represent significant issues.

Understanding these instabilities is important due to their nonnegligible contribution to electrode erosion as well as to electron mobility, which is the second source of performance limitation of HETs. Over the years, extensive research has been conducted to identify and analyze the various factors contributing to electron mobility, with ECDI emerging as a key driver, as demonstrated by both simulations [Adam *et al.* 2004, Lafleur *et al.* 2017], Collective Thomson Scattering (CTS) [Tsikata *et al.* 2009, Tsikata *et al.* 2010, Tsikata *et al.* 2013, Tsikata *et al.* 2014] and different probe techniques [Lazurenko *et al.* 2007a, Brown & Jorns 2019, Kaganovich *et al.* 2020].

Finally, the change in the scale also prompts a reconsideration of the approaches employed for exploring novel designs, which, until now, have largely relied on a trial-and-error methodology. Issues such as performance characterization and cost reduction are of central interest to the industry stakeholders. As far as thruster design is concerned, significant efforts have been put into simulations, both kinetic and fluid, to self-consistently simulate the plasma and provide a fast-reliable tool for better designs and performances. Nevertheless, the simulations need to be validated against experiments, which requires a framework capable of accounting for the inherent differences between the experiments and simulations as well as challenging their assumptions. As far as monitoring the thruster's performance in test facilities or orbit is concerned, optical diagnostics, such as CTS and OES have proven, to be extremely promising to non-invasively determine the plasma parameters. However, involved, CTS is not ideal for thruster manufacturers for monitoring purposes, while, on the other hand, OES can easily provide an optical footprint, that reflects the discharge parameters. This is achieved by using a Collisional Radiative Model (CRM). This model is a 0-dimensional model relating the emission spectra to the plasma parameters via a detailed description

of the kinetic mechanisms that lead to populating the radiative excited states [Karabadzhak *et al.* 2006, Zhu *et al.* 2019, Priti *et al.* 2019a].

1.3 Thesis context, content and objectives

The *future Plasma thrusters for lOw earth orbit SatEllite propulsiON systems* (POSEIDON) project at Laboratoire de Physique de Plasmas (LPP) has been dedicated to advancing the field of EP, with a primary emphasis on numerical simulations from 2016 to 2022 and it was financially supported by the national research agency ANR and Safran. A significant milestone within this project is the *LPPic* Particle-In-Cell (PIC) code, involving collaborative efforts with Safran, as documented in prior theses by [Tavant 2019, Charoy 2020, Petronio 2023]. This previous work focused extensively on the study of plasma dynamics within the radial-azimuthal and axial-azimuthal planes of HET. Moreover, they explored plasma-wall interactions, leading to the introduction of a conceptual "virtual radial direction" to account for losses at the walls. The *LPPic* code was also part of two international benchmarks in 2019 [Charoy *et al.* 2019, Villafana *et al.* 2021].

Building upon this solid numerical foundation, the present work introduces an optical diagnostic aimed at characterizing the Electron Energy Distribution Function (EEDF) within the HET channel. This distribution function stands as a pivotal factor in predicting the anomalous transport phenomena that theoretical and simulation studies have consistently investigated. The overall objective of this research effort unfolds into two primary goals: firstly, the validation of existing simulations within *LPPic*, and secondly, the development of a diagnostic tool favorable to an in-orbit evaluation of HET performance. The significant contributions within this thesis are delineated as follows:

- The establishment of a comprehensive framework to compare numerical simulations and experimental data.
- The development of an optical diagnostic based on OES, CRM, and Artificial Neural Network (ANN) to effectively characterize the in-orbit performance of HET.
- The verification of theoretical predictions and the validation/challenge of numerical simulation codes.

The distinctive aspect of the research methodology in this thesis is the integration of simulations to guide and inform the experimental designs. This novel approach revolves around the concept of virtual diagnostics, paving the way for a dual understanding of simulations and diagnostics. This is structured as follows:

- The initial step looks into the anomalous transport within *LPPic* simulations via the implementation of the virtual equivalent of CTS diagnostic. The choice of CTS is justified because it is the diagnostic most adept at investigating the

millimeter scale of the **ECDI**. This will serve to prove the relevance of the virtual diagnostic framework.

- The subsequent phase encompasses the development of a **CRM** for xenon. This step is essential to generate emission spectra from **PIC** simulations and to allow virtual **OES**.
- The third axis of this research involves the use of the **PIC** simulations from *LPPic*, in conjunction with the **CRM**. This approach enables the prediction of numerical emission spectra, which will be compared to experimental spectra, thereby offering an essential validation layer for the simulation outcomes.
- The final phase consists of a series of experiments to validate the simulations and the **CRM** and gain further insights into their correlation with real-world scenarios as well as to prove that **OES** can effectively characterize **HET**.

The thesis unfolds across eight chapters, each contributing to the previous objectives:

- Chapter 2 introduces the concept of virtual diagnostics, within the context of the **CTS** diagnostic. Building upon prior work by [Honoré *et al.* 2011], this chapter contextualizes it within a recent, highly resolved 2D **PIC** axial-azimuthal benchmark test case developed by [Charoy *et al.* 2019]. This chapter endeavors to identify the principal parameters influencing the evaluation of electron density fluctuation rates and to understand the difference between **PIC** simulations and **CTS** experiments. The approach consists of applying a Gaussian-windowed Fourier transform of 2D electron density maps from **PIC** simulations which are interpreted/processed as a **CTS**-like signal.
- Chapters 3 and 4 introduce the Hall Effect Thruster 0D (**HET0D**) code, a **CRM** developed during this Ph.D., capable of accounting for both argon and xenon. The focus of the manuscript will be on xenon only. These chapters provide a comprehensive exploration of the major collisional and radiative processes that influence the population densities of neutral $6p$ levels. Detailed discussions of the model's development, including key assumptions, are presented. These chapters serve to establish a solid foundation, elucidate challenges, and pose multiple questions regarding cross-sections, validation procedures, and sensitivity analyses within **CRM** and plasma modeling in general.
- Chapter 5 establishes the framework for performing **OES** on **PIC** simulations. This approach allows us to critically evaluate several assumptions within **PIC** simulations, particularly about the neutral model and the impact of boundary conditions on dominant kinetic mechanisms within the plasma discharge. Additionally, it challenges assumptions inherent to the diagnostics itself, such as neglecting the metastable transport and assuming a Maxwellian **EEDF** for the **CRM** calculations. This chapter also sheds light on the dynamic coupling occurring between plasma dynamics and light emission.

- Chapters 6 and 7 shift the focus towards the experimental domain, detailing the setup designed to compare PIC spectra with experimental spectra. These chapters encompass the extraction of plasma parameters across various thruster operating conditions, proving the relevance of OES and CRM in characterizing HET performance during in-orbit operations.
- Chapter 8 addresses limitations inherent in the prior implementation, primarily reliant on a time-consuming least-square optimization approach, and endeavors to enhance it through the integration of ANN. This pioneering effort places radiative emission at the crossroads, enabling the probing of both plasma parameters, particularly the electron temperature, and macroscopic parameters, including discharge voltage and xenon injection flow rate.
- Chapter 9 concludes the thesis with key findings and contributions in this work. It also outlines recommendations for future research in EP using OES and engenders a discussion on potential improvements to CRM.

Analysis of Hall Effect Thruster Using Virtual Collective Thomson Scattering on Particle-In-Cell Simulations

Ensemble, nous considérons la pleine lune qui se balançait là-haut dans le ciel. Le vent du soir s'élevait et, au travers du firmament, une procession de nuages blancs tourbillonnait avec la rapidité de grands oiseaux blancs, tantôt obscurcissant la face de la lune, tantôt la laissant d'une pureté magique.

Pearl Buck, *Vent d'Est, Vent d'Ouest*

Contents

2.1	Methods	11
2.1.1	Axial-azimuthal PIC simulation	11
2.1.2	Collective Thomson scattering analysis	15
2.1.3	Pre-processing of the PIC results	18
2.2	Results	18
2.2.1	Amplitude variation of the dominant modes	18
2.2.2	Dispersion relation	20
2.2.3	Electron density fluctuation rate	21

*This chapter is an adaptation of the following published article
[Ben Slimane *et al.* 2022b].*

Introduction

To motivate developing virtual OES for PIC simulations, we start with implementing a virtual CTS because it is a well-established diagnostic in the EP community to investigate the anomalous electron transport, a central challenge in HET to the understanding of the electron anomalous mobility. Several contributions to the anomalous

mobility have been extensively studied throughout the years [Taccogna *et al.* 2009, Raitses *et al.* 2011, Frias *et al.* 2012] and recently the ECDI was identified as a key driver for electron transport. Indeed, the asymmetry between the electron fast azimuthal motion and the ions' axial motion creates a kinetic, MHz (millimeter scale) azimuthal instability that was observed in PIC simulations [Adam *et al.* 2004, Lafleur *et al.* 2017, Lafleur *et al.* 2018, Hara 2019, Charoy *et al.* 2019] as well as in experiments [Lazurenko *et al.* 2005a, Lazurenko *et al.* 2007a, Tsikata *et al.* 2009, Cavalier *et al.* 2013, Brown & Jorns 2019] and was associated with enhanced electron transport. The linear theory of the ECDI is well developed, however, its nonlinear saturation is still the subject of active research [Kaganovich *et al.* 2020]. Given the complexity of mode saturation in the 3D geometry of Hall thrusters, only large-scale 3D PIC simulations can provide a full understanding of the mechanism of anomalous transport. However, these simulations are still out of reach and most PIC simulation studies are carried out in simplified 1D and 2D configurations, despite the tremendous advancement in the past few years in including the third dimension [Taccogna & Minelli 2018, Villafana *et al.* 2023, Petronio *et al.* 2023a].

Experimentally, the investigation of instabilities at millimeter scales in HET is challenging and was done so far using CTS [Tsikata *et al.* 2009, Tsikata *et al.* 2010, Tsikata *et al.* 2013, Tsikata *et al.* 2014] and different probe techniques [Lazurenko *et al.* 2007a, Brown & Jorns 2019, Kaganovich *et al.* 2020]. Furthermore, most measurements are performed outside the thruster channel, in the vicinity of the exit plane, and downstream in the plume. In 2009, a previous work by [Honoré *et al.* 2011] used an analysis method that combines 2D PIC axial-azimuthal simulation results with a virtual CTS. The approach consisted of generating a theoretical scattering signal from PIC data and showed an excellent agreement with CTS observations of the plume on the static form factor which is a measure of the intensity of the electron density fluctuations. However, the time resolution of the PIC simulation used was limited to $\Delta t = 1 \mu\text{s}$ so that neither a spectral comparison nor a comparison of the electron density fluctuation rate was performed.

In this chapter, we apply a virtual CTS method to the highly resolved PIC simulations of a 2D PIC axial-azimuthal benchmark test case developed recently in by [Charoy *et al.* 2019] to identify the main parameters impacting the evaluation of the electron density fluctuation rate between PIC simulations and CTS experiments. This is achieved by comparing the reference fluctuation rate derived from PIC data with the one obtained from virtual CTS analysis. CTS experiments usually measure an electron density fluctuation rate of the order of 1% [Tsikata *et al.* 2010], whereas PIC simulations tend to produce large electron density fluctuations at around 10%-15% with significant axial variations [Lafleur *et al.* 2018]. This difference is often explained by stating that 2D simulations are unable to account for the 3D structure of the ECDI. Nevertheless, experiment-wise, the determination of the absolute electron fluctuation rate in CTS is also challenging since it requires a precise measurement of the electron density in the scattering volume and absolute calibration of the setup [Tsikata *et al.* 2017]. Still, recent work using incoherent Thomson scattering to measure this density reported a local electron density lower than previous

estimates and a fluctuation density rate of the order of 8% [Tsikata & Hara 2019], closer to the value reported by simulations.

In this respect, the local electron density inside the scattering volume seems to have a significant impact on the value of the fluctuation rate. The probed volume, which is defined by the intersection of two laser beams, depends on the waist of the laser. Usually, experiments on HET use a CO₂ laser beam with a typical waist in the range of 2 mm to 3 mm. Experimentally, it is very burdensome to vary this parameter and keep a good-quality signal, since it directly impacts the measurement resolution. On the other hand, since PIC simulations are only limited by the mesh resolution, it is possible to numerically produce the scattering signal from PIC data for different waists and assess the impact of the waist on the estimation of the electron density fluctuation rate. Furthermore, PIC results offer more flexibility in terms of the accessible zones for the diagnostic. Indeed, contrary to CTS experiments where the diagnostic has only been done outside the thruster channel, by applying a virtual CTS on PIC results, it is also possible to explore the thruster channel. Interestingly, a similar virtual diagnostic was also performed within an incoherent Thomson scattering setup in [Powis & Shneider 2018] to investigate the impact of the laser intensity on the measurement of the electron density. The study also highlighted the valuable flexibility and insight that virtual diagnostics can bring to experiments.

The organization of the chapter is as follows. The 2D axial-azimuthal PIC simulation and the virtual collective Thomson scattering analysis are presented in Section 2.1. Then, in section 2.2, first, we present the virtual CTS observation at a fixed time to identify the dominant modes in the plume as well as in the thruster channel. Then, we perform a temporal-Fourier analysis to identify the main frequencies and derive the dispersion relations for the dominant propagating modes. Finally, we discuss the impact of the waist of the laser beams on the derivation of electron density fluctuations.

2.1 Methods

2.1.1 Axial-azimuthal PIC simulation

As mentioned in the introduction, an absolute comparison with CTS experimental results would require a full highly-resolved 3D PIC simulation of the whole thruster. However, the latter is still out of reach due to its computational cost. Currently, 2D PIC simulation results in both axial-azimuthal and radial-azimuthal simulation planes [Adam *et al.* 2004, Boeuf 2017, Lafleur *et al.* 2017, Lafleur *et al.* 2018, Hara 2019, Charoy *et al.* 2019, Tavant 2019] are the most reliable data to study azimuthal instabilities (benchmarked and validated). In particular, the axial-azimuthal plane allows the study of the development of azimuthal instabilities and their impact on axial electron transport. Therefore in this work, the virtual CTS analysis was applied to the axial-azimuthal PIC benchmark results from [Charoy *et al.* 2019]. Although the chosen simulation case is non-self-consistent,

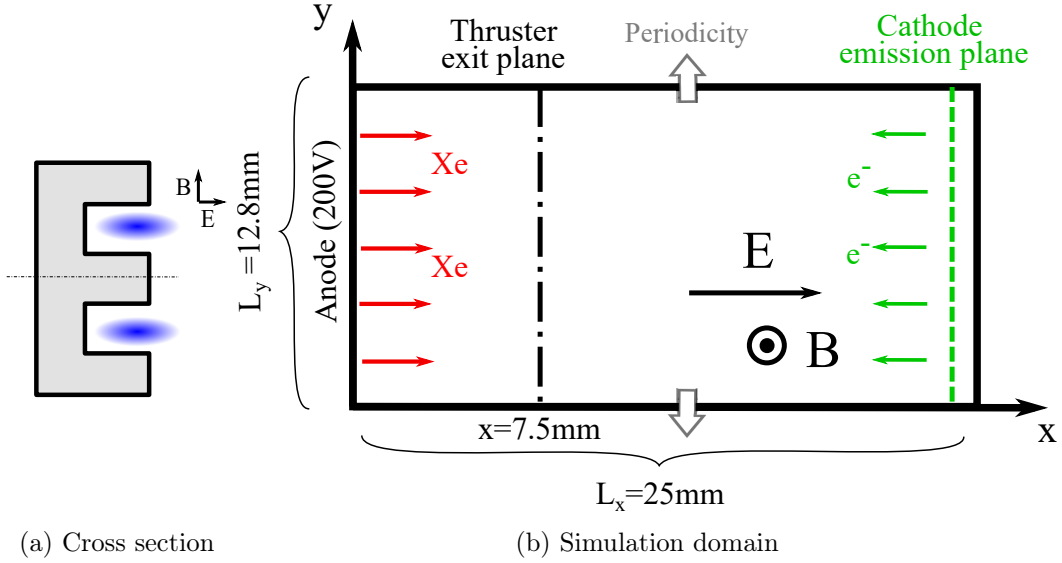


Figure 2.1: Schematic of a transversal cross-section of the thruster and the simulation domain adapted from [Charoy *et al.* 2019]. The x axis is the axial direction, and the y axis is the (periodic) azimuthal direction. The black dashed line at $x = 7.5$ mm corresponds to the position of the maximum radial magnetic field and the exit plane of the thruster. The green dashed line at $x = 24$ mm is the plane from which electrons are emitted.

it was subject to an international benchmark effort, and the instabilities involved in the simulation are well characterized making it a solid analysis framework to test the virtual CTS. In the following, a summary of the conditions of the 2D benchmark and key results are presented, but additional details are given in [Boeuf & Garrigues 2018, Charoy *et al.* 2019]. The 2D simulation domain consists of a 500×256 Cartesian mesh in which the x -axis corresponds to the axial direction while the y -axis corresponds to the azimuthal direction, as illustrated in Figure 2.1. The curvature of the domain was hence neglected. The axial length L_x was fixed to 25 mm while the azimuthal length L_y was fixed to 12.8 mm. A periodic boundary condition was imposed in the azimuthal direction to circumvent the finite azimuthal length and to reduce the computational time.

Initially, ions and electrons are uniformly distributed over the simulation domain at a density of $5 \times 10^{16} \text{m}^{-3}$ and are subject to a 200 V voltage, which was applied between the anode and the cathode. The radial magnetic field profile, as well as the ionization profile, were fixed to remove the low-frequency BM oscillations and highlight the high-frequency instabilities including the ECDI. To maintain the discharge current balance, electrons were injected from the cathode side from an emission line positioned at 1 mm from the right boundary of the simulation domain (green dashed line in Figure 2.1), and its potential is adjusted at each step to ensure a zero azimuthally averaged potential at this position [Boeuf & Garrigues 2018, Charoy *et al.* 2019]. This allows keeping a con-

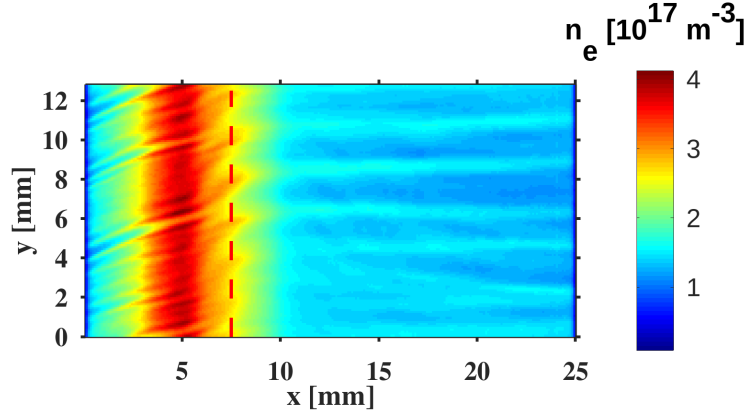


Figure 2.2: Typical results from PIC simulations. This snapshot of the electron density is taken at $t = 12.5 \mu\text{s}$. The dashed red line at $x = 7.5 \text{ mm}$ indicates the limit between the ionization zone and the acceleration zone which also corresponds to the position of the maximum radial magnetic field and the exit plane of the thruster

stant averaged potential drop between the anode and the emission line. With this method, the right boundary plane has a varying negative potential but this drop in potential between the emission plane and the right boundary plane does not have any useful physical meaning and does not affect the main discharge physics [Boeuf & Garrigues 2018, Charoy *et al.* 2019]. The integration used an explicit scheme with a grid size $\Delta x = 50 \mu\text{m}$ and a time step $\Delta t = 5 \text{ ps}$. A total of 4×10^6 time steps were simulated resulting in a discharge simulation up to around $20 \mu\text{s}$. Nevertheless, due to limited storage capacity, the plasma parameters are only stored every 5000-time steps, thus yielding a sampling time for the electron density of $T_s = 25 \text{ ns}$.

A quasi-steady-state was reached at around $12 \mu\text{s}$ featuring an almost constant discharge current. In Figure 2.2, a typical 2D map of the electron density at $t = 12.5 \mu\text{s}$ is shown. It highlights millimetric fluctuations of the electron density propagating mainly along the azimuthal y -axis. These are marked with a change in the wavelength around the exit plane of the thruster at $x = 7.5 \text{ mm}$. In the ionization zone which extends from $x = 2 \text{ mm}$ to 7.5 mm , the fluctuations have a small wavelength and their wavevector has both an axial and an azimuthal component. From $x = 7.5 \text{ mm}$ to 25 mm , which corresponds to the acceleration zone, the structures have a larger wavelength and are almost azimuthal.

A spatial and temporal Fourier analysis of these maps between 16 and $20 \mu\text{s}$ highlights a continuous dispersion relation in the ionization zone (Iz) that shows a good correspondence with the modified ion-acoustic wave dispersion relation from [Lafleur *et al.* 2017, Lafleur *et al.* 2018], as illustrated in Figure 2.3. The mode corresponding to the maximum growth rate under the ion-acoustic wave approximation is identified at $k_{Iz} \approx 8 \text{ rad}\cdot\text{mm}^{-1}$ and has a high frequency $f_{Iz} \approx 5 \text{ MHz}$. In the acceleration zone (Acc), the fit with the modified ion-acoustic dispersion relation is less satisfying. Still, the dynamics are dominated by a single mode at $k_{Acc} \approx 3 \text{ rad}\cdot\text{mm}^{-1}$

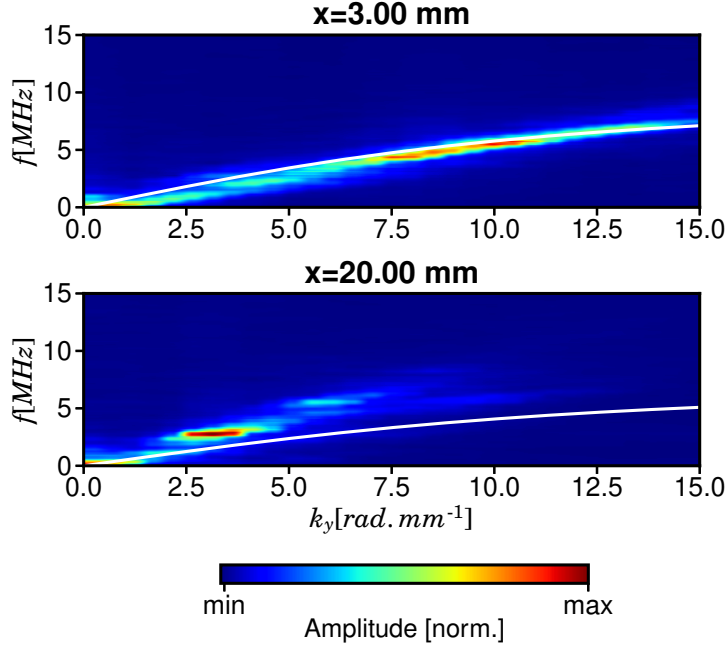


Figure 2.3: 2D FFT of the electron density at $x = 3$ mm and $x = 20$ mm. Solid white line: ion-acoustic dispersion relation.

at a lower frequency $f_{Acc} \approx 3$ MHz. The underlying reason for this change in the dynamics is yet not clearly understood and, in the following, we mainly focus on the estimation of the fluctuation rate from the PIC simulation results.

The fluctuation rate from PIC data is assessed by calculating the fluctuation in time and averaging the results azimuthally for each axial position. It is expressed as follows:

$$\frac{\delta n_e}{n_e} \Big|_{PIC}(x) = \left\langle \frac{\sqrt{\langle n_e^2 \rangle_t - \langle n_e \rangle_t^2}}{\langle n_e \rangle_t} \right\rangle_y. \quad (2.1)$$

The blue curve in Figure 2.4 shows the axial evolution of the fluctuation rate between $12 \mu\text{s}$ and $20 \mu\text{s}$ for the simulated benchmark case. The profile exhibits a large axial variation as already observed by [Lafleur *et al.* 2018] in the first microseconds of a self-consistent 2D (axial-azimuthal) PIC simulation, that seems to be linked to the ionization profile. Indeed, the fluctuation rate decreases from 10% close to the anode to a minimum of 2.6% at $x = 6.4$ mm. This coincides with the maximum ionization rate imposed in the simulation. Then, it increases with small oscillations in the plume to stabilize at around 7% after $x = 20$ mm.

In the following, the blue curve will be used as a reference for the comparison with the virtual CTS results.

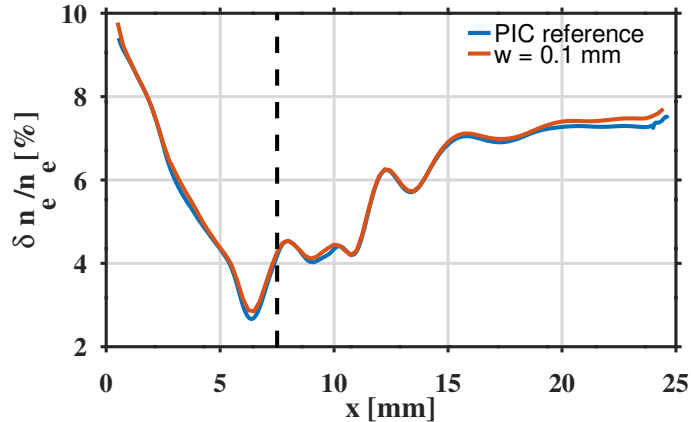


Figure 2.4: The axial variation of the electron density fluctuation rate in the simulation case from [Charoy *et al.* 2019]. The blue curve corresponds to the reference fluctuation rate from PIC results using Eq. 2.1. The red curves correspond to the synthetical fluctuation rate from the virtual CTS at a waist $w = 0.1$ mm based on Eq. 2.7. The black dashed line at $x = 7.5$ mm corresponds to the position of the maximum radial magnetic field and the exit plane of the thruster.

2.1.2 Collective Thomson scattering analysis

Collective Thomson scattering describes a scattering phenomenon in which the scattering wavelength λ is larger or comparable to the Debye length λ_D [Holzhauer & Massig 1978, Froula *et al.* 2011, Meiden 2011]. An incident laser beam at a fixed wave vector \mathbf{k}_i is applied upon the plasma and accelerated electrons behave like dipoles and scatter a part of the incident electromagnetic field at the same wavelength as the incoming field. The scattered fields add up to yield the total scattered field. This sum can be constructive or destructive depending on the phase correlation between the electrons' positions. This correlation might occur if coherent structures are propagating through the medium. If so, these can be highlighted by varying the observation length scale of the scattering experiment to match the length scale of the propagating structures. The wave vector \mathbf{k} along which the CTS is performed is called the scattering vector and is determined using Bragg's relation, relating the wave vector \mathbf{k} to the difference between the laser wave vector \mathbf{k}_i and the scattered wave vector \mathbf{k}_s , as it follows: $\mathbf{k} = \mathbf{k}_s - \mathbf{k}_i$. Hence, by changing the angle between these vectors, it is possible to change the norm of the scattering wave vector \mathbf{k} and thus to probe the medium at different scales. In practice, the scattering wave vector \mathbf{k} is changed using a translating mirror to vary the angle between \mathbf{k}_s and \mathbf{k}_i .

For a fixed \mathbf{k} , the resulting signal is proportional to the Fourier transform of the electron density along \mathbf{k} in the scattering volume \mathcal{V} and is recorded as a function of time, such as:

$$s(\mathbf{k}, t) = \int_{\mathcal{V}} e^{i\mathbf{k}\cdot\mathbf{r}} n_e(r, t) d^3\mathbf{r}. \quad (2.2)$$

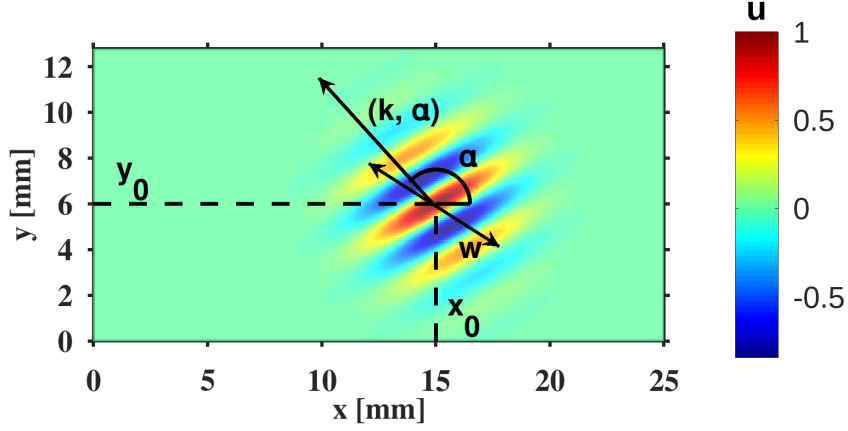


Figure 2.5: 2D configuration for the virtual CTS calculation. The scattering volume is a Gaussian profile with a waist $w = 3$ mm. The phase factor in the Fourier transform is directed along the scattering vector \mathbf{k} , here expressed in polar coordinates with $\alpha = 120^\circ$ and $k = 3 \text{ rad}\cdot\text{mm}^{-1}$

Further frequency analysis is usually performed over the total acquisition duration T and provides the spectral density of the scattering signal $S(\mathbf{k}, \omega)$. This quantity is proportional to the dynamic form factor and is expressed here as follows:

$$S(\mathbf{k}, \omega) = \left| \int_{\mathcal{V}, T} e^{i(\mathbf{k}\cdot\mathbf{r} - \omega t)} n_e(r, t) d^3\mathbf{r} dt \right|^2. \quad (2.3)$$

The integral over all frequencies of Eq. (2.3) is noted $S(\mathbf{k})$ and is proportional to the static form factor, usually measured in CTS experiments. $S(\mathbf{k})$ is written as:

$$S(\mathbf{k}) = \int_{\omega} S(\mathbf{k}, \omega) d\omega. \quad (2.4)$$

Finally, the total fluctuation of the electron density can be related directly to the static factor, using Parseval's theorem, yielding the following relation:

$$\langle n_e^2 \rangle = \int_{\mathbf{k}} S(\mathbf{k}) d\mathbf{k}, \quad (2.5)$$

To perform a virtual CTS on PIC results, we adapt the former integral to a 2D geometry. This is illustrated in Figure 2.5. The scattering volume V_s , defined as the intersection between the laser beam and the 2D map, is modeled using a Gaussian intensity profile u in polar coordinates with a fixed waist w , such as:

$$u(r) = \frac{1}{\pi w^2} e^{-\frac{r^2}{w^2}}.$$

A 2D local spatial Fourier transform is applied to the electron density maps from the PIC simulation along a fixed scattering vector \mathbf{k} given in polar coordinates

(k, α) . This enables to probe structures at a given scale k and that are propagating at a given angle α . The virtual scattered field is thus expressed as:

$$S_{PIC}(\mathbf{k}, \mathbf{r}_0, t) = \int_{\mathcal{A}} e^{i\mathbf{k} \cdot (\mathbf{r} - \mathbf{r}_0)} u(\mathbf{r} - \mathbf{r}_0) n_e(r, t) d^2\mathbf{r}, \quad (2.6)$$

where \mathbf{r}_0 is the center of the 2D equivalent of the scattering volume \mathcal{A} , i.e the center of the Gaussian profile.

The laser intensity profile is applied at each point $r_0 = (x_0, y_0)$ of a rectangular grid at a step $\Delta x_0 = \Delta y_0 = 1$ mm. Each position represents a different Thomson scattering experiment where the scattering vector $\mathbf{k} = (k, \alpha)$ is varied by changing both the norm k and angle α . The angle was varied with a resolution of 1° from 0° to 180° , whereas the norm k is varied with a resolution of 0.3 rad.mm^{-1} from 0.5 rad.mm^{-1} to 12.5 rad.mm^{-1} . The laser waist is fixed to 3 mm for the reference case as usually used in CTS experiments. Besides, this value offers good analysis features for simulations, considering the size of the structures we want to investigate.

Virtual CTS can be understood as a windowed Fourier transform, for which the chosen window is a 2D Gaussian function, centered at r_0 and which has a standard deviation $\sigma = \frac{w}{\sqrt{2}}$. Similar to windowed Fourier transform, virtual CTS has two main advantages. First, it limits the analysis to an area proportional to the laser beam waist w^2 . Second, it introduces a diagnostic length scale $\lambda = \frac{2\pi}{|k|}$ to highlight fluctuations occurring at the same scale as λ . This offers both spatial localization and selectivity over the k -component within the uncertainty inequality limit.

The electron density fluctuation rate is calculated also from the static form factor, using Eq. (2.5). However, the calculation yields the Root-Mean-Square (RMS) of the electron density, weighted by the square of the laser intensity profile u^2 , denoted as $\langle n_e^2 u^2 \rangle_{\mathcal{A}, T}$. The operator $\langle . \rangle_{\mathcal{A}, T}$ corresponds to the average over the area delimited by the weighting function u^2 , such as :

$$\langle n_e^2 u^2 \rangle_{\mathcal{A}, T} = \frac{\int_{\mathcal{A}, T} n_e^2 u^2 d^2r dt}{\int_{\mathcal{A}, T} u^2 d^2r dt}$$

which ensures that $\langle n_e^2 u^2 \rangle_{\mathcal{A}, T}$ is homogeneous to a density. The u^2 stems from Parseval's theorem since the scattering integral is also the Fourier transform of a Gaussian weighted electron density map. Ergo, the fluctuation rate is expressed as:

$$\left. \frac{\delta n_e}{n_e} \right|_{CTS} = \left\langle \frac{\sqrt{\langle n_e^2 u^2 \rangle_{\mathcal{A}, T} - \langle n_e u^2 \rangle_{\mathcal{A}, T}^2}}{\langle n_e u^2 \rangle_{\mathcal{A}, T}} \right\rangle_y. \quad (2.7)$$

This definition of the fluctuation rate is consistent with Eq. (2.1) for small waists. Indeed as the waist tends to 0, the normalized laser profile converges to the Dirac distribution. Consequently, the axial profile of the weighted electron density in the scattering volume converges also to the reference PIC profile, as it is illustrated in Figure 2.4 for a waist of $w = 0.1$ mm.

2.1.3 Pre-processing of the PIC results

To obtain the results presented in the following sections, PIC results were pre-processed before generating a virtual Thomson scattering signal. The time average was subtracted from the typical 2D map to highlight the fluctuations of the density. This was possible because the benchmark test case reached a quasi-steady state. Moreover, to reduce the computational cost, the spatial resolution of the PIC simulation was divided by a factor of 2. Namely, the 2D electron density maps were interpolated over a 251×128 grid instead of the initial 501×256 grid. We have checked that the percent error introduced by this interpolation was less than 0.03% on the averaged plasma parameters and the reference fluctuation rate calculated for PIC results with Eq. (2.1).

A total of $N = 150$ time samples were analyzed using this method, resulting in a temporal signal that extends on 3.75 μs . In the azimuthal direction y , using the periodic boundary condition, each 2D map of the electron density was extended by a length equal to L_y (Figure 2.1) to reduce the edge effect in case the waist extends beyond the simulation domain in that direction. Along the axial direction x , the data was not extended when applying the virtual CTS. Then, edge effects close to the axial boundaries will impact virtual CTS results. In the following, for waists of $w = 0.1 \text{ mm}$, 1 mm and 3 mm , the comparison of results will be carried out mostly for $3 \leq x \leq 21 \text{ mm}$. The time step of the temporal scattering signal is $\Delta t = 25 \text{ ns}$ which corresponds to a sampling rate of 40 MHz. A complex time-Fourier transform was performed over the sample. The modulus of the spectrum was averaged along the y -direction, to reduce the numerical noise. This was possible since the spectral properties of the azimuthal modes in the benchmark model do not depend on the azimuthal positions.

2.2 Results

2.2.1 Amplitude variation of the dominant modes

First, we examine the virtual CTS results at a fixed time t to identify the dominant structures present in the discharge. Figure 2.6 shows the variation of the scattering signal along the wave vector k_x and k_y at different axial positions, at $t = 12.5 \mu\text{s}$, when the simulation has reached a quasi-steady state, for $|\mathbf{k}|$ between $0.5 \text{ rad}\cdot\text{mm}^{-1}$ and $12.5 \text{ rad}\cdot\text{mm}^{-1}$. Figure 2.6a reports a snapshot of the 2D polar map of the scattering signal at $x = 3 \text{ mm}$ and shows multiple modes propagating inward, to the anode, at an angle of 110° . First, there is an intense and highly peaked mode at $k_y = 8 \text{ rad}\cdot\text{mm}^{-1}$ that is identified as the ion-acoustic wave based on the plasma parameters from the PIC simulation. Then, there is a less intense but broad mode at around $k_y \approx 3 \text{ rad}\cdot\text{mm}^{-1}$. These two modes (at $k_y = 8 \text{ rad}\cdot\text{mm}^{-1}$ and $k_y = 3 \text{ rad}\cdot\text{mm}^{-1}$) correspond to the dominant coherent structures propagating in the thruster's channel and we will focus on their axial variation. Downstream in the ionization zone, at $x = 7 \text{ mm}$, the intensity of the $k_y = 8 \text{ rad}\cdot\text{mm}^{-1}$ mode

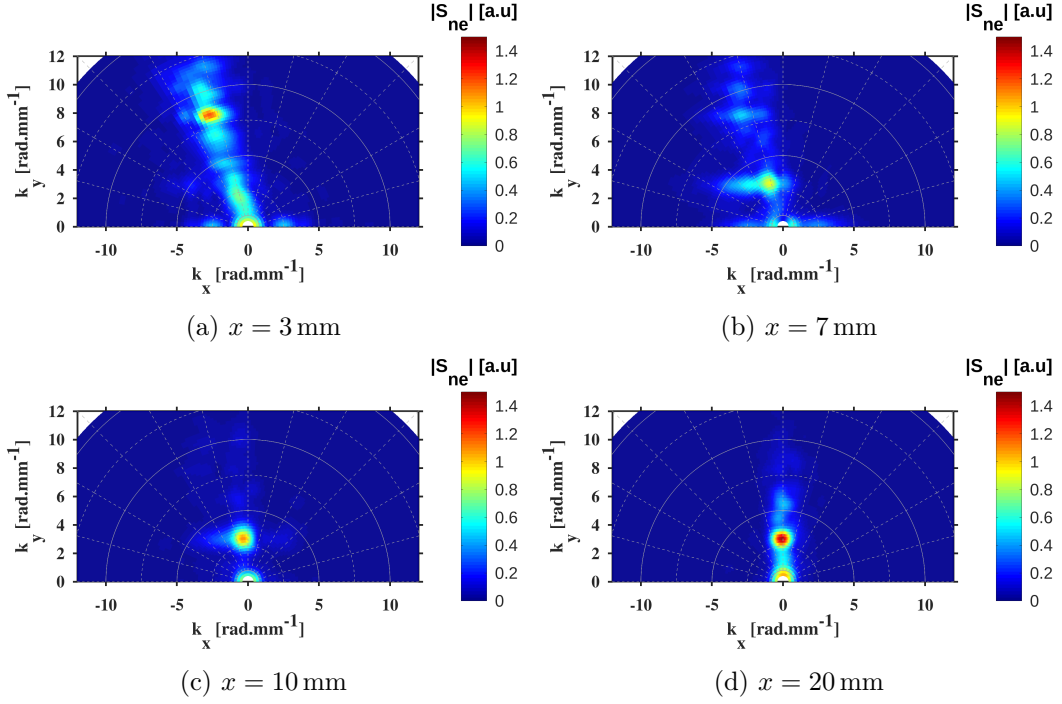


Figure 2.6: 2D polar maps of the intensity of the scattering signal at different axial positions

weakens favouring the second mode at $k_y = 3 \text{ rad.mm}^{-1}$ which becomes dominant as shown in Figure 2.6b. In the acceleration zone, at $x = 10$ and 20 mm , (Figure 2.6c and 2.6d), the 3 rad.mm^{-1} mode increases in intensity and its direction shifts slowly from 110° to 90° . The change of direction occurs mainly at the beginning of the acceleration zone where the ion velocity increases greatly. This is consistent with previous observations in [Honoré *et al.* 2011] suggesting that the modes are convected with ions as they are accelerated. The inward negative component k_x , in the ionization zone, is canceled to an almost zero value, in the observation frame of reference, as the positive outward velocity component of the ions begins to increase in the acceleration zone.

Moreover, this change of direction concurs with a change in the intensity of the modes. This is illustrated in Figure 2.7 which shows the intensity evolution of the two dominant modes as a function of the axial position x . In addition to the previous observations, the intensity of the 3 rad.mm^{-1} mode increases linearly along the thruster axis. The change in the direction of the modes happens at a constant k_y while the magnitude of the k_x component slowly decreases to 0. The decrease of the intensity at $x = 21 \text{ mm}$ is due to the edge effects near the simulation boundaries and the local extremum at $x = 3 \text{ mm}$ is mainly due to the presence of multiple small peaks at small k that are difficult to resolve. The mode at 8 rad.mm^{-1} demonstrates also similar dynamics concerning the wave vector variation. Its decrease at the beginning of the acceleration zone is however very sharp and the k_x component blue

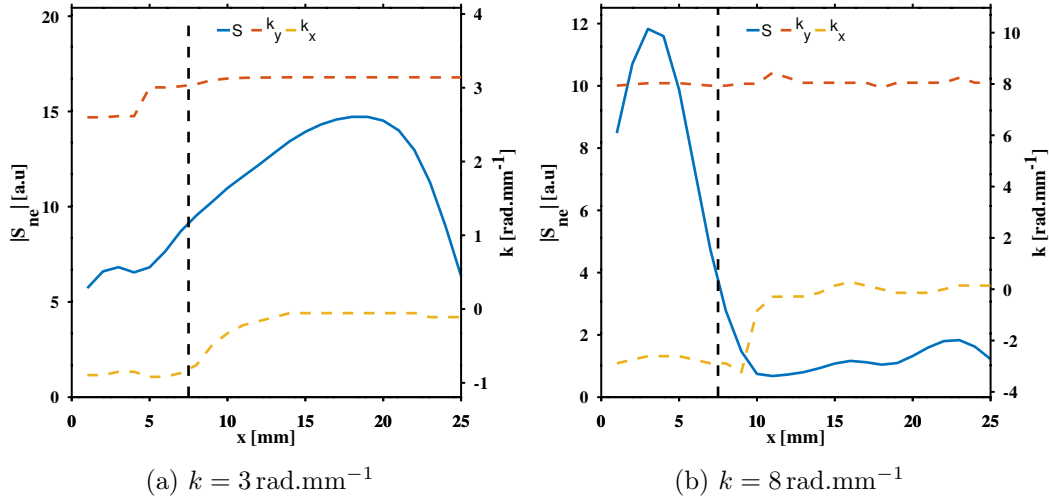


Figure 2.7: Variation of the dominant modes along the axial direction. The blue curves show the intensity of the scattering signal while, on the secondary axis, the dashed curves show the variation of the axial component k_x and the azimuthal component k_y . The dashed black curve indicates the thruster exit plane and the position of the maximum radial magnetic field.

converges quickly to 0, contrasting with the smooth behavior of the small k modes.

2.2.2 Dispersion relation

In the previous section, two coherent modes at $k_y = 8 \text{ rad.mm}^{-1}$ and $k_y = 3 \text{ rad.mm}^{-1}$ were identified in the simulation. To determine the frequencies of these modes, a spectral analysis of the time-dependent scattered signal is performed in the following paragraph.

Figure 2.8 shows the normalized Fourier transform of the time-dependent scattered signal in the ionization zone, at $x = 3 \text{ mm}$ and at an angle $\alpha = 110^\circ$ and in the acceleration zone, at $x = 20 \text{ mm}$ and at an angle $\alpha = 90^\circ$. The spectra illustrate one well-defined peak in each case for both modes.

Figure 2.8a shows that for the $k_y = 3 \text{ rad.mm}^{-1}$ the frequency is different depending on the observation zone. The mode's mean frequency increases from 1 MHz in the ionization zone to 3 MHz in the acceleration zone. The results for the mode at $k_y = 8 \text{ rad.mm}^{-1}$ are presented in Figure 2.8b. The mode's mean frequency also increases from 4.5 MHz in the ionization zone to 6.5 MHz in the acceleration zone. We also observe a broad peak at a negative frequency that suggests a wave back-flow, however, this would need further investigation.

The dispersion relation, from the virtual Thomson scattering experiment is computed for different observation angles α and at different axial positions. The results show a linear progression of the frequency with the wave number for all the tested angles. The maximum signal is obtained, though, when the angle of the observation is along the main propagation direction i.e $\alpha = 110^\circ$ in the ioniza-

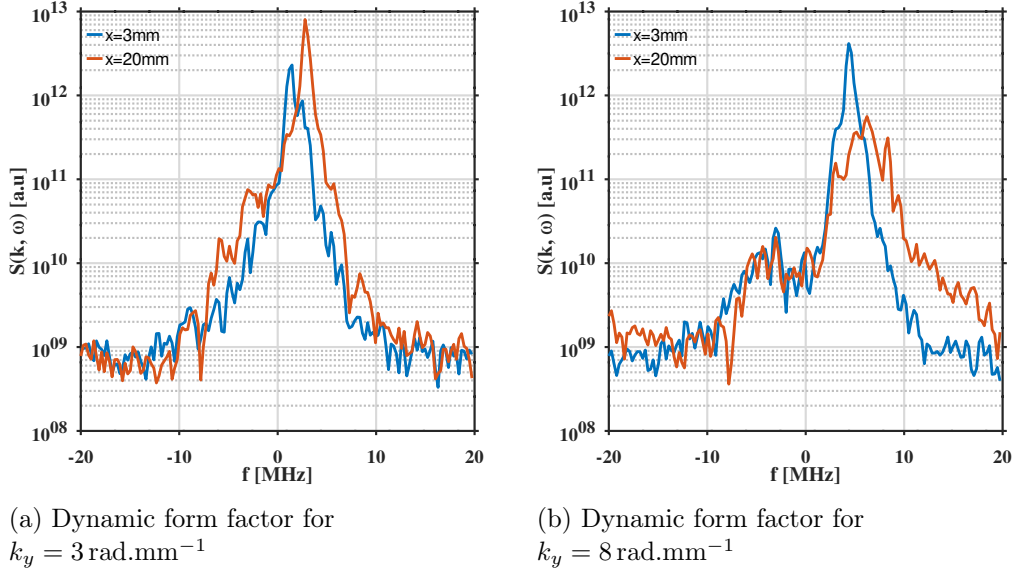


Figure 2.8: Dynamic form factor for $k_y = 3 \text{ rad.mm}^{-1}$ and $k_y = 8 \text{ rad.mm}^{-1}$ at $x = 3 \text{ mm}$ and 20 mm . Blue curves correspond to $x = 3 \text{ mm}$ and an angle $\alpha = 110^\circ$ and the red curve correspond to $x = 20 \text{ mm}$ and an angle $\alpha = 90^\circ$

tion zone and $\alpha = 90^\circ$ in the acceleration zone. Figure 2.9a and Figure 2.9b show the respective dispersion relations along these privileged observation angles at $x = 3 \text{ mm}$ and $x = 20 \text{ mm}$ respectively. Two phase velocities are identified using a linear fit, $v_{g,Iz} = 3.5 \text{ km.s}^{-1}$ and $v_{g,Acc} = 6.6 \text{ km.s}^{-1}$. These values are of the same order of magnitude as the measured phase velocities from CTS experiments [Tsikata *et al.* 2009, Tsikata *et al.* 2010], that were conducted on a similar range of wave vectors.

2.2.3 Electron density fluctuation rate

In this section, we derive the electron density fluctuation rate using the virtual CTS for different values of the waist w of the laser beam. The results are then compared with the reference PIC values. In Eq. (2.7), the waist appears when we calculate both the mean electron density and its RMS since these values are averaged over the scattering volume.

At first, we examine the mean electron density profile. Figure 2.10 shows the axial profile of the electron density for two different values of the laser waist: $w = 1$ and 3 mm . The laser-beam-weighted electron density maps were averaged over $3.75 \mu\text{s}$ and the azimuthal direction. The profiles diverge significantly for axial distances between $x = 3 \text{ mm}$ and $x = 10 \text{ mm}$, where a steep density gradient is observed. This is most noteworthy for a $w = 3 \text{ mm}$ waist with a maximum 11% deviation from the PIC profile at around $x = 5 \text{ mm}$. For a $w = 1 \text{ mm}$ waist, on the other hand, the deviation is estimated to be a mere 2%. These observations are mainly due to the presence of gradients in the electron density profile inside the scattering volume.

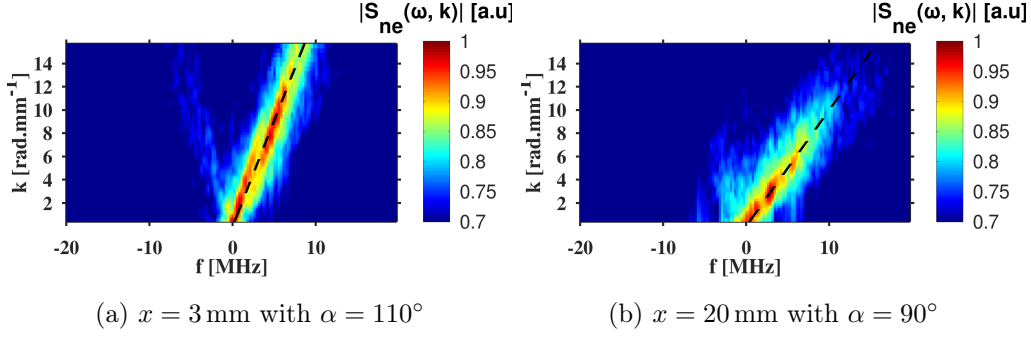


Figure 2.9: Dispersion relations derived from the virtual Thomson scattering experiment along the privileged observation angle relative to each zone: (a) corresponds to the ionization zone with $\alpha = 110^\circ$ while (b) corresponds to the acceleration zone with $\alpha = 90^\circ$. The dashed black lines correspond to the best linear fit

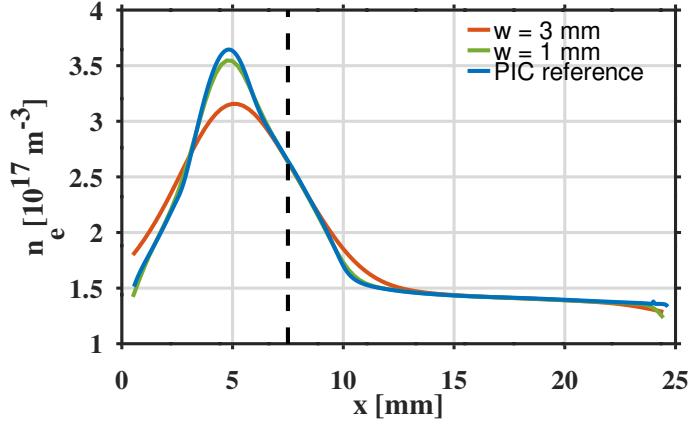


Figure 2.10: Axial profile of the electron density for different values of the laser waist: $w = 1$ and 3 mm in the CTS analysis and from the PIC simulations.

Indeed, if the scattering volume has a sufficient spatial extension, the laser profile behaves like a Gaussian filter and smoothens the electron density profile. Depending on how the electrons are distributed in the scattering volume, the locally averaged electron density is either underestimated or overestimated at a given axial position. In the acceleration zone, between $x = 10$ mm and $x = 214$ mm, where the axial evolution of the electron density is much smoother, the virtual CTS analysis gives results close to the reference PIC profile for $w = 1$ mm and $w = 3$ mm.

Then, we examine the electron density fluctuation rate as introduced in Eq. (2.7) for two different values of the laser waist: $w = 1$ and 3 mm and compare it to the PIC reference value. The results are reported in Figure 2.11. As mentioned in Section 2.1.3, we limit our analysis to $3 \leq x \leq 21$ mm. Between $x = 3$ mm and $x = 10$ mm, the virtual CTS estimates an average fluctuation rate at around 20% for $w = 3$ mm, 3 times higher than what the reference PIC profile yields. In contrast, in the acceleration zone, between $x = 10$ mm and $x = 24$ mm, where the

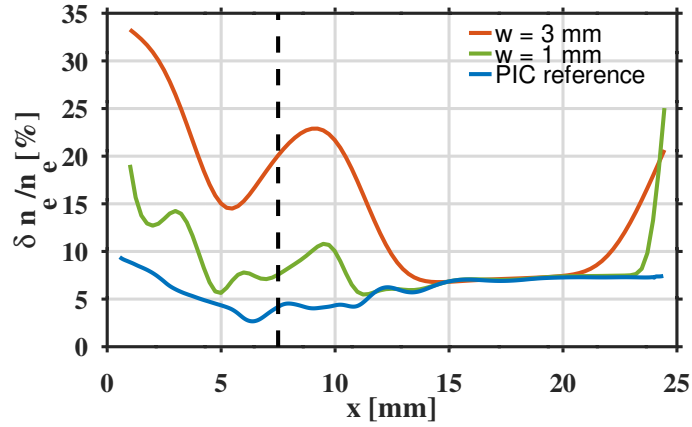


Figure 2.11: Axial profile of the electron fluctuation rate for different values of the laser waist: $w = 1$ and 3 mm in the CTS analysis and from the PIC simulations.

axial electron density is almost constant, the virtual CTS for $w = 1$ and 3 mm gives results coherent with the 7% fluctuation rate of the reference PIC profile. The aforementioned smoothing effect of the axially averaged electron density profile could not explain alone this difference. Indeed a factor of 2 is also observed for $w = 1$ mm for which the difference in the mean electron density profiles is estimated to be only 2%.

In this regard, the difference, observed in Figure 2.11 stems then from the numerator of Eq. (2.7). This term corresponds, in the framework of CTS, to the integral of the form factor over all possible fluctuations in the scattering volume. Since the volume (Figure 2.5) has a spatial extension both in the azimuthal and the axial direction, the integrated profiles of the fluctuation rate take into account not only azimuthal fluctuations associated with the propagating modes but also the axial density standard deviation associated with the density gradient. This results in a relatively high value compared to the PIC reference value.

These observations favor the use of smaller waists in CTS experiments for positions where gradients are high to reduce the impact of the waist on the measurement of the density fluctuation rate. However, this is more challenging in CTS experiments since a smaller w would lead to a degraded k resolution.

Chapter conclusions

In this work, 2D axial-azimuthal PIC simulations were analyzed using a virtual CTS. It has been shown that compared to the non-windowed Fourier transform, virtual CTS offers a localized and directional tool to analyze PIC data. The analysis of PIC results using a virtual CTS diagnostic allowed an enhanced characterization of the modes present in the stationary state of a 2D axial-azimuthal PIC simulation [Charoy *et al.* 2019], not only in the plume but also in the thruster channel. It permitted to resolve two modes at $3\text{rad}\cdot\text{mm}^{-1}$ and $8\text{rad}\cdot\text{mm}^{-1}$ propagating all

along the thruster axis. Their direction is slightly oblique near the anode and becomes almost azimuthal at the thruster exit plane as they are convected by ions. The observation shows also that when the ions' convection becomes very large, the change in direction concurs with a change in the amplitudes of the modes. The amplitude of the $3\text{ rad}\cdot\text{mm}^{-1}$ mode grows linearly in the acceleration zone while the $8\text{ rad}\cdot\text{mm}^{-1}$ is sharply damped. The dispersion relations (f, k) have been computed using this approach inside the ionization zone in the thruster channel and the acceleration zone and are consistent with the observations in CTS experiments.

On the other hand, the examination of the electron density fluctuation rate shows a strong dependence on the axial position x . Far in the thruster plume, the fluctuation rate is almost constant, while in the ionization zone inside the thruster and near the exit plane, the profile exhibits strong variations. Moreover, the results are shown to strongly depend on the value of the laser beam waist (1 mm and 3 mm in this work). The study first highlights the importance of an accurate measure of the electron density inside the scattering volume. Since the electron density appears as a dividing factor, a gross estimation can lead to a large difference in the order of magnitude of the fluctuation rate. Recent measurements using incoherent Thomson scattering to estimate the electron density [Tsikata *et al.* 2017] also suggest a similar conclusion. The observations also highlight the impact of the waist on the evaluation of the electron density Root-Mean-Square. Because of its spatial extension, the diagnostic integrates both axial and azimuthal fluctuations. This leads to a different estimation of the fluctuation rate especially in areas with a strong electron density gradient.

Finally, this work has allowed us to clarify further the discrepancies between PIC simulations and CTS experiments on the value of the electron density fluctuation rate. It also underlines the interest in performing virtual plasma diagnostics on either PIC or fluid simulations since they allow us to relate simulations and experiments and foster common ground for comparison and discussion. In this work, the CTS diagnostic was applied to a simplified 2D (axial-azimuthal) test case with a stationary state. In future work, the virtual CTS will be used to analyze a self-consistent time-dependent 2D (axial-azimuthal) simulation closer to the real operation conditions of Hall effect thrusters.

Confident in the relevance of virtual diagnostics to both simulation and experiments on HET, we proceed in the following chapters to develop a virtual OES based on the use of a CRM on PIC simulations. This aims to assess the feasibility of implementing OES as an in-orbit diagnostic tool for HETs.

Optical Emission Spectroscopy and Collisional Radiative Modelling

La lumière était si belle sur les fleurs... Qu'est-ce que c'était ces fleurs ? On dit qu'il n'y a pas de vraies fleurs bleues. Pourtant... Qui sait s'il les voyait bleues, le grand vieillard, là-dedans.

Aragon, *Aurélien*

Contents

3.1	Collisional and radiative data for xenon	28
3.1.1	Spectroscopic notations, electronic configuration, and main radiative emissions	28
3.1.2	Electron impact excitation cross sections	31
3.2	HET0D neutral xenon collisional radiative model	36
3.2.1	Model overview	37
3.2.2	Included kinetic processes	38
3.2.3	Balance equation	45
3.3	HET0D implementation	45
3.3.1	Code inputs	45
3.3.2	Module structure	47
3.3.3	Sampling, interpolation, extrapolation, and integration schemes	49
3.3.4	Example of calculations	50
3.4	HET0D verification and quantification of uncertainties . . .	51
3.4.1	Verification of the model	51
3.4.2	Quantification of the uncertainties in HET0D	55

Introduction

Despite the plethora of parameters covered by the different types of plasmas that exist in nature or the laboratory, all plasmas emit light as a result of the electronic

excitation of their constituent atoms, ions, and molecules. Whether it is a tokamak plasma or a Hall thruster plasma, light emission has been the primary source of knowledge about plasma properties, providing valuable information about their density, temperature, electric and magnetic fields, and elemental composition. This study of the light emitted by the plasma is broadly known as OES.

Compared to CTS, OES is quite desirable for propulsion applications since it is a non-bulky, non-invasive diagnostics that easily allows real-time monitoring of the discharge, thus emerging as the prime candidate for in-orbit non-invasive assessment of the plasma parameters. However, interpreting the complexity of plasma emissions or coupling them with heavy simulation tools such PIC simulations can be challenging since it requires a thorough understanding of the emission sources. The simplest emission scenario occurs in thermal equilibrium plasmas: the radiative emission follows the Max-Planck black body expression, ionization is described by the Saha-Boltzmann equation, and the distribution of excited species follows the Boltzmann distribution. In Local Thermodynamic Equilibrium (LTE) plasmas, the previous equilibrium descriptions hold, except for the radiative field, which is no longer in equilibrium with the particles. Conversely, for non-LTE, which is the case of propulsion plasmas, none of the previous assumptions apply. Indeed, the radiative field is influenced by a combination of radiative mechanisms between free and bounded states, and the distribution of excited species and the ionization ratio depend strongly on the effectiveness of different collisional mechanisms.

One widely used approach to calculate plasma emission consists of a CRM. Introduced over 60 years ago by [Bates *et al.* 1962], this approach allows for the determination of excited states densities and the resulting spectra by considering the elementary interactions between electrons, neutrals, and ions. It involves balancing the time variation of the density of every excited species p due to collisional and radiative processes which translates to the following balance equation:

$$\frac{\partial n_p}{\partial t} = \frac{\partial n_p}{\partial t} \Big|_{coll,rad} \quad (3.1)$$

where n_p is the density of the excited level p . Note that the previous equation only holds if the contribution from convective and diffusive transport is negligible compared to the collisional radiative contribution [Bates *et al.* 1962, van der Mullen 1990].

The main task in collisional radiative modeling is to accurately determine the right-hand side of Eq. (3.1). Indeed, CRMs rely on a detailed representation of relevant elementary interactions, and hence require an back-and-forth between atomic physics and plasma properties. To illustrate the approach, consider a simplified model where collisional excitations are dominated by electron impact excitations from the ground state to higher levels and all downward transitions are radiative. This kind of model is commonly called *Corona model*. It consists of a neutral atom in the ground state colliding with an electron, which, after the collision, is excited to a higher level p . Subsequently, the atom relaxes to the ground state by emitting a photon. Note that here the electron-impact deexcitation and radiation trapping

are neglected as well as any quenching effect¹.



The electron impact excitation contribution to Eq. (3.1) depends on the EEDF f_e via the rate coefficient K_{0p} . This coefficient is determined by averaging the electron impact excitation cross-section σ_{0p} multiplied by the square root of the energy over f_e :

$$K_{0p} = \sqrt{\frac{2}{m_e}} \int_{E_p}^{+\infty} \sqrt{E} \sigma_{0p}(E) f_e(E) dE. \quad (3.2)$$

The EEDF f_e can be assumed Maxwellian for lack of an *a priori* knowledge of its shape. In this case, f_e is fully determined by the electron temperature T_e , and the rate coefficient will depend solely on T_e . Conversely, if PIC simulations are available, The EEDF from PIC can be used to yield a more realistic kinetic description of the discharge. In this case, f_e is fully determined from the kinetic simulation, and the rate coefficient will depend in addition on the overall shape of the EEDF not only T_e , hence deviating from the Maxwellian calculation.

The radiative contribution to Eq. (3.1) involves the radiative transition probability from the upper level p to the lower level q , A_{pq} , called Einstein coefficient; and the population of the upper level p , denoted n_p . The radiative contribution then reads:

$$R_{pq} = A_{pq} n_p. \quad (3.3)$$

Ergo, the time variation of the density of the excited level p is expressed as follows:

$$\frac{dn_p}{dt} = K_{0p} n_e n_0 - \sum_{q < p} A_{pq} n_p \quad (3.4)$$

where the first term in the right-hand equation is the electron impact excitation from the ground state and the second term is all the spontaneous emissions stemming from the level p . The use of the total derivative sign here reflects the volume-averaged character of CRMs such as no spatial gradients are included.

At steady state, by setting the left-hand term to 0 in Eq. (3.4), it is possible to determine the excited species densities with respect to the plasma parameters and the collisional-radiative data as follows:

$$n_p = \frac{n_e n_0 K_{0p}(T_e)}{\sum_{q < p} A_{pq}}. \quad (3.5)$$

This example demonstrates how the density distribution of excited species is connected to the plasma parameters like the electron temperature and the electron density through the CRM. For a given n_e and T_e , the model determines the density

¹The corona model is valid for low pressure discharges $P \leq 0.1$ Pa. In this range, quenching coefficients are in the range of kHz

of the excited species from which the intensity of the light emission can be calculated using the following expression:

$$I_{pq}(T_e, n_e) = \frac{hc}{\lambda_{pq}} A_{pq} n_p(T_e, n_e), \quad (3.6)$$

where I_{pq} is the radiant power density in $\text{W}\cdot\text{m}^{-3}$ per unit of solid angle of the emission line from the level p to the level q at the wavelength λ_{pq} . This allows in the same way as virtual CTS, to generate virtual emission spectra from PIC simulations. Nevertheless, the success and accuracy of the modeling depend on the availability of accurate atomic data, including collision cross-sections and radiative transition coefficients for the plasma species under investigation.

The first section focuses on presenting the xenon atom and the atomic data relevant to xenon CRM. The second section focuses on HET0D, the neutral xenon CRM developed in this work for HET. The third section focuses on the model implementation in Python and finally, the last section looks into the verification of the code and the quantification of uncertainties.

3.1 Collisional and radiative data for xenon

Building a CRM requires a detailed collisional and radiative data set to model the elementary processes relevant to the HET discharge. To this purpose, understanding the atomic configuration of xenon, collecting the data set from the literature, and validating the collected data to the electronic configuration is paramount for "consistent" modeling. In this section, we present first the xenon atom, highlighting the strong ion core splitting which has an important impact on the xenon chemistry at low pressure. Second, we perform a literature review of xenon excitation cross-sections. Finally, we refer to Appendix C in which we perform quantitative validation between the electronic configuration of xenon, the excitation data sets relevant to CRM, and the radiative data.

3.1.1 Spectroscopic notations, electronic configuration, and main radiative emissions

Xenon electronic configuration and notations The ground state electron configuration of xenon is

$$1s^2 2s^2 2p^6 3s^2 3p^6 3d^{10} 4s^2 4p^6 4d^{10} 5s^2 5p^6,$$

which can be abbreviated to $5p^6$. The excited xenon species have a core electron configuration of $5p^5$ with an orbital quantum number $l_e = 1$. The core quantum numbers are $l_c = 1$ and $s_c = \frac{1}{2}$, resulting in a core angular momentum of $j_c = \frac{3}{2}$ or $\frac{1}{2}$ in virtue of the angular momentum addition rules [Moisan *et al.* 2021]. For the first excited levels of xenon, which are on a $6s$ layer, $l_e = 0$, hence, the allowed values for the quantum numbers $K = j_c + l_e$ and $J = K + s_e$ are as follows:

- for $j_c = \frac{3}{2} = K, J = 2, 1$
- for $j_c = \frac{1}{2} = K, J = 1, 0$

Using Racah's notation¹, the four levels of the $6s$ manifold are divided into two tiers $6s$ and $6s'$, based on their core angular momentum j_c . They are denoted as $6s[\frac{3}{2}]_2$, $6s[\frac{3}{2}]_1$, and $6s'[\frac{1}{2}]_0$, $6s'[\frac{1}{2}]_1$, with the prime indicating that $j_c = \frac{1}{2}$.

In Paschen notation¹, these levels are simply denoted $1s5$, $1s4$, $1s2$ and $1s3$. The $1s5$ and $1s3$ are called the metastable levels, while $1s4$ and $1s2$ are the resonant radiative levels.

Likewise, the excited levels of the $5p^56p^1$ configuration in xenon are divided into two groups based on their j_c quantum number. The non-primed $6p$ tier with $j_c = \frac{3}{2}$, are denoted in Paschen notation as $2p5$ through $2p10$ in decreasing energy order. The primed $6p'$ tier with the $j_c = \frac{1}{2}$, are denoted in Paschen notation as $2p1$ through $2p4$ in decreasing energy order. Table 3.1 provides the equivalences between Racah and Paschen notation for the $1s$ and $2p$ levels of xenon.

Table 3.1: Xenon energy levels in Paschen and Racah notations

Paschen	J	j_c	Racah	E (eV)
$1s5$	2	$3/2$	$6s[\frac{3}{2}]_2^o$	8.315
$1s4$	1	$3/2$	$6s[\frac{3}{2}]_1^o$	8.437
$1s3$	0	$1/2$	$6s'[\frac{1}{2}]_0^o$	9.447
$1s2$	1	$1/2$	$6s'[\frac{1}{2}]_1^o$	9.570
$2p10$	1	$3/2$	$6p[\frac{1}{2}]_1$	9.580
$2p9$	2	$3/2$	$6p[\frac{5}{2}]_2$	9.686
$2p8$	3	$3/2$	$6p[\frac{5}{2}]_3$	9.721
$2p7$	1	$3/2$	$6p[\frac{3}{2}]_1$	9.789
$2p6$	2	$3/2$	$6p[\frac{3}{2}]_2$	9.821
$2p5$	0	$3/2$	$6p[\frac{1}{2}]_0$	9.934
$2p4$	1	$1/2$	$6p'[\frac{3}{2}]_1$	10.976
$2p3$	2	$1/2$	$6p'[\frac{3}{2}]_2$	11.078
$2p2$	4	$1/2$	$6p'[\frac{1}{2}]_4$	11.105
$2p1$	0	$1/2$	$6p'[\frac{1}{2}]_0$	11.187

The energy diagram of xenon in Figure 3.1 shows that the lowest excited states are the four $6s$ states around 8.3 eV. Above these states, there are 10 $6p$ levels with a first excitation energy of 9.5 eV. Around 11 eV, there are additional excited states, corresponding to the $5d$, $6d$, $7s$, and so on. Since the main radiative contribution of xenon in the visible range involves the $6p$ manifold, we will further the description

¹cf Appendix B

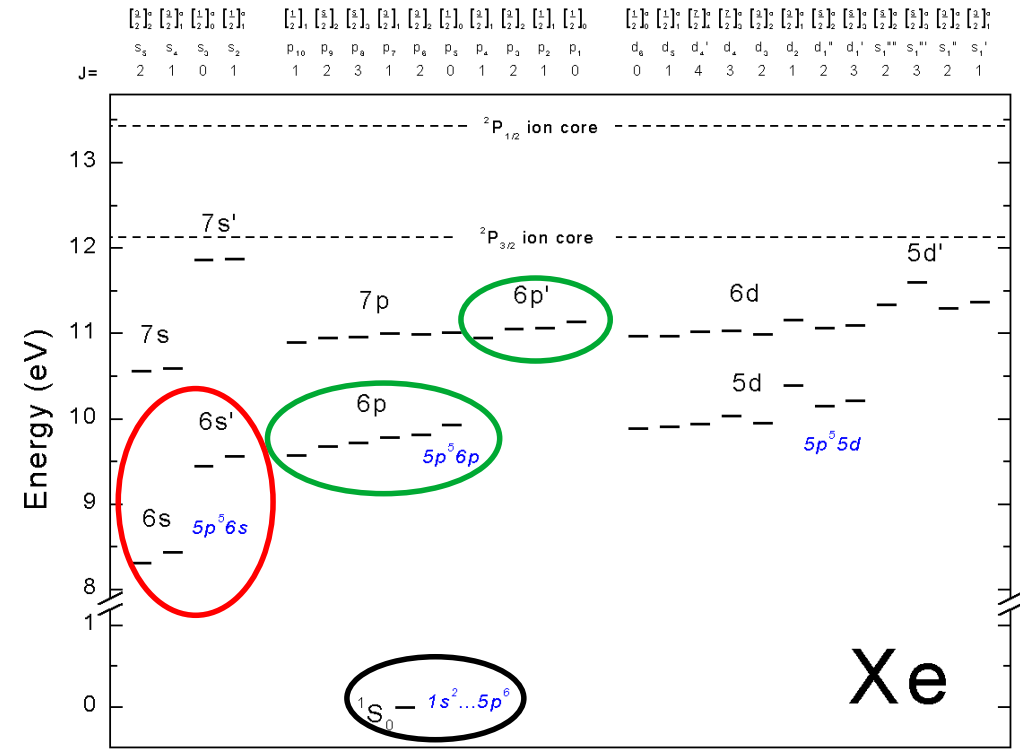


Figure 3.1: Xenon energy diagram [Raptor 2003]. The black circle indicates the ground state. The red circle indicate the 6s levels while the two green circles are the 6p levels split into 6p tier and 6p' tier.

of the 5d, 6d, and 7s excited levels. The first ionization threshold occurs at $E_I = 12.13$ eV. All these groups are split, energy-wise, in two tiers with respect to their core angular momentum j_c , making j_c an appropriate quantum number to label the energy levels. The splitting is by 1.306 eV and contrasts a lot with lighter noble gases like argon or neon for whom such an energy separation is negligible.

The two-tier structure has significant implications for xenon excitation cross-sections. Excitations that preserve the core quantum state are expected to be more favorable than those that involve core-changing processes since core-changing excitations would alter both the quantum state of the outer electron and the core itself. An exception to this might arise when the levels with different j_c are energetically close which is true, for instance, for the 6s' and 6p tiers (≈ 0.1 eV). In this case, 6s' to 6p should be favored compared to the 6s' to 6p'.

Radiative transitions Selection rules for optical transitions require $\Delta l_e = \pm 1$ for the excited electron and $\Delta J = 0$ or ± 1 , excluding $J = 0 \rightarrow J = 0$ transitions [Moisan *et al.* 2021]. For the 6s configuration, the 1s2 and 1s4 levels allow dipole transitions at 129 nm and 146 nm, respectively. However, the metastable levels 1s3

and $1s5$ have no optical transitions to the ground state².

The transitions from the $5p^56p$ configuration are only connected to the $5p^56s$ levels (not the ground state) and consist of the prominent xenon's emission in the visible-near infrared range³:

- the $6p \rightarrow 6s$ transitions occur between 823 nm to 1084 nm,
- the $6p' \rightarrow 6s'$ transitions range from 764 nm to 893 nm, and
- the $6p' \rightarrow 6s$ transitions are in the blue range (450 nm to 492 nm).

The atomic data relative to these radiative transitions were collected from National Institute of Standards and Technology (NIST) [Kramida & Ralchenko 1999] and are reported in Table 3.2 with their respective accuracy⁴.

Table 3.2: Radiative transitions from $6s$ and $6p$ levels. The Einstein coefficients are collected from NIST and are expressed in units of 10^6 s^{-1} .

λ [nm]	Transition	A_{ij}	Acc. ⁴	λ [nm]	Transition	A_{ij}	Acc.
129.5	$1s2 \rightarrow gs$	253.00	$\leq 2\%$	469.2	$2p4 \rightarrow 1s5$	0.28	$\leq 18\%$
146.9	$1s4 \rightarrow gs$	273.00	$\leq 2\%$	491.7	$2p4 \rightarrow 1s4$	1.60	$\leq 18\%$
980.2	$2p10 \rightarrow 1s5$	31.10	$\leq 7\%$	820.8	$2p4 \rightarrow 1s3$	20.00	$\leq 25\%$
1084.1	$2p10 \rightarrow 1s4$	1.80	$\leq 18\%$	893.3	$2p4 \rightarrow 1s2$	22.00	$\leq 25\%$
904.7	$2p9 \rightarrow 1s5$	12.40	$\leq 7\%$	452.5	$2p3 \rightarrow 1s5$	0.46	$\leq 18\%$
992.5	$2p9 \rightarrow 1s4$	13.00	$\leq 7\%$	473.5	$2p3 \rightarrow 1s4$	1.38	$\leq 18\%$
882.1	$2p8 \rightarrow 1s5$	30.00	$\leq 2\%$	834.9	$2p3 \rightarrow 1s2$	42.00	$\leq 18\%$
841.1	$2p7 \rightarrow 1s5$	3.06	$\leq 7\%$	450.2	$2p2 \rightarrow 1s5$	1.46	$\leq 18\%$
916.5	$2p7 \rightarrow 1s4$	24.00	$\leq 18\%$	764.4	$2p2 \rightarrow 1s3$	21.00	$\leq 18\%$
823.3	$2p6 \rightarrow 1s5$	28.60	$\leq 7\%$	826.8	$2p2 \rightarrow 1s2$	16.20	$\leq 18\%$
895.4	$2p6 \rightarrow 1s4$	8.10	$\leq 18\%$	458.4	$2p1 \rightarrow 1s4$	1.30	$\leq 25\%$
828.2	$2p5 \rightarrow 1s4$	36.90	$\leq 10\%$	788.9	$2p1 \rightarrow 1s2$	35.00	$\leq 18\%$

3.1.2 Electron impact excitation cross sections

Literature review The first studies on xenon cross sections by [Felt'san 1967] were focused on understanding the dependence of xenon's emission from the $6p$

²The metastable can decay via magnetic dipole and their lifetime is estimated to 42s [Walhout *et al.* 1994]

³Note that transitions from the $6p \rightarrow 6s'$ transitions are tabulated in databases and are in the far-infrared range. However, they are very faint and they lack diagnostic data

⁴The accuracy corresponds to the NIST accuracy classification of the transition strength, expressed here in percentages instead of letters.

levels on pressure which persists even at low pressures. Initial investigations of excitation cross sections to the $6p$ levels suffered from poor resolution near the threshold region and covered only emission cross sections [Heddle & Gallagher 1989]. Subsequent later studies [Filipović *et al.* 1988, Buckman *et al.* 1983, Korotkov *et al.* 1988] provided more resolved measurements at lower energy ranges. Notably, [Buckman *et al.* 1983] reported high-resolution observations of resonant structures in the excitation cross-section near the xenon threshold. A more comprehensive review of these cross-sections can be found in the following references [Heddle & Gallagher 1989, van der Burgt *et al.* 1989, Mityureva & Smirnov 1994].

In 1998, [Fons & Lin 1998] performed a complete description of the excitations *from the ground state to $6p$ levels* and reported both direct and apparent electron-impact cross-section. The fluorescence at a wavelength λ from a level p to a level q was measured to retrieve the optical emission cross sections σ_{pq}^λ from which the apparent cross sections were derived. The latter, by construction, included both direct excitation to the level p as well as the radiative cascade from higher levels.

Measurements of cross sections *from the metastable levels to $6p$* are limited. Only the ones from the $1s5$ level have been measured, while the $1s3$ level remains hardly detected. Indeed, the strong ionic core splitting in xenon exacerbates the difference in densities between the metastables, leading to a reduced population of the $1s3$ level compared to the $1s5$ [Sadeghi & Sabbagh 1977]. Measurements by [Jung *et al.* 2005, Jung *et al.* 2009] using a hollow cathode confirmed this population difference, with a ratio of 200 to 1 between the two metastable levels. Note that these measurements agree only in shape but not in magnitude with previous studies by [Mityureva & Smirnov 1994]. But still, they are the most comprehensive and resolved near the threshold to our knowledge.

Furthermore, limited measurements have been performed on the excitation *from the ground state to the resonance levels* in xenon. [Kanik *et al.* 2001] conducted measurements and observed broad excitation functions, consistent with theoretical expectations. They found that the cross-section into the $1s4$ level was approximately twice as large as the cross-section into the $1s2$ level. Measurements of excitation cross sections to higher levels, specifically the four levels in the $5p^56d$ configuration, were conducted using Fourier transform spectroscopy by [Jr & Clark 1990]. The work of Fons and Lin [Fons & Lin 1998] also investigated excitation cross-sections from higher levels to evaluate the cascade cross-section to the $6p$ level.

In a nutshell, the work of [Jung *et al.* 2009, Fons & Lin 1998, Jung *et al.* 2005] provides the most complete and consistent experimental investigation for xenon, covering cross-sections of xenon from the ground state to the $6p$ and out of the $1s5$ metastables to the upper tier of the $6p$ levels.

Stimulated by these experiments, numerous theoretical and numerical studies have been published for both electron-impact excitation from the ground state and metastable levels of xenon [Kaur *et al.* 1998, Zatsarinny & Bartschat 2010, Nakazaki *et al.* 1997, Zatsarinny & Bartschat 2013, Priti *et al.* 2019b].

One of the main challenges in developing theoretical models for xenon cross

sections is accurately addressing the $n+1$ electrons problem under the strong ion core splitting of xenon atom [Moiseiwitsch & Smith 1968]. Early modeling efforts used Bethe-Born approximation which yields a cross section proportional to $\frac{\ln(E)}{E}$. An empirical generalization of this formula was proposed by [Darwin 1963] expressing cross sections as follows :

$$\sigma_{ij}(E_{ij}) = 4\pi a_0^2 \left(\frac{R_y}{E_{ij}}\right)^2 \alpha_{ij} f_{ij} \frac{U_{ij} - 1}{U_{ij}} \ln(1.25\beta_{ij}U_{ij}) \quad (3.7)$$

The α_{pq} and β_{pq} are adjusted in the formula to fit experimental or calculated values that are available. This method has been used extensively in the past to remedy the lack of available cross-section of xenon and showed relatively good efficiency in reproducing important xenon atom properties.

Numerical methods for calculating cross-sections in xenon also involve using compiled experimental data validated against experimental swarm parameters through an iterative process. Several cross section sets, such as BIAGI-v8.9 [Biagi 2022, Biagi 1988], HAYASHI [Hayashi 2003, Makato 2022], and PUECH [Puech 2022, Puech & Mizzi 1991], are available using this approach. These data sets are in agreement on the total excitation cross sections when grouped by electronic configuration and provide consistent results with respect to swarm parameters. A comprehensive comparison of these results and their use in modeling can be found in the article by [Bordage *et al.* 2013] in which they discuss xenon and other noble gases. However, comparison of level-to-level excitation cross sections was not possible due to varying degrees of details between the dataset and only BIAGI gives enough details to be used for CRM.

Theoretical calculations of xenon cross-sections have also been performed using the R-Matrix and relativistic distorted wave approaches. The R-Matrix method [Yu *et al.* 2000, Allan *et al.* 2006, Zatsarinny & Bartschat 2010, Zatsarinny & Bartschat 2013] provides a highly resolved description of xenon cross sections near the threshold. The work of [Zatsarinny & Bartschat 2010, Zatsarinny & Bartschat 2013] provides the most complete set of cross-sections with 74 excitation levels out of the ground state. Relativistic distorted wave calculations were conducted by [Bartschat *et al.* 2004, Madison & Shelton 1973] and most recently by [Priti *et al.* 2019a]. The latter provides consistent results at higher energies but has a lower resolution near the threshold. Yet it provides detailed atomic descriptions of xenon cross-sections and is in good agreement with other datasets, such as B-Spline R-matrix cross sections (BSR), on the excitation cross-section from the ground state.

Cross sections for a neutral xenon CRM Given these prospects, the calculated cross sections from [Zatsarinny & Bartschat 2013] and [Priti *et al.* 2019a] are thus most fit for CRM because they are the most detailed. Still, experimental data from [Fons & Lin 1998] and [Jung *et al.* 2005, Jung *et al.* 2009] should provide a reference point to assess these calculated cross-sections for modeling.

It is important to note that there are uncertainties in both the experimental measurements and the numerical calculations. The experimental data might not include radiative cascade corrections, while numerical methods calculate direct excitation cross sections and depend on the choice of the set of target wave functions, resulting in potentially different magnitudes. These differences should not impact the trends, the shapes, and the decay at high energies of the cross sections that should align with the fundamental atomic configurations of xenon presented earlier, in particular its two-tier configuration. In this sense, selection rules play a major role, favoring optically allowed transitions, core-preserving transitions over core-changing ones, and transitions between nearby energy levels over distant ones.

Therefore, we perform a qualitative comparison detailed in the Appendix C as recommended by [Boffard *et al.* 2007] to assess the shape and magnitude of the calculated cross sections. Since the numerical methods also calculate energy levels and Einstein coefficients, a comparison of these parameters against the reference values tabulated in NIST [Kramida & Ralchenko 1999] was performed. Table 3.3 provides a detailed summary of the databases that were considered in this comparison. The next section only presents the main takeaway.

From the comparison in the Appendix C, we derive several relevant insights to help choose the cross-section data set:

- First, the qualitative comparison between calculated and experimental cross-sections suggests that the four sets of cross-sections are relatively in agreement, despite the clear discrepancies in the magnitude. The comparison of the radiative parameters (Einstein coefficient and oscillator strength) indicates that BSR and NIST are consistent, while Priti shows slight deviations. For this reason, we recommend primarily using BSR and Fons & Lin measurements for modeling if NIST values are used. Still, since Priti cross-sections are defined on a larger energy range and that Relativistic Distorted Wave (RDW) are more reliable for high energies than the R-Matrix method, we use them to extrapolate the previous cross-section to higher energies, instead of using ad-hoc extrapolation.
- Second, by using the apparent cross section from [Fons & Lin 1998] instead of direct cross sections, models automatically incorporate the excitation into higher atomic levels and can be limited to the $6s$ and $6p$ levels. This offers the advantage of maintaining the accuracy of the description by including a few well-understood levels and mechanisms without incurring a large number of individual atomic levels [Boffard *et al.* 2004].
- Third, we expect to have a strong coupling between levels with the same angular momentum j_c since this coupling plays a significant role in determining the magnitude of the excitation cross section from one level to another in xenon.
- Forth, since the metastable states are unable to decay radiatively to the ground state, they primarily de-excite either by diffusing to the nearest reso-

Table 3.3: List of the databases investigated in this work in Appendix C

Ref	Details	Reference and comment
BIAGI	50 Excitation cross sections	Swarm derived cross sections transcribed from SF Biagi's Fortran code MAGBOLTZ, Version 8.97, 2011. All excitation functions are on LXCat and stem from the ground state to $6s$, $6p$, $5d$, $7s$, and other high-lying levels.
BSR	74 Excitation cross sections	Theoretical calculation based on the Dirac B-Spline R-Matrix method detailed in [Zatsarinny & Bartschat 2010] and are available on LXCat. It includes excitation functions from the ground state to $6s$, $6p$, $5d$, $7s$, and other high-lying levels. It also covers excitation functions from $6s$ to $6p$ and $5d$. These were reported in the work of [Zhu <i>et al.</i> 2019], but are not on LXCat. They were acquired via a private communication directly from Pr. Bartschat.
PRITI	127 Excitation cross sections	Theoretical calculations based on the relativistic distorted wave method detailed in [Priti <i>et al.</i> 2019a, Priti <i>et al.</i> 2019b]. It includes excitation functions from the ground state to $6s$, $6p$, $5d$, $7s$, and other high-lying levels, excitation functions from $6s$ to $6p$ and $5d$, excitation function for $6s$ and $6p$ collisional mixing. The excitation functions for $1s2$, $1s3$, and $1s4$ to $2p8$ were not found in the mentioned references. We used a digitized version of the graphs
FONS	15 Excitation cross sections	Measurements of apparent cross sections detailed in the following papers [Jung <i>et al.</i> 2009, Fons & Lin 1998, Jung <i>et al.</i> 2005]. This work includes apparent, cascade, and direct cross sections from the ground state to the 10 $6p$ levels. The work of Jung <i>et al.</i> contains 5 excitations cross sections from the $1s5$ metastable state to the $2p5 - 10$ levels.

nant levels or by being excited to the $6p$ level with the same primed signature, followed by a radiative decay to a resonant level. This applies in particular to HET plume as described in the work of [Karabadzhak *et al.* 2006]. However, it should be noted that these observations hold only in the absence of additional mechanisms that can affect the lifetime of resonant levels (e.g., absorption) and decrease the metastable density (e.g., diffusion to the walls in the thruster channel).

Provided these observations, we build in the following section a neutral xenon CRM for HET and we start with an overview of CRM for electric propulsion.

3.2 HET0D neutral xenon collisional radiative model

Literature review Previous studies utilizing CRM for low-temperature plasmas have primarily focused on determining key plasma parameters such as electron temperature [Zhong *et al.* 2020], EEDF shape [Boffard *et al.* 2010, Zhu *et al.* 2012], and electron density [Zhu *et al.* 2009, Akatsuka 2019, Lin *et al.* 2023] from OES measurements. These investigations often employed techniques like line ratio analysis or least square optimization to minimize the prediction error and align with experimental observations.

However, for this work, we will narrow our focus to CRMs in the context of electric propulsion rather than delving into the broader scope. For an in-depth exploration of CRMs, we refer to several excellent articles and topical reviews available in the literature, such as [Vicek & Pelikan 1990, Boffard *et al.* 2004, Zhu & Pu 2010, Boffard *et al.* 2018, Ralchenko 2016], among others.

For electric propulsion, several previous works on xenon CRMs focused on Hall effect thrusters. Early studies primarily concentrated on assessing the erosion rate by measuring the light emission from the thruster plume [Manzella 1993, Pagnon *et al.* 2004]. In 1997, [Leray *et al.* 1997] performed OES mapping along the discharge channel of a Stationary Plasma Thruster (SPT)-type Hall thruster with a lateral slit to have optical access to the channel region. The OES measurements were performed for various discharge voltages and flow rates coupled with a CRM to study the trends in temperature and electron densities and concluded on the feasibility to determine the electron density based on a neutral Xe/He CRM with helium being injected as traces.

Notably, [Karabadzhak *et al.* 2006, Karabadzhak *et al.* 1997] conducted extensive OES measurements on different configurations of Hall Effect Thrusters (HETs), with a focus on the D-55 Hall thruster. They presented spectral measurements of the D-55 Hall thruster plume and discharge regions, comparing them to spectra obtained from controlled experiments involving energetic electrons, Xe^+ , and Xe^{2+} beams on a neutral xenon target gas [Karabadzhak *et al.* 1997]. In 2006, [Karabadzhak *et al.* 2006] developed a simplified collisional-radiative model for xenon radiation emission, specifically targeting the TAL-type Hall thruster. The CRM used experimental emission cross section from [Chiu *et al.* 2006] using a setup

similar to [Fons & Lin 1998] and modeled the intensities of the $6p$ Near Infra-Red (NIR) emission lines to predict the electron temperature. Their work emphasized the significance of ion-impact excitation, along with electron-impact excitations from the metastable $1s5$. This model was improved in 2009, by [Dressler *et al.* 2009] by incorporating a more complete set of cross sections from BSR method.

Further independent models were also constructed mainly relying on the theoretical cross sections [Yang *et al.* 2010]. This model included 173 atomic levels of Xe based on cross-sections from the atomic code from the Los Alamos National Laboratory. In 2019, [Priti *et al.* 2019a] developed another xenon collisional radiative model based on the recently calculated RDW cross sections. This work, in particular, investigated the impact of using two different sets of cross-sections and reported no significant impact on the dynamic of the $6s$ levels [Priti *et al.* 2019a]. A more recent and comprehensive model was developed by [Zhu *et al.* 2019] following the calculation using the BSR method of Xe and Xe^+ cross sections by [Wang *et al.* 2019]. This work reported a detailed description of the plasma kinetics in the ionization and acceleration zones. The observations are in agreement with Karabadzhak's observation as to the role of the metastable and also suggest that it is possible to decouple neutrals from ions for the CRM as the neutral-ions interaction contributes by less than 2% to the population mechanisms of the $6p$, which concur with [Hutchinson 2002] since the time scale for relaxation to excited state equilibrium is much shorter than the relaxation time to ionization state equilibrium.

3.2.1 Model overview

Building on the previous considerations from the literature, we present a neutral xenon collisional radiative model involving the 15 xenon levels from the $1s$ and $2p$ manifolds to couple with PIC simulations. The considered xenon levels and transitions are illustrated in Figure 3.2. This choice is made based on the use of the apparent cross-section which allows to limiting of the atomic model to the $1s$ and $2p$ levels [Boffard *et al.* 2004], and the observations from [Hutchinson 2002] and [Zhu *et al.* 2019] which allows for a simplified treatment of the neutral kinetics by neglecting the contribution of Xe^+ to the neutral's light emission in HET.

This model assumes that the $2p$ levels are populated through electron impact excitation from both the ground state and the $1s$ metastable levels and are depopulated through radiative decay. In comparison to the *Corona model* presented in the introduction, this model also includes electron-impact deexcitation and the total radiative emission is corrected for radiation trapping using Mewe approximation [Mewe 1967]. Indeed, per the work of [Zhu *et al.* 2019], we know that the kinetics of neutral xenon in HET discharge is similar to the kinetics of some inductive plasma at very low pressures. Electron impact excitation from the ground state and the metastables contribute up to 60-70% on average to the population of the $6p$ levels. The radiative decay is the main source of depopulation, contributing up to 99% of the loss rate of highly radiative levels of the $6p$. The impact of diffusion to the walls on the metastables was significant only near the anode region and charge exchange

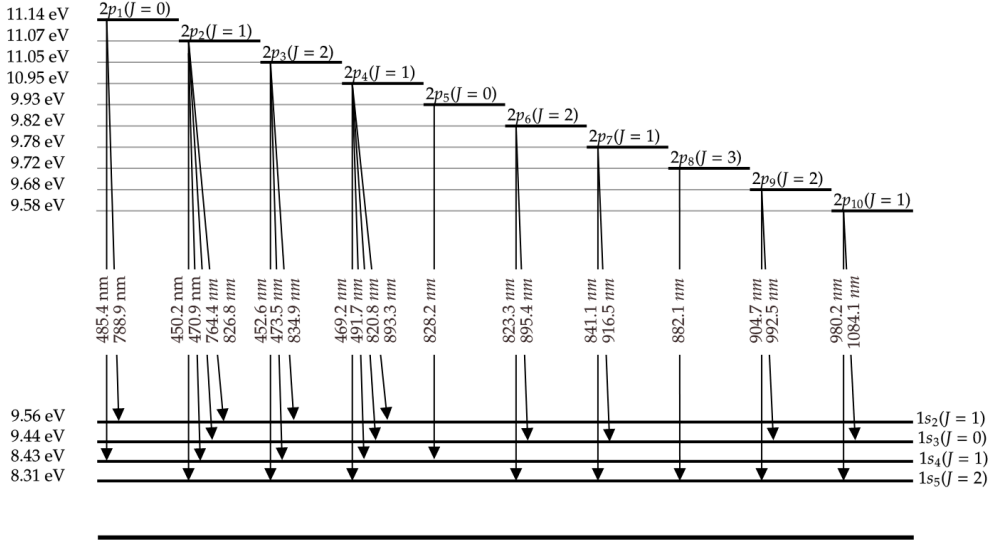
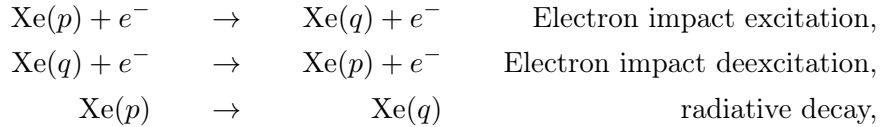


Figure 3.2: Energy diagram for xenon levels included in the CRM

was relevant in the far plume region. Still, their contributions to the kinetics of the $6p$ were relatively low compared to electron impact excitations and radiative decay. Ion electron recombination rates can be neglected relative to the rate of excitation at the range of electron temperatures expected for HET. Finally, the transport effect should be also investigated to validate the 0D assumption and this has not been studied in the subsequent sections. However, we assume that they can be neglected and we will assess the validity of this hypothesis in Chapter 5. Hence, the processes included in the model are as follows:



where $q \leq p$ and $\text{Xe}(k)$ represents an xenon atom in the level k . The balance equation is the same as Eq. (3.1). The following sections were published in a conference proceeding [Ben Slimane *et al.* 2022a]

3.2.2 Included kinetic processes

Electron impact excitation and deexcitation

Electron energy distribution function The EEDF plays a vital role in CRMs as it provides essential information about the distribution of electrons at different energy levels and drives all the electron-impact processes. The integral of the EEDF over the entire energy range yields the electron density n_e :

$$n_e = \int_0^{+\infty} f_e(E) dE. \quad (3.8)$$

Additionally, the first moment of the **EEDF** determines the electron mean energy, also known as the effective electron temperature T_e . Unless it is stated differently, T_e will always refer to *the effective electron temperature* and is given by the expression:

$$E = \frac{3}{2} k_b T_e = \frac{1}{n_e} \int_0^{+\infty} E f_e(E) dE. \quad (3.9)$$

Hereafter, the **EEDF** will be always normalized by the electron density and will be denoted \hat{f}_e . This is mostly useful when numerically calculating the rate coefficients using Eq. (3.2). The ultimate **EEDF** is the Maxwellian **EEDF**, usually valid in **LTE**, and for which the effective electron temperature is equal to *the true electron temperature*. The shape of the Maxwellian **EEDF** depends only on T_e and this is illustrated in Figure 3.3 a):

$$\hat{f}_e(E) = \frac{2}{\sqrt{\pi}} T_e^{-3/2} \sqrt{E} e^{-E/T_e}. \quad (3.10)$$

However, in **HET**, **LTE** does not hold and the **EEDF** strongly deviates from the equilibrium since inelastic collisions lead to a depletion of high-energy electrons. The distribution is also significantly distorted by the $\mathbf{E} \times \mathbf{B}$ drift and wave-particle interactions due to instabilities. This has been seen in **PIC** simulations and is illustrated in Figure 3.3 b). Note that here we plotted the Electron Energy Probability Function (**EEPF**) \hat{g}_e defined as :

$$\hat{f}_e(E) = \sqrt{E} \hat{g}_e(E), \quad (3.11)$$

which is conveniently a straight line in a semi-logarithmic scale for the Maxwellian.

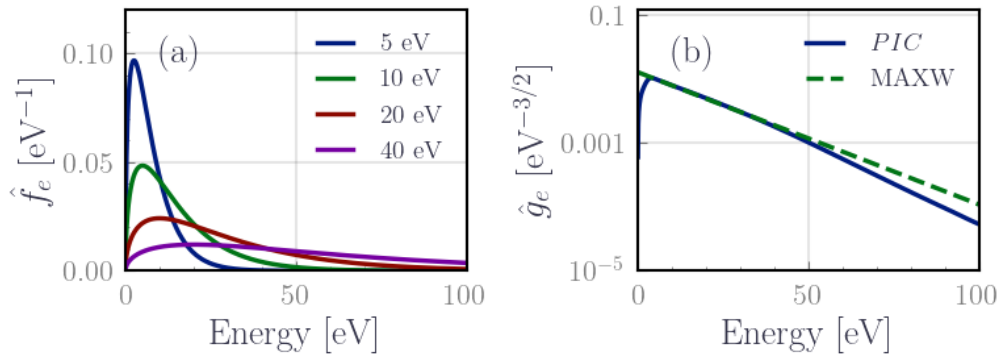


Figure 3.3: Electron energy distribution and probability function: (a) Maxwellian **EEDF** for different temperatures (b) Comparison between a Maxwellian **EEPF** at 21eV with a simulated **EEPF** from **PIC** simulation from [Petronio *et al.* 2023a] in the plume of a hall thruster

To be able to parametrically assess the impact of the **EEDF** on the **HET** emissions for the Maxwellian and non-Maxwellian case, we can introduce the following generalized two-parameter **EEDF** proposed by [Boffard *et al.* 2018]:

$$\hat{f}_e(E) = \beta_1 T_x^{-3/2} \sqrt{E} e^{-\beta_2 (E/T_x)^x}, \quad (3.12)$$

where β_1 and β_2 are chosen to be:

$$\beta_1 = x \left(\frac{2}{3}\right)^{3/2} \frac{\Gamma(\frac{5}{2x})^{3/2}}{\Gamma(\frac{3}{2x})^{5/2}}, \quad \beta_2 = \left(\frac{2}{3}\right)^x \frac{\Gamma(\frac{5}{2x})^x}{\Gamma(\frac{3}{2x})^x}, \quad (3.13)$$

with Γ is the Gamma function. T_x is the effective electron temperature defined using the Eq. (3.9) and x is a shape parameter allowing to change the tail position relative to Maxwellian while keeping the same average energy. For $x > 1$ one finds a depleted tail while for $x < 1$ one gets an enhanced tail. This is illustrated in Figure 3.4.

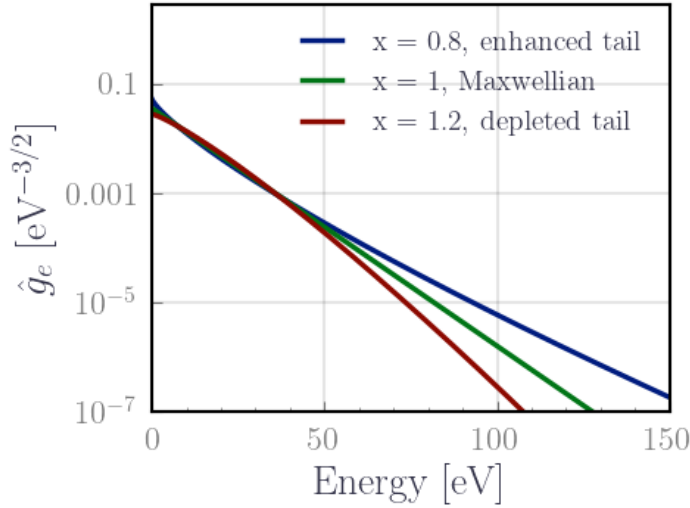
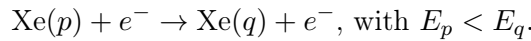


Figure 3.4: Shape of the generalized two parameters **EEDF** for different values of the parameter x .

Electron impact excitation The rate of production for an excited xenon atom transitioning from level p to a level $q \geq p$ due to collisions with an electron of energy E , depends on the electron impact excitation cross-section from p to q denoted σ_{pq} . The excited xenon atom gains a certain amount of potential energy equal to the difference in energy between the two states:



The net transition probability K_{pq} over all possible electron energies is then obtained by averaging this cross-section over the **EEDF**, which is described in the

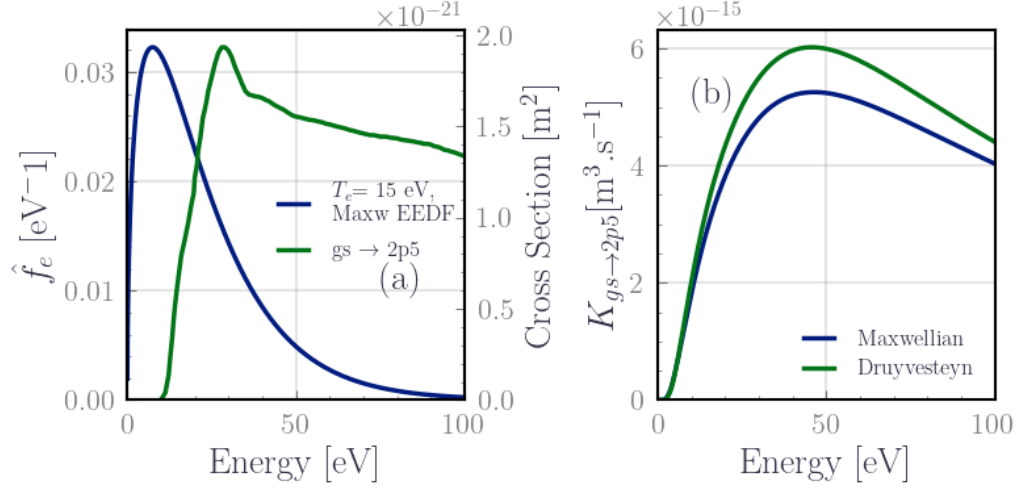


Figure 3.5: Comparison of the rate coefficient for electron impact excitation: (a) Maxwellian EEDF at 15 eV superposed to the excitation cross-section from the ground state to 2p5 with respect to the electron energy to illustrate the integral expression of the rate coefficient. Note that the threshold region has the biggest contribution. (b) Comparison of the rate coefficient calculated with a Maxwellian EEDF and a generalized two parameters Maxwellian with $x = 2$. The energy here should be understood as the effective electron temperature expressed in electronvolts.

following expression and illustrated in Figure 3.5 a):

$$K_{pq} = \sqrt{\frac{2}{m_e}} \int_{E_p - E_q}^{\infty} \sigma_{pq} \sqrt{E} \hat{f}_e(E) dE. \quad (3.14)$$

The change rate $\frac{dn_p}{dt}$ in Eq. (3.1) due to electron excitation is given hence by $n_e n_p K_{pq}$. Table 3.4 lists the cross-sections used in our model based on the discussion in the first section. The energy range of all these cross-sections is extended by appending the RDW cross-section from Priti for high electron energies.

Figure 3.5 b) illustrates the dependence of the rate coefficient with respect to the effective electron temperature for two types of EEDFs: a Maxwellian and a generalized Maxwellian with $x = 2$ also commonly labeled a Druyvesteyn EEDF. Note the deviations in the rate coefficient that appear at high effective energy due to the depleted EEDF tail in the Druyvesteyn compared to the Maxwellian⁸.

⁸Note that the excitation rate from the Druyvesteyn is higher at high energies though it corresponds to a depleted tail of the EEDF. The reason behind this is that compared to a Maxwellian at the same effective temperature T_e , the Druyvesteyn EEDF will have an enhanced population of the electron at low energy leading to a higher contribution to the electron impact excitation. This is explored in detail in chapter 4.

Table 3.4: The collisional processes included in our model. The third column gives the references for the cross sections

Excitation	Process	Reference	Acc.
gs \rightarrow 6s	$\text{Xe}(gs) + e^- \rightarrow \text{Xe}^*(1s) + e^-$	[Zatsarinny & Bartschat 2013]	20% ⁵
gs \rightarrow 6p	$\text{Xe}(gs) + e^- \rightarrow \text{Xe}^*(2p) + e^-$	[Fons & Lin 1998]	15% ⁶
6s Mixing	$\text{Xe}^*(1s) + e^- \rightarrow \text{Xe}^*(1s) + e^-$	[Zatsarinny & Bartschat 2013]	20% ¹
6p Mixing	$\text{Xe}^*(2p) + e^- \rightarrow \text{Xe}^*(2p) + e^-$	[Priti <i>et al.</i> 2019a]	20% ⁷
6s \rightarrow 6p	$\text{Xe}^*(1s) + e^- \rightarrow \text{Xe}^*(2p) + e^-$	[Zatsarinny & Bartschat 2013]	20% ¹

Electron impact deexcitation The principle of detailed balance provides a simple expression as Eq. (3.14) for the deexcitation process, assuming a LTE. This principle states that at equilibrium, each elementary process is balanced by its reverse process [Sobel'man *et al.* 1995, Hartgers *et al.* 2001], resulting in the equality of the production rates:

$$n_e n_p K_{pq} = n_e n_q K_{qp}.$$

When the condition of a LTE does not apply, the previous expression becomes invalid. However, it is still possible to establish a relationship between σ_{pq} and σ_{qp} using the principle of microscopic reversibility applied to electrons with energies between E and $E + dE$ [Sobel'man *et al.* 1995, Hartgers *et al.* 2001]. This approach yields the following relation:

$$\sigma_{qp} = \frac{2J_p + 1}{2J_q + 1} \frac{E + E_{pq}}{E} \sigma_{pq}, \quad (3.15)$$

where E_{pq} is the transition energy from level p to level q with $p > q$ and J_k is the total angular momentum of level k . Noting that Eq. (3.15) does not rely on any thermodynamic parameter, it can be extended even in the absence of a LTE to any type of EEDF. In particular, nonanalytical PIC EEDFs can be used to numerically calculate the rate coefficients and the change rate $\frac{\partial n_p}{\partial t}$ in Eq. (3.1) due to electron deexcitation is given by $n_e n_q K_{qp}$.

In the special case of a LTE, the Maxwell-Boltzmann distribution applies. Then, we can analytically relate the rate coefficient for the electron-impact excitation K_{pq} to that of electron-impact deexcitation K_{qp} by the following expression after integrating over the EEDF:

$$K_{qp} = K_{pq} \frac{2J_p + 1}{2J_q + 1} \exp\left(-\frac{E_{pq}}{k_b T_e}\right). \quad (3.16)$$

Note that the ratio between the direct and inverse coefficient rates in Eq. (3.16) depends solely on the total angular momentum quantum number, the transition energy E_{pq} and the electron temperature T_e . Therefore, it is interesting to use LTE conditions to verify the numerical implementation of electron impact excitation and deexcitation with rates calculated with Eq. (3.14).

Radiative processes

Including the change rate due to bound-bound ($p \rightarrow q$) radiative transitions in the particle balance is straightforward when the density of the lowest excited state is small. In this case, the radiative decay is primarily attributed to the spontaneous emission and the rate of change of the density is given by:

$$R_{pq} = A_{pq}n_p. \quad (3.17)$$

However, for HET plasmas, additional phenomena such as radiation trapping and absorption play a crucial role and need to be considered in the modeling process. This is because absorption can significantly increase the lifetime of excited species through repeated absorption and re-emission of photons, as highlighted in previous work by [Boffard *et al.* 2018]. In the specific context of electric propulsion, studies by [Karabadzak *et al.* 2006] and [Zhu *et al.* 2019] have emphasized the importance of accounting for absorption to accurately describe the xenon plasma chemistry.

The formalism adopted here to model absorption is similar to what was used in previous works [Zhu *et al.* 2015, Zhu *et al.* 2019] which introduced a correction factor Γ_{pq} , also known as the escape factor to Eq. (3.17). The change rate is then expressed as:

$$R_{pq} = R_{pq}^{emission} - R_{pq}^{absorption} = \Gamma_{pq}A_{pq}n_p. \quad (3.18)$$

The challenge in treating radiative processes lies in evaluating the escape factor, as it incorporates both the non-local nature of absorption and the geometry of the medium [Molisch & Oehry 1998]. Early work by [Holstein 1947] was the first to calculate the escape factor by solving the general radiative transport equation, focusing on the case of an infinite slab. Subsequent studies by [Hearn 1963], [Claude 1967], and [Bhatia & Kastner 2000] derived the escape factor for simple geometries such as infinite cylinders and spheres. These works were reviewed by [Irons 1979]. However, for general geometries, the calculations remain highly involved.

The work of [Mewe 1967] proposed an empirical expression that consolidates the previous theoretical calculations by [Hearn 1963] and [Claude 1967] within a 25% margin of error. The escape factor is expressed as follows:

$$\Gamma_{pq} = \frac{2 - e^{-\tau_{pq}/1000}}{1 + \tau_{pq}}, \quad (3.19)$$

where τ_{pq} is the optical depth of the medium for the wavelength λ_{pq} . Figure 3.6 illustrates the variation of this correction factor with respect to the optical depth. When $\tau_{pq} = 0$, there is low absorption, and the radiative contribution is dominated by spontaneous emission. As τ_{pq} approaches infinity, emission, and absorption reach an equilibrium state.

In this model, the plasma is assumed to be homogeneous, and the shape of the emission lines is primarily determined by Doppler broadening. This assumption is valid for HET where the electron density $n_e \leq 1 \times 10^{20} \text{ m}^{-3}$, and the contribution of Stark broadening can be neglected. Considering these broadening considerations

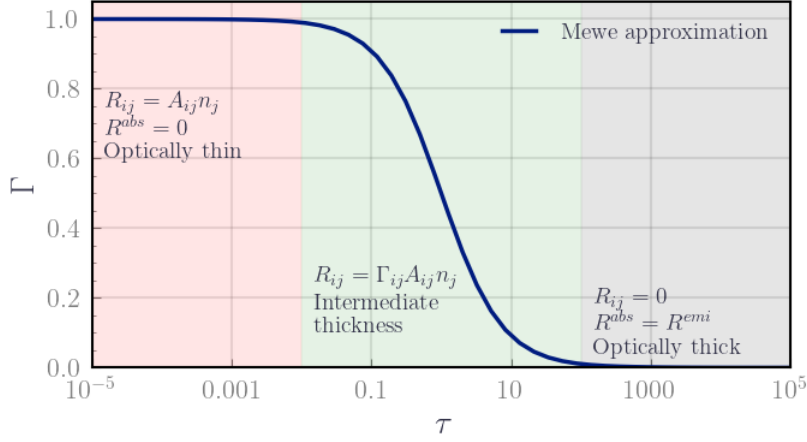


Figure 3.6: Escape factor as a function of the optical depth

and neglecting stimulated emission, the optical depth for the wavelength λ_{pq} is proportional to the number density of the absorbing atoms n_q . It can be expressed as follows:

$$\tau_{pq} = \frac{\lambda^3}{8\pi^{\frac{3}{2}}} \frac{g_p}{g_q} n_q A_{pq} \sqrt{\frac{M}{2RT_g}} \times d, \quad (3.20)$$

where d is the characteristic length of the medium. Here, the optical depth depends not only on the transition characteristics such as the wavelength and the Einstein coefficient but also on the density of the lower level in such a way that larger lower-level densities lead to stronger radiation trapping as well as the neutral temperature stemming from considering the Doppler broadening as the dominant broadening mechanism. This also implies that different transitions will be affected differently by radiation trapping, in particular metastable levels, which will experience stronger radiation trapping compared to resonant levels.

The use of the escape factor provides a simplified approach to model radiation trapping by incorporating a volume-averaged correction factor for photons escaping in all directions. This approximation has been widely used in previous models and has shown surprisingly good agreement with experimental observations. However, it is important to note that this approximation is not strictly valid in cases where there are strong spatial gradients of emitting and absorbing particles, which is often the case in plasmas, including the one of HETs.

To address the non-uniformity of the medium, additional calculations have been performed in specific cases, such as argon plasma columns, to improve the escape factor approximation [Golubovskii *et al.* 2013, Zhu *et al.* 2015]. More extensive studies have been conducted by [Zhu *et al.* 2016] for krypton and xenon. These investigations resulted in a minor improvement of Mewe approximation.

3.2.3 Balance equation

For each excited level p out of the 15 included in the model, we generate the balance equation that is expressed hereafter based on the previously exposed loss and creation terms:

$$\frac{dn_p}{dt} = \underbrace{\sum_{q \rightarrow p} K_{qp} n_e n_q - \sum_{p \rightarrow q} K_{pq} n_e n_p}_{e^- \text{ impact de/excitation}} + \underbrace{\sum_{q \rightarrow p} \Gamma_{qp} n_q - \sum_{p \rightarrow q} \Gamma_{pq} n_p}_{\text{Radiative decay}}. \quad (3.21)$$

Most CRMs consider directly the steady state by setting the left-hand side of Eq. (3.21) to 0 and solving the set of equations. Here, the balance equation is solved with respect to time. This enables us to couple the resolution of the equations with the dynamics observed in HET in PIC simulations. At each time step, the model yields the number density of the excited species. From this distribution, we generate a synthetic spectrum based on the lines that were included in the model and listed back in Figure 3.2. The intensity of an emission line λ_{pq} is given by the following expression:

$$I_{\lambda_{pq}}^{CRM} = \frac{hc}{\lambda_{pq}} A_{pq} \Gamma_{pq} n_p. \quad (3.22)$$

3.3 HET0D implementation

We developed during the thesis a Python module called HET0D to solve numerically Eq. (3.21). This module handles the parsing of user-selected reactions and retrieves the necessary cross-section data sets required for calculating the electronic impact rate coefficients, as well as the radiative emission data. Subsequently, it generates the corresponding set of particle balance equations that are then passed to an Ordinary Differential Equations (ODE) solver. The latter returns an array representing the time evolution of the level densities. In addition to the core code, additional methods for synthetic spectra generation were implemented. Figure 3.7 provides an overview of the general workflow.

3.3.1 Code inputs

The input variables are divided into two types according to their format: on one hand, species and the subsequent collisional-radiative processes, which are specified in a fixed external text file, and on the other hand discharge-related variables, which are provided by the user in their workspace. The external text file describes the chemistry, independently of the plasma parameters. It contains information about the levels included, the various processes, the associated cross-section data, and the path to the radiative data:

- Excited levels: in addition to xenon, the model includes the option to incorporate excited levels of helium and argon.

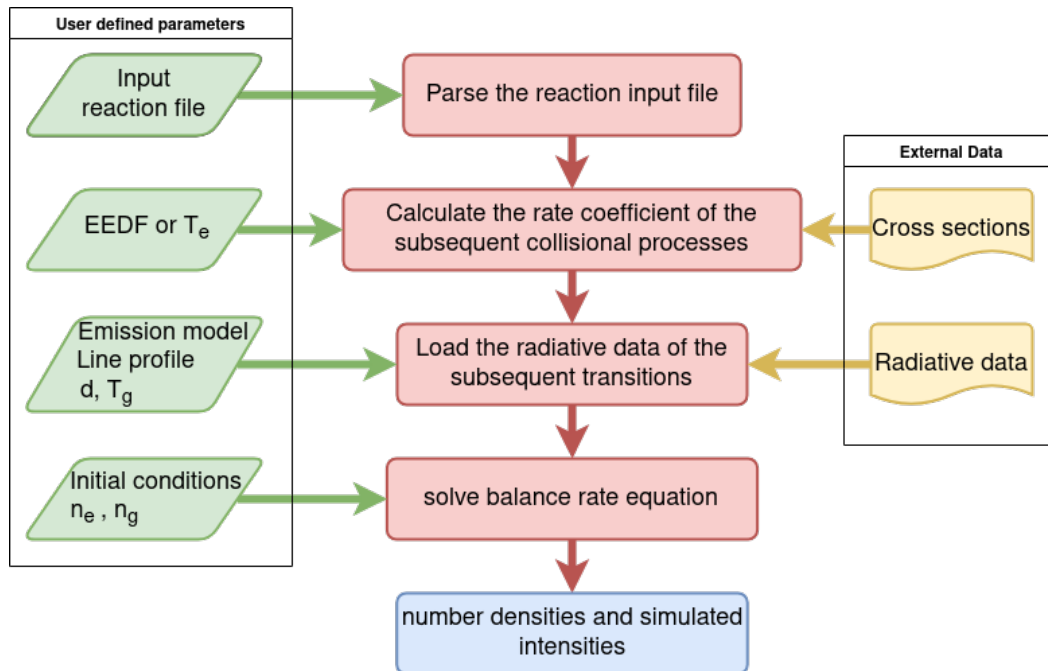


Figure 3.7: Workflow of HET0D

- Collisional processes: for each collisional process, the user has the flexibility to specify how the rate coefficient should be calculated. It can be based on the EEDF and the corresponding cross-section data. Alternatively, the user can provide a tabulated rate coefficient as a function of temperature, or define a custom analytical function for calculating the rate coefficient.
- Radiative processes: the code allows the user to specify the treatment of radiative processes. The user can indicate the Einstein coefficient for each process or choose to utilize the values provided by the NIST.

After defining the chemistry, the code allows for convenient modification of the discharge parameters within the workspace. The following plasma parameters are the essential inputs for the code:

- EEDF $f_e(E, t)$. This parameter is specified for each time step to calculate the rate coefficients. The code supports various types of EEDF. It can handle a Maxwellian EEDF defined by the electron temperature $T_e(t)$. Additionally, the generalized two-parameter EEDF can be utilized and numerical EEDFs obtained from PIC simulations.
- The electron density $n_e(t)$ with respect to the time. This parameter is used as a time-dependent initial condition. The electron creation and loss are not calculated self-consistently with the CRM.
- The gas density $n_g(t)$ with respect to the time. This parameter is also used as the initial condition for the ground state,

- The gas temperature $T_g(t)$. This parameter is employed for calculating the Doppler broadening of the emission lines.
- The optical length d . This parameter is used to calculate the optical thickness of the medium under Mewe approximation.

It is important to note that usually the previously mentioned parameters are taken constant but are here time-dependent. The code is capable of handling both.

3.3.2 Module structure

The module is structured around the `Reactions` class, which serves as a wrapper for the chemistry parser. The fundamental building block is the `Particle` class, accompanied by its derived class `Level`, which stores relevant information for each level, such as its name, mass, charge, energy, and statistical weight.

The collisional processes are represented by classes derived from the general `TwoBodyCollision` class, which describes processes with rate equations of the form $kn_p n_q$. Instances of these classes possess attributes such as the reactants, products, collision particle type, an ID, and the rate coefficient. The `EExcitation` and `IonExcitation` classes inherit the methods from this base class and extend them with process-specific features. Provided a collisional process, the rate coefficient is updated based on the user specifications from the reactions input file. If the user chooses to calculate the rate coefficient using cross sections, the `EEDF` must be provided in the input. In such cases, an instance of the `EEDF` class is expected. This class covers various types of `EEDFs`, including Maxwellian, generalized two-parameter `EEDF`, and numerical reconstructions of the `EEDF` from `PIC` simulations.

The `Radiative` class shares similar attributes with the collisional class, such as reactant, product, and ID. However, it also includes additional attributes, primarily the effective Einstein coefficient. The calculation of this coefficient depends on whether the selected emission model considers absorption or not.

The `ParticleBalance` class is responsible for generating the particle balance equations based on the specified processes in the reaction input file. These equations are then passed to the `Solver` class. The `Solver` class acts as a wrapper for an adaptive-step Backward Differentiation solver from the Scipy module. We have added argument `stepmax` to set the maximum step of the numerical scheme, ensuring a suitable time resolution.

The Backward Differentiation Formula (BDF) scheme is particularly well-suited for solving the particle balance equation Eq (3.1) in this context. This is because the involved processes occur at different time scales, with radiative transitions typically taking place on the order of 1×10^{-8} s to 1×10^{-5} s, while collisional excitations occur on the scale of 1×10^{-3} s to 1×10^{-1} s. Consequently, certain levels may evolve at a much faster rate than others, rendering classical integration scheme methods such as Euler or Newton inefficient. In our implementation, we opted for the BDF solver from the Scipy library, which provides the necessary stability and accuracy for handling these disparate time scales. The paper by Byrne

[Byrne & Hindmarsh 1975] discusses the implementation of the solver, its stability, and its accuracy. Additionally, we have cross-referenced information from Hairer et al. [Hairer & Wanner 1996b, Hairer & Wanner 1996c, Hairer & Wanner 1996a] to ensure that our initial conditions fall within the stability region of the solver conservatively.

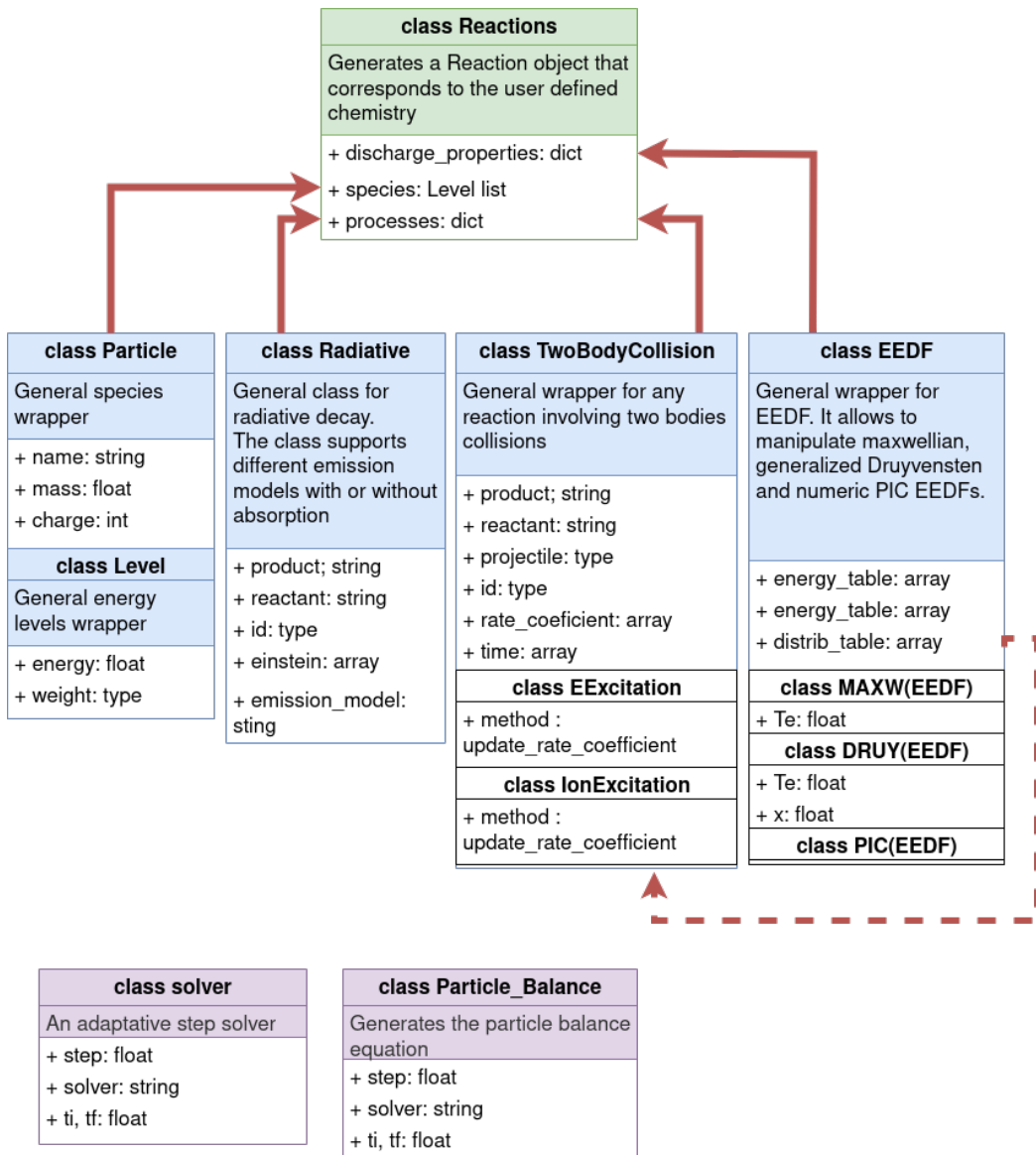


Figure 3.8: Architecture of HETOD

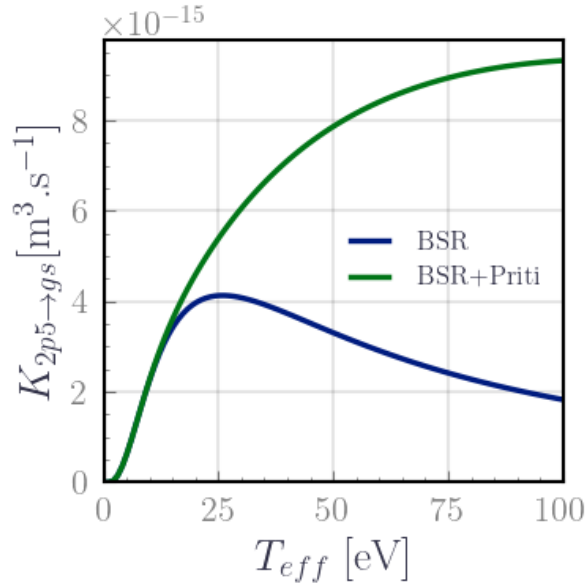


Figure 3.9: Illustration of the impact of numerical extrapolation on the calculation of the rate coefficient. The energy here should be understood as the effective electron temperature expressed in electronvolts.

3.3.3 Sampling, interpolation, extrapolation, and integration schemes

Computation in `HET0D` mainly relies on sampled data, either in the form of cross-section data or `EEDFs`. Throughout the code, these are interpolated or integrated, and it is crucial to ensure the quality of the samples to avoid introducing unwarranted numerical biases. In the initial stages of the project, significant effort was devoted to conservatively estimating and addressing these biases. While a comprehensive review of all the conducted tests is beyond the scope of this section, we present the main conclusions and measures implemented in the code.

First, we resorted to reducing the sampling step of the data by linearly interpolating on a finer energy array to achieve a sampling step of 0.01 eV. This finer interval was chosen to adequately resolve the threshold energy between levels that are within the same configuration as well as to reduce the error when calculating the integral of the rate coefficient. Higher-order interpolation schemes were explored and it was found that a simple linear interpolation provided sufficient accuracy without significantly increasing computational complexity.

Second, since the tail of the `EEDF` can be highly populated in HET, all cross-sections need to be extrapolated to higher energies to mitigate the fall-off in the calculated rate coefficients for high electron energies because of cross-section data cutoff, as illustrated in Figure 3.9. Cross sections in `HET0D` were extrapolated within a window of at least 300 eV using Priti’s cross sections when needed. The

information loss after the extrapolation was estimated to a conservative precision of 5% within the temperature range of 0 to 60 eV. Note that the 5% limit occurs for highly populated **EEDF** tail (for instance large T_e).

Lastly, the integration method employed in **HET0D** is a simple trapezoidal scheme. A comparison between other methods, such as rectangle, Simpson, and Gauss quadrature, was performed. The results indicated that higher-order schemes did not yield significant improvements in precision. The returned values were verified to have a precision of 0.1% using MATLAB and Mathematica.

3.3.4 Example of calculations

Let us consider an example of calculations using **HET0D**. We include all 15 xenon levels as listed in Table 3.1 and all processes and transitions from Tables 3.4 and 3.2. The inputs, assumed to be constant with respect to time, are as follows: the electron density n_e is $1 \times 10^{17} \text{ m}^{-3}$, the electron temperature T_e is 20 eV, the initial population density of the ground state n_g is $1 \times 10^{20} \text{ m}^{-3}$, the gas temperature T_g is 300 K, the optical length d is 15 cm, and the **EEDF** f_e follows a Maxwellian distribution. Initially, all xenon atoms are in the ground state.

We look first at the time evolution of the population densities of the excited species, shown in Figure 3.10 a) as ratios to the initial ground state population. At the beginning of the simulation, the excited species densities increase over time due to electron-impact excitation from the ground state, leading to a constant slope across all excited species. Around 1×10^{-9} s which corresponds to the typical time scale for radiative decay, a significant change in the kinetics occurs evidenced by a change in the slope of the curves followed by a plateau for the population of the $6p$ levels. This indicates a partial balance between the contributions from electron-impact excitation from the ground state and the radiative decay of the $6p$ levels. The metastable states, not being radiatively linked to the ground state, remain unaffected by this change in kinetics.

After approximately 1×10^{-5} ms, another slight change in slope occurs that now is due to the kinetics of the metastable states. Their density becomes sufficiently high so that electron-impact excitation from the metastables to the $6p$ levels becomes the dominant depopulation mechanism for the metastable states, balancing the electron-impact excitation from the ground state. As a result, all excited states eventually reach a steady state where the electron impact excitation from the ground state, the electron impact excitation from the metastables, and the radiative decay are balanced.

From the steady-state distribution obtained, we derive a synthetic spectrum using Eq. (3.22). To mimic the effect of an actual spectrometer, we apply an additional theoretical instrument broadening with a virtual spectrometer having a linewidth of $\sigma = 1.5 \text{ nm}$ and plot the result in Figure 3.10 b). This synthetic spectrum represents what one would observe in a **HET** with these specific parameters, assuming that the kinetics have been validated.

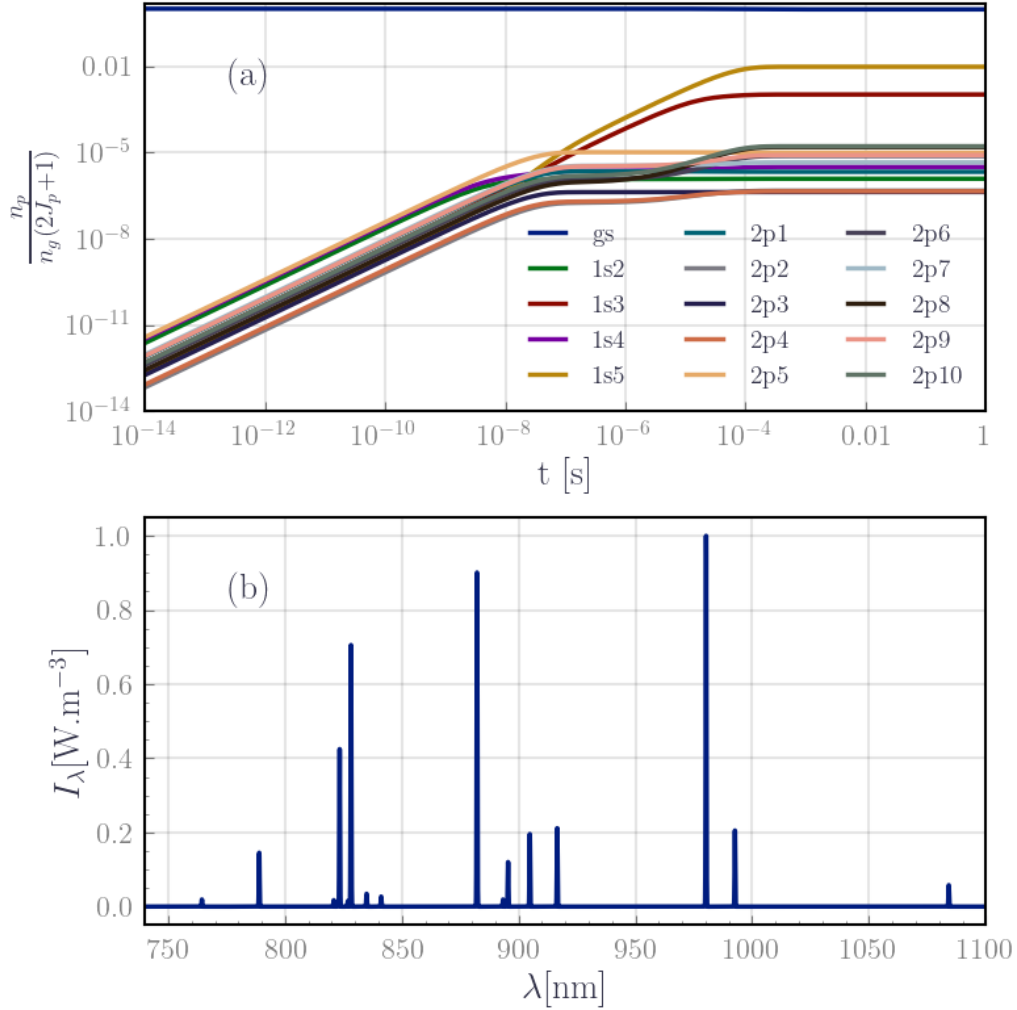


Figure 3.10: Sample calculation using HET0D. The inputs are $n_e = 1 \times 10^{17} \text{ m}^{-3}$, $T_e = 20 \text{ eV}$, $n_g = 1 \times 10^{20} \text{ m}^{-3}$, $T_g = 300 \text{ K}$, d is 15 cm, and the EEDF f_e follows a Maxwellian distribution. Initially, all xenon atoms are in the ground state. a) The time evolution of the ratio of the state densities to the initial density of the ground state b) Synthetic spectra generated from the excited species density distribution at steady state

3.4 HET0D verification and quantification of uncertainties

3.4.1 Verification of the model

Verification refers to evaluating the accuracy of the code in solving Eq. (3.21) and to assessing whether the code correctly implements the mathematical formulations and algorithms. The previous section addressed part of the verification process regard-

ing the stability of the numerical scheme and several considerations on sampling, interpolation, and integration. Here we go one step further and assess the output of the code in two test cases:

- First, a comparison with the analytical solution of a model with only two xenon levels: In this test case, we simulate the time evolution of the density of only two xenon energy levels and compare the numerical results obtained from the code with the known analytical solution.
- Second, a simulation of LTE: In this test case, we simulate a system under LTE conditions and compare the obtained results with the expected Boltzmann distribution.

Comparison with the analytical solution of a model with two levels

Let us consider a model with two xenon energy levels: *gs* and *1s2*. In this scenario, *1s2* populates via electron impact excitation from the ground state and depopulates via electron impact deexcitation. The particle balance (Eq. (3.4)) simplifies to:

$$\frac{dn_{1s2}}{dt} = n_e (n_{gs}K_{gs \rightarrow 1s2} - n_{1s2}K_{1s2 \rightarrow gs}). \quad (3.23)$$

Upon adding the conservation of the initial total particle density n_g , the analytical solution for Eq. (3.23) is expressed as follows:

$$\begin{cases} n_{gs}(t) = n_g - n_{1s2}(t), \\ n_{1s2}(t) = n_g \left(1 - \frac{K_{gs \rightarrow 1s2}}{K_{gs \rightarrow 1s2} + K_{1s2 \rightarrow gs}}\right) (1 - \exp[-(K_{gs \rightarrow 1s2} + K_{1s2 \rightarrow gs})n_e t]). \end{cases} \quad (3.24)$$

The comparison of the temporal evolution of the density of the *gs* and *1s2* between the analytical solution and the simulation is illustrated in Figure 3.11. The initial conditions are as follows: n_e is $1 \times 10^{17} \text{ m}^{-3}$, the initial population density of the ground state n_g is $1 \times 10^{20} \text{ m}^{-3}$, the gas temperature T_g is 300 K, and the EEDF follows a Maxwellian distribution at 20 eV. No excited species are present, initially.

The observed agreement between the analytical solution and the numerical results is within 0.05% relative error in the beginning and stabilizes to less than $10^{-12}\%$ in steady state. Interestingly, the maximum error occurs at the inflection point of the curves when the contributions to the density of *1s2* from excitation and deexcitation become comparable. Note however that this collision-only scenario is unrealistic mainly due to the absence of the resonant line *1s2* to *gs*. To incorporate this line, we introduce the Einstein coefficient $A_{1s2 \rightarrow gs}$ and write the balance equation as follows:

$$\frac{dn_{1s2}}{dt} = n_e \left(n_{gs}K_{gs \rightarrow 1s2} - n_{1s2}K_{1s2 \rightarrow gs} - \frac{A_{1s2 \rightarrow gs}}{n_e} n_{1s2} \right). \quad (3.25)$$

The previous analytical expression remains valid for this scenario after updating the deexcitation rate as follows: $K_{1s2 \rightarrow gs} \leftarrow K_{1s2 \rightarrow gs} + \frac{A_{1s2 \rightarrow gs}}{n_e}$.

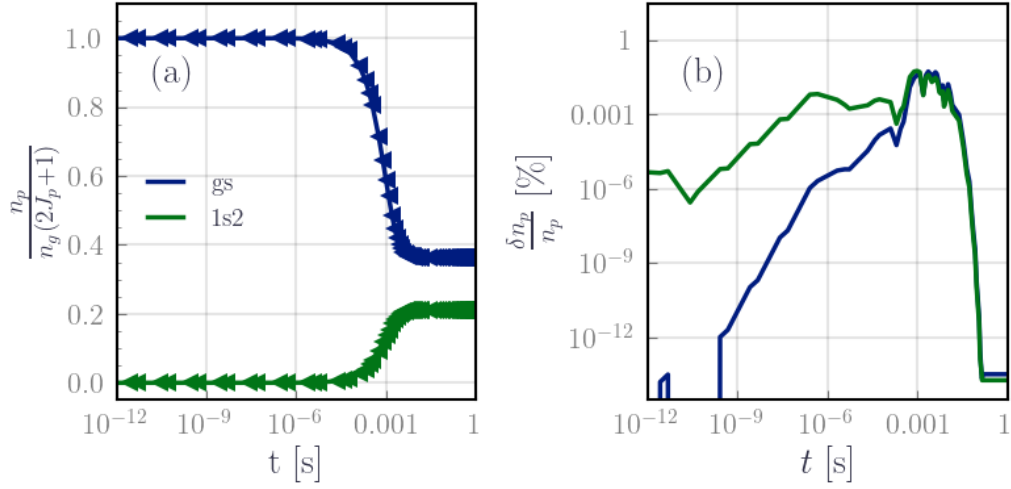


Figure 3.11: Computed and analytical time evolution of the density of the ground state and the $1s_2$ levels. For this model, only electron impact excitations between the two levels are included. The solid lines correspond to the analytical solution, the triangles correspond to the numerical solution from HETOD. Parameters: xenon, $n_e=1 \times 10^{17} \text{ m}^{-3}$, $n_g=1 \times 10^{20} \text{ m}^{-3}$, $T_g = 300 \text{ K}$, Maxwellian EEDF at 20 eV

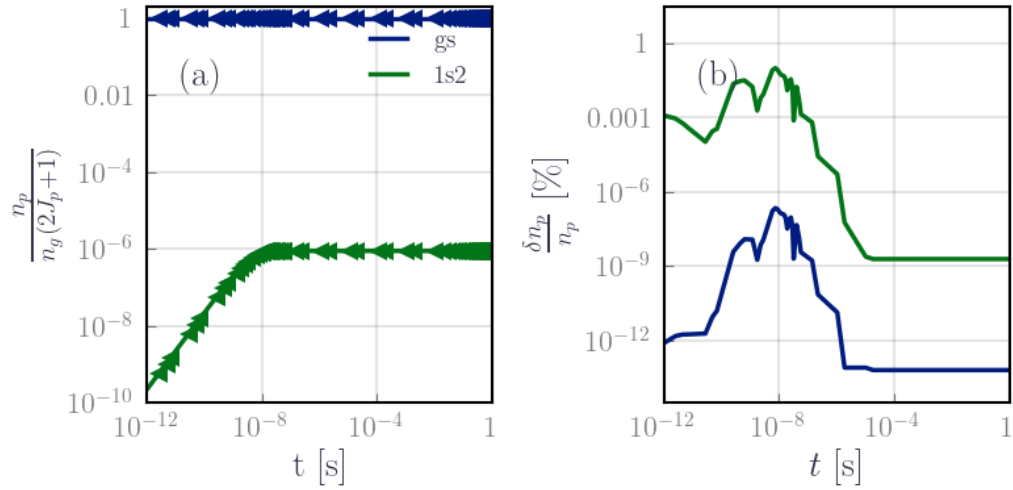


Figure 3.12: Computed and analytical time evolution of the density of the two-state levels. For this model, electron impact excitations between the two levels and the radiative decay from the $1s_2$ level are included. The solid lines correspond to the analytical solution, the triangles correspond to the numerical solution from HETOD. Parameters: xenon, $n_e=1 \times 10^{17} \text{ m}^{-3}$, $n_g=1 \times 10^{20} \text{ m}^{-3}$, $T_g = 300 \text{ K}$, Maxwellian EEDF at 20 eV

The comparison between the analytical solution and the numerical results is shown in Figure 3.12. As a result of the addition of the radiative decay, the steady state is reached now in the time scale characteristic of the radiative decay and the density of the resonant level is 10^{-6} smaller. The agreement between the analytical solution and the numerical simulation remains within 0.05% in the initial stages, but it stabilizes to less than $10^{-9}\%$ for the steady state. Similar to the previous case, the maximum error occurs at the inflection point of the curves, where the population and de-population contributions become comparable.

Simulation of local thermal equilibrium

Let us assess now, the ability of the CRM to reproduce the expected Maxwell-Boltzmann distribution at steady state for a LTE. In this test scenario, HETOD is used to simulate a xenon plasma with 15 excited states from $6s$ and $6p$. The electron-impact excitation is balanced with its corresponding inverse electron-impact deexcitation using the cross-section set from Table 3.3. The initial conditions are as follows: the electron density n_e is $1 \times 10^{17} \text{ m}^{-3}$; the initial population density of the ground state n_g is $1 \times 10^{20} \text{ m}^{-3}$; the gas temperature T_g is 300 K; and the EEDF follows a Maxwellian distribution. The radiation field is at equilibrium such as the radiative emission is compensated by the absorption yielding an escape factor $\Gamma = 0$ for all transitions. Three distinct electron temperatures were considered: T_e^L at 5 eV, T_e^M at 20 eV, and T_e^H at 40 eV. Initially, all species are in the ground state, and a total of $1 \times 10^4 \text{ s}$ was simulated.

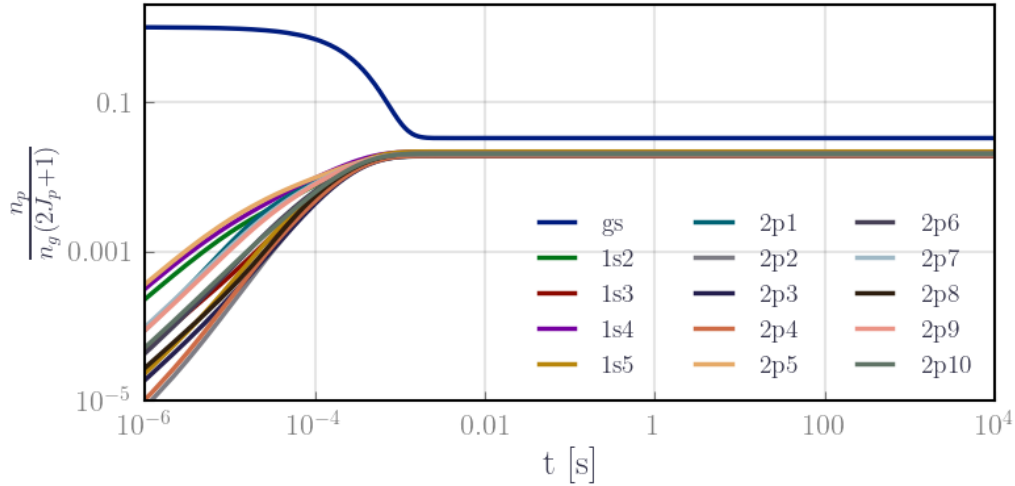


Figure 3.13: Time evolution of the population density to reach LTE. Parameters: xenon, $n_e = 1 \times 10^{17} \text{ m}^{-3}$, $n_g = 1 \times 10^{20} \text{ m}^{-3}$, $T_g = 300 \text{ K}$, Maxwellian EEDF at $T_e^{low} = 5 \text{ eV}$, $T_e^{medium} = 20 \text{ eV}$, and $T_e^{high} = 40 \text{ eV}$

Figure 3.13 illustrates the temporal evolution of the population densities. In the beginning, the excited species exhibit again a consistent increase over time

thanks to the electron-impact excitation from the ground state, displaying a uniform slope across species. The system's evolution changes kinetics around 1×10^{-5} s, as evidenced by a change in the slope, consistent with the collisional excitations from the metastable becoming important. The slope for the metastables slightly decreases whereas it slightly increases for the $6p$ levels. After approximately 1 ms, the system reaches a steady state. The densities remain constant till the end of the simulation ensuring again the solver's stability.

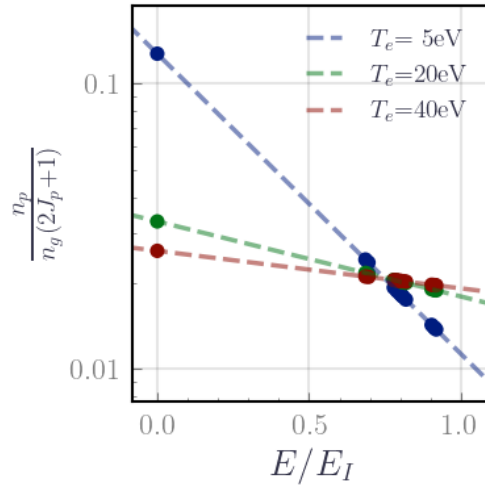


Figure 3.14: Ratio of state population at LTE. Parameters: $n_e = 1 \times 10^{17} \text{ m}^{-3}$, $n_g = 1 \times 10^{20} \text{ m}^{-3}$, $T_g = 300 \text{ K}$, Maxwellian EEDF at T_e^{medium} at 20 eV.

At the steady state, the ratio of population densities between two energy levels follows a Boltzmann distribution given by the equation:

$$\frac{n_p}{n_q} = \frac{2J_p + 1}{2J_q + 1} e^{-\frac{E_{pq}}{kT_e}} \quad (3.26)$$

In this case, the ratio of densities of the excited species to the total density of neutral species n_g results in a straight line with a slope of $1/kT_e$ when plotted against the reduced excitation energy E/E_I with $E_I = 12.13 \text{ eV}$ is the first ionization threshold of xenon.

Figure 3.14 illustrates these ratios for the three simulation cases T_e^L , T_e^M , and T_e^H , and as expected, they yield straight lines with a slope of $1/kT_e$. To assess the alignment quality, a linear regression fit is performed, yielding a correlation score of $r^2 = 1$ and the correct slope for every case.

3.4.2 Quantification of the uncertainties in HET0D

Uncertainty Quantification (UQ) refers to understanding the propagation of errors and uncertainties throughout the model from the inputs to its outputs [Ralchenko 2016]. In this section, we aim to quantify the baseline uncertainty of

our model which involves quantifying the scattering of the excited species densities based on the uncertainties in the atomic data used. These uncertainties in the atomic data are specified in Tables 3.4 and 3.2 and relate to the radiative and cross-section data.

To achieve this, a simple Monte Carlo (MC) implementation is used. We randomly selected the values of the rate coefficients and the Einstein coefficients from a normal distribution $\mathcal{N}(\mu_{pq}, s_{\mu_{pq}})$. The parameters μ_{pq} and $s_{\mu_{pq}}$ respectively correspond to the mean value and standard deviation based on the reported error bars on the corresponding quantities. The error bars were assumed to correspond to a 2σ error bar unless the authors stated differently. Thusly, the standard deviation $s_{\mu_{pq}}$ of the normal distribution is set to $\frac{e}{2}$ with e is the error from the literature expressed in units of μ_{pq} (either s^{-1} for Einstein coefficients or m for cross sections). In cases where the errors were given as percentages, we considered the error e to be $\frac{2s_{\mu_{pq}}}{\mu_{pq}}$.

Special care is taken to propagate the error to the rate coefficients since the uncertainties in Table 3.4 are expressed in terms of cross-sections. To simplify the process, we assumed a worst-case scenario where the error propagated linearly from the cross sections to the rate coefficients. The full mathematical majoration of this error is reported in the Appendix D. To preserve the detailed balance principle between direct and inverse rates, the ratio between these rates was maintained constant across all runs.

We conducted 500 MC runs for three xenon chemistries, each with different optical length d :

- Case (a) $d = +\infty$ representing an optically thick medium, hence $\Gamma = 0$. The involved processes are electron impact collisions only,
- Case (b) $d = 0$ representing an optically thin medium, hence $\Gamma = 1$. The involved processes are electron impact collisions with spontaneous emission,
- Case (c) $d = 0.15 \text{ m}$ representing an intermediate optical thickness. The involved processes are electron impact collisions with spontaneous emission, and absorption

The remaining input parameters were fixed to the same as the LTE verification scenario. We considered only two distinct electron temperatures: T_e^L at 4 eV, and T_e^H at 40 eV. The results are presented in Figure 3.15, which shows that the estimated uncertainty across the excited states falls within the range of 10-20%. For optically thin or intermediate media, the difference between T_e^L and T_e^H is negligible. In the case of an optically thick medium, the uncertainty increases only by 5% for T_e^H , and its range remains within 10-20%. This demonstrates that the uncertainty in the excited species densities is reasonably within 20%, even for varying electron temperatures and different optical lengths d .

To further analyze the contributions by type of process to the total uncertainty, we conducted additional MC runs where we deactivated the random selection for

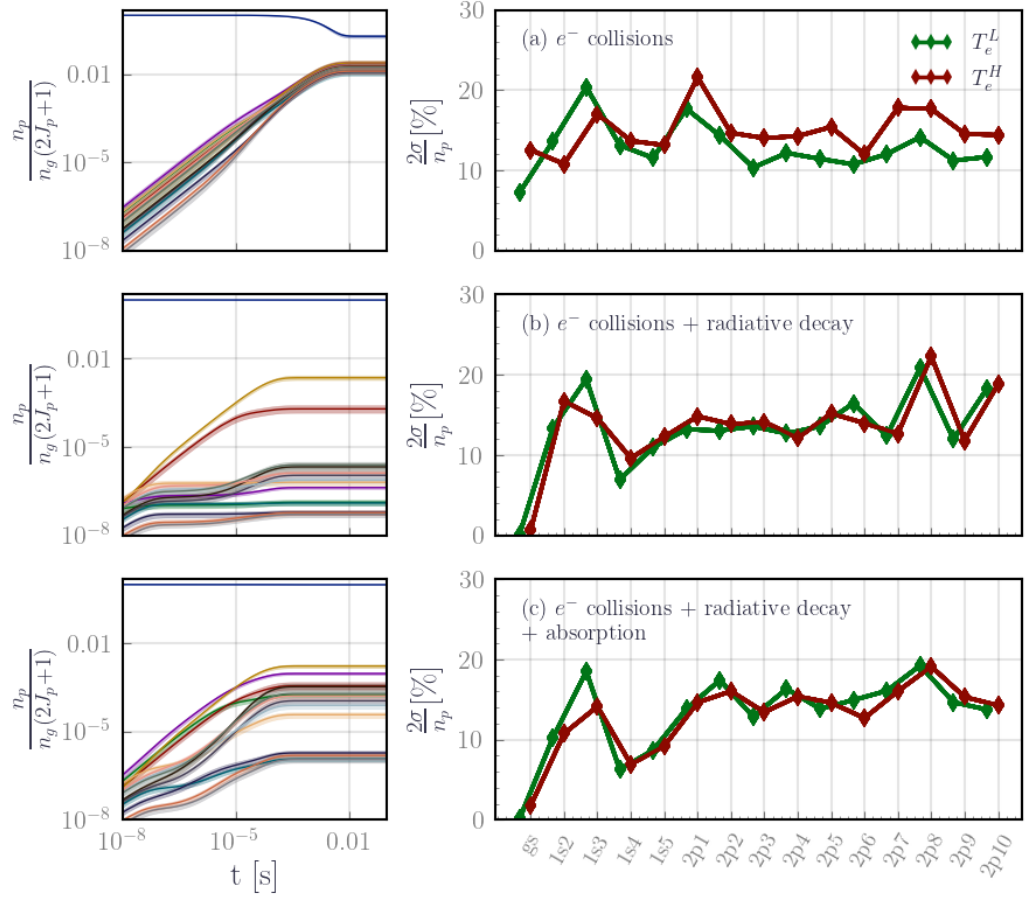


Figure 3.15: The standard deviations across the species included in HET0D for three different xenon chemistries. Parameters: xenon, $n_e=1 \times 10^{17} \text{ m}^{-3}$, $n_g=1 \times 10^{20} \text{ m}^{-3}$, $T_g=300 \text{ K}$, Maxwellian EEDF at $T_e^L=4 \text{ eV}$ and $T_e^H=40 \text{ eV}$

all collisional processes while keeping it for radiative transitions, and vice versa. We applied this approach to Case (b) and (c), which allows also us to quantify the impact of including absorption on the uncertainties. We calculated the standard deviation of the total density of the $6p$ excited species at steady state across the runs for a range of electron temperatures from 1 eV to 40 eV and the results in the form of 2σ are reported in Figure 3.16. The analysis shows that the uncertainty from collisional processes is the dominant source of uncertainty, while uncertainties related to the radiative transitions are extremely negligible. However, it is worth noting that the contribution of radiative transition uncertainties increases by several orders of magnitude, when absorption is included (Case (c)), as they intervene in the escape factor, which is very sensitive to the optical length when $d \approx 1 \times 10^{-3} \text{ m}$ to $1 \times 10^{-1} \text{ m}$.

In conclusion, we estimate the baseline uncertainty to be approximately 20%. This estimate is dominated by uncertainties in the cross-section data as compared

to uncertainties in the radiative data. These uncertainties can be propagated to the intensities calculated by the model which are involved in line ratio methods⁹ explored in chapters 4 and 5.

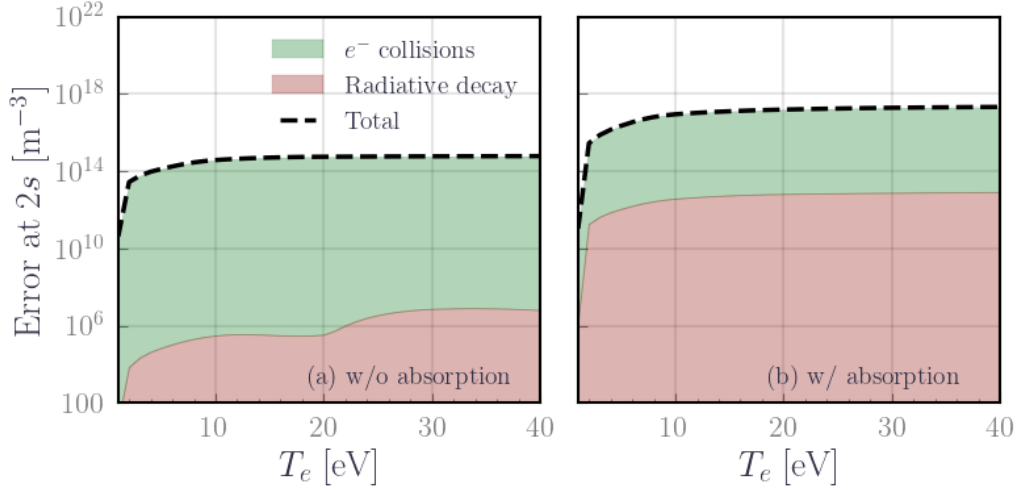


Figure 3.16: Breakdown of the contribution to the total uncertainty between the radiative transitions and the electron collision processes.

Chapter conclusions

In this chapter, a neutral xenon CRM based on the $6s$ and $6p$ levels was developed. The model solves the non-linear steady state balance equations for the $6s$ and $6p$ levels, taking into account electron impact excitation and deexcitation, spontaneous emission, as well as absorption based on the Mewe approximation. These considerations were based on previous works in the literature, which highlighted the importance of the strong ion core splitting in the xenon atom, the negligible contribution of Xe ions to the chemistry of the neutral xenon, and the possibility of using apparent cross-sections to limit the atomic model to 15 levels, while still accurately modeling the $6p$ radiative emission.

The developed model allows for the generation of synthetic spectra from the calculated densities of the excited species at a steady state, which can be compared with experimental observations. The main inputs are n_e , T_e , n_g , T_g , d and the shape of the EEDF. The model was successfully verified against analytical solutions and LTE conditions and uncertainties were quantified to a conservative 20%. Moreover, the code architecture was designed to be modular and easily extensible, enabling the incorporation of additional processes and gas mixtures in the future.

⁹The uncertainties on the excited species densities are propagated linearly to the line intensities I . For a line ratio method, the uncertainty on the line ratios $\frac{I_1}{I_2}$ from the CRM is estimated through uncertainty propagation and is expressed as $\delta\left(\frac{I_1}{I_2}\right) = \frac{I_1}{I_2} \sqrt{\frac{\delta I_1^2}{I_1^2} + \frac{\delta I_2^2}{I_2^2}}$.

However, the model's 0D nature and the use of Mewe approximation are areas where further improvements can be made, especially when applying the model to HET. Although the literature suggests that certain aspects could be overlooked, a more comprehensive modeling approach for absorption and particle transport can be implemented by coupling the CRM with a fluid or a PIC code and solving the radiative and particle transport equations concurrently, and updating the CRM accordingly. This enhancement was not implemented in the current work to prioritize computational speed and simplicity.

The CRM model presented in this chapter will be coupled with PIC simulations in Chapters 4 and 5 and will be coupled with experiments in 7.

Parametric Study of HET0D

Philidor saisit un caillou et le lança contre un moineau, mais il manqua son coup et le moineau s'envola. Le soleil commençait à chauffer. L'Anti-Philidor saisit une motte de terre et la lança contre un tronc d'arbre, qu'elle atteignît.

Witold Gombrowicz, *Fredydurke*

Contents

4.1	Parametric study of HET0D	62
4.1.1	Reduction of the system	63
4.1.2	Parametric study over the collisional parameters	64
4.1.3	Parametric study over the radiative parameters	69
4.2	Dominant kinetic mechanism	70
4.2.1	Dominant kinetic region in the n_e - n_g space	71
4.2.2	Dominant kinetic mechanisms in HET	75
4.3	Validation against the KCD model	78
4.3.1	KCD model	78
4.3.2	Verification against KCD model	82

Introduction

The previous chapter introduced the HET0D model, a neutral xenon CRM designed to be coupled with PIC simulations of HET. However, to ensure the accuracy and reliability of the modeling, the characterization and the validation of the kinetic mechanisms described by the model with respect to HETs is of paramount importance. Indeed, the model captures a wide range of kinetics by adjusting the balance between collisional and radiative processes to the population of the excited species. For instance, Figure 4.1 presents the density distribution of excited species in Boltzmann plots for various absorption levels. From left to right, we have varied the optical distance d along with the escape factor Γ based on Mewe approximation from Eq. (3.19): (a) $d = 0$ and $\Gamma = 1$, (b) $d = 15$ cm and $\Gamma \neq 0$ and (c) $d = \infty$ and $\Gamma = 0$. The levels are denoted using the Paschen notation presented in the previous

chapter and the energy levels are normalized by the xenon's first ionization energy. In Case (a), radiative decay dominates the loss processes, leading to a low population of the excited species. In Case (b), collisions from metastables and radiation trapping are non negligible, resulting in longer lifetimes and higher densities for the excited species. In Case (c), the medium is optically thick, with collisions becoming the main loss mechanism and approaching local thermal equilibrium *LTE*. The validation of the model against existing models and observations in the literature are crucial to ensure its reliability in describing the plasma kinetic mechanisms in *HET*. In this chapter, we adopt the following strategy to validate *HET0D*. First, we reduce the balance equation into non-dimensional variables and explore the behavior of the model to variations in the inputs in a broad range of parameters. Next, we assess the model's dominant kinetic mechanisms based on the parametric analysis and compare it to the literature for typical plasma parameters in *HET*. Lastly, we investigate and benchmark against the reference Karabadzahk-Chiu-Dressler (*KCD*) model from [Karabadzahk *et al.* 2006]. Through this comprehensive analysis, we aim to highlight the code's capabilities, limitations, and potential use cases.

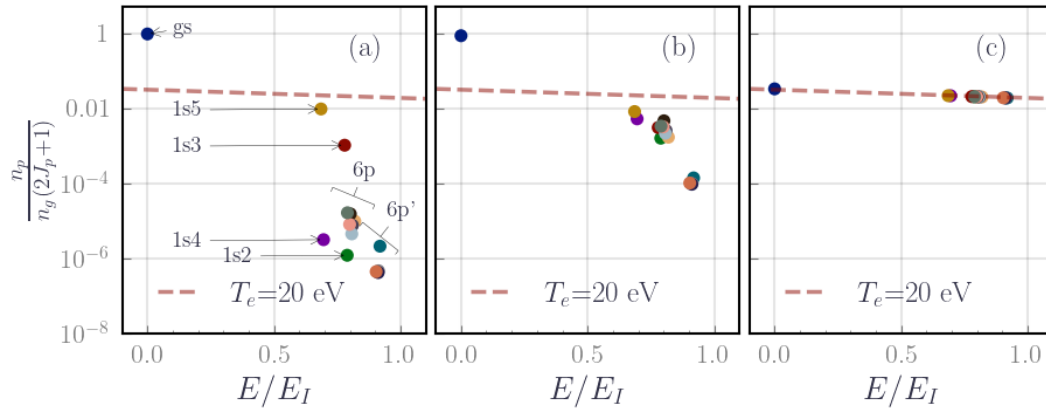


Figure 4.1: Varying the dominant kinetic mechanism of the excited species of xenon in *HET0D* by changing the optical length d and consequently the escape factor Γ . This results in changing the contribution of radiative processes compared to collisional processes in the population of excited species which translates in return in different steady state distributions. (a) $d = 0$ and $\Gamma = 1$, (b) $d = 15$ cm and $\Gamma \neq 0$ and (c) $d = \infty$ and $\Gamma = 0$. Parameters: $T_e = 20$ eV, $n_g = 1 \times 10^{20} \text{ m}^{-3}$, $T_g = 300$ K with the *EEDF* f_e following a Maxwellian distribution. The dashed line correspond to a Boltzmann equilibrium at 20 eV

4.1 Parametric study of HET0D

The model *HET0D* incorporates a chemistry involving 15 xenon levels: the ground state, $6s$ states, and $6p$ states. We use Paschen notation to designate these states, as detailed in Table 3.1. The processes include electron impact excitation, deex-

citation, and radiative decay based on the Mewe approximation (see Eq. (3.19)). The complete list of processes is reported in Tables 3.4 and 3.2. We solve the time-dependent balance equation (see Eq. (3.21)) for these 15 states. Initially, we set all the neutral density in the ground state and allow the system to evolve until it reaches the steady state.

4.1.1 Reduction of the system

Let us consider the rate balance equation and introduce the non-dimensional variables, $x_p = \frac{n_p}{n_g}$, representing the ratio of the density of the level p to the initial total neutral density n_g . With this, the time-dependent rate balance equation reads:

$$\frac{dx_p}{dt} = \underbrace{\sum_{q \rightarrow p} K_{qp} n_e x_q - \sum_{p \rightarrow q} K_{pq} n_e x_p}_{n_e, T_e, EEDF: \text{ Collisional parameters}} + \underbrace{\sum_{q \rightarrow p} \Gamma_{qp} A_{qp} x_q - \sum_{p \rightarrow q} \Gamma_{pq} A_{qp} x_p}_{T_g, n_g, d: \text{ Radiative parameters}}. \quad (4.1)$$

In this chapter, x_p will be referred to as the density ratio of the level p . The initial condition of Eq. (4.1) is now expressed as:

$$\text{Initial condition: } (x_p)_{p \in [1,15]} = (1, 0, 0, 0, 0, 0, 0, 0, 0, 0, 0, 0, 0, 0, 0) \quad (4.2)$$

This formulation of the rate balance equation associates the input parameters with the processes in which they play a crucial role. The electron density n_e , the electron temperature T_e , and the EEDF are "collisional parameters" as they significantly affect the frequency of the electron impact excitations. On the other hand, the gas density n_g , the gas temperature T_g , and the optical length d are "radiative parameters" as they mainly influence radiative processes through radiation trapping and the escape factor. Mind that this separation is simply a consequence of our framework. For instance, n_g has also an impact on the collision frequency, however in our model, its prominent impact is via radiative processes.

Looking at the escape factor, we recall the expression of the optical depth τ_{pq} here (see Eq. 3.20) for the sake of clarity:

$$\tau_{pq} = \frac{\lambda^3}{8\pi^{\frac{3}{2}}} \frac{g_p}{g_q} x_q A_{pq} \times n_g d \sqrt{\frac{M}{2RT_g}}. \quad (4.3)$$

By introducing the parameter $\kappa = n_g d \sqrt{M/2RT_g}$, the dependency on n_g , d , and T_g is consolidated into one parameter. The parameter κ is expressed in units of $[\text{m}^3 \cdot \text{s}^{-1}]^{-1}$ and is homogeneous to the inverse of a volumetric flow rate. It can be understood as an indicator of the efficiency of radiation trapping. A higher value of κ indicates efficient radiation trapping, resulting in fewer photons escaping the medium, i.e. a small "flow" of photons per unit of volume and vice versa. Consequently, the number of parameters in the model can be reduced from 6 to 4, making x_p a function of n_e , T_e , f_e , and κ :

$$x_p = f(n_e, T_e, f_e, n_g, T_g, d) = g(n_e, T_e, f_e, \kappa). \quad (4.4)$$

In the following, we perform a parametric study to inspect the dependencies of the model on n_e , T_e , f_e , and κ . The baseline values are again $n_e = 1 \times 10^{17} \text{ m}^{-3}$, $T_e = 20 \text{ eV}$, $n_g = 1 \times 10^{20} \text{ m}^{-3}$, $T_g = 300 \text{ K}$, and $d = 15 \text{ cm}$, with the EEDF f_e following a Maxwellian distribution. We will systematically vary n_e , T_e , f_e , and κ one by one to analyze their individual effects on the ratios of the density of the excited species x_p at steady state.

4.1.2 Parametric study over the collisional parameters

Impact of the electron density and the electron temperature

Impact of the electron density The density ratios x_p at steady state have been calculated as a function of n_e using HETOD with the other parameters fixed at the baseline values. Four regions are visible in Figure 4.2 based on the variations of the metastables 1s3 and 1s5.

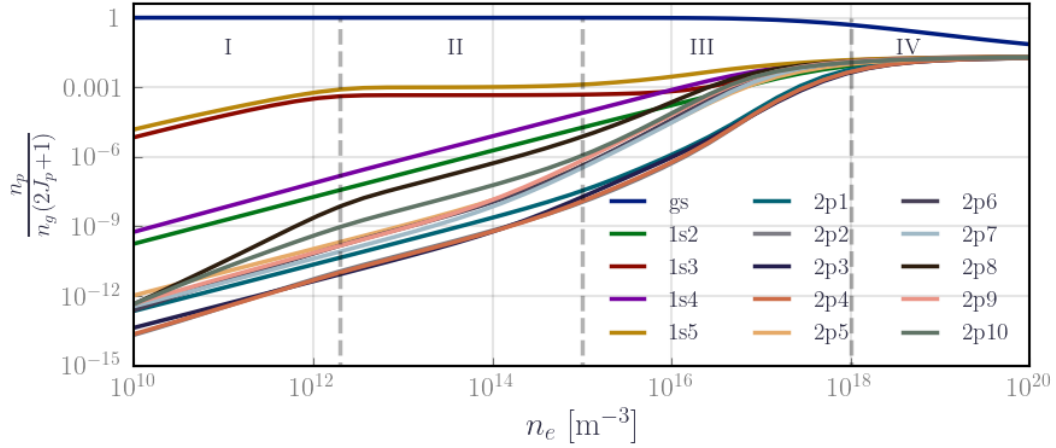


Figure 4.2: Impact of electron density on excited species ratio x_p . Parameters: $T_e = 20 \text{ eV}$, $n_g = 1 \times 10^{20} \text{ m}^{-3}$, $T_g = 300 \text{ K}$, and $d = 15 \text{ cm}$, with the EEDF f_e following a Maxwellian distribution.

The first region, characterized by very low electron densities ($n_e \leq 1 \times 10^{12} \text{ m}^{-3}$), exhibits a linear increase in the density of the metastables. At this low electron density range, radiative decay is the prominent depopulation mechanism for the $2p$ levels. Radiation trapping is negligible due to the low densities of the $1s$ levels, in particular for levels radiatively linked to the resonant levels $1s2$ and $1s4$. Thus, the balance for the $2p$ levels translates symbolically into the following equation: $An_p = Kn_en_{gs}$, ergo the observed linear dependency on n_e . For $2p8$ and $2p10$, the principal radiative decay route is to the metastable $1s5$. Given the relatively high density of the metastables in comparison to the resonant levels, the radiative rates are influenced by the increasing electron density. Collisions to the metastable states enhance the absorption rates, thereby increasing the lifetime of $2p8$ and $2p10$ and consequently their densities translating into the observed quadratic dependency on n_e . The $2p10$ and $2p8$ levels are often called the "pseudo-metastables".

In the second region, the metastable ratios are almost constant, while the $2p$ radiative levels consistently maintain their linear dependence on n_e . Collisions from the ground state to the metastable become significant compared to the radiative transitions from the $2p$ levels. The rates of electron impact excitation from the ground state to the metastables and electron impact deexcitation out of the metastable are balanced as follows $K_{gs}n_en_{gs} = K_{1s5}n_en_{1s5}$ in such a way that the dependency on the electron density cancels out. As a result, the radiative levels now exhibit a consistent linear increase with n_e , including the $2p8$ and $2p10$ levels, which aligns with the characteristics of a Corona model chemistry.

For $n_e \geq 1 \times 10^{15} \text{ m}^{-3}$, the ratios increase slightly with n_e , first starting with the $6p$ levels then the $6p'$ levels. This increase is primarily attributed to the onset of electron impact deexcitation and collisional mixing in this electron density range. Other processes, such as electron collision deexcitation from upper states and excitation from the metastables, also contribute to the observed slightly non-linear behavior.

In the last region, n_e is sufficiently high to approach LTE. The kinetics is dominated by the collisional processes leading to population densities following a Boltzmann distribution and becoming independent of the electron density. This explains why the curves flatten. However, it is important to notice that the model used here does not accurately describe a LTE. Indeed, we are assuming a finite optical length for the escape factor approximation so that the radiation field is not rigorously in equilibrium, i.e. $R^{abs} \neq R^{emi}$.

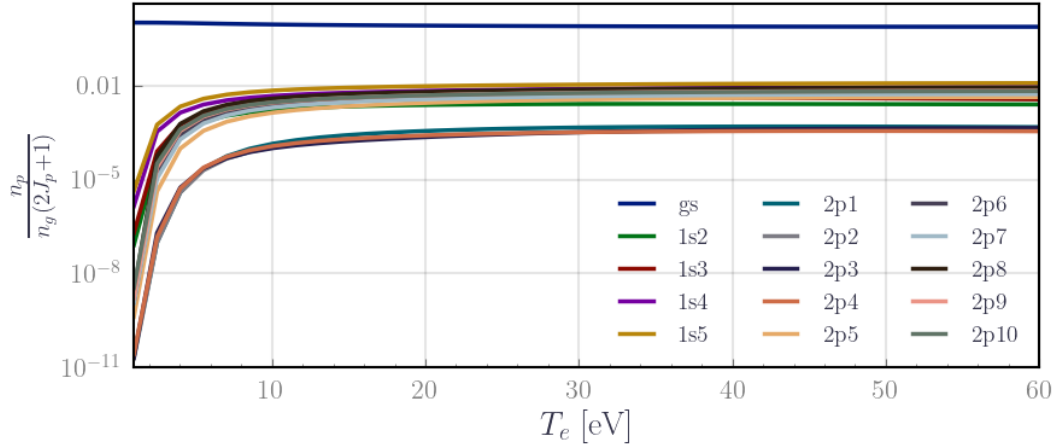


Figure 4.3: Impact of electron temperature T_e on the excited species density ratio x_p . Parameters: $n_e = 1 \times 10^{17} \text{ m}^{-3}$, $n_g = 1 \times 10^{20} \text{ m}^{-3}$, $T_g = 300 \text{ K}$, and $d = 15 \text{ cm}$, with the EEDF f_e following a Maxwellian distribution.

Impact of the electron temperature Subsequently, we calculated the excited species density ratios x_p at the steady state as a function of the electron temperature T_e for $n_e = 1 \times 10^{17} \text{ m}^{-3}$ using HET0D. The results are reported in Figure 4.3. We observe a heightened sensitivity of the excited species density ratios to T_e at

electron temperatures up to 10-15 eV. However, beyond $T_e \geq 30$ eV, the relative increase in the density ratios is less than 5% and the curves display a flattening trend, indicating that the sensitivity to T_e diminishes significantly. Moreover, this behavior seems to be tied to the energy threshold of the collisional processes, as indicated by the subtle shift of the plateau threshold with increasing energies of the excited states. This observation emphasizes the impact of the excitation threshold energy on the sensitivity range to T_e and prompts the consideration that to achieve a broader sensitivity range, the inclusion of higher-level processes in the model may be desirable.

Impact of the EEDF

Qualitative study of the impact of a non-Maxwellian EEDF on the excitation rate coefficients calculation The EEDF is modified using the generalized two-parameter EEDF introduced in Eq. (3.12), by varying the effective electron temperature T_{eff} and the shape parameter x . When keeping T_{eff} and n_e constant, changing the parameter x has diverse impacts on the low-energy and high-energy electron populations. Indeed, for $x \leq 1$, the tail of the EEDF is enhanced compared to a Maxwellian EEDF while depleting the low energy population. Hereafter, we refer to this population as the bulk. On the other hand, for $x \geq 1$, the tail of the EEDF is depleted in comparison to a Maxwellian EEDF but the bulk is enhanced.

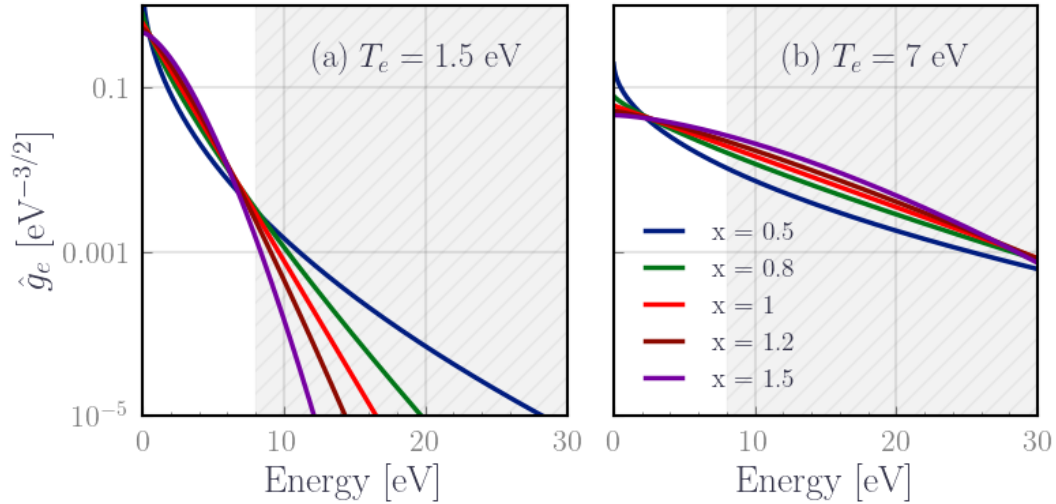


Figure 4.4: The generalized two-parameter EEDF for different shape parameters x and different effective electron temperatures T_{eff} . The gray shaded area is the range of energies greater than the xenon's first excitation energy, ie ≈ 8 eV. In (a), the generalized EEDF are computed for an effective temperature $T_e = 1.5$ eV. The tail is mainly within the threshold region. In (b), the generalized EEDF are computed for an effective temperature $T_e = 7$ eV. The bulk is mainly within the threshold region.

When calculating the excitation rate coefficients, it is crucial to determine the relative position of these effects (i.e. enhanced bulk, depleted bulk, enhanced tail, depleted tail) with respect to the collision threshold energies of the excited species. This allows us to determine whether the rates will be enhanced or reduced by the change in the shape of the **EEDF** when compared to the Maxwellian assumption. To qualitatively illustrate this, we plotted the generalized two-parameter **EEDF** in Figure 4.4 for two values of the effective electron temperature: $T_e = 1.5$ eV and $T_e = 7$ eV. Moreover, we highlighted in hatched-grey color, the range of energies relevant to electron impact excitation from the ground state, i.e. $T_e \geq 8$ eV.

In Figure 4.4 a), we observe that for a low effective electron temperature, only the tail of the **EEDF** lies within the grey hatched region. Consequently, as x decreases, the tail's population is enhanced, therefore the rate coefficients increase and vice versa. However, for high effective electron temperatures, as illustrated in Figure 4.4 b), the electrons in the bulk of the **EEDF** dominantly lie within the grey hatched region and the rate coefficients are influenced by the trends in the **EEDF**'s bulk: as x decreases, though the tail's population is enhanced, the bulk population is depleted, therefore the rate coefficients decrease.

Parametric study of the impact of the a non-Maxwellian EEDF on the steady-state distribution The density ratio x_p of the excited species at the steady state was calculated for various shapes of the **EEDF** with the following constant parameters $n_e = 1 \times 10^{17} \text{ m}^{-3}$, $n_g = 1 \times 10^{20} \text{ m}^{-3}$, $d = 15$ cm, and $T_g = 300$ K. Figure 4.5 illustrates the influence of increasing the effective electron temperature T_{eff} on x_p for different values of the shape parameter x : $x = 1.5$ (a depleted tail), $x = 1$ (Maxwellian), and $x = 0.5$ (an enhanced tail). The level densities are conveniently summed by manifold, i.e. the ground state density, the total density of the $1s$ manifold, and the total density of the $2p$ manifold.

Unsurprisingly, as observed under the Maxwellian **EEDF** assumption (Figure 4.3), an increase in T_{eff} leads to an increase in the population of the excited species. In alignment with predictions from the previous paragraph, an enhanced tail results in a higher population of excited species at low T_{eff} compared to the Maxwellian **EEDF** assumption, whereas at high T_{eff} , it results in a lower population of the excited species. Conversely, a depleted tail exhibits the opposite trend. Moreover, the transition from a relative position to the Maxwellian **EEDF** assumption to the other (i.e. above or under the Maxwellian steady-state density ratios) consistently occurs at approximately $T_c = 3.8$ eV. This critical point marks the region where the dominant contribution of the **EEDF**'s on the electron impact excitation rate coefficients shifts from the **EEDF**'s tail to the **EEDF**'s bulk.

Although this interplay between the tail and the bulk is valid, keep in mind that the numerical value of 3.8 eV might be linked to the parametrization of the **EEDF** we have chosen. We can assume that when the tail of the **EEDF** extends beyond the ionization threshold at ≈ 12 eV, the bulk of the **EEDF** becomes the primary contributor to collisions. Since the tail region starts approximately at around 3 –

$4T_{eff}$ with this parametrization, we can estimate that the critical point lies between 3 eV and 4 eV.

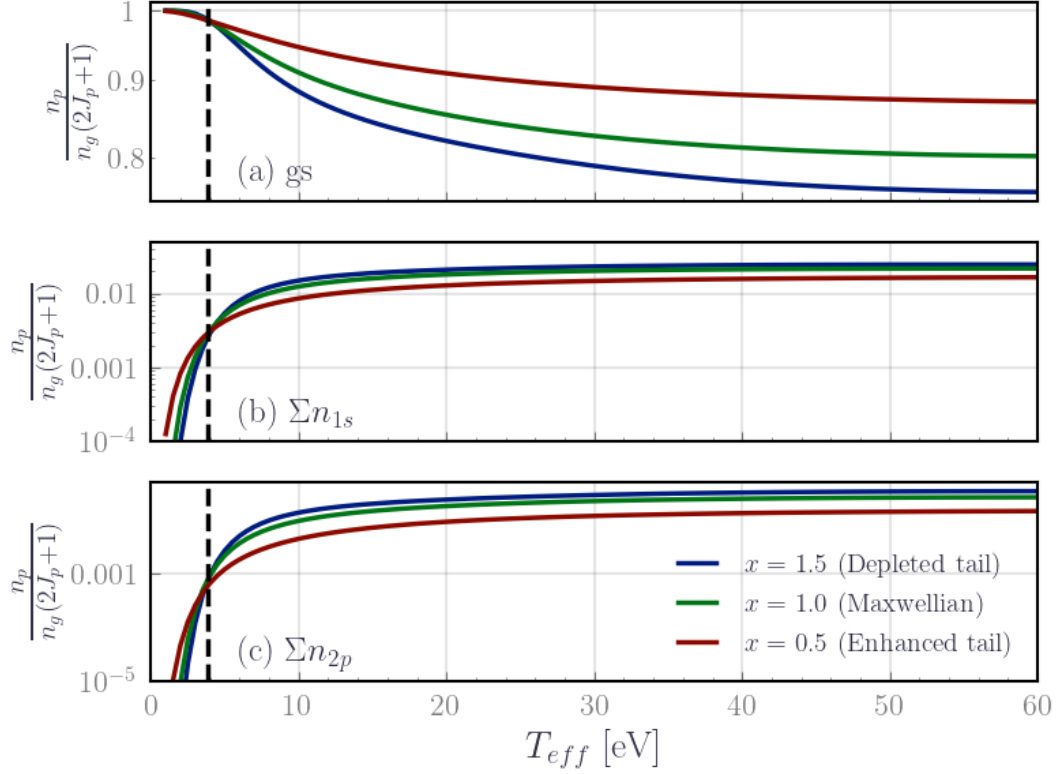


Figure 4.5: Impact of T_{eff} on the excited species population for different values of the shape parameter x : $x = 1.5$ (a depleted tail), $x = 1$ (Maxwellian), and $x = 0.5$ (an enhanced tail). Parameters $n_e = 1 \times 10^{17} \text{ m}^{-3}$, $n_g = 1 \times 10^{20} \text{ m}^{-3}$, $d = 15 \text{ cm}$, and $T_g = 300 \text{ K}$. (a) Density ratio of the ground state population to n_g (b) Density ratio of the total $1s$ population to n_g and (c) Density ratio of the total $2p$ population to n_g .

We can also investigate the deviation from the steady state distribution from the reference Maxwellian case with respect to the shape parameter x . As shown in Figure 4.5, the deviation from the Maxwellian distribution increases as we move further away from T_c in both directions (towards higher and lower effective electron temperatures). To further explore this behavior, Figure 4.6 depicts the evolution of the excited species density ratio x_p with respect to the shape parameter x , considering two cases: $T_{eff} = 1.5 \text{ eV} \leq T_c$ and $T_{eff} = 30 \text{ eV} \geq T_c$. By following the arrows on the graph, we can observe that as the EEDF moves farther away from a Maxwellian shape, more significant deviations occur. These deviations can reach up to a factor of 1000.

For $T_{eff} \leq T_c$, we observe a high sensitivity to the parameter x , with deviations reaching up to a factor of 100. This indicates that for small T_e values, deviations from the Maxwellian EEDF should be noticeable with HETOD on the distribution

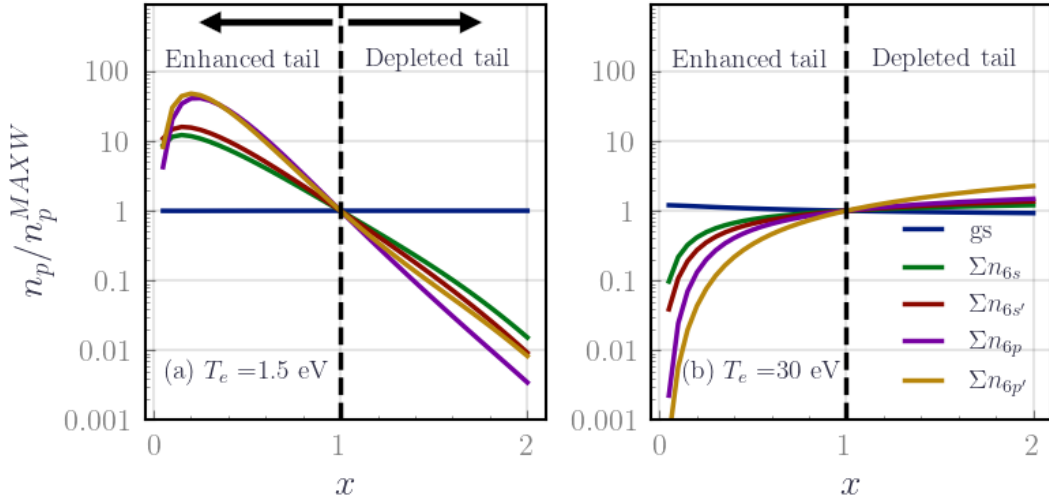


Figure 4.6: Impact of shape parameter x on the deviation from the steady-state distribution of the excited species under the Maxwellian assumption. If the density ratio of the steady state densities $\frac{n_p}{n_p^{MAXW}}$ is smaller than 1, then the excited species are less populated than at the steady state under the Maxwellian assumption and vice versa.

of the excited species and by extension their synthetic emission spectra. On the other hand, For $T_e \geq T_c$, the sensitivity to the parameter x becomes less prominent, and the deviation from the Maxwellian is only up to a factor of 3, except for low values of x ($x \leq 0.4$), where more substantial deviations persist. Still, these low x values are not physical [Boffard *et al.* 2004]. Finally, the high energy $6p'$ states are the most sensitive to the range of x .

4.1.3 Parametric study over the radiative parameters

Here we investigate the influence of the "radiative" parameters, namely, n_g , d , and T_g whose impacts are combined into the parameter $\kappa = n_g d \sqrt{M/2RT_g}$. The impact of the gas temperature T_g is not investigated and we considered it constant at 300 K throughout the parametric study. Initially, the density ratio of the excited species was calculated for varying values of n_g and d while keeping $T_e = 20$ eV, $n_e = 1 \times 10^{17} \text{ m}^{-3}$, and $T_g = 300$ K. The density ratio of the metastable state $1s5$ to neutral density n_g at the steady state is shown in Figure 4.7. The straight lines represent a constant product $n_g d$. These are aligned with the equi-metastables density ratio colormap contour lines, confirming that for constant κ the normalized distribution of the excited species does not change.

Then, we compute the density ratios of excited species for increasing κ with constant $T_e = 20$ eV, $n_e = 1 \times 10^{17} \text{ m}^{-3}$, and $T_g = 300$ K. The curves presented in Figure 4.8 depict how the density ratio of the excited species changes with increasing κ . Based on the variation of the metastables $1s3$ and $1s5$, four distinct regions are

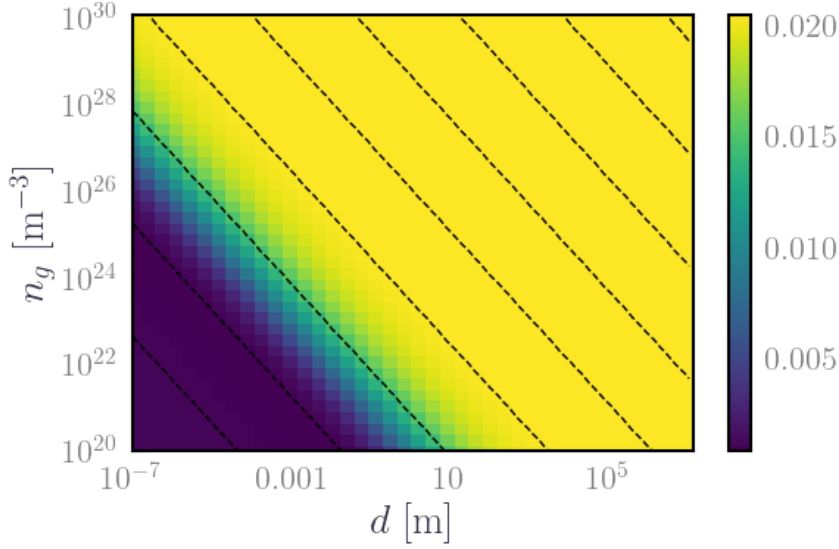


Figure 4.7: Impact of n_g and d on $1s5$ metastable density ratios: The density ratios of the metastable levels $1s5$ are depicted for different values of n_g and d , with $T_e = 20$ eV, $n_e = 1 \times 10^{17} \text{ m}^{-3}$, and $T_g = 300$ K. The EEDF was assumed Maxwellian. The dashed black lines correspond to constant κ values.

identified. The first region is characterized by a low κ . The medium is optically thin, resulting in negligible radiation trapping contribution to the kinetics. This is evidenced by the flat lines in this range. The steady state is primarily determined by the balance between electron impact excitation and spontaneous emission, similar to a *Corona model*. In the second region, the density ratios of the metastable levels slightly decrease as the population of radiative levels increases. Radiation trapping gradually becomes more efficient, leading to an increase in the lifetime of radiative species, particularly the "pseudo-metastables" $2p8$ and $2p10$. The contribution of these levels to the metastables through spontaneous emission is reduced, explaining the decrease in metastable population in this range of κ . The third region shows a consistent increase in the density ratios of the excited species across all levels. In this range of κ , electron impact excitation processes from the ground state and the metastables are significant to support an increase in the density ratios which translates into the observed trends. Finally, the fourth region is characterized by a high κ and the system approaches LTE. The kinetics is dominated by the collisional processes leading to population densities following a Boltzmann distribution.

4.2 Dominant kinetic mechanism

The previous parametric study revealed that the kinetics in HETOD depends on the evolution of the contribution of the electron impact collisions and radiative processes. Among the input parameters, n_e significantly influences collisional processes as compared to T_e , while κ significantly influences radiative processes. Based on this

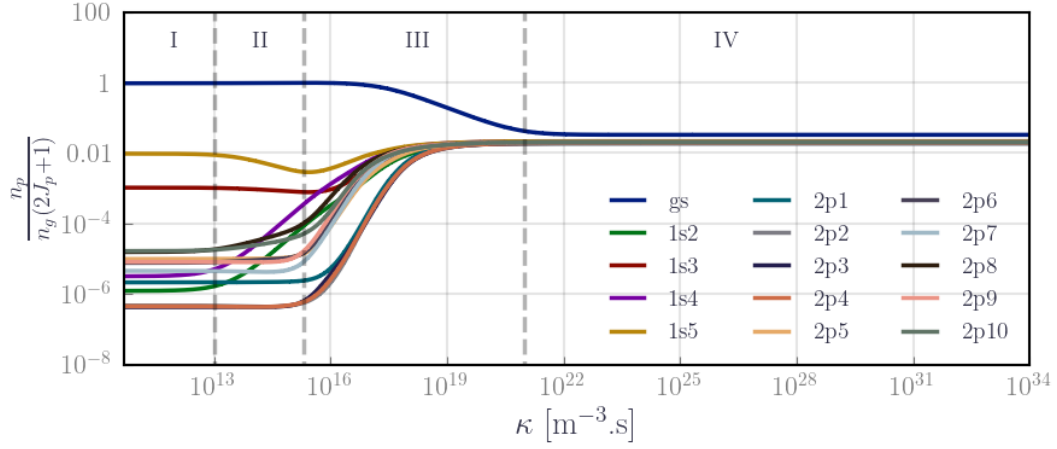


Figure 4.8: Effect of κ on excited species density ratios. The graph showcases the influence of the parameter κ on the density ratios of the excited species.

understanding, we may characterize the dominant kinetic mechanisms by studying the density ratio of the excited species to the total gas density x_p with (n_e, κ) maps or equivalently (n_e, n_g) maps, using again the baseline values for the remaining input parameters.

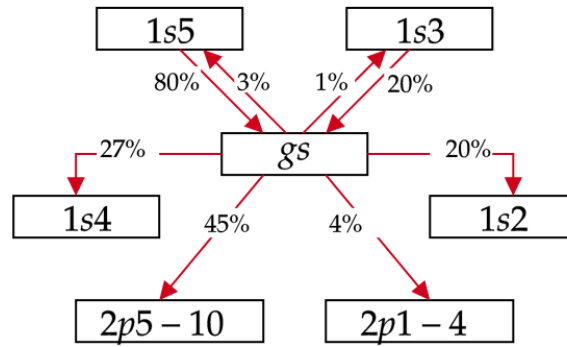
4.2.1 Dominant kinetic region in the n_e - n_g space

First, recall Figure 4.1 in the introduction. The Boltzmann plots reveal, in addition to the change in kinetics with the optical length d , the distinctive grouping in the density distributions of the $6s$ and $6p$ states, reflecting the strong ion core splitting in xenon. The densities of the $6s$ states are grouped into resonant and metastable, while the $6p$ manifold exhibits a grouping of levels into $6p$ states ($j_c = 3/2$) and $6p'$ states ($j_c = 1/2$) and a partial equilibrium-like distribution within each tier. This grouping reflects that similar kinetic mechanisms are afoot within each group. For this reason, our analysis focuses on representative species of each group to illustrate the dominant kinetics mechanisms: the ground state, the $1s4$ for the resonant xenon states, the $1s5$ for the metastable xenon states, the $2p8$ for the $6p$ tier and the $2p1$ for the $6p'$ tier.

For each representative species, we examine their density ratios in the (n_e, n_g) space. We also determine the net contribution of collisions and radiative processes to their population and depopulation rates. The net contribution of a process to the population/depopulation is defined as the change rate of the populating/depopulating process of interest (i.e. either a collisional process C or a radiative process R), divided by the total change rate of all the populating/depopulating processes. For instance, the contribution of electron collisions from the ground state to the population of the $2p1$ level is expressed as follows:

$$\%C_{gs \rightarrow 2p1} = \frac{C_{gs \rightarrow 2p1}}{\sum_p (C_{p \rightarrow 2p1} + R_{p \rightarrow 2p1})}, \quad (4.5)$$

where $C_{p \rightarrow 2p1}$ represents the change rate of the $2p1$ level due to electron impact excitation from other levels p , including the ground state, and $R_{p \rightarrow 2p1}$ represents the change rate of the $2p1$ level due to radiative processes spontaneous radiative decay from other levels p . This allows building a kinetic diagram for each level highlighting the dominant kinetic mechanisms in play. For the sake of clarity, only the ground state diagram is reported in Figure 4.9. Additional diagrams for the excited species are included and they are reported in the Appendix E for the same (n_e, n_g) conditions.





 Radiative decay
 e^- impact

Figure 4.9: Example of a kinetic diagram for the ground state obtained for $n_e = 4 \times 10^{15} \text{ m}^{-3}$ and $n_g = 1 \text{ m}^{-3}$. The percentage on the arrows indicates the contribution to the population of the ground state if it is a population process or the contribution to the depopulation of the ground state if it is a depopulation process. For these plasma conditions, the kinetics is dominated by the electron impact collisions. Radiative processes though present contribute very marginally to the population and depopulation of the ground state.

Figure 4.10 displays the (n_e, n_g) maps of the ground state and resonant levels $1s4$. Three distinct regions are clearly defined based on their dependencies on n_e and n_g :

- Region I - LTE regime: In this region, the density ratio of the excited species is independent of n_e and n_g , and electron impact excitation and deexcitation processes are the dominant population and depopulation mechanisms. The collisional mixing and population transfer inside and between the $1s$ and $2p$ levels are significant and the excited species follow an equilibrium-like distribution.
- Region II - Coronal regime: In this region, the characteristic feature is that $2p$

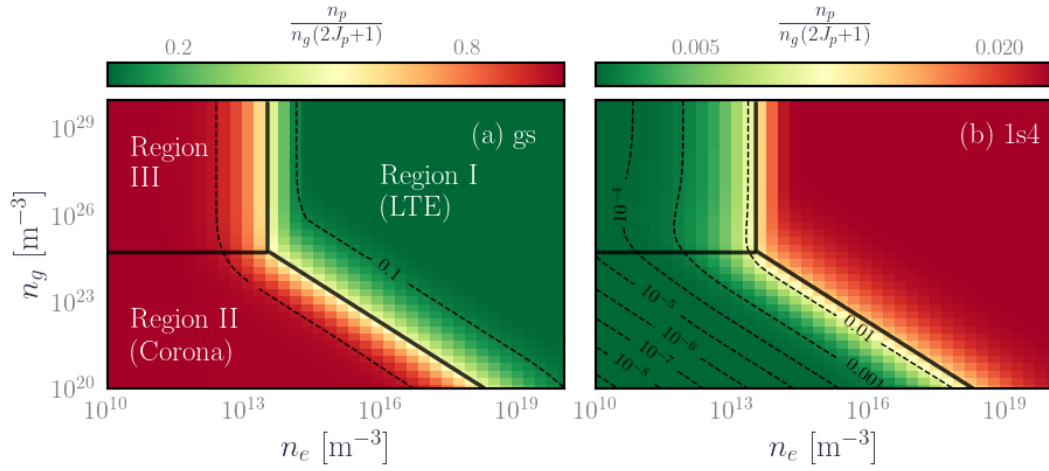


Figure 4.10: Identification of kinetics regions based on the density ratio of the ground state and resonant levels $1s4$ densities to the total gas density at steady state in (n_e, n_g) space.

levels are dominantly populated through electron collisions from the ground state and the metastable states, while they are depopulated via radiative decay to the $1s$ level. The population of the ground state is almost unchanged and only 5% of the xenon atoms are excited to higher levels. The density ratio of the resonant levels exhibits a linear increase with respect to n_e and n_g , evidenced by the density of the contour plots. The ground state is dominantly populated from radiative decay stemming from the resonant levels while depopulating via electron impact excitation to higher levels. The resonant levels are dominantly populated through radiative decay from the $2p$ levels and depopulated via resonant transitions to the ground state. This kinetics is similar to a *Corona model*.

- Region III: In this region, the density ratio of the resonant levels is independent of n_g while it is linearly dependent on n_e . This region is characterized by a change in the depopulation mechanism of the resonant levels. Indeed, the high density of the ground state increases the lifetime of the resonant levels through absorption. The resonant radiation becomes less significant compared to electron-impact deexcitation for $1s$ levels. As a result, the $1s$ levels exhibit an equilibrium-like distribution as the resonant levels densities become comparable to the metastable's. Both electron impact excitation from and into the $1s$ are dominant processes. On the other hand, radiative decay is still a significant process for the $2p$ levels.

Figure 4.11 and 4.12 displays the (n_e, n_g) maps of $1s5$, $2p8$ and $2p1$. Upon examining the (n_e, n_g) maps and the net population and depopulation mechanisms for Region II and Region III, we identify subregions defined with respect to the metastable and resonant levels of dominant kinetics.

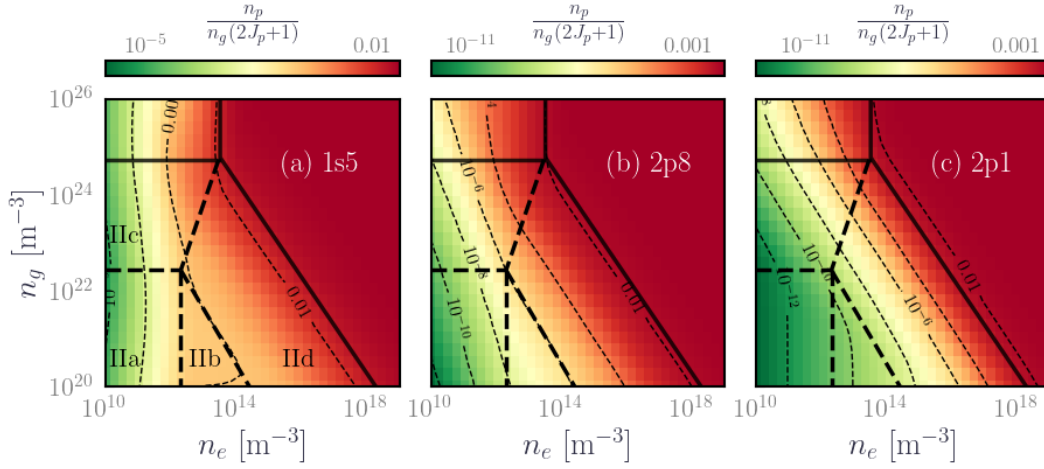


Figure 4.11: Zoom on the dominant kinetics in the Region II based on the density ratio of $1s5$, $2p8$ and $2p1$ at steady state in n_e - n_g space

Region II subregions: Within Region II, 4 subregions are identified based on the increasing importance of electron excitation from the metastable as n_e increases. These are displayed in Figure 4.11 and are as follows:

- IIa is when the electron impact from the ground state is the dominant excitation channel for the $2p$. The metastable $1s3$ is mainly populated through ground state excitation and the metastable $1s5$ is mainly populated through radiative decay from the $2p$ levels. Both are depopulated via excitation to the $2p$ levels. Radiation trapping is negligible, except for the pseudo metastable $2p8$ and $2p10$.
- IIb is when the electron impact from the ground state is the dominant excitation channel also for the $1s$ levels at the expense of radiative decay from the $2p$. The density ratio of the metastable is constant in this subregion which corresponds to region (ii) in Figure 4.2 when we performed the parametric study with respect to n_e .
- IIc is when radiation trapping is no longer negligible due to the increase in the neutral density. The electron impact from the ground state is still the dominant excitation channel for the $2p$. The lifetime of the $2p$ levels is increased however with no change in the dominant mechanisms compared to subregion IIa
- IId is when electron impact excitation from the metastable is significant to the population of the ground state and the $2p$ levels compared to the resonant radiation and the electron impact excitation from the ground state respectively. Population transfer has an important role in the redistribution of the $1s$ population. Absorption is no longer negligible either.

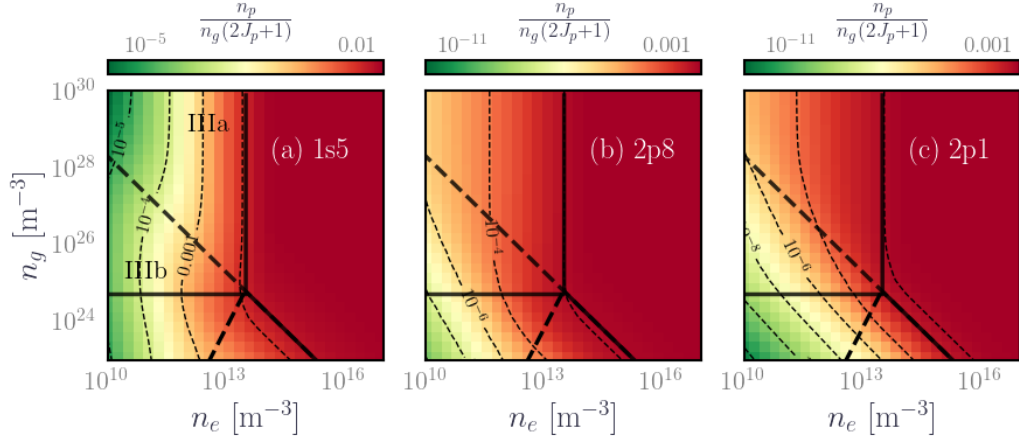


Figure 4.12: Zoom on the dominant kinetics in the kinetic Region III based on the density ratio of $1s5$, $2p8$ and $2p1$ at steady state in n_e - n_g space

Region III subregions: For Region III, 2 subregions are defined based on the kinetics of the resonant levels as n_g increases. These subregions are reported in Figure 4.12 and are as follows:

- IIIb is when the importance of the resonant radiation is decreased due to absorption from the ground state. The population transfer and collisional mixing are the dominant kinetic mechanisms to the population of the $2p$ levels, in particular, the electron excitation from the metastables, compared to the electron impact excitations from the ground state.
- IIIa is when the $1s$ exhibit an equilibrium-like distribution. $2p$ on the other hand is not in equilibrium.

The parameters T_e , d , and T_g can also impact the boundaries of each region in the (n_e, n_g) space. The optical length d and the gas temperature T_g impact the kinetics through the parameter κ . Changing these parameters results in changing κ , shifting the boundaries of the regions upward and downward along the n_g axis. For example, reducing d or increasing T_g will push up the boundary of the Corona region. On the other hand, T_e enhances electron impact excitation. As T_e increases, the boundaries of the regions will shift to the right along the n_e axis, also enlarging the Corona region.

4.2.2 Dominant kinetic mechanisms in HET

Now that HET0D has been thoroughly characterized, we focus on the kinetics relevant to HET. Typical plasma parameters for HET fall within the ranges of $1 \times 10^{15} \text{ m}^{-3}$ to $1 \times 10^{18} \text{ m}^{-3}$ for n_e and $1 \times 10^{18} \text{ m}^{-3}$ to $1 \times 10^{22} \text{ m}^{-3}$ for n_g . As a result, HET can be described mainly by kinetics from the IIb and IId regions.

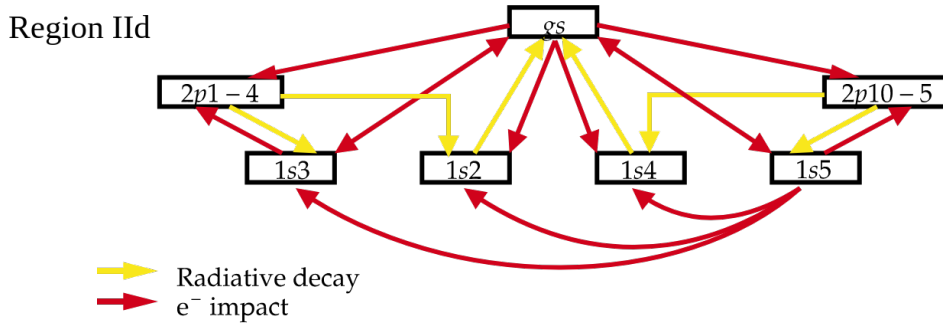


Figure 4.13: Reduced kinetic diagram illustrating dominant mechanisms in the IIb and IId subregions.

We illustrate the dominant mechanisms expected using a reduced kinetic diagram in Figure 4.13. Notably, for the ground state, the dominant population process is deexcitation from the metastable levels rather than resonant radiation. The metastable levels are primarily populated through electron impact excitation from the ground state, with negligible contribution from the radiative decay from the $2p$ levels. On the other hand, the depopulation of the metastables mainly occurs via electron impact excitation to the $6p$ levels. The metastables' deexcitation to the ground state, while important for the ground state's population, represents only a small fraction of the depopulation of the metastable levels.

Regarding the $2p$ levels, they are populated through electron impact excitation from the ground state and the metastables and are primarily depopulated via radiative decay. The contribution of collisional mixing is small, accounting for less than 1% of the overall population rate of the $1s$ levels. Finally, note also that the levels are grouped into prime and unprimed tiers due to strong collisional coupling with the metastable level of the same tier. For instance, $1s5$ is mainly populating the $6p$ tier, and $1s3$ is mainly populating the $6p'$ tier, consistent again with the ion core splitting. Detailed kinetics diagrams by species supporting the previous description are reported in Appendix E.

To validate this kinetics, we compare our results with the CRM of [Zhu *et al.* 2019] for HET. Their work includes comprehensive kinetics of the excited levels of both Xe and Xe^+ . The kinetic processes for atomic and ionic species cover electron/ion impact excitation, electron/ion impact ionization, electron/ion impact ionization-excitation, radiative decay with radiation trapping, and finally diffusion to the walls. The kinetics were analyzed using a laboratory HET in the near-anode, ionization, acceleration, and plume regions, by comparing the emission spectra from the experiment with the emission spectra from the model. Unfortunately, the plasma parameters are not specified in the process. Therefore, we rely on a qualitative comparison of the kinetic diagrams in Appendix E for the baseline plasma parameters.

The comparison is performed with the results of Figures 8 to 11 of the referenced work which provide details on the kinetics of $2p5$ and $2p10$, and also Table 10 of

the same work which lists the production rate ratios of Xe($6p$) from three groups of processes in a working lab HET: group (a) is the ground-state excitation by electrons and radiative decay from high-lying levels (grouped in our model using apparent cross sections), group (b) is the excitation or deexcitation by electrons from metastable levels, and group (c) is the self-absorption. We focus in our comparison on the ratios of (a) and (b), as the ratio of (c) is already included in the radiative decay term and is not separated in our description. The results are reported in Table 4.1.

Table 4.1: Population rate ratio of $6p$ states from three groups of processes: (a) ground-state excitation by electrons and radiative decay from high-lying levels, (b) excitation or deexcitation by electrons from metastable or excited levels, and (c) self-absorption. The ratio of (c) is omitted when very small. This table was transcribed from the work of [Zhu *et al.* 2019]. The levels were conveniently renamed in Paschen’s notation for the sake of consistency with this work. The ratio is reported as follows: Group (a): Group (b): Group (c). The last column reports the values found in HET0D in the region IId with $T_e = 20$ eV, $n_e = 1 \times 10^{16} \text{ m}^{-3}$, $n_g = 1 \times 10^{20} \text{ m}^{-3}$ and $T_g = 300$ K, $d = 15$ cm and a Maxwellian EEDF.

Level	Near-anode	Ionization	Acceleration	Plume	HET0D
$2p8$	34:37:29	31:49:20	30:57:13	37:59	40:60
$2p10$	50:39:11	46:47:7	42:53:4	44:52	50:50
$2p5$	98:2	99:1	98:2	96:2	100:-
$2p4$	75:25	68:32	54:45	64:32	65:35
$2p2$	78:22	72:28	64:36	68:29	66:33
$2p9$	77:21:2	73:26:1	70:28:1	66:27	89:11
$2p6$	53:36:11	48:45:7	45:51:4	48:48	65:35
$2p7$	88:12	84:16	79:20	73:17	95:5
$2p3$	75:25	71:29	60:40	68:30	100:-
$2p1$	29:71	24:76	17:83	23:77	40:60

The results show that HET0D and the work of [Zhu *et al.* 2019] are in decent agreement regarding the dominant kinetic mechanisms governing the population and depopulation of excited species in the relevant range of values. The best agreement is observed in the ionization and acceleration regions of the thruster and can be attributed to the absence of diffusion and heavy atom collisions as compared to the near-anode regions, which are not included in our model. The production ratios are within $\pm 10\%$ of each other, except for the $2p3$ and the $2p1$ states. However, some differences are present, specifically HET0D underestimates the production rates from $1s3$, especially for $2p1$ and $2p3$ (cf corresponding diagram in Appendix E). This can be explained by the high T_e that has been conveniently used as the

baseline value for this analysis. Indeed, since the excitation rate from the metastable to $2p$ varies slowly with T_e in comparison to the excitation rate from the ground state to $2p$, reducing T_e improves the agreement with the work of [Zhu *et al.* 2019] by enhancing the production ratio of the excitations from the metastable at the expense of the production ratio of the excitation from the ground state.

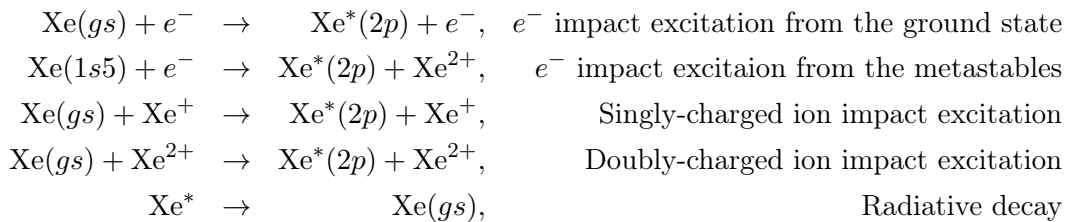
Considering the current stage, we are confident that HET0D adequately describes the relevant kinetics in HET despite the limited number of levels and processes included in the description. The model provides reliable behavior with respect to its inputs and captures the dominant kinetic mechanism. While further refinements and the inclusion of additional processes may be necessary for a more comprehensive description of the near-anode region, the current capabilities of HET0D seem to be well suited for $1 \times 10^{15} \text{ m}^{-3} \leq n_e \leq 1 \times 10^{18} \text{ m}^{-3}$ and $1 \times 10^{18} \text{ m}^{-3} \leq n_g \leq 1 \times 10^{22} \text{ m}^{-3}$ and $T_e \geq 2 \text{ eV}$ to describe the plasma kinetics in the ionization and acceleration regions.

4.3 Validation against the KCD model

The model developed by [Karabadzhak *et al.* 2006] remains the prominent reference model for investigating highly radiative near-infrared transitions of xenon in HET plume. Given its wide acceptance and recognition, this model serves here as an appropriate benchmark for HET0D.

4.3.1 KCD model

The model focuses on the population of excited species from $6s$ and $6p$ levels, considering electron impact excitation from the ground state and metastable states, as well as ion-impact excitation from the ground state by singly and doubly charged xenon ions. The addition of ion impact excitation stems from its high contribution at low T_e and very low pressures compared to the electron impact excitation from the ground state. Indeed, [Karabadzhak *et al.* 2006] showed that approximately 30% of the radiance can be attributed to ions when the electron temperature is below or equal to 3 eV. Radiative decay is considered the sole depopulation pathway, neglecting electron deexcitations, diffusion, and other collisional processes. A simplified schematic of the model is illustrated in Figure 4.14. Note that the kinetic mechanism described in this model is similar to the kinetics of subregion II*d* in HET0D in the absence of absorption ($d = 0$).



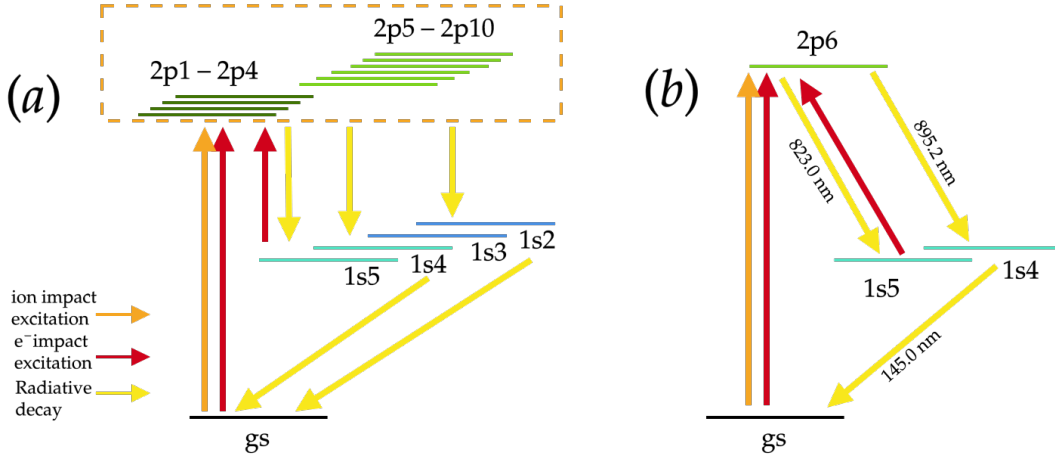


Figure 4.14: Simplified schematics of the KCD model: (a) Diagram of the 2p levels included in the KCD model. The red arrows correspond to electron impact excitation, the yellow arrows correspond to radiative decay, (b) The 2p6 level is shown as an example to highlight the stepwise excitation from the metastable to the 2p followed by radiative decay to 1s4.

Upon writing the particle balance equation for the 6p levels at steady state, the analytical expression for the intensity of the NIR emission line λ_{pq} can be derived with respect to the density of the neutral density n_g and the metastables 1s5 density n_{1s5} and is expressed as follows [Karabadzhak *et al.* 2006]:

$$I_{\lambda_{pq}} = \frac{hc}{4\pi\lambda_{pq}} n_0 n_e \left[K_{gs \rightarrow p}^{\lambda_{pq}} + \frac{n_{1s5}}{n_0} K_{1s5 \rightarrow p}^{\lambda_{pq}} + \alpha K_1^{\lambda_{pq}} + \frac{1-\alpha}{2} K_2^{\lambda_{pq}} \right], \quad (4.6)$$

where:

- $K_{gs \rightarrow p}^{\lambda_{pq}}$ is the emission rate coefficient for electron-impact excitation from the ground state to the level p considering only the portion that then decays to the levels q via the emission line λ_{pq} ,
- $K_{1s5 \rightarrow p}^{\lambda_{pq}}$ is the emission rate coefficient for excitation from the 6s metastables to the level p level that then decays to the level q via the emission line λ_{pq} .
- $K_1^{\lambda_{pq}}$ and $K_2^{\lambda_{pq}}$ are, similarly, the emission excitation rate coefficients for collisions of Xe^+ and Xe^{2+} with neutral xenon atoms,
- α is the ratio of Xe^+ to the electron number density.

The quantity $I_{\lambda_{pq}}$ here is a radiant power density in $\text{W}\cdot\text{m}^{-3}$ per unit of solid angle. Contrary to [Zhu *et al.* 2019] and our model, KCD model does not include all lines from 6p and focuses only on eleven NIR emission lines which are summarized in Table 4.2. Note that the emission probabilities are expressed in terms of branching ratios

rather than Einstein coefficients. The branching ratio would quantify the probability of a specific radiative transition relative to all possible radiative transitions at a given experimental condition, such as $R_{\lambda_{pq}} = \frac{A_{\lambda_{pq}}}{\sum_{\mu} A_{\mu}}$.

The rate coefficients for electron impact excitations are calculated using Eq. (3.2), assuming a Maxwellian EEDF and using emission cross-sections from experimental data presented by [Chiu *et al.* 2006]. These cross-sections, denoted as $\sigma_{\lambda_{pq}}$, account for the direct excitations and radiative cascades from the ground state to a specific $6p$ state, *which subsequently would decay through the radiative transition λ_{pq}* . The branching ratios allow us to relate these cross-sections to the apparent cross-sections from [Fons & Lin 1998] in the following manner:

$$\sigma_{\lambda_{pq}} = \frac{A_{\lambda_{pq}}}{\sum_{\mu} A_{\mu}} \sigma_{pq}^{app} \quad (4.7)$$

Similarly to the apparent cross-section, the emission cross-sections from [Chiu *et al.* 2006] allow for the inclusion of radiative cascade for higher levels. Additionally, it allows for a reduction of the number of radiative transitions, via the use of the branching ratio.

Table 4.2: NIR xenon emission line from the $6p$ tier included in the KCD model. Only the intensities of the lines with the superscript "a" are calculated with the Eq. (4.6). The 895.2 and the 992.3 transitions are included to close the kinetic scheme on the $2p6$ and $2p9$ and create a realistic depopulation pathway

λ_{pq} [nm]	Transition	A_{pq} [$1 \times 10^6 \text{ s}^{-1}$]	Branching Ratio
788.7 ^a	2p1 \rightarrow 1s2	35	0.720
834.7 ^a	2p3 \rightarrow 1s2	42	0.863
828.0 ^a	2p5 \rightarrow 1s4	36.9	0.998
823.2 ^a	2p6 \rightarrow 1s5	28.6	0.743
895.2	2p6 \rightarrow 1s4	8.1	0.243
840.9 ^a	2p7 \rightarrow 1s5	3.06	0.099
916.3 ^a	2p7 \rightarrow 1s4	24	0.901
881.9 ^a	2p8 \rightarrow 1s5	30.0	1.000
904.5 ^a	2p9 \rightarrow 1s5	12.4	0.379
992.3	2p9 \rightarrow 1s4	13.0	0.621
980.0 ^a	2p10 \rightarrow 1s5	31.1	0.975

The measurements by [Chiu *et al.* 2006] are extrapolated beyond 70 eV using the following empirical expression :

$$\sigma_{\lambda_{pq}}(E > 70 \text{ eV}) = \frac{\sigma_{pq}^{app}(70, 1)(E/70)^{c_{\lambda_{pq}}}}{1 + a_{\lambda_{pq}} \left(\frac{E-11.5}{E-9.8} \right)^{n_{\lambda_{pq}}} (1 - e^{-\gamma_{\lambda_{pq}} p})^2} \quad (4.8)$$

Table 4.3: Parameters involved in the high energy extrapolation from [Chiu *et al.* 2006, Karabadzhak *et al.* 2006]

λ_{pq} [nm]	788.7	823.2	828.0	834.7	881.9	904.5	916.3	980.0
$a_{\lambda_{pq}}$	1.394	1.356	1.297	0.275	0.768	3.669	3.000	1.354
$c_{\lambda_{pq}}$	-0.607	-0.77	-0.589	-0.892	-1.07	-0.7	-0.473	-0.86
$n_{\lambda_{pq}}$	19	15	16	8	13	35	15	8
$\gamma_{\lambda_{pq}}$	0.75	0.65	1.47	2.00	0.69	2.56	2.02	1.70

Here, $\sigma_{\lambda_{pq}}^{app}$ is evaluated at 70 eV, $a_{\lambda_{pq}}$, $c_{\lambda_{pq}}$, $n_{\lambda_{pq}}$ and $\gamma_{\lambda_{pq}}$ are reported in Table 4.3.

For the ground state ion impact excitation, the rate coefficients were calculated using the following equation :

$$K_1^{\lambda_{pq}} = \sigma_{\lambda_{pq}}(E_I) \sqrt{\frac{2qV}{m}}, \quad \text{Singly charged} \quad (4.9)$$

$$K_2^{\lambda_{pq}} = \sigma_{\lambda_{pq}}(E_{II}) \sqrt{\frac{4qV}{m}}, \quad \text{Doubly charged} \quad (4.10)$$

where V is the thruster anode voltage expressed in volt and E_{II} is the second ionization energy of xenon expressed in electron-volt. The cross sections $\sigma_{\lambda_{pq}}$ were taken from [Chiu *et al.* 2006, Sommerville 2006]. These cross-sections were shown to be smooth with a relatively small slope in the cited work and for that reason, they are approximated to be constant.

The metastable density n_{1s5} in Eq. (4.6) is determined from the steady-state balance assuming the $1s5$ populates via electron impact excitation from the ground state and radiative decay from the $2p$ levels and depopulates via electron impact excitation to the $2p$, followed by deexcitation to the $1s4$ level. Initially, the cross-sections from these processes were unavailable, leading Karabadzhak and colleagues to make estimations based on the branching ratios and the relative weights of the energy levels. Later, [Dressler *et al.* 2009] proposed an improved version of the KCD model that incorporated the newly calculated BSR and RDW cross sections and demonstrated better agreement with experimental data. Thus, the improved KCD model will be the basis of the benchmark.

The KCD model is used to predict the electron temperature using experimental measurements of neutral xenon NIR emission in the thruster's plume. The approach involves calculating the ratio of intensities of the emission lines at 823, 828, and 835 nm as a function of T_e and comparing it to the experimental line ratio. Specifically, the ratios are 823/828 and 835/828 and are dependent on T_e , α , and V :

$$\frac{I_{823}}{I_{828}} = f_1(T_e, \alpha, V), \quad \frac{I_{835}}{I_{828}} = f_2(T_e, \alpha, V) \quad (4.11)$$

Figure 4.15 displays the calculated ratios from the work of [Karabadzhak *et al.* 2006] for $\alpha = 0.8$ and $V = 300$ V obtained from both the original KCD model and the

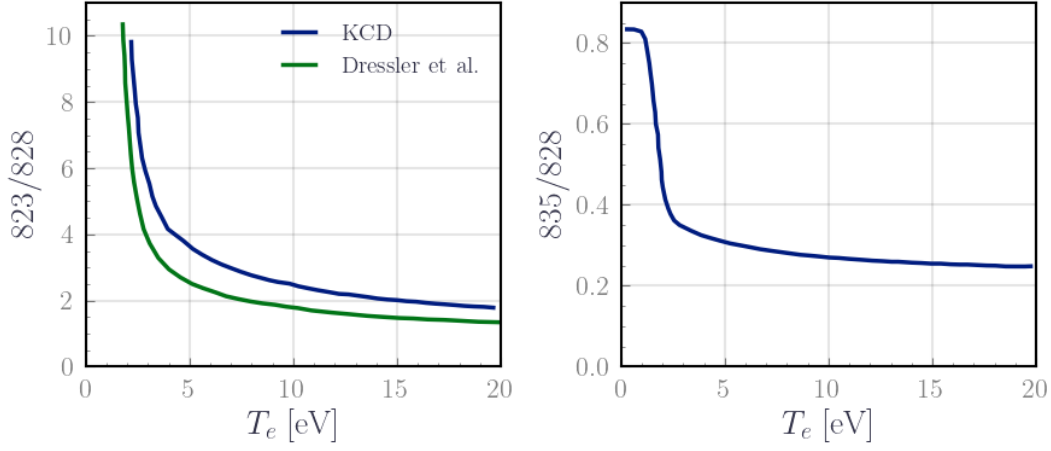


Figure 4.15: Line intensity ratios as a function of T_e predicted for a HET with $V = 300$ V and $\alpha = 0.8$. In blue, the results from [Karabadzhak *et al.* 2006] and in green, the improved results from [Dressler *et al.* 2009]

improved version. Notably, there is a correction in the case of the 823/828 ratio related to the addition of the new cross-sections from the metastable to the $2p$. Now we focus on reproducing these line ratio curves using HET0D.

4.3.2 Verification against KCD model

There are major differences in the model between KCD and HET0D, regarding the cross sections, the included levels, and the transitions. KCD suggests a reduced chemistry based on the $1s5$ and $6p$ tier states, which is primarily focused on the rate balance equation of the radiative states. In contrast, HET0D completes the KCD chemistry by including all the $6s$ and $6p$ levels.

To simplify the comparison, we adapt the HET0D model to work using the same data as KCD. This modified model will be referred to as HET0D-KCD, contrasting with the original HET0D which uses the full chemistry described in Chapter 3. In addition, the ratios in the KCD model do not depend on n_e . However, the dependency on n_e is retained in HET0D-KCD and HET0D, simply because n_e is an input of the model. Furthermore, the absence of radiation trapping in KCD results in the line ratios being invariant to changes in gas density and gas temperature. If we set d to zero in HET0D, this leaves the following dependencies for the considered line ratios for the three models/approaches:

$$\frac{I_{823}}{I_{828}} = f_{\text{KCD}}(T_e, \alpha, V), \quad (4.12)$$

$$\frac{I_{823}}{I_{828}} = g_{\text{HET0D-KCD}}(T_e, n_e, \alpha, V), \quad (4.13)$$

$$\frac{I_{823}}{I_{828}} = h_{\text{HET0D}}(T_e, n_e, V) \quad (4.14)$$

More details on the differences between the models are reported in Table 4.4.

Table 4.4: Highlight of the differences between KCD, HET0D-KCD and HET0D

Model	Levels	Processes
KCD	6s and 6p except 1s3, 2p2 and 2p4	<ul style="list-style-type: none"> • T_e, α and V dependency • e^- impact excitation from the gs and 1s5 [Chiu <i>et al.</i> 2006, Dressler <i>et al.</i> 2009], • spontaneous emission with only 11 lines [Karabadzhan <i>et al.</i> 2006], • ion impact excitation [Somerville 2006]
HET0D-KCD	6s and 6p except 1s3, 2p2 and 2p4	<ul style="list-style-type: none"> • T_e, n_e, α and V dependency • e^- impact excitation from the gs and 1s5 [Chiu <i>et al.</i> 2006, Dressler <i>et al.</i> 2009], • spontaneous emission with only 11 lines [Kramida <i>et al.</i> 2019], • ion impact excitation [Somerville 2006]
HET0D	all 6s and 6p	<ul style="list-style-type: none"> • T_e, n_e, α and V dependency • e^- impact excitation and deexcitation. Cross section were explicated in Table 3.4 • spontaneous emission with 22 lines [Kramida <i>et al.</i> 2019], • ion impact excitation [Somerville 2006] • radiation trapping is not included in this comparison

The line ratios were computed with respect to the electron temperature with the following parameters: $\alpha = 0.8$, $V = 300$ V, $n_e = 1 \times 10^{17} \text{ m}^{-3}$. The obtained line ratio for the three models is reported in Figure 4.16. The HET0D-KCD model (in blue) shows an excellent agreement with the target line ratio curves of KCD model (in red). This is expected since both models are using the same data. A sensitivity analysis conducted on n_e for HET0D-KCD revealed that it has a negligible impact on the line ratios, aligning with the KCD model on the independencies of the line ratios on n_e . At low $T_e \leq 1$ eV, the agreement is slightly off and is attributed to two reasons. Firstly, the modeling of ion impact excitation in the HET0D model is not optimized. Secondly, the use of Einstein coefficients in the HET0D-KCD contrasts with the use of the branching ratios in the KCD model.

Furthermore, when overlaying the ratios computed with the full HET0D model (in green) to the previous ratios, the curves deviate by at least a factor of 2. Ad-

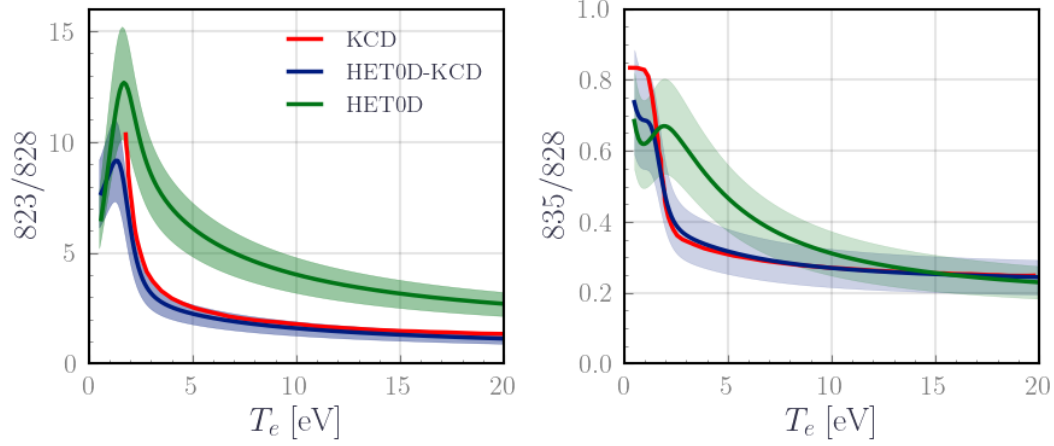


Figure 4.16: Line ratio curves from the KCD model. A 20% error bar is used, based on the propagation of error from the previous UQ in Chapter 3.

justing the electron density within the range of $1 \times 10^{15} \text{ m}^{-3}$ to $1 \times 10^{18} \text{ m}^{-3}$ does not improve the agreement, as the curves are barely affected despite the formal dependency on n_e . To gain deeper insights, we specifically examined the evolution of the line intensity for the 8 lines included in KCD from both models. Figure 4.17 illustrates the variation of these 8 lines with respect to T_e , calculated using both HET0D-KCD and HET0D. Remarkably, both models exhibit a decent agreement between the line intensities and comparable trends with a consistent scaling factor of approximately $\approx 1.5 - 2$, indicating that they capture similar kinetic mechanisms. The only exception is the 980 nm line from $2p10$ to $1s5$, which shows a more significant discrepancy.

These observations and the agreement on the line intensities suggest that the contributing factor to the discrepancies between the models might not be differences in the dominant kinetic mechanisms but rather differences in the choice of processes, radiative lines data, and cross-sections data, included in HET0D compared to KCD. To delve deeper into this matter, we conducted a systematic investigation by gradually substituting the atomic data set in HET0D-KCD, and the results are presented in Figure 4.18. We first changed the cross-section data from emission cross-section to apparent cross-section while keeping only 8 lines in the model (CS gs, blue curve). Second, we included the 22 xenon lines while still using the emission cross-sections (Rad, green curve). Third, we made both changes, i.e., changing the emission cross-section and including all 22 lines (CS gs + Rad, dark red curve). Finally, we compare to the full HET0D model as described in Chapter 3, specifically adding mixing and electron deexcitation to the chemistry model (HET0D, black curve). It is clear from the plots that changing the cross-section data alone has little impact on the line ratios. However, including all 22 xenon lines in the model leads to significant discrepancies between the models, mainly on the I_{823}/I_{828} . This highlights the critical role of considering all relevant radiative transitions and atomic data in achieving a reasonable agreement between the models.

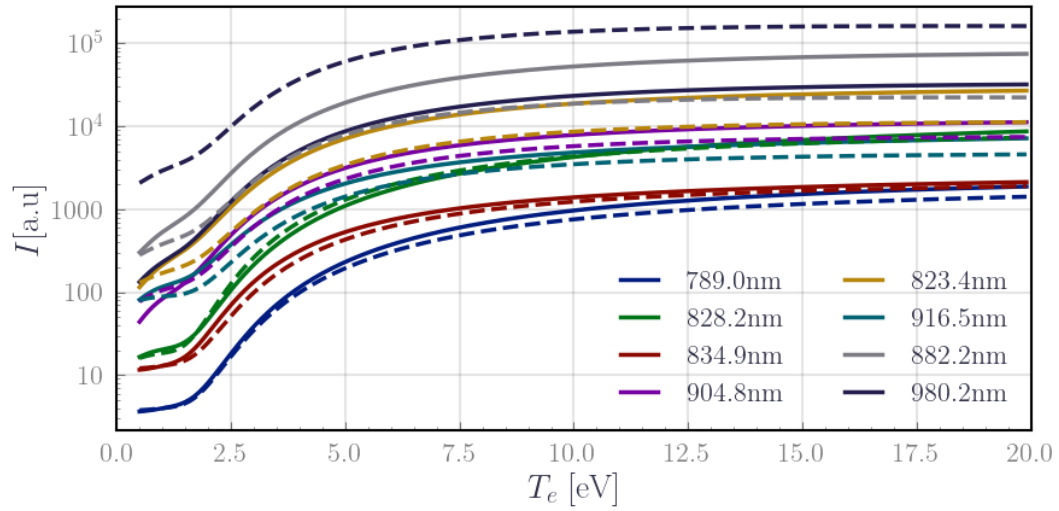


Figure 4.17: Evolution of the calculated line intensity of NIR transitions with respect to T_e . In solid line is the output from HET0D and in dashed lines is the output from KCD

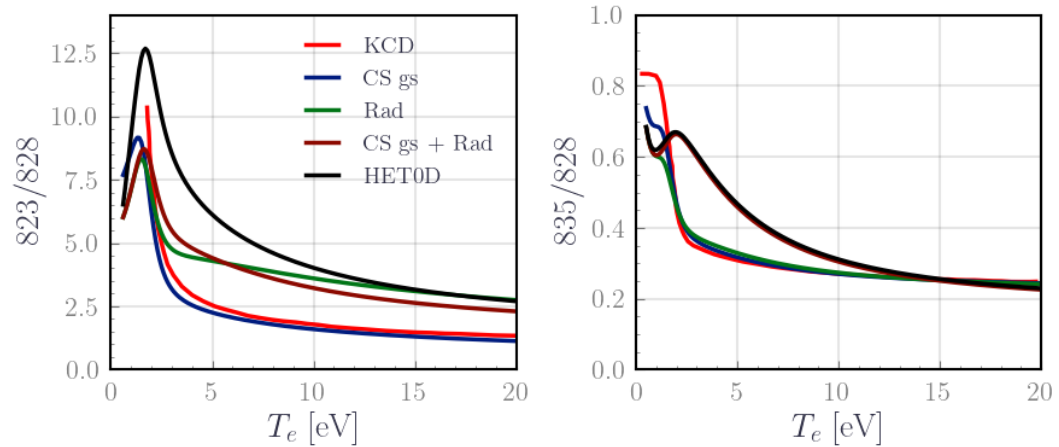


Figure 4.18: Comparison of line ratios in HET0D-KCD model with varying atomic data sets: blue (CS gs) changing the emission cross-section to apparent cross-section, green (Rad) including all the 22 xenon lines while keeping the emission cross-sections, dark red (CS gs + Rad) we made both changing the emission cross-section and including all 22 lines. The red curves are the ratios from the KCD model and the black curves are the ratios from HET0D

At this stage, it becomes evident that making an absolute comparison between different CRMs with different approaches is a challenging task, especially if they are based on different choices of atomic data [Ralchenko 2016]. The comparison with the KCD model demonstrated that capturing the dominant kinetics mechanisms does not necessarily guarantee a complete agreement between the two models, making a perfect fit between different models very difficult. Therefore, it is more adequate in the framework of virtual diagnosis and coupling with PIC to focus on validating the dominant kinetic mechanisms in HET of the model, which has been done qualitatively in the previous sections. The comparison of the kinetics with the results from [Zhu *et al.* 2019] and the line intensities in the KCD model provide confidence in our model when applied to HET. Another way of validating the model will be experimental validation with Langmuir probes. This will be explored in Chapter 7.

One last comment regarding UQ, here, we have stumbled across a different type of uncertainty related to the choice of the approach for modeling, as discussed in [Ralchenko 2016]. For instance, an 823/828 line ratio of 5 may yield a predicted temperature that varies between 2 and 6.5 eV depending if we use KCD or HET0D. While it may be interesting to quantify this uncertainty related to the choice of the "method", for coupling with PIC and qualitatively validating the kinetics, it may not be necessary.

Chapter conclusions

In this chapter, we conducted an extensive investigation of the parametric space of HET0D, which effectively characterized the kinetics described by the model. Introducing the reduced variables n_i/n_g provided valuable insights into the impact of electron density (n_e) and electron temperature (T_e) on electron impact excitation and the role of $\kappa = n_g d \sqrt{M/2RT_g}$ in radiative processes. While T_e showed a relatively minor influence compared to n_e , both parameters significantly affected the dominant kinetics in the (n_e, n_g) space, with the primary impact being on the metastables kinetics. On the other hand, κ primarily influenced the absorption of resonant radiation, promoting more population transfer within the 1s levels.

To further enhance the model sensitivity to T_e , future improvements can be made by incorporating higher-level reactions and processes. This will provide a more comprehensive understanding of plasma behavior across a broader range of operating conditions, though it is crucial to consider that higher energies can lead to increased sensitivity to errors.

The investigation of the EEDF shape shed light on its crucial impact on the distribution of excited species. Notably, the most significant part of the EEDF lies within the collision threshold energy range of excited xenon levels. The shape parameter x allowed us to explore the dynamic between the EEDF tail and bulk on the collision rate coefficients. Substantial deviations from the Maxwellian case were observed at low effective temperatures ($\times 100$), while at high effective temperatures, the deviations were less prominent but significant ($\times 3$).

Validation of the model was performed in various regions of HET, including the ionization region, acceleration region, and plume. Although discrepancies were observed, we highlighted the challenges of achieving absolute validation of CRM due to the complex nature of plasma behavior, the variety of atomic data, and differences in modelling approaches. Nonetheless, we are confident in the consistency of the model kinetics within these regions of the HET. However, it is essential to acknowledge the validity range of these findings at $1 \times 10^{15} \text{ m}^{-3} \leq n_e \leq 1 \times 10^{18} \text{ m}^{-3}$ and $1 \times 10^{18} \text{ m}^{-3} \leq n_g \leq 1 \times 10^{22} \text{ m}^{-3}$ and $T_e \geq 2 \text{ eV}$. Indeed, at low $T_e \leq 2 \text{ eV}$ and small $n_e \leq 1 \times 10^{15} \text{ m}^{-3}$, recombination and heavy atom excitation become significant, rendering HET0D less applicable. Similarly, very high n_e levels result in an elevated ionization ratio, leading to interactions with ions that can no longer be neglected along with neutral atom collisions and three-body collisions. Additionally, near the HET anode, diffusion to the wall becomes prominent so that HET0D is not valid. A further validation would be experimental validation which will be introduced in Chapter 7. In the next chapter, we will couple HET0D with PIC simulations. This will allow us to explore the interactions between plasma emission and fields in the plasma discharge.

Coupling the CRM with PIC Simulations

*When thou shalt be disposed to set me light
And place my merit in the eye of scorn,
Upon thy side, against myself I'll fight,
And prove thee virtuous, though thou art forsworn.*

William Shakespeare, *Sonnet 88: When Thou Shalt be Disposed to set me Light*

Contents

5.1	PIC simulation and coupling methodology	90
5.1.1	Self-consistent axial-azimuthal PIC simulation	90
5.1.2	Description of the case results	92
5.2	Coupling methodology and assumptions	99
5.3	Insights into the dominant kinetic mechanisms along the thruster axis	102
5.4	Application of the line ratio method on synthetic spectra .	103
5.5	Maxwellian EEDF and non Maxwellian EEDF comparison	110
5.6	Time analysis of the synthetic spectra	115
5.7	Discussion	117

Introduction

In the previous chapters, we presented the neutral xenon CRM, HET0D. We investigated the parametric domain, highlighting the dominant kinetic mechanisms covered by the model. It was established that the CRM has a range of validity far from the anode region of HET, aptly characterizing ionization, acceleration, and plume regions. This validity envelope covers plasma parameters in the following range $1 \times 10^{15} \text{ m}^{-3} \leq n_e \leq 1 \times 10^{18} \text{ m}^{-3}$, $1 \times 10^{18} \text{ m}^{-3} \leq n_g \leq 1 \times 10^{22} \text{ m}^{-3}$, and $T_e \geq 2 \text{ eV}$. The integration of the CRM with PIC simulations provides a framework to challenge OES practices, similar to CTS in Chapter 2. The coupling with PIC

offers the opportunity to challenge unexamined assumptions which might betray the implementation of OES as an in-orbit diagnostic for HET. It allows to shed light on aspects of the diagnostics itself, allowing to probe fundamental hypotheses, the definition of the diagnostic limitations, and the suggestions of potential experimental designs. Notable among these hypotheses is the treatment of neutral and metastable species transport, a facet often eschewed by traditional CRM approaches. Additionally, the assumption of a Maxwellian EEDF—common in the literature—particularly in references such as [Karabadzhak *et al.* 2006] and [Zhu *et al.* 2019], can be challenged. The PIC code employed herein is identical to that used for the virtual CTS in Chapter 2. However, the test case takes up several improvements from the work of [Petronio *et al.* 2023a, Petronio *et al.* 2023b] which introduces self-consistent calculation of the ionization source and the mitigation of the low-frequency discharge oscillations associated with the BM by linking the domain with an external circuit.

In the ensuing sections, several questions will be explored as per the following layout. The PIC simulations and coupling methodology shall be presented first. Then the light evolution will be examined, unveiling the spatial and frequency features. Subsequently, the line ratio methodology for [Karabadzhak *et al.* 2006] will be challenged to predict plasma parameters from virtual optical emission. The distinction between Maxwellian and non-Maxwellian EEDF will be examined via the comparison of virtual emission spectra calculated with both a Maxwellian and non-Maxwellian EEDF. Finally, the size of the collection area will be varied assuming a cylindrical shape to assess its impact on OES predictions.

5.1 PIC simulation and coupling methodology

5.1.1 Self-consistent axial-azimuthal PIC simulation

In comparison to the simulation of the benchmark case presented in chapter 2, several improvements have been introduced to reach a closer-to-reality PIC simulation of HET. While a comprehensive presentation of these improvements is provided in [Charoy 2020, Petronio 2023], the following section will highlight the main modifications, starting with the simulation setup which is graphically depicted in Figure 5.1.

The simulation domain maintains its Cartesian geometry, denoted as (x, y) for the axial-azimuthal plane. The domain curvature remains unaccounted for, and the periodic boundary condition also remains in the azimuthal y direction. The axial magnetic field profile is fixed and its amplitude varies only in the axial direction x , while it is constant in the azimuthal direction y . The amplitude profile reaches its maximum of 170 G at $x = 25$ mm, coinciding with the thruster’s exit plane.

Accordingly, the dimensions of the domain have been increased to 40 mm in both the axial and azimuthal directions. This choice was motivated by its convenience to follow the development of the IAW/ECDI and ITTI. The integration still uses an explicit scheme with now a grid size of $\Delta x = 160 \mu\text{m}$ and a time step $\Delta t = 16$ ps. Plasma parameters are still stored every 5000-time steps, yielding a time resolution

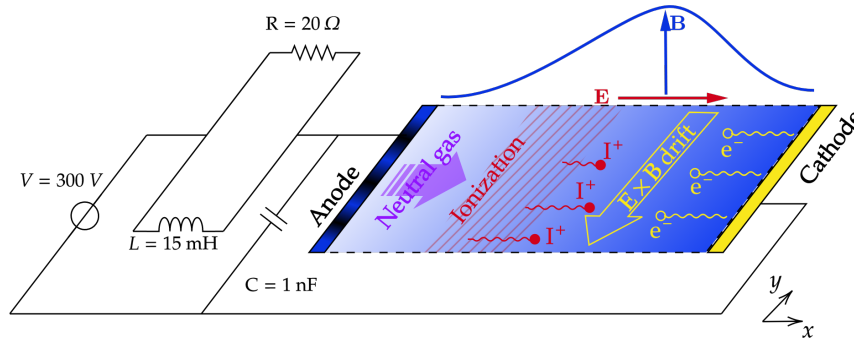


Figure 5.1: The simulation domain for the axial-azimuthal simulation coupled with the external circuit. (Courtesy to Federico Petronio)

of $\Delta t^{diag} = 80$ ns for the plasma parameters.

The cathode is grounded and is located to the right boundary of the simulation domain at $x = 40$ mm. The electron emission from the cathode uses a quasi-neutrality assumption, a departure from the model used in the benchmark case, which had used a current equality model. This stems from the observation that the current equality model results in the formation of a cathode sheath that highly disrupts the current during the transient. In the benchmark case, this was not an issue since the simulation reached a well-defined steady state. Electrons are now injected following a Maxwellian EEDF at 0.1 eV. This injection temperature seems to exert also a discernible influence on the discharge behavior. However, substantial investigation is still needed to quantify that in the simulation.

The use of a permittivity scaling factor, $\alpha_0 = 64$, ensures a substantial speed-up of the simulation by reducing the vacuum permittivity. The main effects of this artifact are the increase of both temporal and spatial steps by $\sqrt{\alpha_0}$, accompanied by changes in the discharge behavior, as exposed in [Charoy 2020] and [Petronio 2023]. Foremost, the IAW frequencies and wavenumbers scale uniformly with $\sqrt{\alpha_0}$. The spatiotemporal evolution of plasma parameters is significantly influenced, with certain electrostatic instabilities (i.e. ECDI) being damped at high α_0 while others are accentuated (i.e. ITTI). These intricate effects are documented in greater detail in the mentioned dissertations [Charoy 2020, Petronio 2023].

The chosen test case also integrates electron-neutral and ion-neutral collisions but not Coulomb collisions. To this end, the self-consistent calculation of the ionization and excitation source terms is made viable through their inclusion in the Monte Carlo collision module. Moreover, the recombination of ions into neutral atoms at the anode was also accounted for. In terms of species, the simulation includes neutral and singly ionized xenon species i.e. Xe, Xe⁺. The domain is initialized with a uniform neutral density at $5 \times 10^{18} \text{ m}^{-3}$ with a permanent neutral injection at the anode with a velocity of 200 m.s^{-1} and a flow rate $\dot{m} = 5 \text{ mg.s}^{-1}$. The neutral dynamic is solved using a 1D fluid equation in which the neutral temperature is maintained constant at 640 K [Charoy 2020].

Concerning the electric parameters of the simulation, the domain is coupled to an external circuit introduced in [Petronio *et al.* 2023a]. Unlike the direct application of the voltage drop at the anode as done in the benchmark case, the potential drop is imposed at a DC generator connected to an RLC filter. This filter serves as a protective element for the spacecraft’s Power Processing Unit (PPU) and associated components against the oscillation of the BM. It is characterized by a resistance $R = 20 \Omega$, an inductance $L = 1.5 \text{ mH}$, and capacitance $C = 1 \text{ nF}$.

5.1.2 Description of the case results

This section describes the plasma parameters from the chosen PIC simulation during the last 2 periods of the BM oscillations, from $350 \mu\text{s}$ to $476 \mu\text{s}$. Usually PIC simulations provide a comprehensive view into the plasma parameters along both the x and y axes, however, the scope of the investigation is narrowed to the variables that are inputs for the CRM, specifically, the electron density n_e , the gas density n_g , the kinetic electron temperature T_e , and the EEDF.

Averaged axial profiles of n_g , n_e and T_e Figure 5.2 shows the time and azimuthally-averaged axial profiles of plasma parameters. The graph emphasizes two key regions along the axial direction, already discussed in Chapter 2. First, is the upstream ionization zone, where ions and electrons are primarily created via collisions. This area exhibits a peak in the ionization source term S_{iz} , which also coincides with a peak in the electron density n_e . Second, is the downstream acceleration zone, where ions gain the necessary exhaust velocity. This zone is marked by a sharp peak in the axial electric field E_x , occurring just before reaching the peak of the radial magnetic field. As for the gas density n_g and velocity v_g , they display opposite trends along the axial direction and show strong axial variations, spanning at least two orders of magnitude from the anode to the plume. The gas density n_g experiences a steep decline, while v_g sees a marked increase as one moves through the ionization and acceleration zones. The electron density n_e increases from the anode—repelled away by the anode sheath—and reaches its maximum in the bulk of the ionization zone, before declining towards the plume. Lastly, the electron temperature T_e displays a pattern somewhat akin to E_x , peaking just before the maximum magnetic field in the acceleration zone.

Spatio-temporal evolution of the axial profile of n_g , n_e and T_e Complementing the spatial trends, Figure 5.3 shows the temporal dynamics of the normalized axial profiles from $t = 350 \mu\text{s}$ to $476 \mu\text{s}$. Consistent with findings from [Charoy 2020] and later [Petronio 2023], the plasma discharge varies per the growth and decay cycles of the BM. In Figure 5.3 a), the discharge current I_d displays sawtooth-like oscillations, which occur at a frequency of approximately 16 kHz which in turn impacts the temporal evolution of n_g in Figure 5.3 b), n_e in Figure 5.3 c), and T_e in Figure 5.3 d). Focusing on the neutral density n_g , minor fluctuations occur both near the anode and in the plume. In the ionization and acceleration regions,

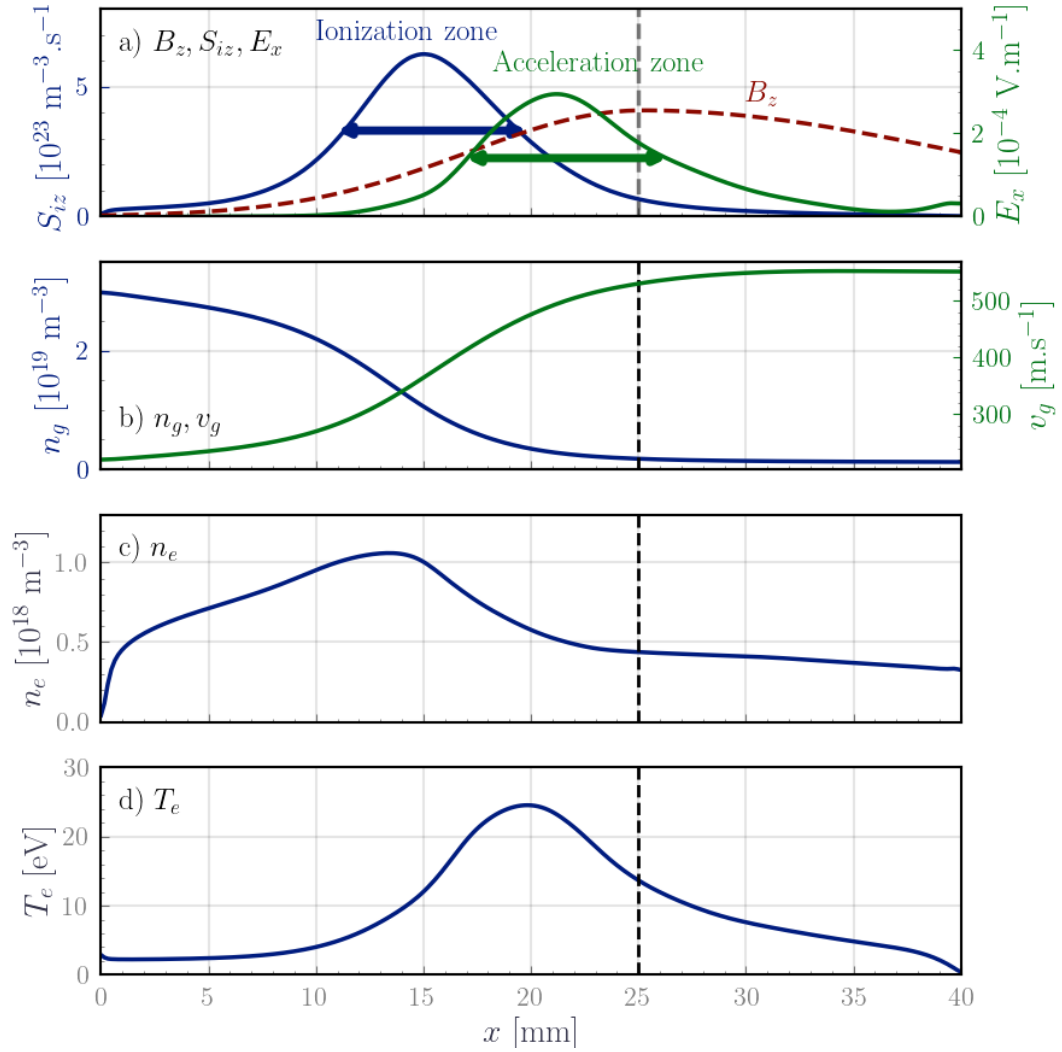


Figure 5.2: Axial profiles averaged over $120 \mu\text{s}$ of plasma parameters: a) The normalized radial magnetic field B_z (in red), the ionization source term S_{iz} (in blue), and the axial electric field E_x (in green). The blue arrow delineates the ionization zone, while the green one defines the acceleration zone. b) Axial profiles (azimuthally and time-averaged over $120 \mu\text{s}$) of the neutral density (in blue) and neutral axial velocity (in green). c) Axial profile of the electron density n_e . d) Axial profile of the mean kinetic electron temperature ($3T_e = T_{e,x} + T_{e,y} + T_{e,z}$). The vertical black dashed lines correspond to the position of the maximum magnetic field, which also represents the exit plane of the thruster.

gas density isocontours oscillate in phase with the BM. During its increasing phase, n_g diminishes near the anode due to ionization. Conversely, in the decreasing phase, n_g starts to recover as the ionization source decreases. Note that these oscillations are not in phase along the x axis but show a time delay relative to the discharge current, following the ionization wave as it "travels" axially.

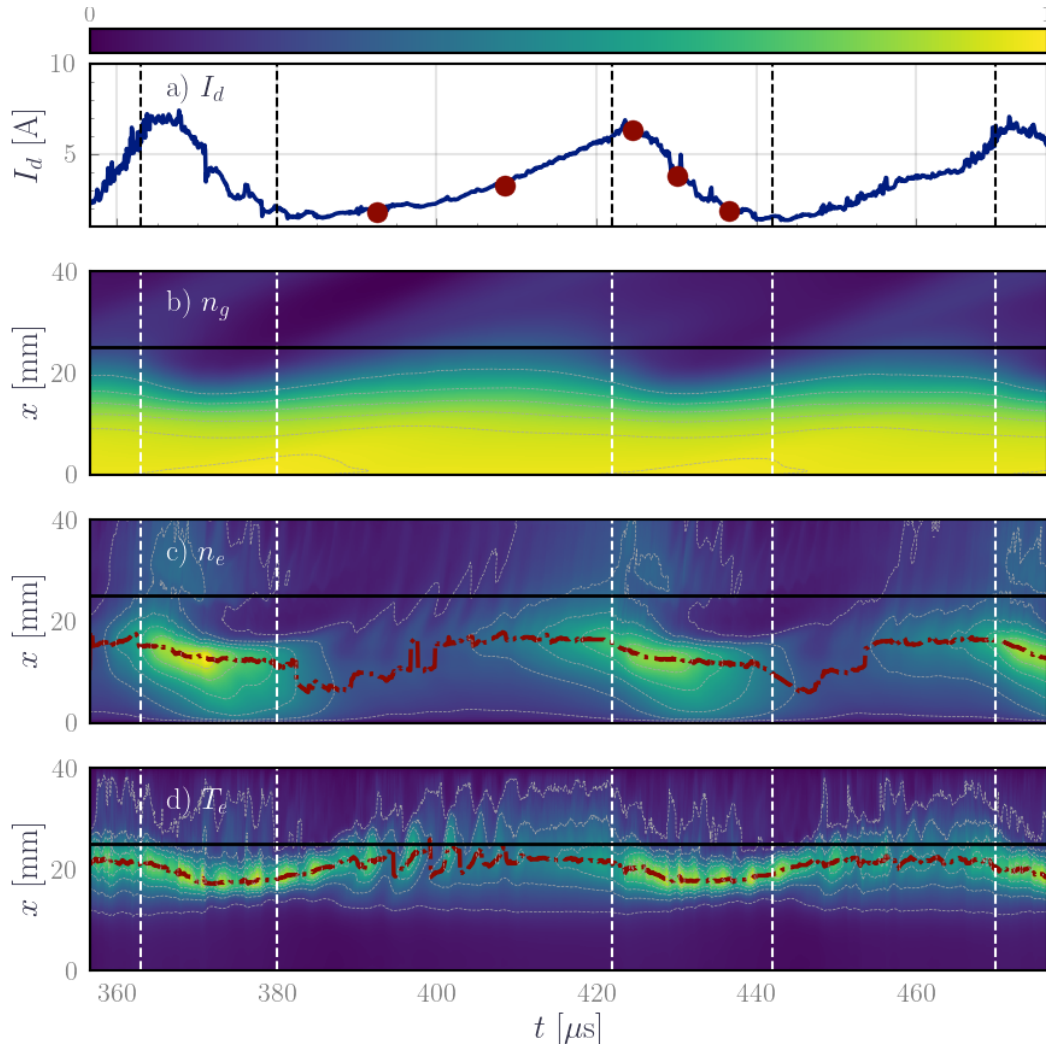


Figure 5.3: Temporal evolution of normalised axial profiles of plasma parameters from $350 \mu\text{s}$ to $476 \mu\text{s}$. a) The discharge current I_d b) The gas density n_g c) The electron density n_e and d) The mean kinetic electron temperature T_e . The black solid line represents the position of the maximum magnetic field, which also denotes the exit plane of the thruster. Dashed white lines help distinguish the increasing phase of the discharge current from its decreasing phase, and the dashed red line tracks the axial position of the maximum of T_e and n_e over time.

Much like the discharge current, n_e displays a sawtooth pattern. The axial position of the peak in n_e , marked by a dashed red line, shifts following the BM-advancing in the channel when the current increases, and retreating when it decreases. In the acceleration and plume regions, the temporal profile of n_e is synchronous with the discharge current, peaking during the growth phase and declining during the decreasing phase. Similarly to n_g , a delay in the oscillation is observed depending on the position in the channel. For instance, within the ionization zone,

the oscillations of n_e lag behind those of the BM.

Close to the anode, T_e remains fairly stable with minor fluctuations. In the ionization region, T_e increases during the BM's growth phase, due to enhanced electron collisions and heating. Contrarily, it remains fairly stable during the BM's decreasing phase. Near the plume, around the magnetic field's maximum, T_e remains largely unchanged during the growth phase but decreases in the decreasing phase. Regardless of the phase, T_e exhibits high-amplitude, high-frequency oscillations, overlaying on the breathing mode oscillations.

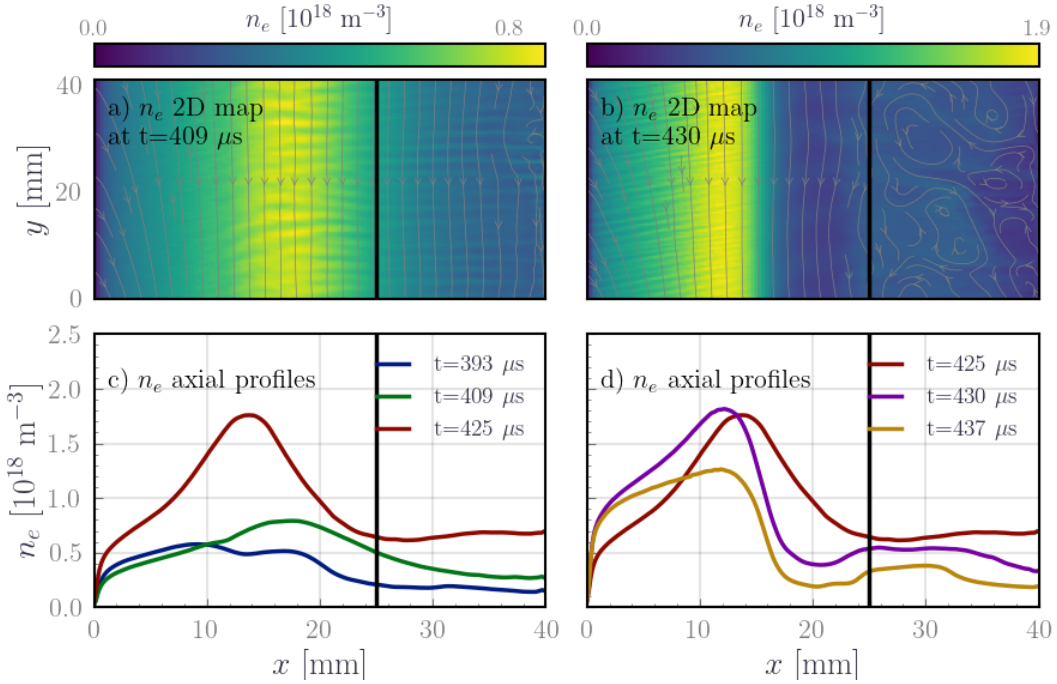


Figure 5.4: Evolution of the electron density during one BM period from $380 \mu\text{s}$ to $440 \mu\text{s}$. a) 2D map of n_e during the increasing phase of the BM. b) 2D map of n_e during the decreasing phase of the BM. c) Axial profiles of n_e at three different times of the increasing phase. d) Axial profiles of n_e at three different times of the decreasing phase. The black solid line represents the exit plane of the thruster. The dark gray stream field corresponds to the velocity field of the electrons.

2D maps of n_e and T_e Figure 5.4 and Figure 5.5 offer further insight into the temporal and spatial evolution of n_e and T_e throughout one cycle of the BM, from $380 \mu\text{s}$ to $440 \mu\text{s}$. In line with the findings reported by [Charoy 2020, Petronio 2023], Figures 5.4 a) and b) reveal two different plasma instabilities during the BM oscillations: the IAW/ECDI and the ITTI. During the growth phase of the BM, IAW/ECDIs dominate, mainly propagating in the azimuthal direction. Conversely, the decay phase of the BM features the dominance of the ITTIs, which exhibit an axial propagation within the plume. Figures 5.4 c) and d) exhibit pronounced gradients in T_e and n_e , especially when the current decreases. The values for T_e range

between 2 eV and 30 eV, and for n_e , they span from $1 \times 10^{17} \text{ m}^{-3}$ to $1 \times 10^{18} \text{ m}^{-3}$. These Figures further point to the localized heating patterns in T_e during the BM's increasing phase, corroborating the data presented in Figure 5.6.

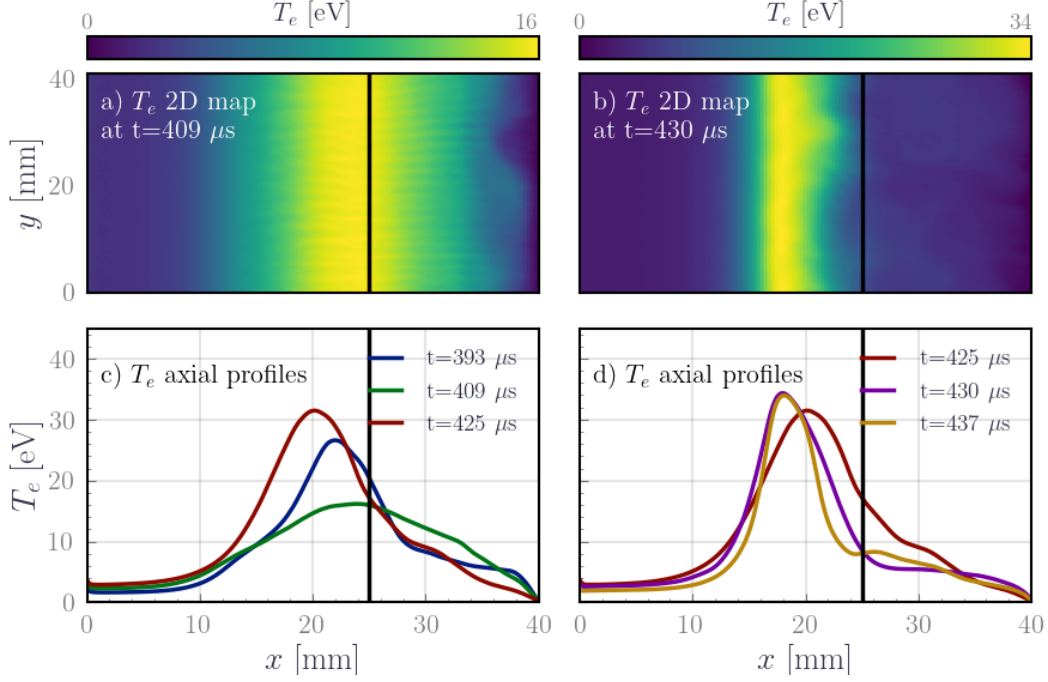


Figure 5.5: Evolution of the mean kinetic electron temperature T_e during one BM period. a) 2D map of T_e during the increasing phase of the BM. b) 2D map of T_e during the decreasing phase of the BM. c) Axial profiles of T_e at three different times of the increasing phase. d) Axial profiles of T_e at three different times of the decreasing phase. The black solid line represents the exit plane of the thruster.

Axial variation of the EEDF Figure 5.6 shows axial variation of the EEDF at two snapshots, one during the growing phase of the BM at $t = 409 \mu\text{s}$, one during the decreasing phase at $t = 430 \mu\text{s}$. During the growth phase, as depicted in subfigure a), the axial variation of the EEDF illustrates concentrated electron heating within the ionization and acceleration zones. This is marked by an increase in the population of the high-energy tail between $x = 10 \text{ mm}$ and $x = 30 \text{ mm}$. As the BM transitions to its decay phase, this high-energy tail becomes limited to the acceleration zone, reflecting a localized heating process thanks to an enhanced axial electric field.

The EEDF displays also significant variations over time and across the x -axis, most notably in its high-energy tail. Figures 5.7 and 5.8 compare the isotropic EEDF-derived from PIC simulations by tabulating electron energies per cell with the Maxwellian EEDF based on the kinetic electron temperature T_e . This comparison is conducted for five axial positions (rows) at three times during the increasing and decreasing phases of the BM.

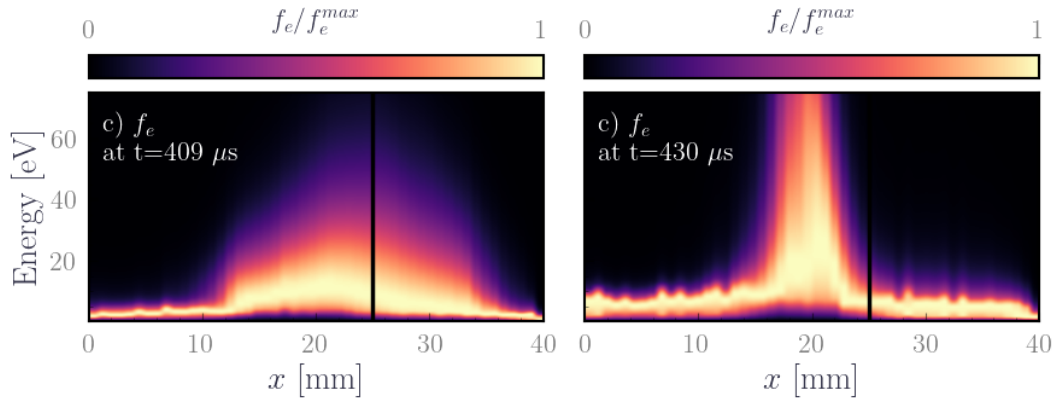


Figure 5.6: Axial evolution of the normalized EEDF during a) the increasing phase of the discharge current and b) its decreasing phase. The black solid line represents the exit plane of the thruster.

The side-by-side evaluation emphasizes the non-Maxwellian nature of the EEDF, particularly evident in the high-energy tail of the isotropic EEDF. This feature is typical of $\mathbf{E} \times \mathbf{B}$ discharges and is most pronounced near the anode and in the plume. In the energy range of 8 eV to 20 eV, the Maxwellian approximation seems reasonably good, implying only minor discrepancies in the expected emission. However, during the BM's decreasing phase, not only does the high-energy tail continue to diverge from Maxwellian behavior, but new disparities also emerge at lower energies. These features were also observed in the experimental work of [Dannenmayer & Mazouffre 2013, Dannenmayer *et al.* 2014] in probe measurement at the exit plane of the thruster, but to a lesser extent. The heating of the tail is less pronounced in the experiments compared to PIC with a more pronounced depletion of the high energy tail after the ionization threshold. This is also observed in the results of the coming Langmuir probe measurement conducted in this work and reported in Chapter 7.

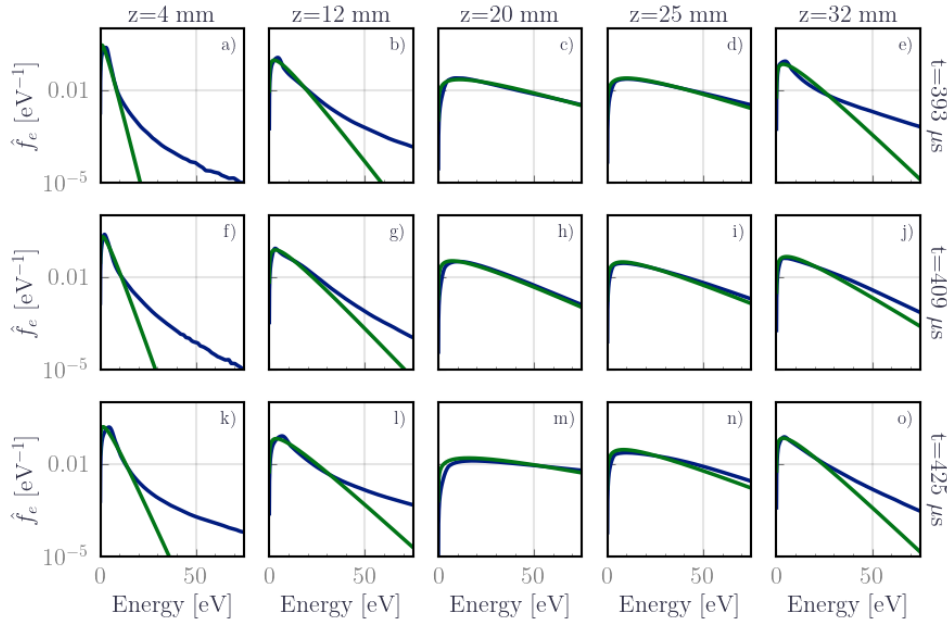


Figure 5.7: Isotropic EEDF from PIC (in blue) compared to the Maxwellian EEDF at the kinetic electron temperature T_e also from PIC for 5 axial positions (columns) and at 3 distinct times (rows) during the increasing phase of the discharge current.

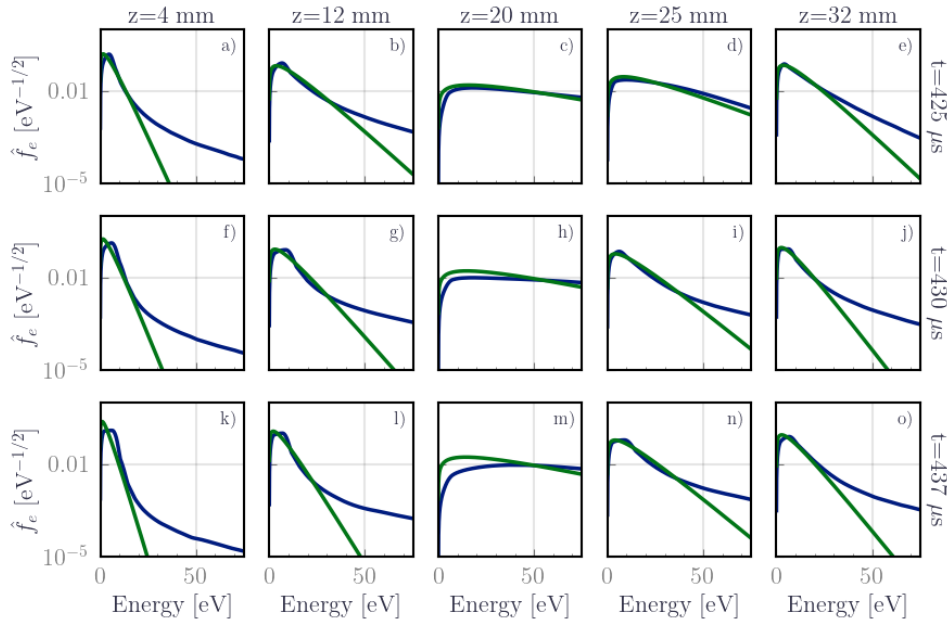


Figure 5.8: Isotropic EEDF from PIC (in blue) compared to the Maxwellian EEDF at the kinetic electron temperature T_e also from PIC for 5 axial positions (columns) and at 3 distinct times (rows) during the decreasing phase of the discharge current.

5.2 Coupling methodology and assumptions

To couple the CRM into the PIC simulations, a standard steady-state coupling methodology is used, as depicted in Figure 5.9. The electron density n_e , the kinetic electron temperature T_e , EEDF, and gas density n_g are collected from the PIC simulations at intervals $\Delta t_{diag} = 80$ ns over the simulation grid. These parameters then are injected into the CRM.

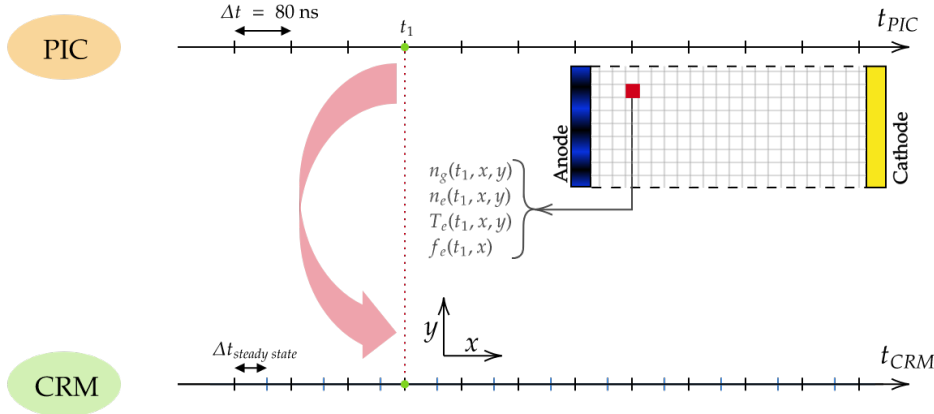


Figure 5.9: Coupling methodology between CRM and PIC simulations

To set the initial condition for the rate balance equations of HETOD, the procedure is as follows: at each time $t_0 + \Delta t$, the density distribution of the excited species is initialized to the steady-state values from the preceding time step t_0 . Subsequently, the ground state density is adjusted to reflect any changes in the neutral density between t_0 and $t_0 + \Delta t$, ensuring a consistent gas density profile between the PIC and CRM models.

After the initialization, the balance equations (Eq. (3.4)) are solved to obtain the steady-state distribution of the excited species. Synthetic spectra are then generated. The CRM included the complete chemistry model described in Chapter 3. It accounts for the 15 neutral xenon levels and the 24 transitions, detailed in Figure 3.2, with the relevant processes and cross-sections listed in Table 3.4. Absorption and radiation trapping are accounted for using the Mewe approximation with an optical characteristic length $d = 10$ cm. Two EEDF scenarios are considered: Case I utilizes the isotropic EEDF from PIC, while Case II employs a Maxwellian EEDF based on T_e from PIC as well. The isotropic EEDF is calculated by binning the electron kinetic energy from the PIC simulation into a distribution function EEDF whereas the Maxwellian EEDF is calculated by injecting the T_e defined as the second moment of the Electron Velocity Distribution Function (EVDF) in Eq. 3.10.

Static time-scales and length-scale compatibility Before proceeding to the results, it is crucial to verify the time-scale compatibility between PIC and CRM. The primary assumption is that the excited species achieve a steady state within

the 80 ns PIC interval. This is quantitatively assessed by evaluating t_{eq}^{CRM} , defined by a relative density variation of the excited species less than 1%. Figure 5.10 a) confirms that steady-state is reached within the 80 ns frame in both cases, with an average time of approximately 20 ns. In comparing the length scales traveled by the excited species x_{eq}^{CRM} before reaching the steady state to the size of a PIC cell, Figure 5.10 b) confirms that the excited species are not transported to the next node. This allows us to consider that light is emitted where the excited state is created and to neglect the contribution of the transient to the generated light emission.

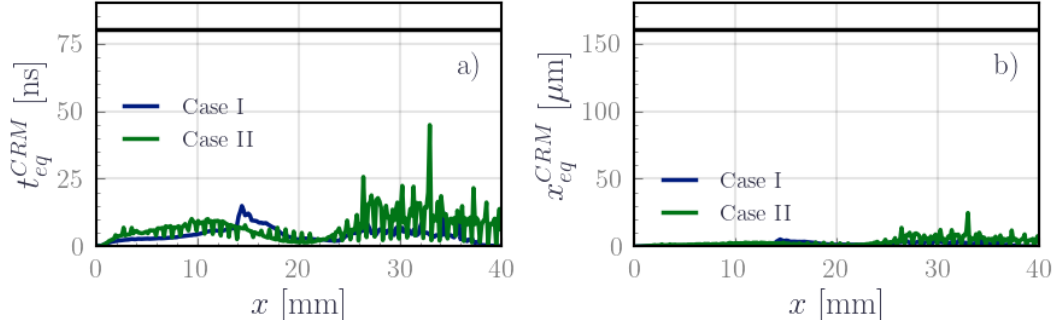


Figure 5.10: Validation of the time-scale compatibility between PIC and CRM. Figure a) shows the time required by the CRM to reach the steady state across the simulation domain for both Case I and Case II. It can be seen that it is well within the 80 ns of PIC time step, indicated here by the solid black line. Figure b) shows the distance traveled by the neutral particles based on their time-averaged axial neutral velocity, during the time required by the CRM to reach the steady state across the simulation domain for both Case I and Case II. It can be seen that it is well below the PIC 160 μm mesh size, indicated also by the solid black line.

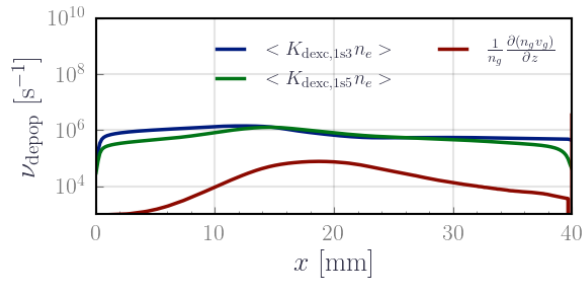


Figure 5.11: Comparison of the rate of collisional depopulation of the metastables to the rate of convective transport of excited species. The blue line corresponds to the axial profile of the time-averaged, azimuthally-averaged deexcitation rate of the 1s3 metastable level. The green line corresponds to the axial profile of the time-averaged, azimuthally-averaged deexcitation rate of the 1s5 metastable level. The red line corresponds to the average convection loss rate calculated using the axial profile of the neutral velocity and density.

Excited species transport as a loss mechanism Additionally, we examine the convective depopulation rate term ν_{conv} , to validate the 0D assumption of neglecting convection as a depopulation mechanism. This term is derived from the neutral continuity equation and is given by $\frac{\partial n_g}{\partial t} = -\frac{\partial(n_g v_g)}{\partial z} = \nu_{conv} n_g$. This convective term can be disregarded if the depopulation rates of the excited species exceed it. Specifically, the convective rate is estimated to be on the order of $\nu_{conv} \approx 1 \times 10^5 \text{ s}^{-1}$. For radiative species, the rate of spontaneous decay A_i is approximately $1 \times 10^6 \text{ s}^{-1}$, surpassing ν_{conv} . For the metastable species, the depopulation rate is calculated by summing overall excitation rate coefficients, taking into account the average axial profiles of T_e and n_e along the thruster axis. Figure 5.11 shows that the rate of collisional depopulation for metastable species exceeds that due to convective transport by an order of magnitude. Consequently, the influence of excited species convection on emission line intensities can be neglected. Diffusion of the neutrals to the walls contributes also to the transport of the excited species, however since the chosen PIC simulation assumes a 1D neutral dynamics, we are not able to evaluate it similarly. However, assuming Fick's law applies to the neutrals, we can show that the volume-averaged diffusion frequency for the ground state $\nu_{diff} = kT_g/m\nu_{iz}S_{diff}$ is roughly in the order of magnitude of $1 \times 10^2 \text{ s}^{-1}$ to $1 \times 10^3 \text{ s}^{-1}$ for a neutral temperature $T_g = 640 \text{ K}$, a collision frequency with the ions $\nu_{iz} = 1 \times 10^4 \text{ s}^{-1}$ and characteristic diffusion surface $S_{diff} = 10 \text{ cm} \times 1 \text{ cm}$. This is way below the rate of collisional depopulation of the metastables, therefore diffusion can also be neglected.

Experimental synthetic spectra Finally, the coupling yields spatial maps of excited species densities and spectral line intensity profiles, which are included in the CRM. A sample of synthetic spectra, incorporating both natural and Doppler broadening effects via a Voigt profile, is illustrated in Figure 5.12. Further details on emission line profile modeling can be found in Appendix F.

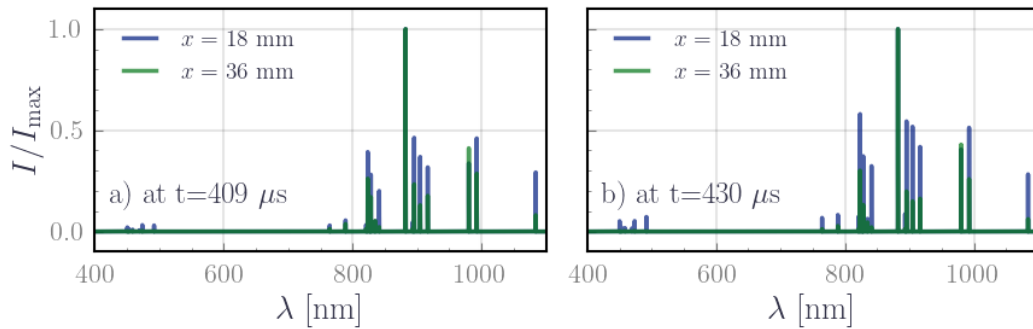


Figure 5.12: Synthetic spectra generated by the coupled CRM and PIC simulation: a) depicts the spectral profile during the BM growth, and subfigure and b) during the BM decay. Locations in the thruster channel and plume are indicated as $x = 18 \text{ mm}$ and $x = 36 \text{ mm}$, respectively.

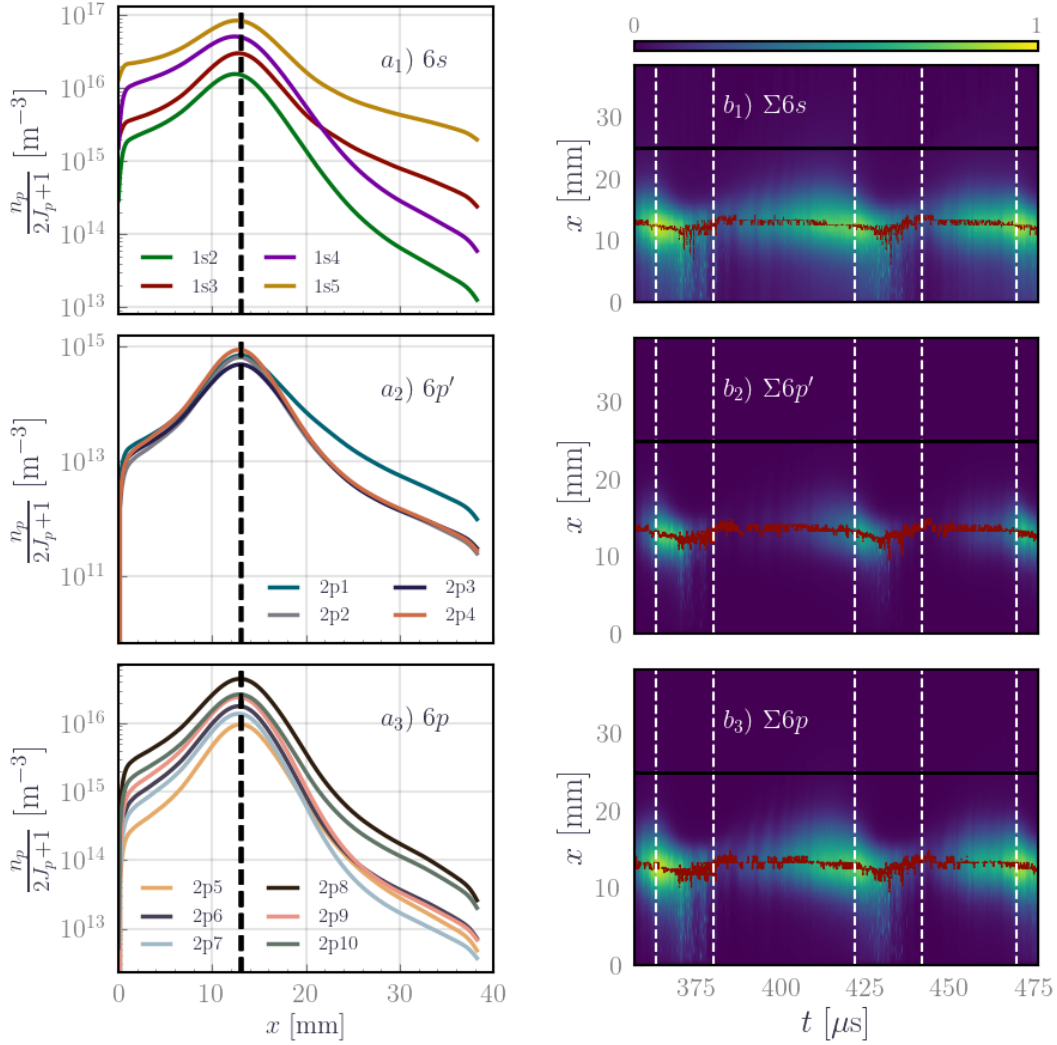
5.3 Insights into the dominant kinetic mechanisms along the thruster axis

Figure 5.13 shows the evolution of the average axial density profiles of the excited species. As depicted in Figure 5.13 a), a pronounced peak is evident in the axial profile of the density of excited species at $x = 13$ mm, coinciding with the electron density maximum in the ionization region (note the logarithmic scale). Near the plume and in the ionization region, the excited species exhibit comparable densities and display a hierarchical organization. Specifically, the $6s$ levels are sorted by their increasing energy, whereas the $6p$ levels are grouped by their quantum number j_c , followed by the prominence of their excitation cross-section from the metastable state $1s5$. These observations indicate a kinetic regime governed by the metastable-state collisions, as corroborated by Region II d from the kinetic diagrams discussed in Figure 4.11 in the previous chapter.

In the acceleration region and the plume, the density of the excited species sharply decreases which is primarily attributable to the concomitant decrease of n_g , n_e , and T_e . A different ordering of level densities is observed, induced by a gradual shift in the dominant kinetic mechanisms to a Corona model-like kinetics (Region II c). Here, excited levels group around their radiative attributes, i.e. resonant, metastable, and pseudo-metastable features. From these observations, we conclude that the ionization zone separates the thruster into two kinetically distinct regions: the near anode region characterized by dominant kinetics from Region II d and the acceleration region and the plume characterized by dominant kinetics from Region II c. This transition is particularly marked by the maximum in the excitation source terms, which is closely approximated by the peak in the electron density.

Temporal fluctuations in the excited species densities are reported in Figure 5.13 b) and they unveil simpler dynamics compared to other plasma parameters. Unlike T_e and n_e , whose peaks oscillate in the thruster's channel due to propagating instabilities and changing heating processes, the excited species peak is localized and undergoes minor axial shifts. At a given axial position, the excited species density oscillates at the same frequency as the discharge current, however, displaying a temporal lag of approximately $10 \mu\text{s}$ in the plume, which has also been observed in time-resolved spectroscopy of HET by [Gonzales *et al.* 2014]. The BM-induced variations in plasma parameters do not significantly alter the prevailing kinetic regimes, thereby maintaining the same dominant kinetics near the anode and in the plume. Nevertheless, some back-and-forth oscillations between the two regimes occur near the transition region.

All in all, the axial profiles delineate two kinetically distinct regions within the thruster, especially in the light of the sharp gradients in n_e and n_g . This warrants the crucial inclusion of n_e and/or n_g dependency as input parameters to any CRM for HET.



(a) Averaged axial profile of the density of the excited species

(b) Temporal evolution of the axial profile of the density of the excited species

Figure 5.13: Evolution of the density of the excited species. The dashed black line in a) indicates the maximum in the excitation source term, while the solid black line in b) indicates the thruster's exit plane. The dashed white lines punctuate the phases of the BM. Finally, the red line in b) follows the position of the peak in the excited species densities in the thruster's channel.

5.4 Application of the line ratio method on synthetic spectra

In this section, we treat the synthetic spectra generated by the previous coupling as experimental spectra to which we can apply the line ratio method to estimate plasma parameters with no prior knowledge of the EEDF. We insist that the synthetic spectra generated from PIC use the PIC EEDF which is highly non-Maxwellian at

high electron energy. Whereas, similar to the **KCD** model, the line ratio curves used to estimate the plasma parameters from the synthetic line ratios, are generated by assuming a Maxwellian **EEDF** as input of the **CRM**. Therefore, it is expected to have discrepancies in the estimations of the plasma parameters given this fundamental difference in the shape of the **EEDF**. To emulate light integration along the line of sight, we also average all quantities along the azimuth y , hence considering only axial profiles of light emission.

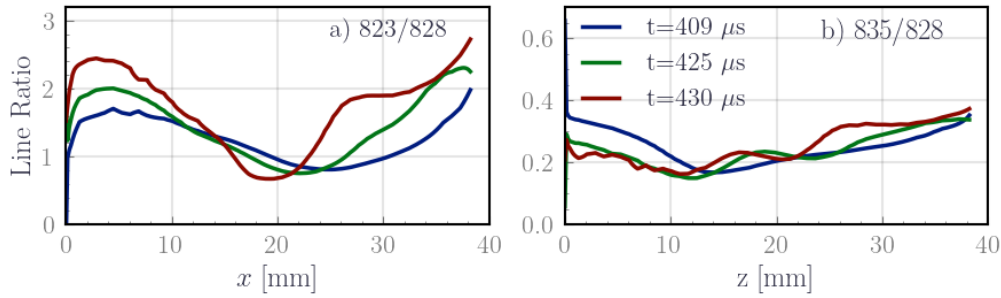


Figure 5.14: Axial variation of the $\frac{I_{823}}{I_{828}}$ and $\frac{I_{835}}{I_{828}}$ line ratio for three different times of the **PIC** simulation. The blue curve is mid the growth phase of the **BM** the green curve is when the discharge current is maximum and the red curve is mid the decreasing phase of the **BM**.

Analysis using **KCD line ratios** Initially, we use the line ratio curves of the **KCD** model to analyze the synthetic spectra obtained from the previous coupling. Upon temporal averaging, we see that the 823/828 and the 835/828 line ratios from **KCD** model vary along the thruster channel, as illustrated in Figure 5.14 for different times of the **BM**. Importantly, these ratios seem to be sensitive to the changes in n_e , n_g , and T_e . The comparison of the predicted T_e from the line ratio curve to the actual T_e profiles for different times is reported in Figure 5.15 for three time instants: mid growing **BM**, the peak of the **BM** and mid decreasing **BM**. We found that the **KCD** model consistently overestimates electron temperature, in particular in the middle of the channel. Within the ionization and acceleration regions, where variations in n_e and n_g are significant, the **KCD** model overestimates T_e values. This overestimation might be a mechanism to align predicted emissions with actual values, underlining the need to account for additional parameters than T_e . Despite this, the 823/828 ratio does align well in trends and shape with the temporal and axial variations of the actual T_e profile from **PIC**. For the 835/828 ratio, predictions deviate substantially, mainly due to the model's reduced sensitivity of this line ratio at higher electron temperatures (indeed, the curves are flat at high T_e). Moreover, the discrepancy between the line ratio predictions suggests an incomplete representation of the kinetic processes in the **KCD** model, particularly involving the 835/828 ratio related to the $2p3$ level. The predictions are off by one order of magnitude suggesting that probably, the **KCD** model oversimplifies

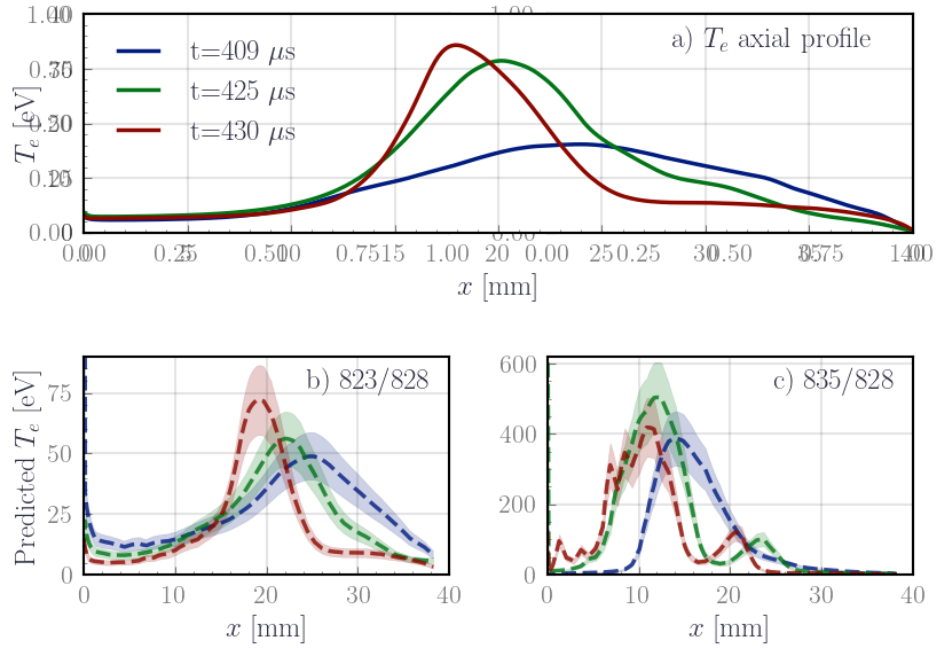


Figure 5.15: Estimated electron temperature from the line ratios of the KCD model from Figure 4.15 based on the synthetic spectra generated from PIC results using HETOD: a) Reference T_e axial profiles from PIC simulations, b) Predicted T_e based on the $\frac{I_{823}}{I_{828}}$ line ratio and c) Predicted T_e based on the $\frac{I_{835}}{I_{828}}$ line ratio

the processes involved in the population/depopulation of the $2p3$ levels. Hence, we completed the chemistry with the available processes in HETOD and performed the same predictions with all the 15 levels of xenon and all the electron impact processes and radiative transitions listed in 3. Still, similar inconsistencies were observed, indicating an incomplete kinetic scheme for the $2p3$ level also in the HETOD scheme, potentially necessitating the inclusion of additional minor processes involving, for example, the $5d$ levels of neutral xenon that are close energy-wise to the $6p'$ tier. As for the $823/828$, we conclude that it is a good line ratio.

Improving the model To incorporate n_e , we replace the conventional ratio curves with calibration abacuses. These are 2D emission intensity surfaces with T_e and n_e as variables, while n_g and d held constant. To generate the calibration abacus, we use the complete chemistry model from HETOD, to explore the parametric space of T_e and n_e ranging from $n_e = 1 \times 10^{16} \text{ m}^{-3}$ to $5 \times 10^{18} \text{ m}^{-3}$, and $T_e = 3 \text{ eV}$ to 40 eV . The rate coefficients are calculated under the assumption of a Maxwellian EEDF. Also, n_g is set at $1 \times 10^{19} \text{ m}^{-3}$ and d is fixed at 10 cm . Two line ratios are chosen, and their corresponding values are calculated over the selected ranges of T_e and n_e . The analysis then proceeds as follows: given the values of the two line ratios, they identify unique contour lines on their respective calibration surfaces. The intersection of these contour lines yields the estimated values of T_e

and n_e . A sample contour plot is reported in Figure 5.16.

Choice of the line ratios The first line ratio candidate is 823/828, primarily because it effectively captures the anticipated trends observed in the PIC simulations. The criteria for selecting the second line ratio focused on two key considerations: first, to span a broad energy range, and second, to minimize sensitivity to n_g and d , since these parameters are held constant. From the parametric study presented in Chapter 3, we understand that higher energy levels tend to be more susceptible to variations in n_g and d . Trying different combinations of line ratios suggested that ratios involving the $2p_{10}$ and $2p_9$ levels are good candidates.

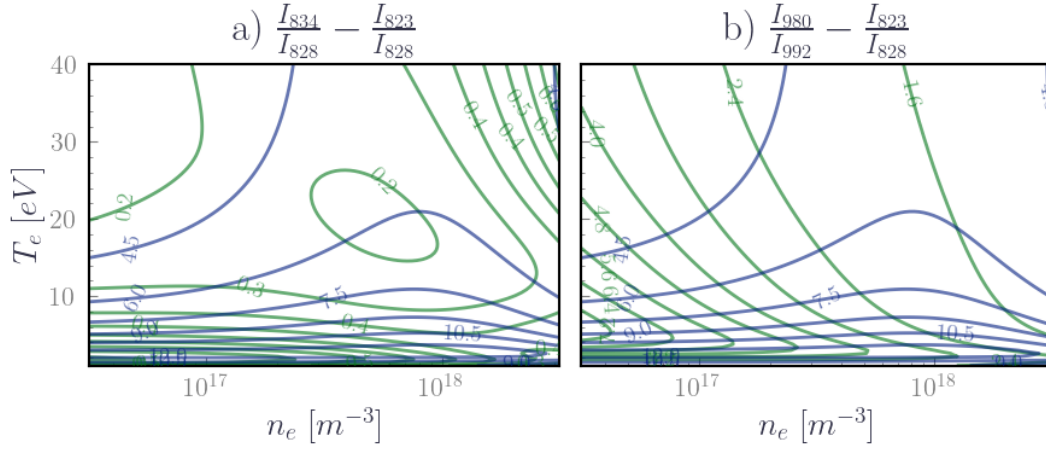


Figure 5.16: Calibration abacuses generated from the complete chemistry model in HETOD. a) corresponds to the 823/828 – 835/828 abacus and b) corresponds to the 823/828 – 980/992 abacus. Both abacuses assume a constant $n_g = 1 \times 10^{19} \text{ m}^{-3}$ and $d = 10 \text{ cm}$. The 823/828 line ratio (in blue, panel a) and b)) shows mainly horizontal contour lines reflecting a sensitivity to T_e . This is the same for the 835/828 line ratio (in green panel a)). The 980/992 line ratio (in green, panel b)) show vertical contour lines reflecting on the contrary a sensitivity to n_e .

After surveying the existing literature, we found that the 980 nm line from the pseudo-metastable $2p_{10}$ level is commonly used. To maintain proximity and thereby mitigate the effects of light calibration in eventual experiments, we selected the 992 nm line from the $2p_9$ level as the second line. The resulting calibration abacuses are displayed in Figure 5.16. Figure 5.16 a) showcases the 823/828 – 835/828 abacus based on the KCD line ratio while Figure 5.16 b) on the right corresponds to the 823/828 – 980/992 abacus. The shape of the contour lines reveals more information about the sensitivity of each ratio to the plasma parameters T_e and n_e . Specifically, the 823/828 – 835/828 abacus predominantly features horizontal contour lines, signaling a higher sensitivity to variations in T_e rather than n_e . This characteristic confirms our earlier conclusion that these ratios may not be optimal for applications where variations in n_e are prevalent. In contrast, the 823/828 – 980/992 abacus

presents both horizontal and vertical contour lines. Here, 823/828 shows sensitivity to T_e (horizontal contour lines), while 980/992 is more sensitive to n_e (vertical contour lines).

Prediction using the abacus method Upon evaluating the results derived from the calibration abacus 823/828 – 980/992, we find excellent agreement in the values and trends of T_e during the BM, in particular in the channel and the near plume, as illustrated by Figure 5.17. However, in the far plume region, we notice an overestimation of the temperature. This can be primarily attributed to not accounting for the gas density variations. Additionally, the pronounced non-Maxwellian nature of the EEDF in this region might also contribute, albeit to a lesser degree. It is worth noting that the boundary condition, which presumes a cathode plane emitting electrons at a constant electron temperature, is potentially questionable which raises further questions regarding the true shape and nature of the EEDF in this specific region in the simulation.

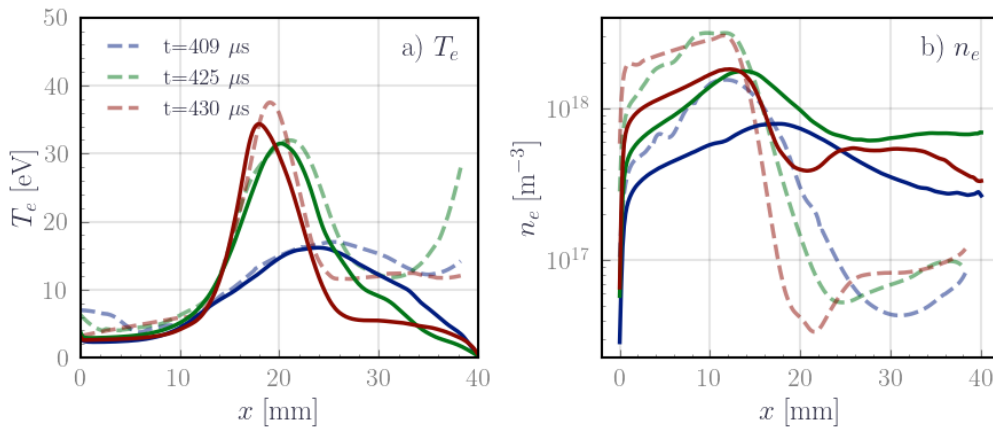


Figure 5.17: Prediction of plasma parameters using the 823/828 – 980/992 abacus. In solid lines are the reference profiles from PIC and in dashed lines are the predictions from the abacus

The fit for n_e is less satisfactory but remains reasonably good in the thruster channel. In the acceleration region and the plume, the difference is drastic and the reason is the decrease in the gas density in those regions. In the absence of n_g as a parameter in the CRM predictions, the electron density compensates by decreasing more. Adjusting for the gas density in the plume improves the estimates in the plume. Moreover, we hypothesize that the overestimation of n_e , near the anode, might also stem from the Maxwellian approximation. Figures 5.8 and 5.7 suggest an overpopulated Maxwellian EEDF at low energies for some time, implying that the PIC light emission from the Maxwellian perspective sources from more electron collisions-though this is a hypothesis yet to be explored.

Sensitivity n_g and d Regarding the impact of fixing n_g and d on the predictions of T_e , we looked at the prediction from the abacus method for different values of constant n_g and d . The predictions reported in Figure 5.18 appear fairly robust against variations in d and n_g . This has a major implication mainly on the estimation of d in real-life cases since it suggests that taking a correct order of magnitude of the optical length is sufficient to reproduce the correct T_e trends. Moreover, what is particularly interesting is the ability to estimate a kinetic temperature profile, which exhibits a significantly non-Maxwellian behavior at higher energies, using a Maxwellian assumption. This finding draws our attention back to Figures 5.8 and 5.7. Here, within the energy ranges pertinent to the excitation threshold of neutral xenon, the Maxwellian approximation seems to be reasonably accurate.

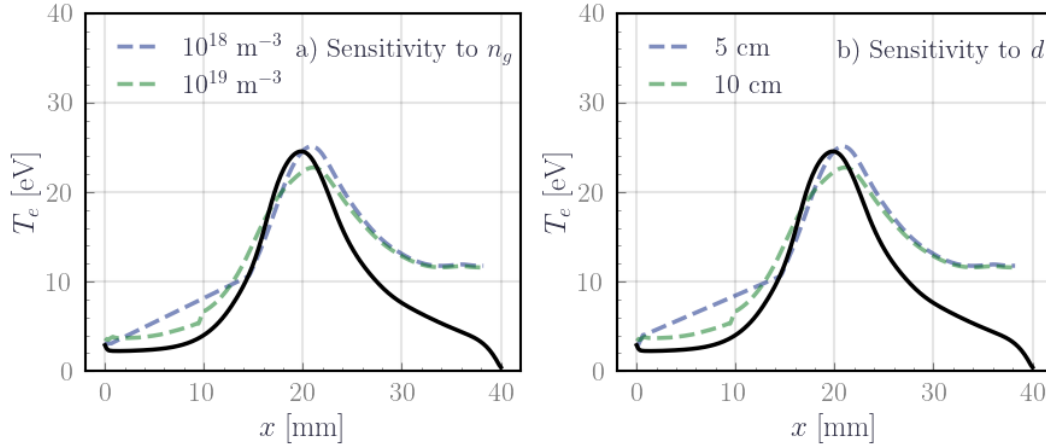


Figure 5.18: Sensitivity analysis of T_e predictions to variations in n_g and d . In solid lines are the reference profiles from PIC and in dashed lines are the predictions from the abacus method

Finally, our study yields compelling evidence supporting the reliability of time-averaged OES and CRM diagnostics in HET. Indeed, the target profile in Figure 5.18 represents the axial profile of the electron temperature averaged over two BM and the agreement is quite reasonable. Given the temporal gradients in HET, one might assume that time-averaged light emissions do not directly reflect time-averaged plasma parameters. Instead, they are more indicative of time-averaged kinetic processes, such as rate coefficients, from which an effective T_e can be deduced. However, our findings suggest otherwise: the effective T_e estimated from time-averaged OES is an excellent approximation of the true time-averaged T_e .

In conclusion, this approach provided several valuable insights into the effective application of the line ratio method. Most notably, the inclusion of both n_e and n_g is essential for more accurate predictions of T_e . The line ratios 823/828 and 980/992 prove useful in predicting T_e that are relatively robust to changes in n_g and d .

Further improving the model To enhance the predictions, we incorporate n_g into the analysis, akin to how n_e was considered. This extension transforms the

abacus space into three dimensions so that it is more convenient to cast the problem of plasma parameter predictions as an optimization problem. The aim is to minimize the discrepancy between the CRM spectra and the synthetic PIC spectra across the n_e , T_e , and n_g parametric space. The CRM line intensities are calculated assuming a Maxwellian EEDF at T_e . Comprehensive implementation details are discussed in Chapter 7, while here, we focus on presenting the optimization outcome.

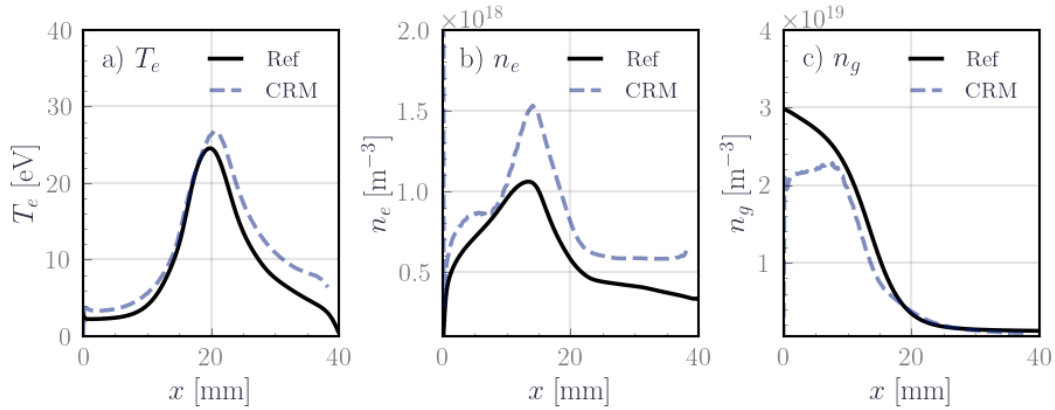


Figure 5.19: Comparison between azimuthally and time-averaged spectra profiles and plasma parameters.

Figure 5.19 contrasts the prediction, based on the azimuthally and time-averaged spectral profile (in blue), against the averaged plasma parameter profile (in black). Notably, this approach yields a satisfactory alignment in the plasma parameters, particularly for the electron and gas densities when compared with the prior abacus-based analyses. This underscores the significance of including n_g to accurately trace n_e trends. However, certain discrepancies persist, potentially attributable to time-averaging or non-Maxwellian characteristics of the EEDF.

Additional exploratory comments on line ratios We also explored some additional line ratios. Interestingly, the line ratio between $6p$ and $6p'$ ratio should perform well as they cover a large energy range [Boffard *et al.* 2004]. However, they performed very poorly both in T_e and n_e . The same observation was obtained when we tested line ratios involving only $6p'$ levels, confirming potential gaps in the kinetic mechanisms involving the $6p'$.

Amidst these tests, we also stumbled upon intriguing behaviors in specific line ratios that remained stable even with varying plasma parameters for instance the 452/834 or the 473/826. These stable ratios are interesting topologically speaking as they correspond to a contour line in the n_e , T_e , and n_g space of an operating condition of the thruster. This might offer unique insights into the health or operations of the thruster, but further investigation is required.

5.5 Maxwellian EEDF and non Maxwellian EEDF comparison

When comparing the EEDFs in Figure 5.7 and 5.8, our observation suggests that the Maxwellian approximation serves as a reasonable good representation near the threshold energy of the excited species, which is the key range for excitation processes as elucidated in Section 4.1.2.

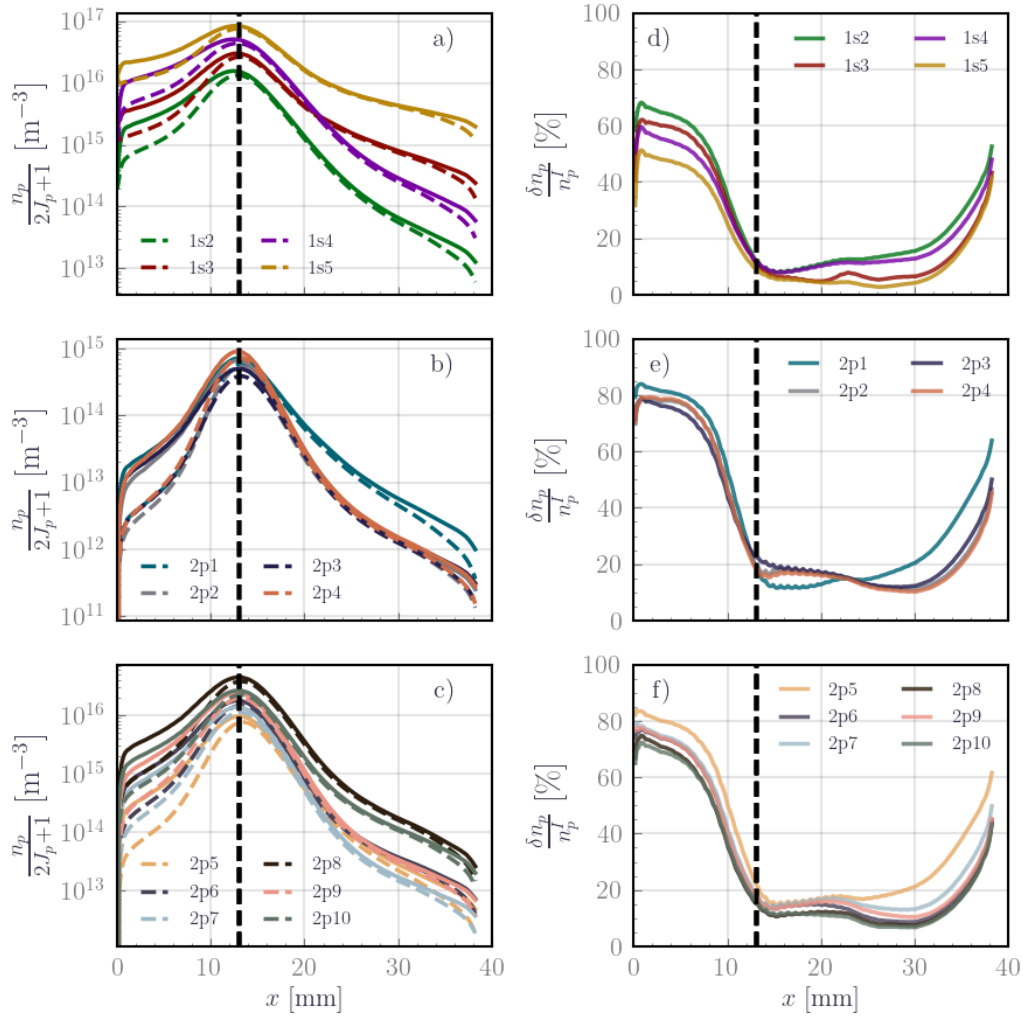


Figure 5.20: Axial profiles of excited species density for Cases I with an isotropic EEDF (solid lines) and II with a Maxwellian EEDF (dashed lines). Panels a), b), and c) show the axial profile grouped by manifold. Panels d), e), and f) show the relative difference in density by level between Case I and Case II.

Figure 5.20 illustrates the observed differences in the axial profile of the excited species density between the two EEDF scenarios. Case I, featuring the PIC isotropic EEDF, yields systematically higher average densities than Case II, utiliz-

ing a Maxwellian EEDF. Significantly, the extent of these differences seems to be spatially segmented by the maximum in the excitation source term, aligning closely with the distinct kinetic regions within the thruster. For instance, near the anode- $x \leq 11$ mm-the relative differences concerning the Case I calculations, denoted by $\delta n_p/n_p^I$, soar up to 80%. This strong discrepancy underscores the sensitivity of the excited species densities to the choice of the EEDF in this region. Conversely, in the mid-channel area, which covers the ionization and acceleration zones as well as the near-plume, the relative differences are smaller, ranging from 10-20%. The calculations in these zones, therefore, appear to be close, irrespective of the EEDF employed. As for the cathode boundary limits-specifically at $x \geq 35$ mm- the relative error increases again, however given the nature of the boundary condition and the cathode injection model further investigations are warranted to verify if this increase is not artificial.

To assess whether the impact of a non-Maxwellian EEDF exhibits temporal dynamics associated with the BM, we extracted the time evolution of the total population of the $6p$ manifold for both Case I and Case II. The results, illustrated in Figure 5.21, reveal that the maximum discrepancies between the two cases systematically occur during the collapse of the BM, coinciding with its minimum. Conversely, the minimum discrepancies manifest at the peak growth of the BM. These observations are particularly prominent near the anode ($z = 4$ mm and $z = 12$ mm, while they are insignificant in the ionization, acceleration, and near plume region. We hypothesize that this variability is due to fluctuating collision rates and heating processes, which are in turn directly influenced by the ionization losses and the BM dynamics.

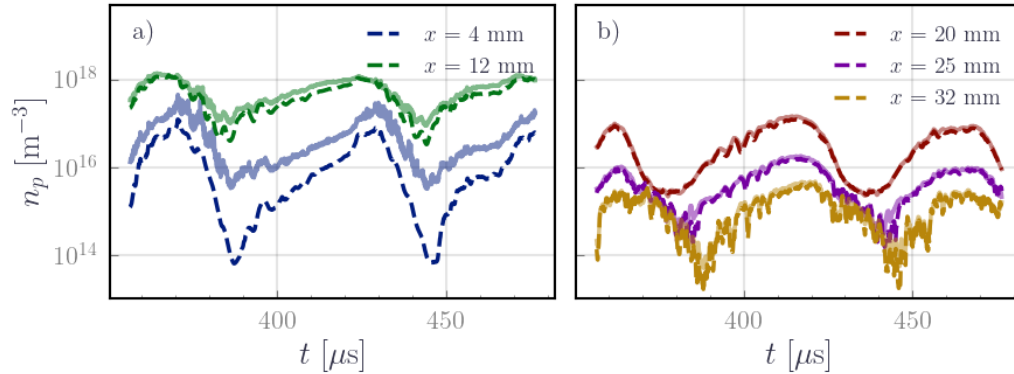


Figure 5.21: Time evolution of the total $6p$ manifold population for both Case I with an isotropic EEDF (solid lines) and Case II with a Maxwellian EEDF (dashed lines), emphasizing the temporal dynamics associated with the BM and the time evolution of the gap between the two cases

The comparison of the normalized synthetic spectra at five positions and five different times of the BM further supports these observations and is reported in Figure 5.22 and 5.23. While the mid-channel and ionization zone spectra exhibit virtually subtle differences, the spectra near the anode and in the plume are slightly

distinct, potentially serving as a basis for determining *EEDF* shape parameters. It is important to remember, however, that our model is not valid in that region. Near the anode, wall diffusion and ion recombination come into play, and in the far plume, the cathode boundary condition sets the temperature at 0.1 eV, which foremost is unphysical and second falls below the *CRM* validity range.

In summary, although the Maxwellian assumption may not be strictly accurate for describing the electron population in the *EEDF*, it does prove to be a valid approximation for characterizing the electrons contributing to the excitation of the $6p$ and $6s$ levels in the mid-channel, including ionization, acceleration, and near-plume regions. Extremely minor deviations in the spatiotemporal profiles of excited species densities and spectra are observed, thereby justifying the retention of the Maxwellian assumption in our model. This assumption is not valid though near the anode.

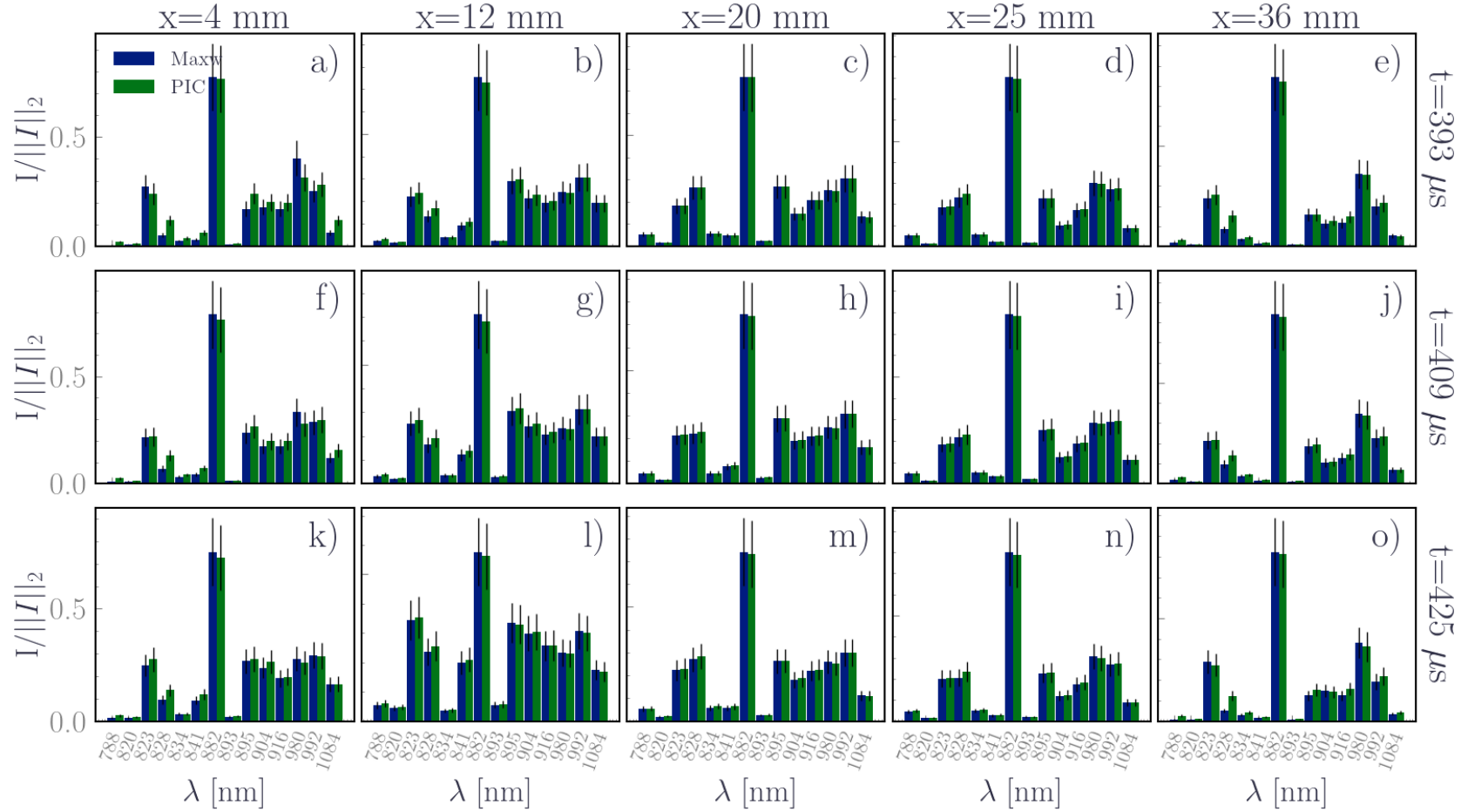


Figure 5.22: Comparison of the normalized synthetic spectra at five different positions and three times during the decay phase of the BM. Focusing on the mid-channel and ionization zone $x = 12$ mm, 20 mm and 25 mm, the spectra reveal minimal differences, validating the use of a Maxwellian EEDF in these regions. Looking near the anode and in the far plume regions, $x = 4$ mm and 32 mm, some differences are observed, indicating the limitation of the Maxwellian approximation in these regions.

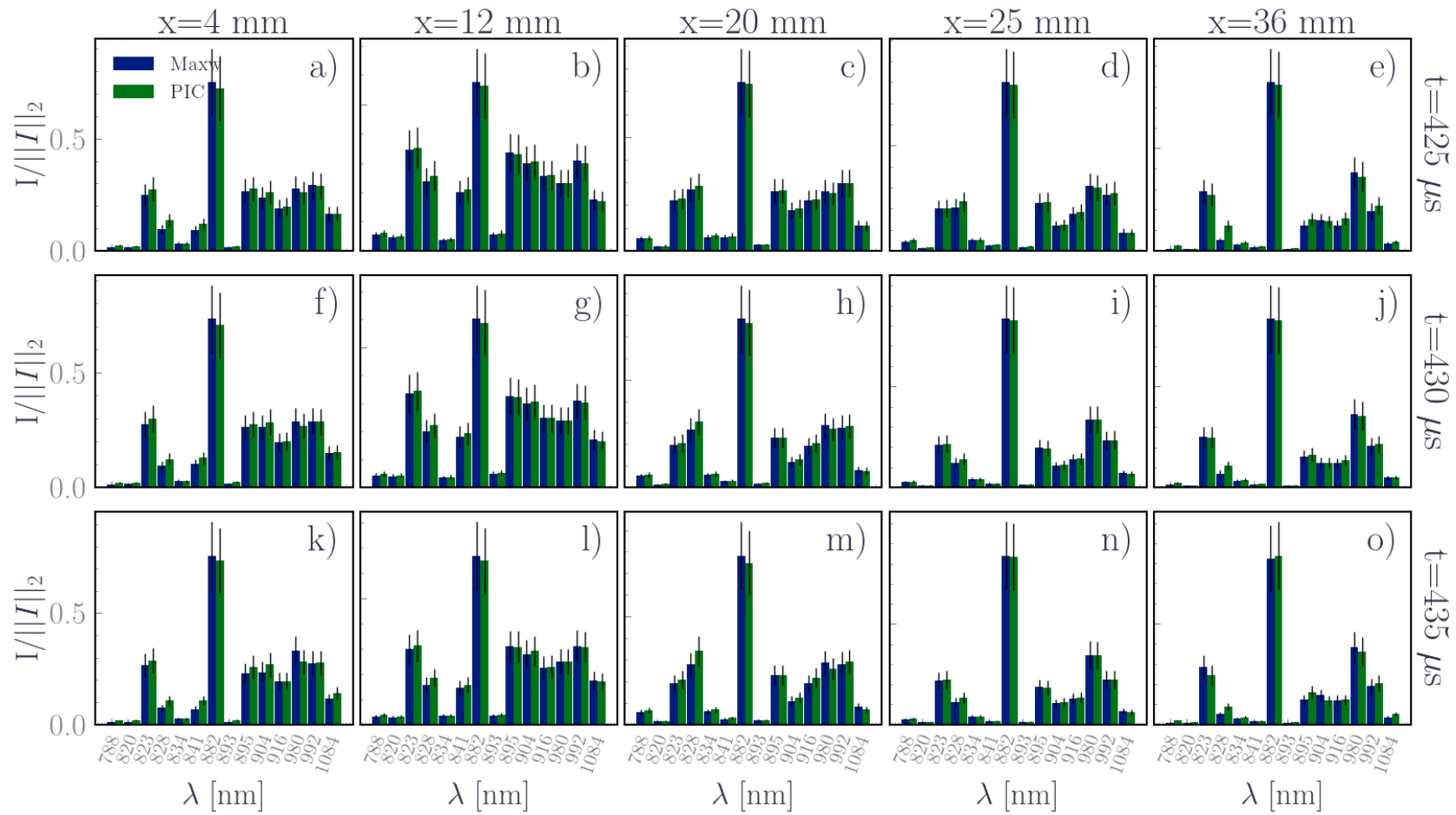


Figure 5.23: Comparison of the normalized synthetic spectra at five different positions and three times during the growth phase of the BM. Focusing on the mid-channel and ionization zone $x = 12$ mm, 20 mm and 25 mm, the spectra reveal minimal differences, validating the use of a Maxwellian EEDF in these regions. Looking near the anode and in the far plume regions, $x = 4$ mm and 32 mm, some differences are observed, indicating the limitation of the Maxwellian approximation in these regions.

5.6 Time analysis of the synthetic spectra

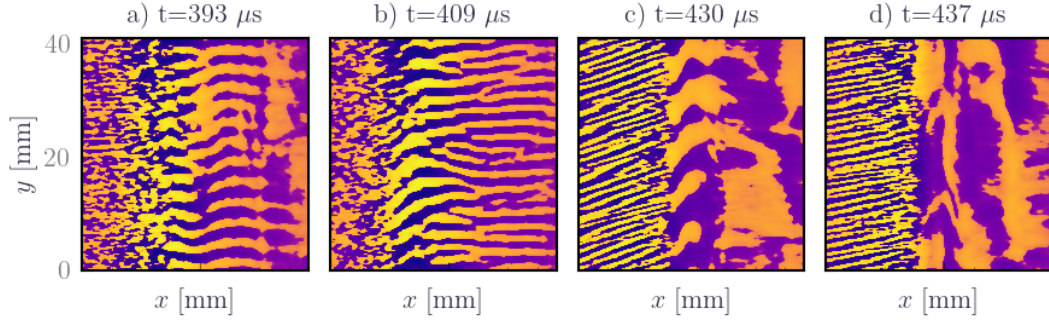


Figure 5.24: Density fluctuations of $2p8$ state during the growth and decay phases of the BM: The patterns observed here mirror the structures found in electron density and electron temperature maps.

In this section, we explore the implementation of OES for studying plasma instabilities identified in the electron density and electron temperature maps. Figure 5.24 illustrates the density fluctuations of the $2p8$ level and reveals matching structures with those observed in n_e and T_e maps during the growth phase of BM and its decay phase. The maps clearly show changes in the instabilities propagating in the discharge channel with the IAW/ECDI dominating the growth phase and the ITTI the decay phase, prominently in the plume.

Experimentally, we can focus on the 882 nm emission line from the $2p8$ level, given its intensity and the ease of capturing it using a collimated optical fiber and an interference filter. Using the results of the CRM-PIC coupling, we can explore the hypothetical results derived from analyzing the spatio-temporal evolution of the 882 nm emission. Two orientations are considered for the light collection: side view, averaging over the azimuthal axis y , and front view, averaging over the axial axis x . Figure 5.25 shows the temporal evolution from the signal for both perspectives. Notably, the side view captures the breathing mode BM oscillations, while the front view reveals small wavelength structures.

To further investigate, we perform Fast Fourier Transform (FFT) analyses, spanning approximately two BM periods $\approx 120 \mu\text{s}$. The FFT results (Figure 5.26) confirm a dominant BM frequency at 16 kHz but reveals no evidence of the axially propagating ITTI, despite its visibility in Figure 5.24. This discrepancy may be attributed to the Nyquist-Shannon sampling theorem limitations, as the wavelength of the ITTI is about 25 mm, close to the limit of the resolution. More advanced methods like the Two-Point Power Density Spectra, reported in [Petronio *et al.* 2023b], could potentially resolve this. The emission collected from the front-view collected distinctly features the azimuthal branch of the IAW/ECDI dispersion relation, with a frequency and wavenumber measured at 0.95 MHz and $0.4 \text{ rad}\cdot\text{mm}^{-1}$, respectively. These findings align with the numbers reported by [Petronio *et al.* 2023b].

These observations resonate also with previous studies on HET on the use of

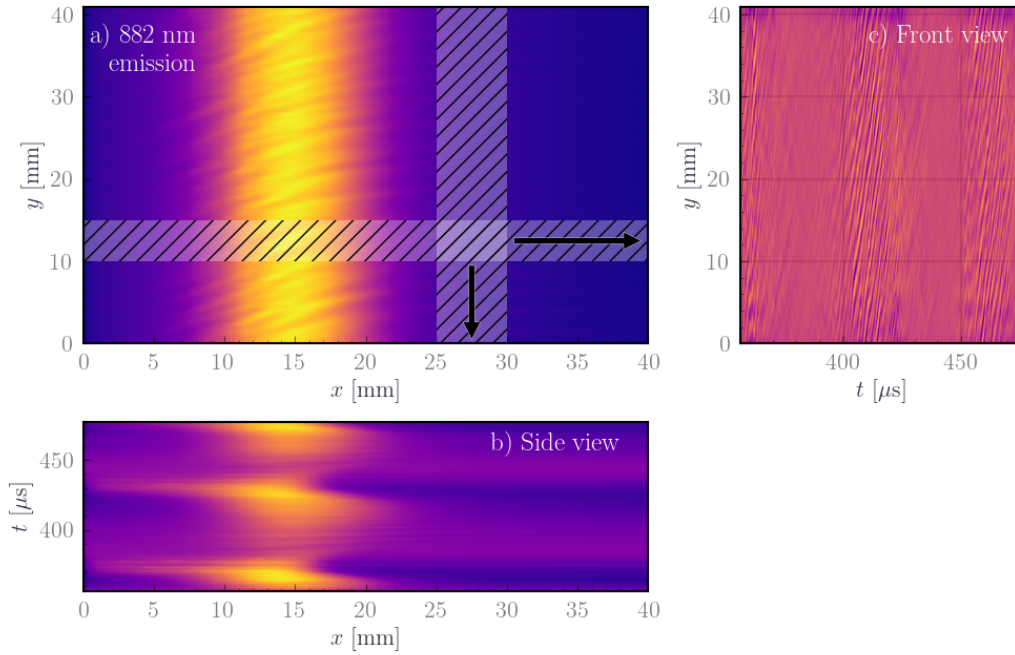


Figure 5.25: Temporal evolution of the intensity of the 882 nm emission line from the side and the front views: b) Side view reveals the breathing mode oscillations, whereas c) the front view reveals small wavelengths structures.

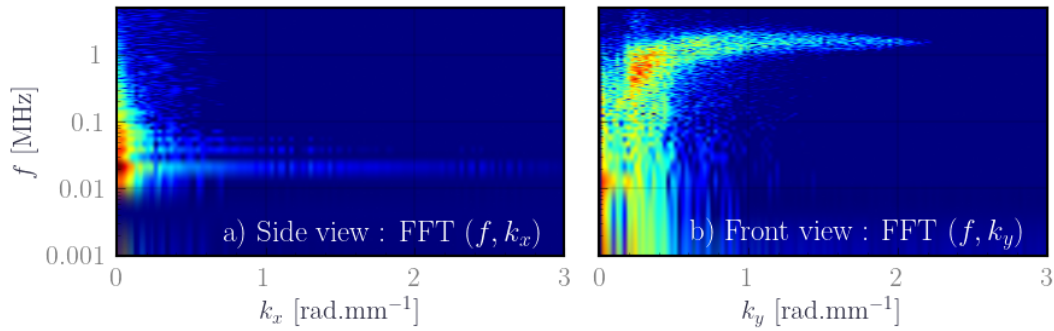


Figure 5.26: Spectral analysis of the intensity of the 882 nm emission line. Dominant frequencies and their corresponding modes are highlighted. The side view spectrum notably shows the BM at 16 kHz but lacks evidence of the ITTI. The front view notably features the IAW/ECDI.

time-resolved OES [Gonzales *et al.* 2014] to study the BM specifically. However, the data analyzed here is essentially a 2D perspective of the thruster, and more advanced techniques are needed to be able to capture the previous results in real experiments.

A central challenge, to obtain these observations in a real experiment, beyond the question on localized versus line-of-sight integrated diagnostic, lies in controlling

the depth of field. This control critically influences the spatial resolution of the data acquisition. Achieving precise depth of field settings often requires larger sensors and smaller apertures, which can compromise both acquisition time and the number of photons collected. Positioning the equipment nearer to the thruster's plume might alleviate some of these constraints, as it has been successfully implemented by [Gonzales *et al.* 2014]. There are other promising diagnostic avenues worth exploring, such as phase-resolved spectroscopy and tomography. In particular, Optical Emission Tomography, implemented by [Nakles & Matlo 2019, Kim *et al.* 2022], holds the potential for facilitating 3D scans of the plasma plume using OES.

5.7 Discussion

The compatibility of the dynamic time scale The steady-state coupling between PIC and CRM has yielded reliable results, particularly with regard to the plasma kinetics along the thruster axis and the line ratio method. However, it is important to consider the limitations of this approach, especially as they pertain to the dynamics of the excited species and non-linear systems.

One notable constraint is that the steady-state assumption doesn't capture the finer details of the excited species dynamics. Since the methodology focuses on a stable state, transient physicochemical interactions are overlooked. Particularly, time scales of kinetic processes that are comparable to the frequency of the system perturbations could give rise to more complex dynamics around the baseline steady-state solution. To account for these effects, one could use fully coupled, high-fidelity simulations; however, such approaches are often prohibitively expensive in terms of computational resources. An alternative avenue to explore could be the utilization of an adapted version of the Lagrangian Diffusive method to HET [Boccelli *et al.* 2019].

However, in an attempt at our level to quantify these limitations and characterize these finer effects, we examined the time response of the CRM to oscillating input parameters, particularly the electron temperature T_e since most instabilities translate in fluctuations in the electron temperature. Previous research suggests that rigorous study for non-linear systems would involve the use of Volterra series expansion [Jing & Lang 2015], but we opted for a simplified yet effective approach based on linear systems theory. The study uses the time-dependent CRM, to solve the rate balance equations for constant plasma parameters $n_e = 1 \times 10^{18} \text{ m}^{-3}$ and $n_g = 9 \times 10^{19} \text{ m}^{-3}$ and $d = 15 \text{ cm}$ with temporal fluctuations in T_e modeled as

$$T_e(t) = T_{e,0}(1 + \delta T_e \sin(2\pi f_{T_e} t)).$$

Here, $T_{e,0}$ is the mean electron temperature, δT_e is the fluctuation rate expressed in percent, and f_{T_e} is the frequency of the perturbation. The values covered by these parameters in this analysis are summarized in Table 5.1.

The calculations were done assuming a Maxwellian EEDF and Mewe approximation within a time interval of 0.3 ms and a fixed time step of 25 ns, conforming to Shannon-Nyquist criteria for capturing a frequency bandwidth from 3 kHz to 20 MHz, which is highly sufficient to cover the range of frequencies in HET.

Table 5.1: Parametric space for the analysis of the CRM time response

Parameter	Range
$T_{e,0}$	5 eV to 60 eV
δT_e	0.1 %, 1 % and 10 %
f_{T_e}	3 kHz to 1×10^4 kHz

Figure 5.27 illustrates how the fluctuations in the densities of the excited species, denoted as δn_p , oscillate in response to variations in the electron temperature, $T_e(t)$. These oscillations center around their temporal mean values, which correspond to the steady-state solution at $T_{e,0}$. Interestingly, the oscillations occur at the same frequency as f_{T_e} and exhibit a discernible phase shift that varies depending on the excited level. Furthermore, the amplitude of these oscillations is proportional to δT_e and is decreasing with increasing $T_{e,0}$. This observed decrease in amplitude aligns well with the understanding that rate coefficients become less responsive at elevated $T_{e,0}$ levels, subsequently affecting the magnitude of the fluctuations in rate coefficients.

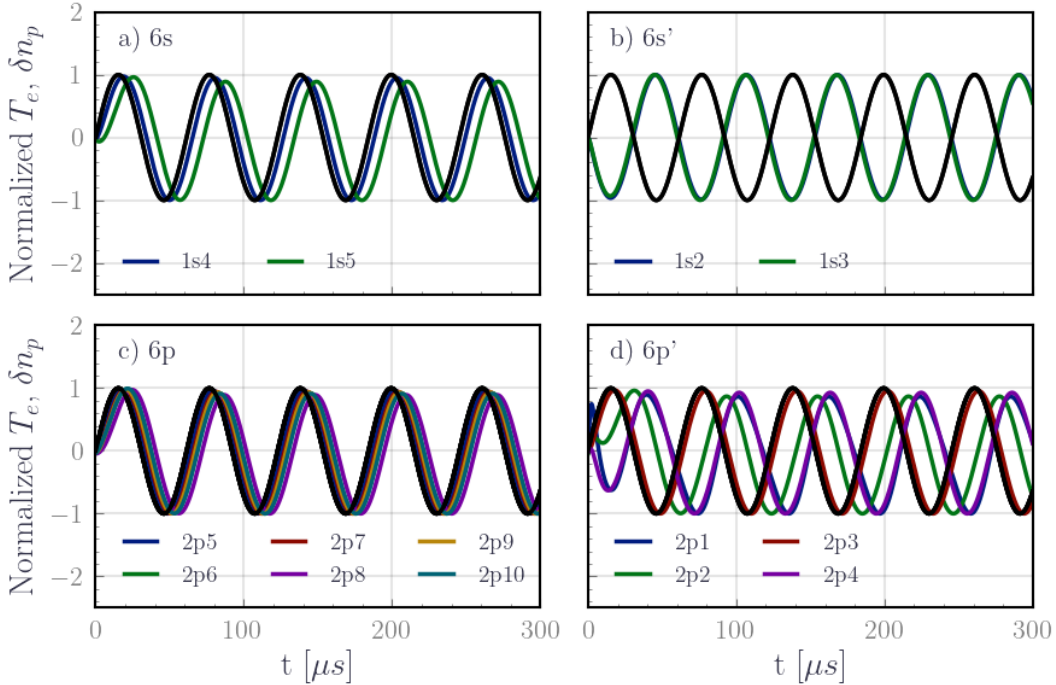


Figure 5.27: Normalized Frequency response of excited species densities. The temporal mean was subtracted to highlight the fluctuations in the excited species densities δn_p . The dark solid line corresponds to the oscillating part of the electron temperature perturbation. Here $T_{e,0} = 35$ eV, $f_{T_e} = 16$ kHz and $\delta T_e = 1\%$

To investigate both the phase and amplitude dynamics of the excited levels, we use Bode diagrams. Each excited level has its transfer function, characterized by a cut-off frequency related to its lifetime. Specifically, for metastable levels, the lifetime is governed by $K(T_e) \times n_e$, while for radiative levels, it is affected by $K(T_e) \times n_e - A$, when compared to the fluctuation frequency f_{T_e} . As delineated in Figure 5.28, the Bode diagrams present both amplitude and phase shifts for the excited levels $2p8$ and $2p1$. These diagrams make it evident that the amplitude gain diminishes as the frequency increases, suggesting that the CRM operates akin to a first-order filter based on the decrease on the amplitude. We can identify a cutoff frequency that is both level-specific and temperature-dependent. The ability to define these cutoff frequencies has noteworthy implications for system diagnostics and optimization. Each level essentially has a "dedicated response time," beyond which external perturbations become imperceptible or are not effectively transmitted. This nuanced understanding aids in the choice of which excited levels to monitor, thereby contributing to the refinement of the steady-state coupling methodology. Specifi-

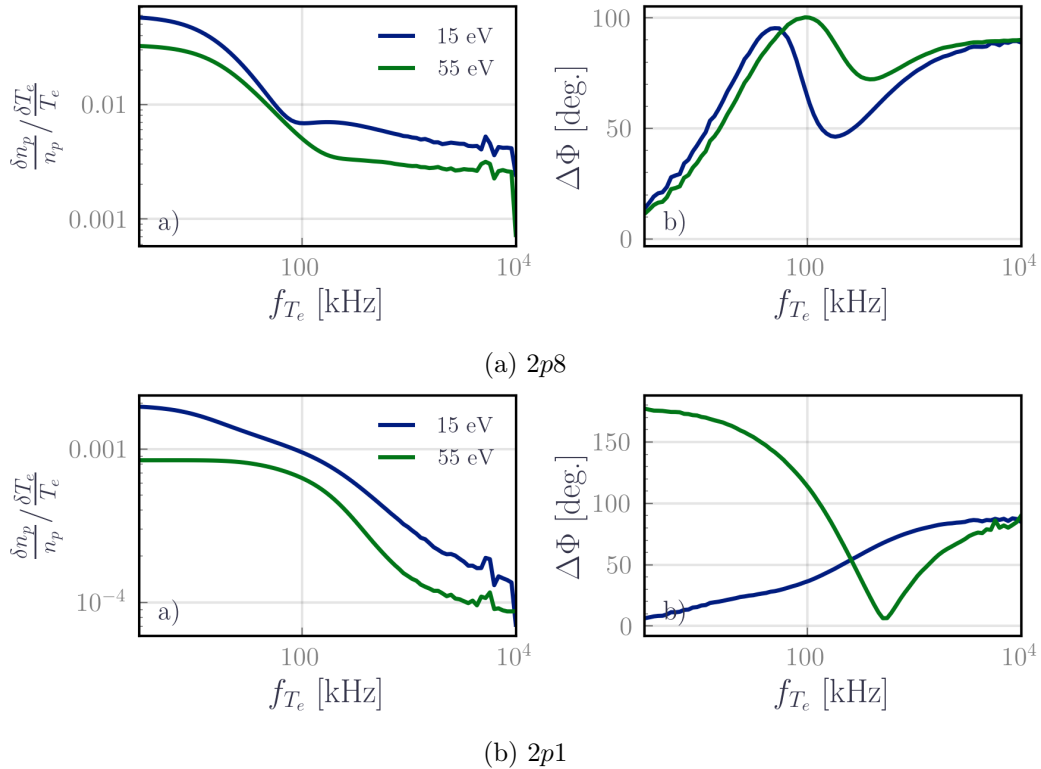


Figure 5.28: Frequency response of the density of the excited species: Bode diagram for amplitude and phase shift. Here the input perturbation has $T_{e,0} = 15\text{ eV}$ and 55 eV and $\delta T_e = 10\%$. The frequency was varied from 3 kHz to $1 \times 10^4\text{ kHz}$. Subfigure a) Bode diagram for $2p8$ level and subfigure b) for $2p1$ levels. The diagrams show the amplitude gain defined as the amplitude of the oscillation δn_p normalized by the mean value n_p times the temperature fluctuation rate δT_e .

cally the levels involved in the 823/828 – 992/980 ratios have a minimum cut-off frequency at around 40 kHz for $T_e = 10$ eV and a minimum cut-off frequency at around 110 kHz for $T_e = 50$ eV. For clarity, the cutoff frequency is defined here as the frequency at which the gain falls by 3 dB of its maximum value.

The observed phase shifts were highly unexpected and are dependent on the excited level, the fluctuation frequency f_{T_e} , and the electron temperature $T_{e,0}$. These observations agree with recent work by [Konopliv *et al.* 2021], which also found that metastable densities exhibit a phase shift that is dependent on the frequency of the oscillating electron temperature. This finding could have significant implications for the application of OES in studying system instabilities. For example, the observed phase shifts could influence the timing required to trigger the emission signal about phenomena such as BM oscillations and necessitate modifications to the operational protocol of time-resolved OES to capture the accurate trends as evoked in [Gonzales *et al.* 2014] and discussed briefly in [Konopliv *et al.* 2021].

However, it is worth noting that the amplitude gains observed in this work are relatively small, peaking at around ≈ 0.03 all levels considered suggesting that the impact of these phase shifts on the results produced by the steady-state coupling would likely be moderate. Thus, while these findings add nuance to the understanding of the system, they also reinforce the validity and reliability of the steady-state approach.

Examining the frequency response, we discern also interesting behaviors, notably the appearance of second and even third harmonics starting from intermediate electron temperatures ($T_{e,0} > 30$ eV) when subjected to high-temperature fluctuation rates, δT_e . These higher-order harmonics signal the manifestation of the equation's non-linearities within this parameter range. This is illustrated in Figure 5.29.

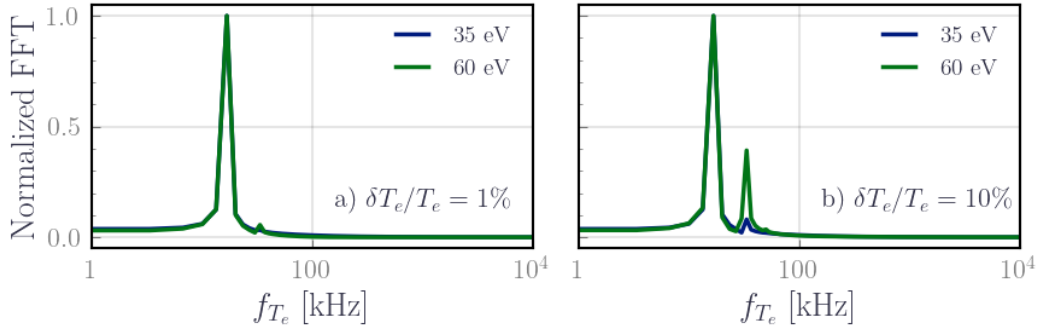


Figure 5.29: Spectral analysis of the density fluctuation of the $2p3$ level. Here the input perturbation has $T_{e,0} = 35$ eV and 60 eV and $\delta T_e = 1\% - 10\%$.

In summary, while the steady-state assumption has proven to be highly informative, providing an optimized balance between computational complexity and physical accuracy, it is not without limitations. It is unable to capture the more intricate dynamic behaviors of the system, particularly the level-specific bandwidth, the eventual phase shifts, and nonlinearities inherent to the equations of the CRM. While linear system theory has suggested these effects to be negligible for our current

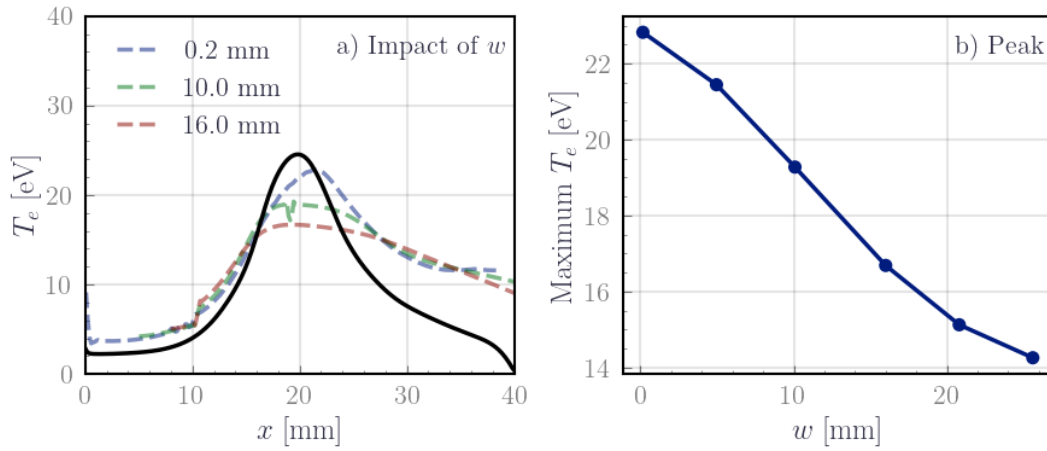


Figure 5.30: Impact of collection area width on predicted axial electron temperature profiles. This graph illustrates how varying the width w of a cylindrical collection area influences the axial profiles of the electron temperature.

scope, the complete validation of these findings requires more advanced methods, such as full-time-dependent CRM simulations. One particular challenge that needs to be addressed is the inclusion of fluctuations in n_e and n_g which could not be accommodated within the current framework of linear system theory contrary to T_e . The current CRM framework does not include self-consistent source terms for electrons and neutral thereby including time-dependent n_e or n_g would violate mass conservation and electron balance. Future work should prioritize this aspect, aiming to augment the current methodology with capabilities that allow for a more comprehensive understanding of these physicochemical dynamics.

Impact of the width of the optical fiber Up until this point, the collection area was assumed to align with the spatial resolution of the PIC simulation. However, in practice, light is collected over a solid angle that defines the diagnostic volume. While CTS clearly defines this volume through the intersection of two laser beams, the light in OES is integrated over the line of sight which is often represented by a diverging cone, or in the best-case scenario, a cylinder with a width, denoted as w . Thus, it becomes important to evaluate the effect of varying w on the temperature predictions.

To this aim, we place a hypothetical collimated optical fiber on the side view as previously defined in Figure 5.25. For each axial position, we average the light over a rectangular area representing the collection zone of the collimated fiber (gray hatched area in Figure 5.25). This yields an axial profile of the light collected by the fiber. Based on this profile we use the 823/828 – 980/992 abacus to predict the electron temperature. We do this for different widths of the rectangle w .

In Figure 5.30, we see that the width of the hypothetical cylindrical collection area significantly influences the predicted axial profiles of the electron temperature. Indeed, as the collection area expands, two principal outcomes are observed: the T_e

profile flattens, and the peak temperature value diminishes. This behavior echoes observations made using virtual CTS. Essentially, the spatial extent of the probed volume acts as a convolution filter, smoothing the original profile of T_e .

It is worth noting that the decline in peak temperature is not linear; it becomes increasingly pronounced as the size of the collection area enlarges. Consequently, a larger collection area does not merely lead to a modest, proportional drop in peak temperature. Instead, the decline becomes significantly more noticeable, warranting attention when interpreting data based on varying collection areas.

Chapter conclusions

In this chapter, we have performed an extensive exploration of the intersection between the CRM and PIC simulations within the landscape of HETs. This analysis in conjunction with the insight from past PIC simulation has yielded critical insights that are both illuminating and practical.

The steady-state coupling approach with PIC simulations was established as a valuable initial approximation tool for studying optical emissions generated from simulations of HETs. The transport assumptions and the Maxwellian assumption, often deemed critical in similar studies, were found to have negligible impact on the emission, in particular in the mid-channel and near-field plume. We were able to demonstrate that the breathing mode has a significant impact on plasma emissions through the modulation of plasma parameters. Furthermore, we identified the existence of two kinetically distinct zones within the thruster channel: one near the anode dominated by $1s5$ collisions and another in the plume dominated by radiative decay. These zones are separated by the maximum in the excitation source term.

The influence of gradients in electron density n_e and neutral gas density n_g on plasma emissions was established, affirming the necessity of their consideration when applying the line ratio method in CRM for HETs. We also established that the line ratios 823/828 and 980/992 are robust candidates for determining electron temperature T_e , even though they fall short for the electron density n_e . Interestingly, the Maxwellian hypothesis turned out to be a valid approximation for modeling the $6p$ tier population in the mid-channel zones, namely the ionization, acceleration, and near-plume areas. However, for regions near the anode and the far plume, more comprehensive kinetics and a larger simulation domain are essential for a fully validated coupling.

From the standpoint of instabilities, we established that OES can detect the same types of instabilities commonly observed in simulations. The choice of view also impacts what instabilities are observable: a side view reveals axial propagating instabilities, whereas a front view exposes azimuthally propagating instabilities. Implementing corresponding experimental setups to observe these, however, remains a challenge in practice. Another aspect is the level bandwidth limit instigated by the lifetime of the excited species which limits their response time to external fluctuations. Preliminary time-dependent aspects of a dynamical coupling were also

explored, revealing phase shifts and second harmonics arising from fluctuations in T_e . These time-dependent aspects still have a minor impact and the steady-state approach still offers an excellent first approximation, providing a compromise between computational time and complexity.

As we move forward, it will be vital to extend this work to validate our observations thoroughly on more simulation cases and also experimentally. More advanced techniques such as time-dependent CRMs could offer deeper insights, particularly for conditions that break from the assumptions we have discussed. There is also scope for including fluctuations in electron and neutral gas densities to better capture the system's dynamic behavior. Moreover, experimental verification of the line ratio method and the identified instabilities, and how they are viewed, could provide a more comprehensive understanding of the system.

In summary, while our coupling strategy between CRM and PIC has provided substantial insights into the application of OES on HET, further research and development are both promising and necessary for a more complete understanding, this includes applying the diagnostic to a real HET which will be the subject of the next chapter.

Overview of the Experimental of HET0D

Les matins d'hiver sont faits d'acier, ils ont un goût métallique et des bords acérés.

Olga Tokarczuk, *Sur les ossements des morts*

Contents

6.1	The main experimental setup	126
6.1.1	The Hall effect thruster	126
6.1.2	Electrical and magnetic configuration	128
6.1.3	Gas injection and vacuum configuration	129
6.1.4	Ignition sequence	130
6.1.5	Thruster characterization	130
6.2	Overview of the diagnostics and their calibration	132
6.2.1	Optical emission spectroscopy	132
6.2.2	Langmuir probe	135

Introduction

The coupling of PIC simulations with HET0D has provided insights into the chemistry at play in HET. Among these insights, the most impactful is arguably the ability to use the neutral radiative emission to account for gradients of T_e along the channel. This is achieved by optimizing the CRM inputs either via the line ratio method or the abacus method. Moreover, it has been shown that the Maxwellian assumption does not majorly change the neutral emission intensity from a non-Maxwellian case. These findings can be seen as beneficial practices for implementing HET0D as an experimental diagnostics tool for HET. It is worth mentioning that HET were also studied using plasma probes, often deployed to explore the discharge properties. While generally useful, they are not without their challenges due to their invasive nature and the high electron temperature in HET, often demanding an intricate setup and involved implementations [Lazurenko *et al.* 2005b,

Lazurenko *et al.* 2007b, Lee *et al.* 2021, Giannetti *et al.* 2020]. Optical diagnostics circumvent these issues and have proven to be a profoundly promising non-invasive diagnostic technique to monitor the plasma parameters in HET [Mazouffre 2012, Hargus & Charles 2010, Young *et al.* 2018, Tsikata *et al.* 2013]. Particularly, OES has demonstrated its capacity to capture an optical footprint of the thruster and the discharge parameters [Karabadzhak *et al.* 2006, Zhu *et al.* 2019, Priti *et al.* 2019a, Konopliv *et al.* 2021, Abrantes & Martin 2021].

However, the key distinction in this work lies in establishing that the assumptions considered previously as shortcomings are not as detrimental as once thought thanks to the virtual diagnostics approach. In previous chapters, we qualitatively validated and virtually tested the limits of what OES and CRM can do; now, we move from the virtual to the real diagnostic to put these validations through their paces with experiments. The endeavor is then threefold: initially, suggest a practical experiment which is described in the first sections, secondly, provide experimental validation for the CRM and finally examine the plasma parameters on a wide range of operating conditions. The experimental observations will be operational regime-specific, covering a wide range of parameters of HET and testing the CRM, which has not been done in previous CRM implementations, to our knowledge.

The investigation will focus on the plume and the channel of a laboratory HET. The thruster is placed in a medium-sized vacuum chamber with two viewports: a front view and a lateral view, which allows to collect spectra. A Langmuir probe is placed on a two-axis arm perpendicular to the thruster's axis allowing us to collect electron densities and temperatures providing a reference experimental profile, against which we can validate the predicted profiles from OES. In this chapter, we will introduce the main setup and the calibration of both Langmuir probes and OES. The Langmuir probe, OES, and CRM results are reported in the next chapter.

6.1 The main experimental setup

As shown in Figure 6.1, the experimental setup consists of four main components: the vacuum system (orange), the gas injection (green), the electrical circuit (blue), and the thruster itself (red).

6.1.1 The Hall effect thruster

We use a 500 W HET, called PPSX00-CHEAP. This thruster is based on the prototype of Safran's ultimate PPSX00 model, itself based on the SPT series, and is illustrated in Figure 6.2. The nominal operating parameters are summarized in Table 6.1. The thruster consists of a 3.0 cm-long cylindrical channel made of borosil nitrate silica (BNSiO₂). This channel has an inner diameter of 3.2 cm and an outer diameter of 5.2 cm. Mounted on top of the channel is a hollow cathode operating in xenon. This cathode is a standard design with a thermo-emissive surface made of LaB₆. It is based on the same cathode for the PPS-1350 model used in the SMART-1 mission. During the ignition sequence, the cathode features an independent circuit

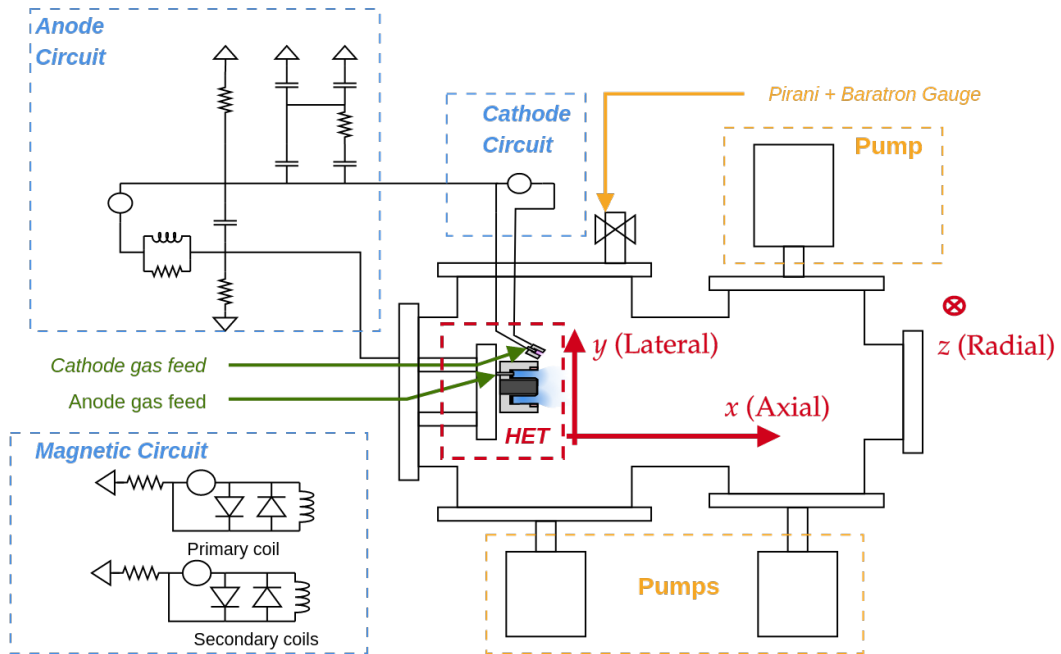


Figure 6.1: Schematic overview of the Hall-Effect Thruster experimental setup. The figure illustrates the four primary components involved: the vacuum system (colored in orange), the gas injection system (green), the electrical circuit (blue), and the thruster itself (red). Each component is color-coded for easy identification and will be discussed in detail in the following sections.

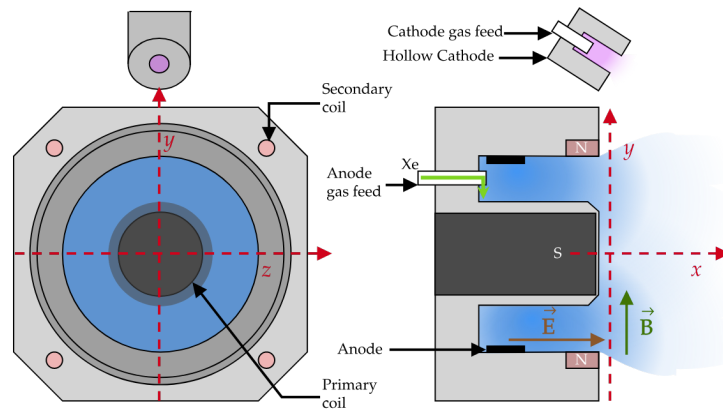


Figure 6.2: Front view (left) and lateral view (right) of the PPSX00-CHEAP Hall-Effect Thruster. The origin $(0,0,0)$ is defined at the intersection of the thruster's axis and its exit plane.

Table 6.1: Nominal Operating Parameters of the PPSX00-CHEAP Thruster

Nominal Thruster Parameters	
Power	150-1000 W
Voltage	150-320 V
Current	0.75-3.5 A
Anode flow rate	0.8-2.5 mg.s ⁻¹
Cathode flow rate	0.3 mg.s ⁻¹
Thrust	12 mN
Specific impulse	700-1050 s
Anode Efficiency	18%

used for heating, while during the operation, the heating circuit is turned off and the cathode is heated by the discharge current.

To maintain consistency with PIC notations, a Cartesian frame of reference (x, y, z) is used to designate the channel axis. The axial direction is represented by x , which is parallel to the ground and points away from the channel. The lateral direction is denoted by y , and it extends from the ground upwards. Lastly, the z direction is parallel to the ground plane and is referred to as the radial direction. The origin $(0, 0, 0)$ is defined at the intersection of the thruster's axis and its exit plane.

6.1.2 Electrical and magnetic configuration

The electrical and magnetic setup consists of three independent circuits. The anode circuit features an external power supply controlling the voltage drop across the anode. A pass-band filter is placed between the power supply and the thruster to dampen the BM oscillations, thus stabilizing the thruster during its operation. Secondly, the cathode circuit, usually called the Heater, is responsible for heating the cathode during the ignition sequence, thereby ensuring sufficient electron emission. Finally, the magnetic circuit controls the generation of the radial magnetic field, denoted by \mathbf{B} . This circuit incorporates five coils—one at the center and four at the corners (as depicted in red in Figure 6.2)—housed in an armature made of soft iron (depicted in dark gray).

The magnetic circuit is tailored to produce a radial magnetic field that is very small near the anode and maximum near the thruster's exit plane, which is a feature common to standard SPT models. The radial component of the magnetic field, B_z , within the experiment, was characterized using a Hall Effect Gaussmeter. The axial profile at the mid channel $B_z(z = 2.3 \text{ cm})$ as well as the radial profile at the maximum $B_z(x = -0.7 \text{ cm})$ are reported on Figure 6.3. The radial magnetic field within the thruster channel is directed toward the internal coil. The magnetic field

strength varies at different points: around 100 G near the top of the external coils, approximately 240 G near the top of the internal coil, and about 150 G in the channel at the thruster's exit plane and then decreases to zero at approximately 5 cm from the exit plane.

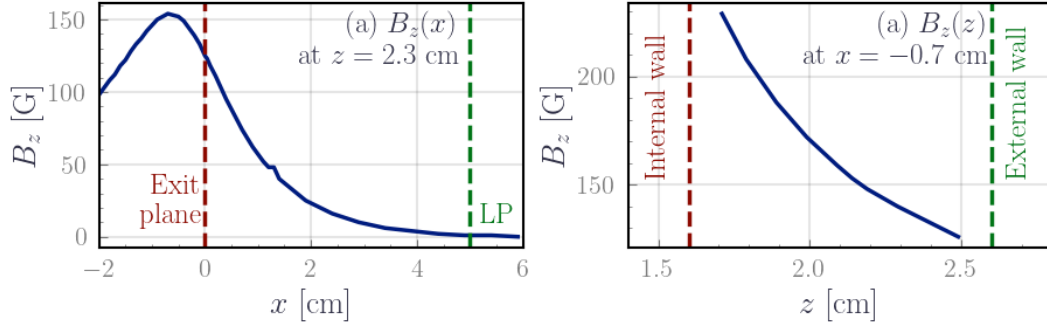


Figure 6.3: Axial and radial evolution of the radial component of the magnetic field. $z = 2.3$ cm corresponds to the mid-radius of the channel and measurements were made parallel to the thruster's axis. The position $x = -0.7$ cm corresponds to the axial position at which the radial magnetic field was maximum. Measurements were made inside the channel from the inner wall to the outer wall.

6.1.3 Gas injection and vacuum configuration

The thruster is placed in a stainless steel vacuum chamber with a diameter of 35 cm and a length of 1 m. The chamber features three high-capacity turbo pumps from Seiko, Agilent, and Edwards, providing a combined pumping rate of $5060 \text{ L}\cdot\text{s}^{-1}$, measured on nitrogen. Pressure within the chamber is continuously monitored by two independent pressure gauges: a PIRANI gauge and a Baratron gauge. The xenon is injected through two mass flow controllers at two points: into the cathode at a flow rate denoted q_c , and into the anode at a rate denoted q_a . In particular, the anode's dielectric wall accommodates an annular-shaped gas injection system comprising numerous small, evenly spaced holes that inject the gas perpendicularly to the axis of the thruster as indicated by the green arrow in Figure 6.2.

The pressure is measured from the two gauges which are placed on top of the vacuum chamber as indicated by the orange arrow in Figure 6.1. This configuration allows readings over a wide range of pressures. The baseline pressure in the chamber is about 4×10^{-7} mbar and rises up to 1×10^{-3} mbar when the total xenon injection rate is $q_T = 3.6 \text{ mg}\cdot\text{s}^{-1}$. The dependency of the pressure on the flow rate is shown in Figure 6.4. Note the pressure levels are 3-4 magnitude higher than those traditionally used in HET experiments.

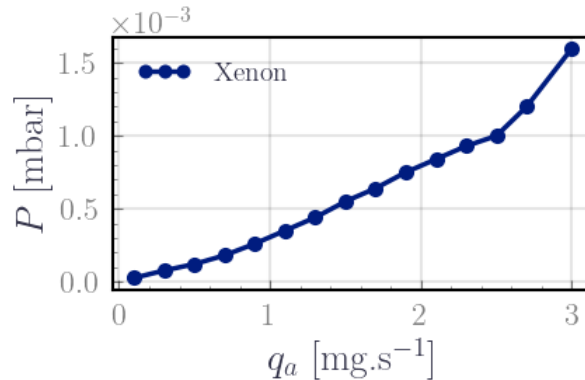


Figure 6.4: Relationship between the chamber pressure and xenon mass flow rate while the thruster is off.

6.1.4 Ignition sequence

In conventional HET experiments, a separate circuit, commonly referred to as the Ignitor is used to send electrical pulses to ignite the plasma. Our setup does not include a dedicated Ignitor circuit. Instead, we followed a modified ignition sequence. To start the thruster, the cathode is first preheated to a current of 12.4 A. This ensures adequate electron emission. Concurrently, xenon gas is injected into both the anode and the cathode at rates of $2.5 \text{ mg}\cdot\text{s}^{-1}$ and $0.6 \text{ mg}\cdot\text{s}^{-1}$, respectively. During this preheating phase, the anode is maintained at a bias of 40 V. After 2 min and 40 s, the magnetic circuit is activated. The power supply is then switched to constant voltage mode and set to 350 V. If the plasma ignites, the voltage is immediately reduced to 110 V. In the event of a failed sequence, the voltage is reset to zero, the magnetic field is deactivated, and a voltage of 250 V is applied to attempt plasma ignition without the magnetic field. Once the plasma is stable, the voltage is lowered to 40 V before reactivating the magnetic field. The voltage is then systematically adjusted back to 110 V with the magnetic field on.

6.1.5 Thruster characterization

Given the changes in the circuit configuration, the ignition sequence, and the background pressure used with the setup, it was paramount to recharacterize the operational regimes of the PPSX00-CHEAP. The results presented here are limited to the $I - V$ characteristics, though a broadband frequency analysis was also performed using 3 diagnostics: the floating potential, light emission with a photomultiplier and the anode voltage. This study is not reported here.

The classification adopted in this study is primarily based on the works of [Tilinin 1977, Choueiri 2001, Gascon *et al.* 2003]. Given the high flow rate at the anode, not all regimes reported in the referenced works are observable; notably, only four out of the six regimes discussed by [Gascon *et al.* 2003] are identified. The $I - V$ characteristics curves are depicted in Figure 6.5, showcasing three dis-

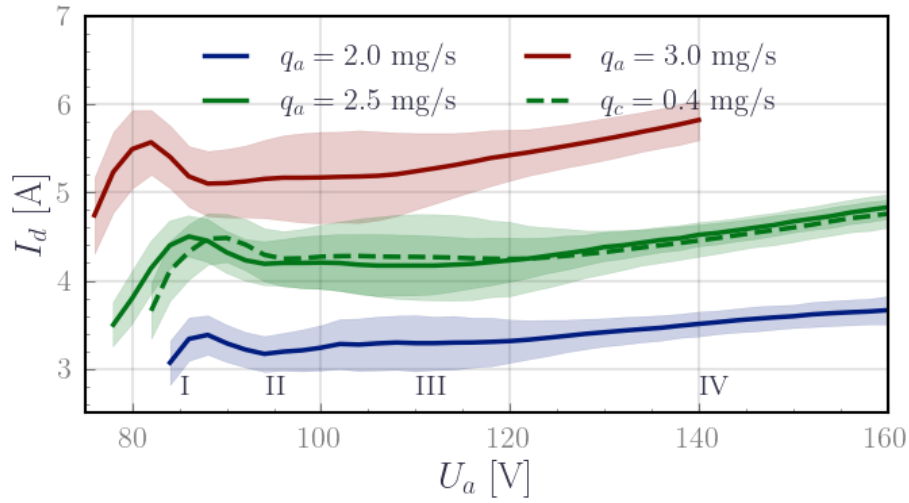


Figure 6.5: Current-voltage characteristics of the PPSX00-Compact Hall Effect Advance Propulsion System (PPSX00-CHEAP). The transparent envelope corresponds to the standard deviation of the current signal. Solid lines are for a cathode flow of $q_c = 0.6 \text{ mg}\cdot\text{s}^{-1}$ with for each color a different value of the anode flow rate. The dashed line is for an anode flow of $2.5 \text{ mg}\cdot\text{s}^{-1}$ and a cathode flow of $q_c = 0.4 \text{ mg}\cdot\text{s}^{-1}$

tinct anode flows: $2.0 \text{ mg}\cdot\text{s}^{-1}$, $2.5 \text{ mg}\cdot\text{s}^{-1}$ and $3.0 \text{ mg}\cdot\text{s}^{-1}$. For an anode flow of $q_a = 2.5 \text{ mg}\cdot\text{s}^{-1}$, two cathode flows were investigated to check its impact on the characteristics, $0.4 \text{ mg}\cdot\text{s}^{-1}$ and $0.6 \text{ mg}\cdot\text{s}^{-1}$.

The shape of the $I - V$ curve aligns with the well-established behavior of SPT models with borosil nitrate ceramics. Initially, there is a rapid increase in the current with the voltage, called the ionization branch (I). Usually, it exhibits a minor inflection point at lower anode flow rates that remains absent here. The rapid increase in the discharge current within this branch primarily arises from the enhanced electron density via increased ionization, leading to a maximum ion current. Following the ionization branch, there is a minor decrease in the current, which subsequently flattens before increasing once more and plateauing. On one hand, the minor decrease corresponds to regime 3 in Gascon's classification, identified as the negative resistance regime (II) in this work. On the other hand, the slight increase in the current followed by the plateau (III) corresponds to regimes 4 and 5 in the work of Gascon, but in our work, the delimitation is not very sharp. In this range of voltages, the acceleration zone starts to extend and the plume has a swallow tail shape. The ionization is efficient and the current is constant [Gascon *et al.* 2003]. This plateau is also characterized by the development of broadband plasma oscillations in the range of the 10 kHz to 50 kHz and the propellant utilization efficiency is supposed to be at maximum [Gascon *et al.* 2003]. For higher voltages, the discharge current continues to increase. For the investigated flows, the discharge became unstable at around 210 V and would sometimes extinct.

Increasing the anode flow rate tends to increase the discharge current and reduce

the upper and lower voltage boundaries defining these operation regimes without impacting their extension. This contrasts with the discussions in [Gascon *et al.* 2003] where higher flows lead to decreasing the extension of these regimes by increasing the lower boundary voltage and decreasing the upper boundary voltage. Altering the cathode injection does not change the general trend of the discharge current, which is in agreement with the effect described by [Gascon *et al.* 2003] and resonates with the observations in the work of [Hofer *et al.* 2008, Raitses *et al.* 2009]. The cathode flow should be looked at as a boundary condition that strongly impacts the value of the discharge current and the plasma plume. Its position relative to the magnetic field also impacts the electron emission and thus the plume dynamics.

6.2 Overview of the diagnostics and their calibration

Two diagnostics are implemented on the setup as shown in Figure 6.6: Optical Emission Spectroscopy and Langmuir probes. The following subsections detail the implementation and calibration of these diagnostics on the setup.

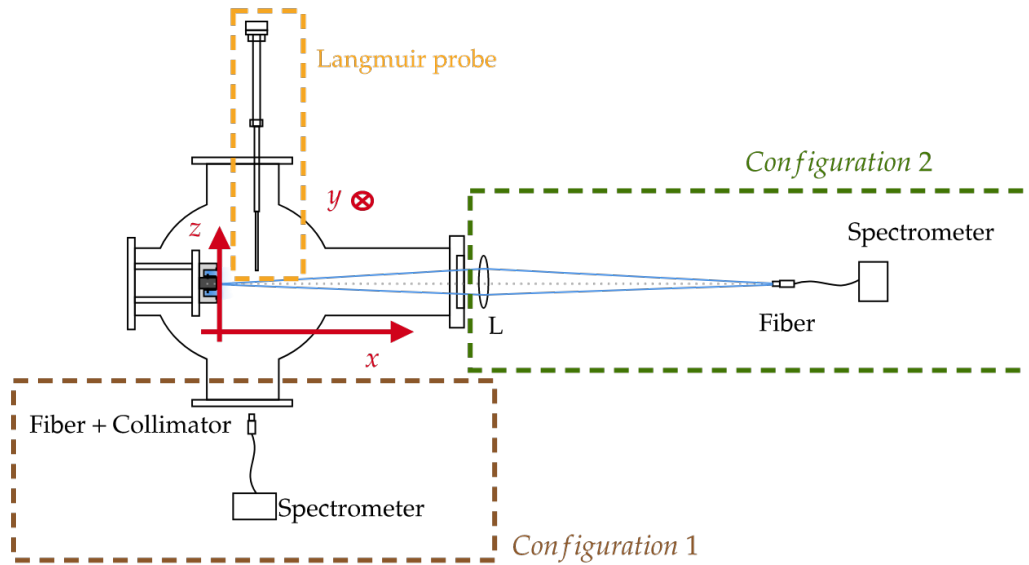


Figure 6.6: Top view of the experimental setup consisting of a 500 W Hall effect thruster, a Langmuir probe placed at $z = 6$ cm from the exit plane of the thruster, a 50 cm-focal length lens in a $2f - 2f$ configuration, an Avantes Spectrometer, optical fiber and a collimator for visible and near-infrared wavelengths. The origin of the frame of reference is placed on the intersection between the axis of the thruster and its exit plane.

6.2.1 Optical emission spectroscopy

We used an Avantes *AvaSpec - Dual* spectrometer, designed in a Czerny-Turner setup. The spectrometer captures a spectral range from 180 nm to 1060 nm, using

a blazed-grating which is optimized for both blue and near-infrared wavelengths. The grating features a density of 600 lines per millimeter and a blazing step of 700 nm. The device has a CMOS linear image sensor. It uses a 10 μm slit, providing a resolution at Full Width at Half Maximum between 0.3 to 0.36 nm. The optical fiber is bifurcated, allowing for the simultaneous acquisition of blue and near-infrared range spectra. It has a 400 μm diameter with a numerical aperture of 0.22. The setup includes a quartz detector collection lens to focus light from the fiber's core onto the detector, thereby enhancing photometric sensitivity. Two measurement geometries were implemented:

Configuration 1 for axial and lateral scans along the x and y axis For these scans, the optical fiber had a collimator and was placed at 30 cm from the median plane of the thruster. The collimator consisted in a 6 mm diameter lens with an 8.7 mm focal length. This collimator provided a cylindrical collection area and was mounted on an optical rail. The spectra were recorded every 5 mm, from $x = 0$ cm to $x = 10$ cm for the axial scan and from $y = -6$ cm to $y = 6$ cm for the lateral scan. To guarantee a perpendicular line of sight to the axis, the fiber was positioned adjacent to the viewport window and aligned using a laser beam. The spatial resolution is achieved only perpendicular to the optical axis, while the system integrates along the cylindrical collection area. The cylindrical shape simplifies the correlation of the spectral data with other diagnostic measures, thereby providing a simple framework for validating the CRM against Langmuir probes.

Configuration 2 radial scan along the z-axis For this configuration, a lens with a focal length $f = 50$ cm was aligned in a $2f - 2f$ configuration with the thruster's axis (i.e. the x axis) allowing a 1:1 magnification. The setup was focused on the leading edge of the inner wall of the thruster, at approximately 5 mm before the thruster exit plane. The light was collected using an optical fiber from the image focal point to the spectrometer's entrance slit. To facilitate scans perpendicular to the optical axis (i.e z axis), the fiber was secured on an optical rail parallel to the thruster exit plane, recording emission spectra at 1 mm intervals from $z = -4$ cm to $z = 4$ cm. To shield the lens from stray light, a black cloth was put around the lens, and alignment of the optics was ensured using a laser beam.

Note, however, that this configuration restricted the depth of field along the optical axis. Indeed, light is collected/detected from the focal point, however, the lens collection area is a cone-shaped collection area, which broadens as it moves away from the focal point. Therefore, we collect light from before and after the focal point, and for that reason, the measurements include emission from within the thruster channel and some of the plume. However, we expect the more intense emission near the exit plane where the electron temperature is maximal which is also the focal plane in this setup.

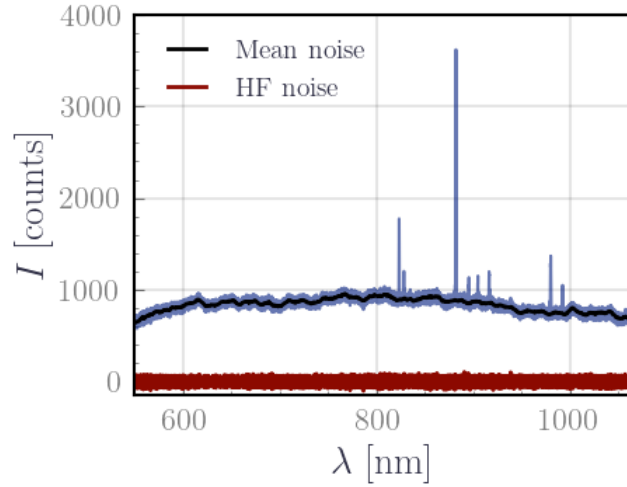


Figure 6.7: Background noise subtraction: The solid transparent blue corresponds to a typically measured spectrum. After filtering, we separate the random noise component (red) from the dark background (dark blue).

Integration time and background signal The spectrometer’s integration time was set to achieve a good signal-to-noise ratio without causing saturation. For that, we evaluated the position of maximum intensity first to determine the minimum integration time required. Then, the same integration time was set across all measurements at a fixed operating condition. The measurements were averaged over several spectra to further enhance the signal-to-noise ratio.

Using a fixed integration time is also advantageous to subtract the background signal, as the latter does not scale necessarily linearly with the integration time. For every operational condition, the background signal was recorded and then subtracted. Instead of a direct subtraction, we used a Savitzky-Golay filter to isolate the continuous background, providing a baseline noise level. Lines with an intensity below this level were not considered, as illustrated in Figure 6.7

Calibration Calibration was a two-fold process: wavelength calibration and irradiance calibration. The wavelength calibration was conducted by identifying the xenon lines and associating the measured spectral lines with their corresponding wavelengths. This was possible in this setup because the xenon lines, mainly from the $2p$ levels, are identifiable. The irradiance of each setup was calibrated in the range 230 nm to 1100 nm using a Deuterium-Halogen light bulb. This allowed us to calculate the system’s spectral response according to the formula:

$$R(\lambda) = \frac{E_{measured}(\lambda)}{E_{lamp}(\lambda)}$$

where $E_{measured}$ is the signal collected from the setup and E_{lamp} is the lamp calibrated spectra. The procedure encompassed several elements of the experimental setup, including the spectrometer, the optical fiber, the collimator, and the lens in

Configuration 1, as well as the viewport. Figure 6.8 reports the normalized calibration curves for the wavelength of interest. While absolute calibration requires a precise characterization of the solid angle of light detection and the detection surface, these factors cancel out if we consider normalized spectra or line ratios. This is particularly useful in our case since this is exactly what we are looking at with the CRM. It is worth mentioning that there's a considerable sensitivity gradient towards the edge of the spectrum as the $R(\lambda)$ goes to zero.

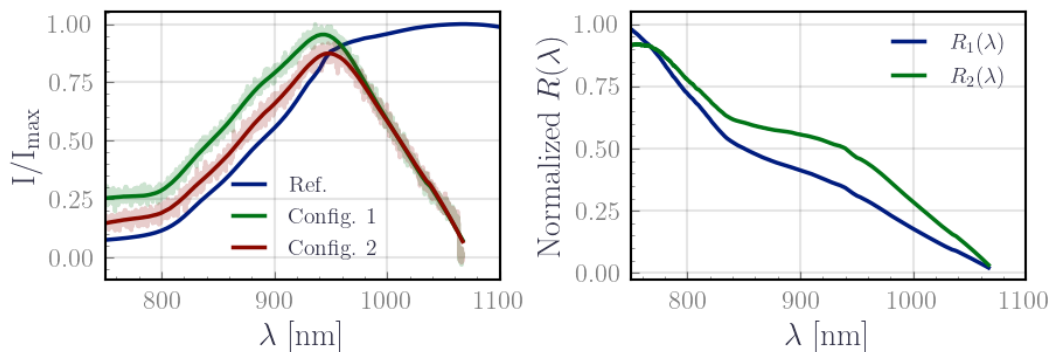
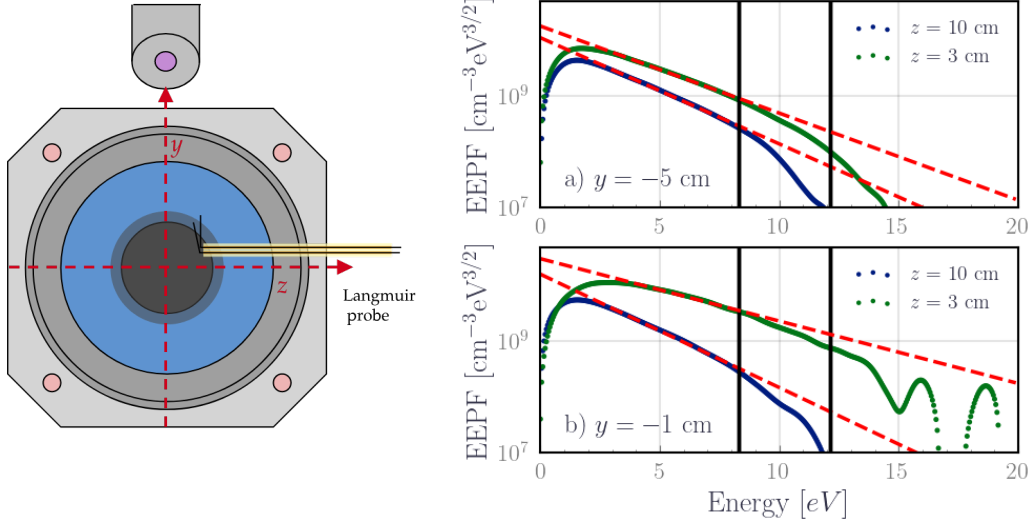


Figure 6.8: Relative intensity calibration. Left panel: Normalized irradiance of Configuration 1 (green) and Configuration 2 (red) from the Deuterium Halogen light bulb (blue). Right panel: Normalized spectral response of Configuration 1 R_1 and Configuration 2 R_2 .

6.2.2 Langmuir probe

Acquisition To validate the CRM predictions, we compared them with measurements from Langmuir probes. The measurements were purposefully placed in the far plume at a distance $x = 6$ cm from the plasma source to minimize the effect of the magnetic field on Langmuir probe characteristics. The measurement setup involved conducting 15×10 scans along both the z - and y -axes, thereby creating a 2D spatial map of both the electron temperature, T_e and the electron density, n_e , at that $x = 6$ cm. The Langmuir probe consists of two tungsten wires, each with a diameter of $75 \mu\text{m}$, which are inserted into a ceramic tube. One wire serves as a reference probe, while the other serves as the measuring probe. The probe is mounted on a movable arm to allow scans in both z and y directions at a fixed x . The data acquisition was conducted using the Multifunction Plasma Probe Analyzer (MFPA) from Plasma Sensors. After each voltage scan, both a cleaning cycle and a heat cycle were performed to mitigate surface contamination and any effects it may have on the measurements.

The EEPF were extracted using the Druyvesteyn method, as elaborated by [Godyak 2021, Godyak & Demidov 2011]. This method involves taking the second derivative of the current-voltage ($I - V$) characteristic curve concerning the bias voltage, which is mathematically represented by Eq. (6.1):



(a) Schematics of the probe placed in front of the thruster. (b) Typical EEPF measured at $y = -5$ cm (peripheral) and $y = -1$ cm (near the center).

Figure 6.9: Schematics of the Langmuir probe measurements geometry. The probe is placed at a fixed $x = 6$ cm and is able to move in the $y - z$ plane.

$$f_e(E) = \frac{4}{e^2 A} \sqrt{\frac{mV}{2e}} \frac{d^2 I}{dV^2} \quad (6.1)$$

Here, A denotes the area of the probe tip, m represents the electron mass, e is the elementary charge, and V is the plasma potential. The resulting n_e and T_e values are then calculated by taking the zeroth and first moments of the measured EEDF, as given by Eqs. (6.3):

$$n_e = \int f_e(E) dE \quad (6.2)$$

$$T_e = \frac{2}{3n_e} \int E f_e(E) dE \quad (6.3)$$

Reliability of the measurements of the EEPF To ensure the reliability of the measurements, several precautionary measures were set. First, care was taken to avoid saturation of the current, as this would distort the $I - V$ characteristics. Second, given the size of the chamber, we verified a stable return of the current, mitigating potential inaccuracies arising from charge imbalance. Third, the effects of temporal fluctuations were averaged out to improve the signal-to-noise ratio. Additionally, validation checks were performed at both the beginning and the end of each scan to assess the consistency of the measurements. Also, the value of T_e was checked in both directions after each scan by interchanging the reference

and measuring probe to verify that anisotropies induced by the magnetic field are negligible at $x = 6$ cm, i.e. $T_{e,\parallel} = T_{e,\perp}$. It is worth noting that closer to the center of the chamber, the plasma exhibited more fluctuations and higher temperatures, making it challenging to obtain measurements.

Then, to verify the quality of the measurements, two primary criteria were checked. The first is the capture of low-energy electrons. These electrons are essential for the electron density n_e and temperature T_e . Specifically, an **EEPF** measurement is considered acceptable when $\delta_E < T_e$ where δ_E is the energy at the peak of the measured **EEPF**. The second criterion concerns the dynamic range, which needs to be large enough to capture high-energy electrons that are responsible for inelastic processes like excitation and ionization. A dynamic range exceeding 10^3 is recommended for high accuracy.

The measured **EEPFs** are obtained by averaging over a thousand **EEPF** measurements. All **EEPF** measurements guaranteed a dynamic range between $10^{1.5} - 10^4$, which still allowed to resolve the tail of the **EEPF** responsible for excitation and ionization up to 13 eV in the worst cases. The first criterion was harder to ensure since low energy electrons were more difficult to resolve in our discharge due to plasma fluctuations, however, we were able to ensure $\delta_E < 0.8T_e$.

Correction of the **EEPF and uncertainties** After these measurements, a correction was applied to adjust for the depletion of the **EEPFs** at low electron energies. Given that the **EEPF** tends to be Maxwellian for energies below the xenon's first excitation energy (8.32 eV), we fitted the measured **EEPF** to a Maxwellian distribution between the measured electron temperature T_e and 8.32 eV, as depicted in Figure 6.9b. The fitted curve was then extrapolated to zero energy, enabling the recalculation of n_e and T_e from the corrected **EEPFs**. Figure 6.10 shows the corrected n_e and T_e values obtained after correcting the low electron energy region of the **EEPF** (green) compared to raw values without this correction (blue). We can see significant adjustments are observed especially at high electron energy with the correction lowering the electron temperatures but increases the electron density as expected. Uncertainties were assumed to be dominated by random error. To assess the instrument calibration and uncertainties, measurements were taken five times at a reference position $y = -5$ cm across all z positions. The error bars reported here correspond to a 2σ confidence interval based on the standard deviation of the repeated measures for each position z after the **EEPF** correction. As a result, the average estimated uncertainties are ± 0.3 eV for the electron temperature T_e and $\pm 4 \times 10^9$ cm $^{-3}$ for the electron density n_e . It is worth noting that the uncertainty values are higher near the center of the plasma, approximately ± 0.4 eV for T_e and $\pm 4 \times 10^9$ cm $^{-3}$ for n_e , accounting for about 12% of their respective mean values.

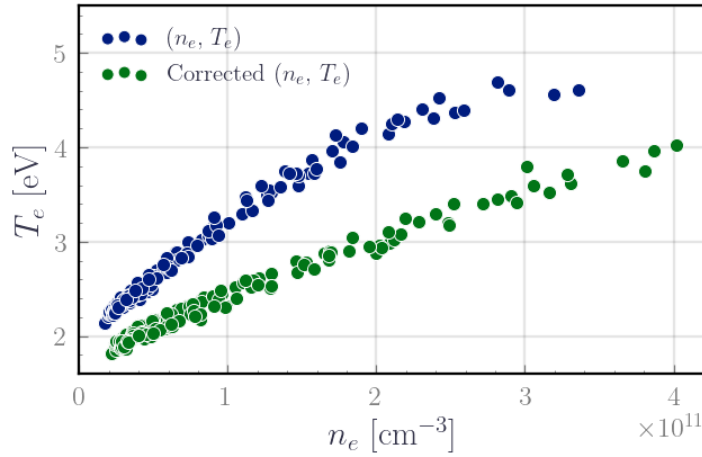


Figure 6.10: Comparison of the electron temperature and density before and after the correction at low electron energy of the **EEPF**. Compensating for the depletion of the **EEPF** at low energy results in increasing the electron density and reducing the electron temperature.

Chapter conclusions

The experimental setup offers three access points to a **SPT** like **HET**. Two optical access: Configuration 1, which scans the plume axially (from the exit plane of the thruster to the far plume) and laterally (from bottom to top), and Configuration 2, which offers a radial view of the thruster (direct front view of the thruster’s annular channel). Additionally, there’s a third access, perpendicular to the thruster and facing Configuration 1, dedicated to Langmuir probe measurements. This will be used to compare Langmuir probe results with predictions from **OES** and **CRM**.

Our setup deviates from standard **HET** testing conditions, operating under high flow and increased back pressure. This necessitated a re-characterization of the thruster regimes. The thruster’s $I - V$ characteristics align with existing **SPT** literature, with an ionization branch, a negative resistance branch, a nominal operation plateau, and a subsequent increase of the current. This characterization will help us steer regime-specific observations. For the calibration of the diagnostics, we primarily used relative methods for optics, while probe calibration was done via the **MFPA** software while respecting the guidelines ensuring measurement validity and accuracy. Chapter 7 will look into the results and discussion of our findings.

Results Langmuir probes, OES and HETOD

*Solen skiner, vardagslivet går sin gilla gång, arbetarnas
bullen stämmer sinnena till glädje. Det är i sådana ögonblick
som upprorsmodet stegrar sig, och som man slungar sin ut-
maning, sina tvivel mot himmelen.*

August Strindberg, *Inferno*

Contents

7.1	Langmuir probe results	140
7.1.1	Structure of the plume	141
7.1.2	Isentropic expansion	143
7.2	Emission spectra results	144
7.2.1	Lateral OES measurements results	144
7.2.2	Axial OES measurements results	145
7.2.3	Radial OES measurements results	149
7.3	Coupling the CRM with experimental spectra	152
7.3.1	Relating the spectral measurement to CRM output	153
7.3.2	Relating spectral measurements to CRM inputs	153
7.3.3	Relating Langmuir probes measurements to CRM predictions	155
7.3.4	Validating the CRM with Langmuir probe measurements	157
7.4	CRM results	159
7.4.1	Axial scan of the plume	159
7.4.2	Radial scan of the plume	160
7.5	Discussion	164
7.5.1	Impact of the optimization method	164
7.5.2	Gas density variation	165
7.5.3	Electron temperature dynamics	168
7.5.4	Preliminary insights from PIC simulations vs. experimental results	168

Introduction

In the preceding chapter, we detailed the experimental setup (Figure 7.1). Here we shift the focus to the presentation and analysis of the results. The chapter begins with an analysis of the Langmuir probe results, which is then validated against the CRM. Sections 2 and 3 provide preliminary insights from the OES and Langmuir probes. In Section 4, we elucidate the methodology that uses HET0D to correlate optical emissions with plasma parameters. Subsequent sections delve into the results obtained from integrating the CRM with the OES, emphasizing their alignment with Langmuir probe data and their implications in both axial and radial contexts. We conclude the chapter by evaluating the predicted plasma parameter profiles.

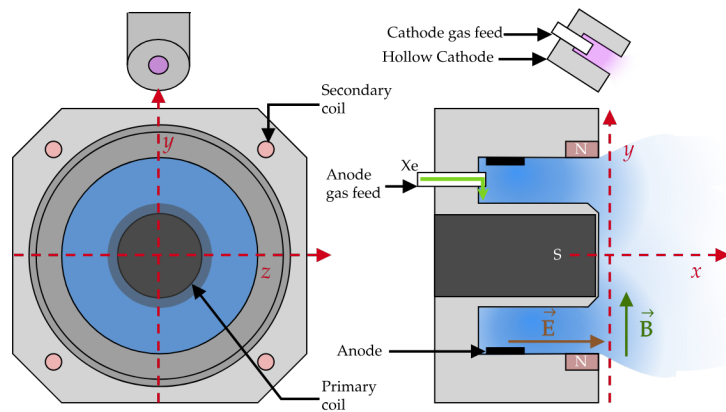


Figure 7.1: Front view (left) and lateral view (right) of the PPSX00-CHEAP Hall-Effect Thruster. The origin $(0, 0, 0)$ is defined at the intersection of the thruster's axis and its exit plane.

7.1 Langmuir probe results

The Langmuir probe measurements were carried under the following operating conditions: voltage 110 V, anode flow rate $q_a = 2.5 \text{ mg}\cdot\text{s}^{-1}$, and cathode flow rate $q_c = 0.4 \text{ mg}\cdot\text{s}^{-1}$. These conditions correspond to a nominal operating regime III as per the $I - V$ characteristics in Figure 6.5.

Figure 7.2 shows the EEPF results at different radial positions z at a constant lateral position (height) $y = -1 \text{ cm}$ (near the axis of the thruster) for $x = 6 \text{ cm}$. The EEPF is Maxwellian before the first excitation energy threshold of xenon which is consistent with previous axial probe measurements in HET [Dannenmayer & Mazouffre 2013, Dannenmayer *et al.* 2014]. Beyond the first excitation energy threshold, the EEPF tends to exhibit a two-temperature Maxwellian shape up to the ionization energy, evidenced by the change of the slope. After the

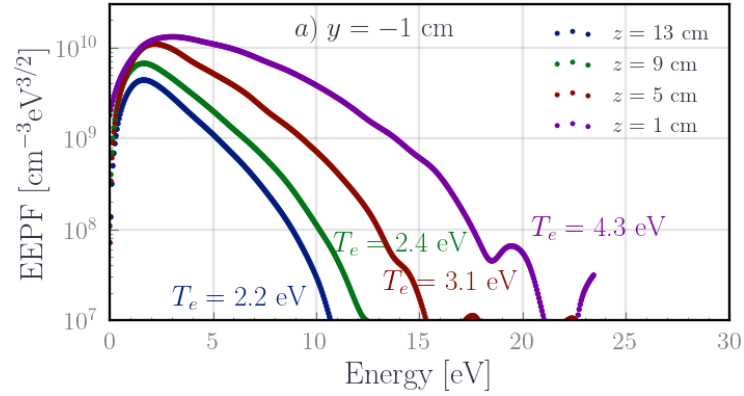


Figure 7.2: The measured EEDF at different radial positions z at $y = -1$ cm and $x = 6$ cm within the thruster's plume.

ionization threshold, the electron population is depleted. This depletion occurs at higher energies closer to the center. This is different from the PIC results which do not show a depleted electron population at high energy (cf Figures 5.7 and 5.8), highlighting the limitation of the current PIC setup to model the far plume.

7.1.1 Structure of the plume

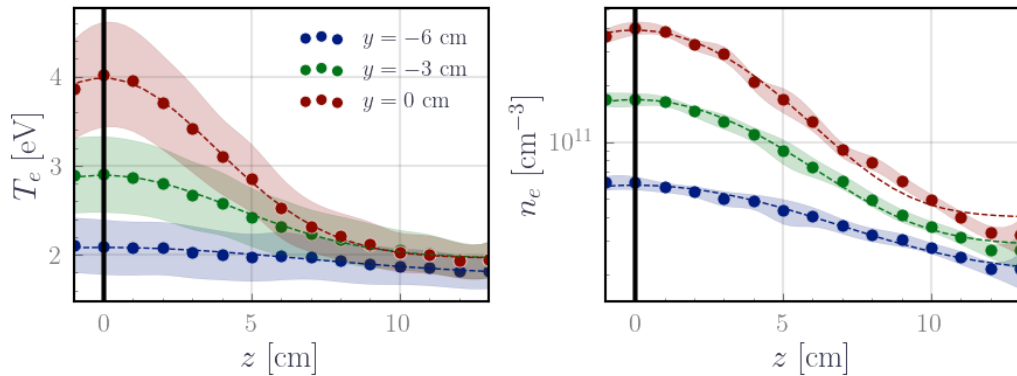


Figure 7.3: Radial profiles of electron temperature and density after the processing of the EEDF at three different lateral positions at $x = 6$ cm. Higher values are observed near the thruster axis, diminishing towards the plume's periphery. The dashed line represents the Gaussian fit to the data.

Figure 7.3 shows the radial profiles of the electron temperature and density at three different lateral positions. The plasma parameters have higher values close to the thruster axis and taper off towards the plume's periphery. Figure 7.4 presents a 2D map derived from the Langmuir probe measurements, portraying a hot core near the axis that cools down as we move towards the chamber walls which is characteristic of an expanding plasma. Under the assumption of an expanding

quasi-neutral ion beam with a Gaussian profile, the beam density profile can be modeled as:

$$n_e = n_{e0} \exp\left(-\frac{z^2 + y^2}{2R^2}\right) + c_{n_e}, \quad (7.1)$$

$$T_e = T_{e0} \exp\left(-\frac{z^2 + y^2}{2R^2}\right) + c_{T_e}, \quad (7.2)$$

where R denotes the beam waist. The constants c_{n_e} and c_{T_e} are introduced as background constants to facilitate the curve fitting. We can fit these expressions to the profiles obtained from the Langmuir probe measurements which are represented by the dashed lines in Figure 7.3. This suggests that these temperature and density profiles can be approximated well with a Gaussian beam structure at the far plume with a waist $R \approx 3.5$ cm. The radius of the beam r at 2σ can be approximated with $2R = 7$ cm.

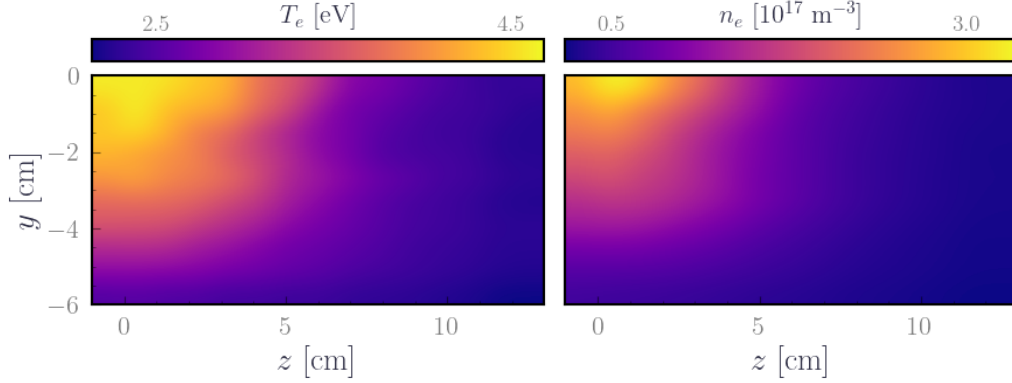


Figure 7.4: 2D map depicting the spatial distribution of electron temperature and density derived from the Langmuir probe measurements at $x = 6$ cm. A hot core near the thruster axis that cools while advancing toward the chamber walls is shown. The 2D image was smoothed using a 2D Gaussian filter.

In [Parks & Katz] and [Goebel & Katz 2008], the beam expansion was studied with a simple model, albeit under an isothermal temperature assumption which is not valid based on the T_e measurements. The model assumes a quasi-neutral electric field and solves the ion continuity and momentum equations without an ionization term. The beam was assumed to be Gaussian and is modeled by introducing a time-dependent function h such that the time-dependent beam waist is expressed as $r(t) = R_0 h(t)$ with R_0 being the initial waist of the beam at the exit plane. The complete derivation can be found in the work of [Goebel & Katz 2008, Parks & Katz]. The practical feature of the solution is that it is self-similar, requiring only the knowledge of a profile front to reconstruct the profile propagation. This enables the estimation of the ion velocity from the experimental measures. In the absence of the initial radial velocity of the ion beam, h can be approximated by:

$$h(\tau) \approx 1 + 0.6524\tau + 0.0552\tau^2 - 0.0008\tau^3$$

where $\tau = \sqrt{2} \frac{v_b}{R} t$ with v_b being the Bohm velocity and $t = v_x x$ with v_x as the axial velocity of the beam. We can assume that the initial beam waist corresponds to the annular chamber radius i.e. $R_0 = 5.2 \text{ cm}/2 = 2.6 \text{ cm}$. Based on the previous fit to a Gaussian beam, the product $h(\tau)R_0$ is 3.5 cm at $z = 6 \text{ cm}$, allowing us to solve $h(\tau)$ for 3.5/2.6 and get the value of τ . Then using the electron temperature at the center to calculate the Bohm speed, we can extract from τ the value t , the time required to propagate from the initial front at the exit plane of the thruster to $z = 6 \text{ cm}$. From there, we can estimate the speed $v_x = 4.8 \text{ km.s}^{-1}$, which falls within a correct order of magnitude. A more accurate model would necessitate simulations. Nonetheless, these profiles appear to provide a compelling fit for a preliminary and simple description of the structure of the plume for both n_e and T_e .

7.1.2 Isentropic expansion

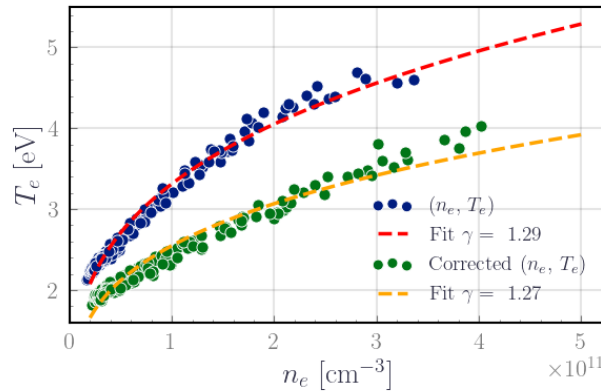


Figure 7.5: Plot of electron temperature as a function of electron density. The points are fitted to an isentropic expansion with an exponent $\gamma = 1.29$ (red dashed curve).

The Gaussian profile of T_e shows clearly that the far-field plume is not isothermal in the radial direction. We can investigate simple adiabatic expansion models, similar to [Dannenmayer & Mazouffre 2013]. Under the assumption of laminar flow, the plasma expansion can be deemed adiabatic. In this case, the state equation for the electron can be fitted to a polytropic relation such as:

$$\left(\frac{n_e}{n_{e0}} \right)^{\gamma-1} = \frac{T_e}{T_{e0}},$$

Here, γ corresponds to the specific polytropic exponent, and T_{e0} and n_{e0} are reference electron temperature and density. We chose the reference value to c_{T_e} and c_{n_e} found from the fit to the Gaussian profile earlier. Figure 7.5 portrays the electron temperature as a function of the electron density, before the correction of EEDF at low energy (in blue), illustrating that the data are well fitted with an isentropic expansion with an exponent $\gamma = 1.29$. This coefficient falls in the range of values found in [Dannenmayer & Mazouffre 2013] ($\gamma = 1.37$ for the PPS-100 and $\gamma = 1.18$

for the PPS-1350). Note that using the corrected values of n_e and T_e yields a coefficient of 1.27. However, the fit is not as good and it is probably due to the Maxwellian correction of the EEDF at low electron energy.

7.2 Emission spectra results

In this section, the emission spectra acquired from the OES experiment across the lateral, axial, and radial scans are analyzed. The investigation is structured as follows: the operating conditions are specified initially, followed by an exploration of the raw spectra along the scanned axes. Two specific regions in the spectra are investigated-500 nm to 750 nm, which houses multiple ionic lines, especially at 540 nm, 597 nm and 604 nm, yielding information about the singly ionized xenon ion, and 750 nm to 1100 nm encompassing lines from the $6p$ levels, providing information about the xenon atom excited states. Among the 15 neutral lines identified from the $6p$ levels, 7 representative lines are reported in the figures to illustrate the spatial gradients in the intensity profiles.

7.2.1 Lateral OES measurements results

The lateral OES measurements (Configuration 1 of Figure 6.6) were simultaneously conducted with Langmuir probes measurement at the same operating conditions ($U_a = 110$ V, $q_a = 2.5$ mg.s⁻¹, and $q_c = 0.6$ mg.s⁻¹). The fiber was pointing at the tip of the probe during the acquisition. Looking at Figure 7.6, the emission line intensities show a significant variation along the lateral direction y which is in line with the variation in the electron density and temperature variations observed in Langmuir probes results. Notably, all lines peak at the thruster's center, $y = 0$ as expected. Additionally, a secondary peak appears at $y = 3$ cm, which might be attributed to the increase in n_e due to the thermionic emission of the cathode. This was not observed in the Langmuir probe measurement since the measurements were limited to the lower half of the thruster.

Diving deeper into the spectra, Figure 7.7 presents the emission spectra at three characteristic positions:

- The peripheral lower region, ($y = -5$ cm), showing some faint neutral lines between 750 nm to 1100 nm and faint ionic lines between 540 nm to 750 nm reflecting lesser ionization.
- The plume's center, ($y = 0$ cm), showcasing a mix of ionic and neutral lines.
- The peripheral upper region, near the cathode ($y = 3$ cm), where neutrals dominate again.

The reduced intensity of the ionic lines near the cathode might be explained by the nature of the electrons emitted from the cathode. Indeed, the emitted electrons from the hollow cathodes are not very energetic [Potrivitu *et al.* 2019]. Thus, they mainly contribute to neutral excitations rather than ionization.

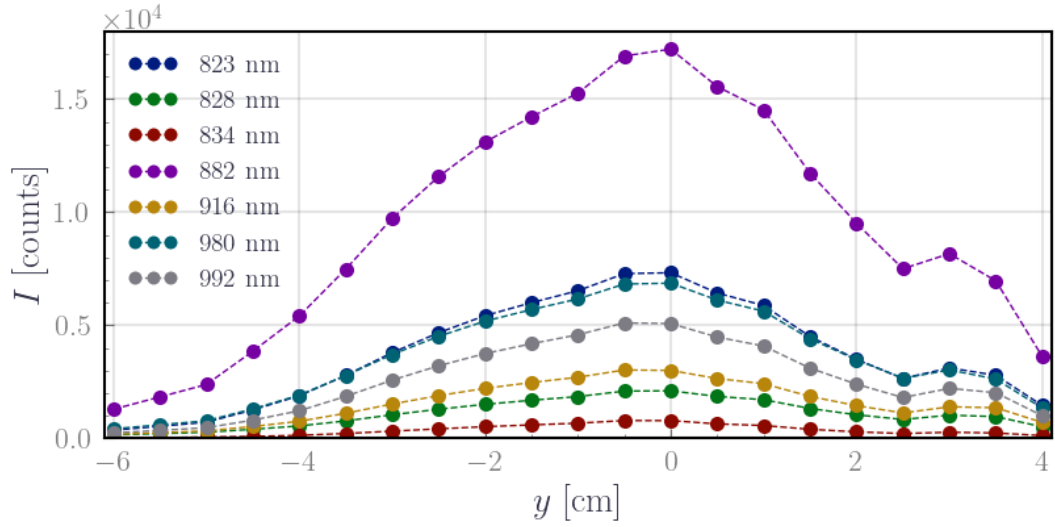


Figure 7.6: Evolution of line intensities in the lateral direction along the y axis (Configuration 1 of Figure 6.6).

7.2.2 Axial OES measurements results

This section presents the OES measurements in the axial direction. The optical setup is in Configuration 1 and the operational conditions for the axial scans are summarized in Table 7.1. The unmarked cells represent positions where the thruster failed to ignite or exceeded a power of 1 kW, which was a threshold we chose to avoid overheating the thruster's ceramics. The explored voltages depict two distinctive operational regimes: Regime III ($U_a = 100$ V) and Regime IV ($U_a = 150$ V and 200 V). The integration time was set to 2 ms for all the investigated conditions.

Table 7.1: Operational parameters for axial scan analysis

Voltage	2 mg.s ⁻¹	2.5 mg.s ⁻¹	3 mg.s ⁻¹
75 V			×
100 V	×	×	×
150 V	×	×	
200 V	×	×	

As illustrated in Figure 7.8, the emission line intensities systematically decrease as we move away from the exit plane of the thruster for both neutrals and ions, with ionic lines fading faster than the neutral lines. At $x = 2.5$ cm, intense ionic lines are observed, which rapidly decrease in intensity as the plume expands farther from the exit plane. This trend suggests a decrease in singly ionized excited species within the plume, which might be attributed to the sharp decrease of the electron temperature along with the plume expansion.

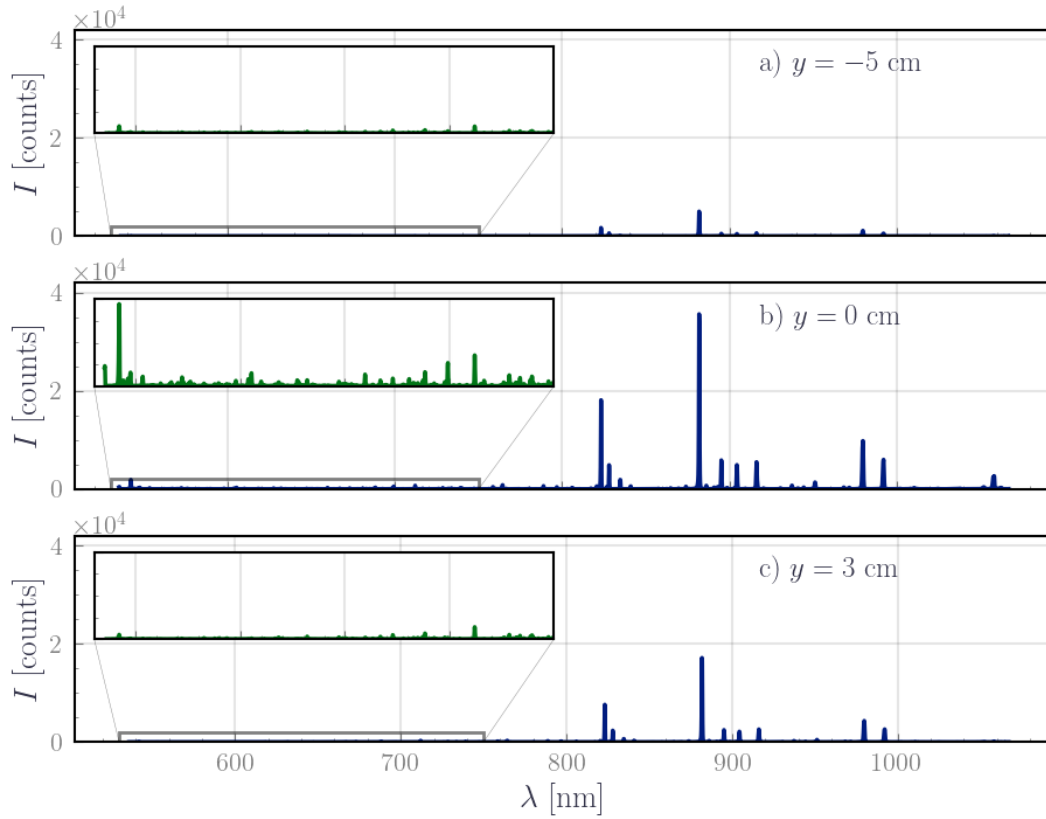


Figure 7.7: Comparison of ionic and neutral emission lines at three distinct lateral positions: peripheral ($y = -5$ cm), plume center ($y = 0$ cm), and near the cathode ($y = 3$ cm) in Configuration 2 of Figure 6.6.

Figure 7.9 shows the spatial evolution of the emission lines along the axis. As observed, the intensity of the emission lines initially experiences a slight decrease before reaching $x = 2$ cm, then sharply increases at $x = 2.5$ cm, and subsequently declines. These variations were also observed in previous experimental work by [Leray & Bretagne 1997], although they were not elaborated.

The low emission intensity on the two first points is associated with the cylindrical collection area being partially obstructed by the thruster's edge. For the measurements between 1 cm to 2 cm, the collected signal is weak but is decreasing. We can suggest several hypotheses here. First, the annular form of the exit plane might create a rarefied density pocket where the neutral density is lower hence resulting in lower neutral emission intensity, near the center of the thruster. This hypothesis is not corroborated by the results of axisymmetric simulations in HET plume, for instance, in the work of [Domínguez Vázquez 2019]. Indeed, the simulations showed a negligible difference in the neutral density between the exit of the annular channel and the center of the thruster. A second possibility is to say that the initial drop in the neutral lines intensity is indicative of a depletion in the neutral density, due to ionizing collisions, thanks to the hot electron temperatures,

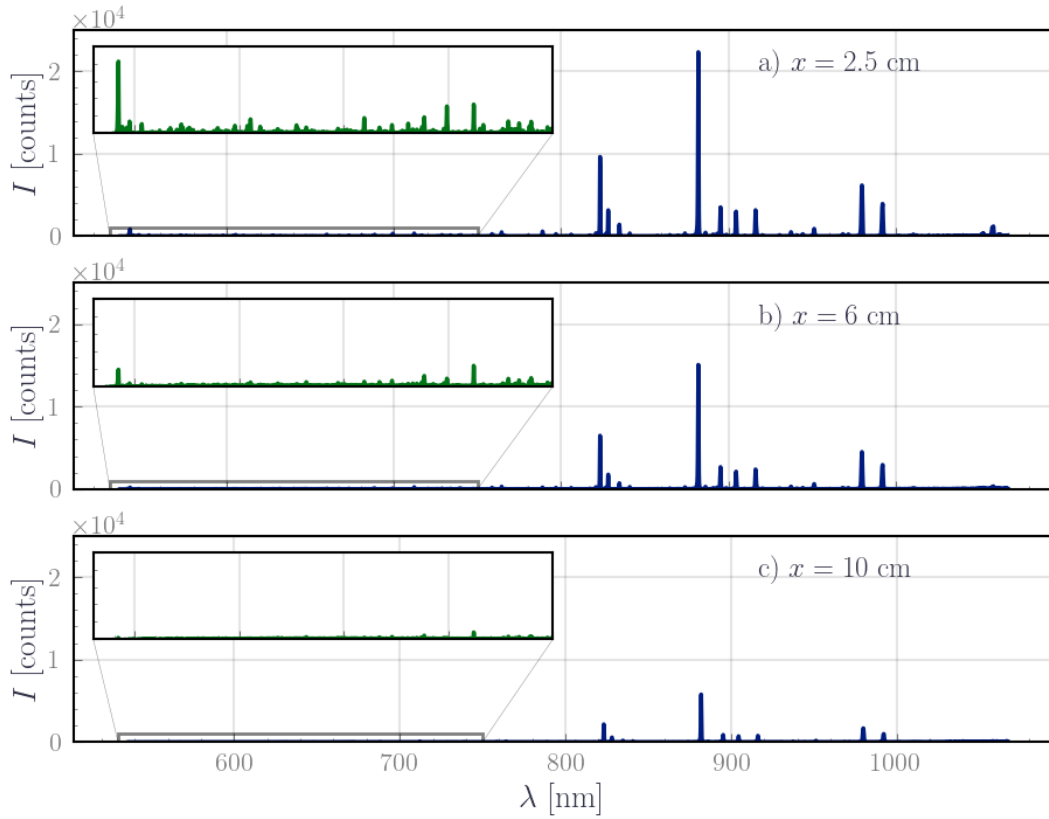


Figure 7.8: Spectra along the thruster’s axial direction in Configuration 1 of Figure 6.6.

the high electron densities, and the energetic ion beam near the exit plane. Thereby neutral atoms are expected here, which favors a decrease in the neutral emission. This might be true since the ionic emission between 1 cm to 2 cm is increasing and might reflect also a higher ion density. This possibility can be verified with results from the CRM. In any case, the decrease in the neutral emission requires further analysis.

We look at the subsequent increase in the detected intensities at $x = 2.5$ cm. Reasons for this dwell either in an increase in the electron temperature or the electron density. Since the plume is expanding and in the process, the electron temperature is decreasing, the most plausible explanation is then an increase in the electron density. The location of $x = 2.5$ cm is approximately where the cathode is placed. This favors that the increase in the neutral emission is related to the enhancement of the electron flux due to the proximity to the cathode. This is to be confirmed with trends from the CRM. The subsequent decline in the intensity within the plume, after 2.5 cm may be attributed to either a decrease in the electron temperature relative to the channel or a decrease in the electron density or both.

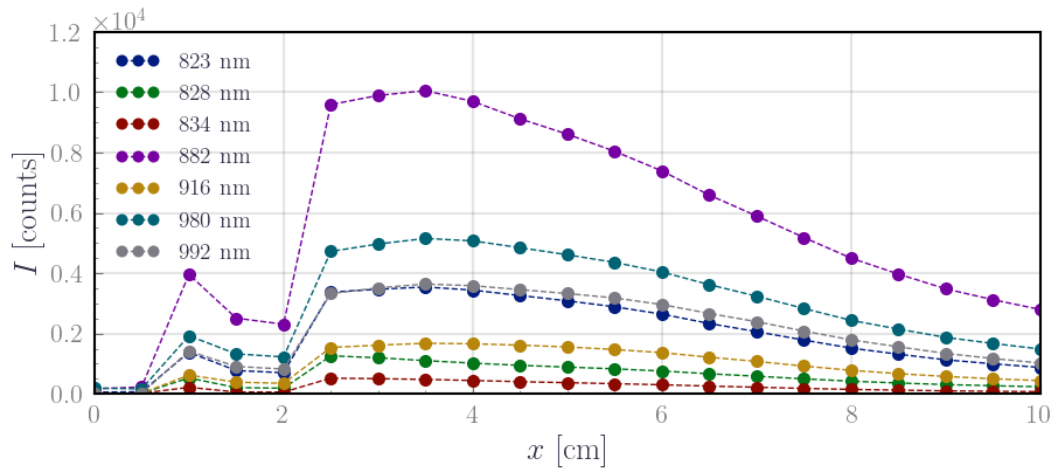


Figure 7.9: Spatial evolution of emission lines intensities along the axial direction.

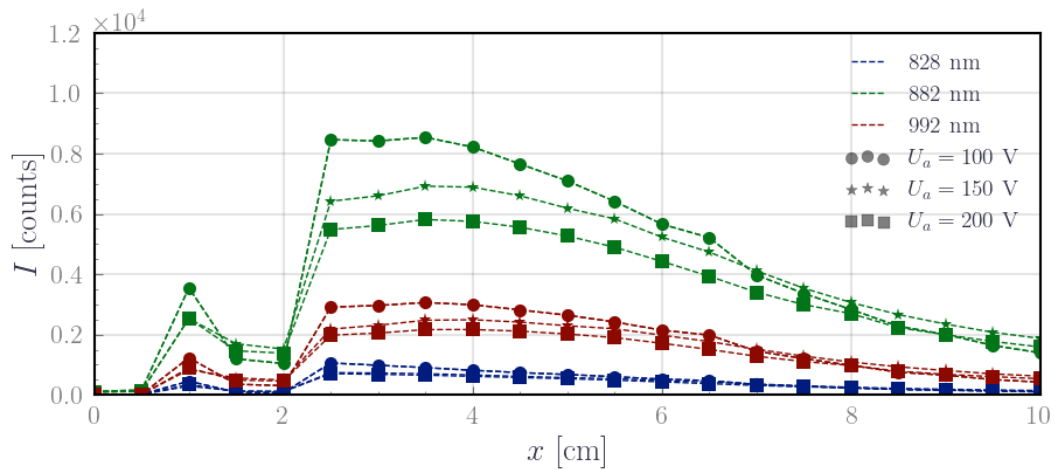


Figure 7.10: Effect of the anode voltage on the intensity of selected emission lines.

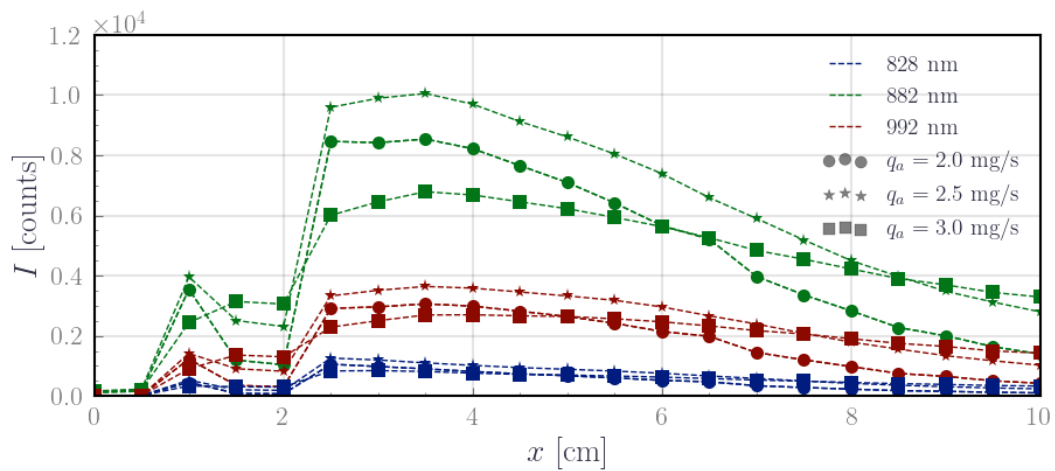


Figure 7.11: Effect of the anode flow on the intensity of selected emission lines.

Impact of the voltage variations on axial emission spectra Figure 7.10 illustrates the effects of the voltage on the gradient of three emission lines at 828 nm, 882 nm and 992 nm at a constant anode flow $q_a = 2.5 \text{ mg.s}^{-1}$. These curves are representative of all examined flow conditions. First, spanning from $x = 1 \text{ cm}$ to $x = 2 \text{ cm}$, neutral lines show a weak sensitivity on the voltage rendering the trends in this region challenging to interpret. Second, from $x = 2.5 \text{ cm}$, the neutral emission decreases with increasing voltage. Third, at $x = 7 \text{ cm}$ is characterized by a weak sensitivity to the voltage.

Impact of the flow variations on axial emission spectra Figure 7.11 presents the evolution of the same three emission lines with the flow rate while maintaining a constant voltage of 100 V. The operating regimes are Regime III and IV. The neutral emission intensity increases with the increased neutral density injected at the anode for 2.0 mg.s^{-1} and 2.5 mg.s^{-1} . However, there is a strange drop between 2.5 cm and 6 cm with a decrease in the neutral emission at 3.0 mg.s^{-1} . Although the inherent cause for this observation is difficult to deduce at this stage, we think that the drop at 3.0 mg.s^{-1} might be linked to the elevated background pressure influencing the plume dynamics or a non-detected decrease in the transparency of the viewport due to deposition since the measurements were not performed on the same day.

7.2.3 Radial OES measurements results

This section discusses the observations from the OES measurements in the radial direction. The optical setup is in Configuration 2 and the investigated conditions are summarized in Table 7.2. The explored voltages depict three distinctive operational regimes of the thruster: Regime I ($U_a = 85 \text{ V}$), Regime III ($U_a = 110 \text{ V}$) and Regime IV ($U_a = 150 \text{ V}$). The cathode injection was reduced to $q_c = 0.3 \text{ mg.s}^{-1}$. The $I - V$ characteristics shifted slightly with no change in the operating regimes. The integration time is 10 ms except for the $q_a = 3.0 \text{ mg.s}^{-1}$ condition, for which the integration time was set to 8 ms, because the emission was more intense.

Table 7.2: Operational parameters for radial scan analysis

Voltage	2 mg.s^{-1}	2.5 mg.s^{-1}	3 mg.s^{-1}
85 V	×	×	
110 V	×	×	×
150 V	×	×	×

Figure 7.12 shows the spectrum at three positions in the radial direction for $y = 0 \text{ cm}$, specifically at $z = 0 \text{ cm}$ corresponding to the center of symmetry of the thruster and $z = 2.35 \text{ cm}$, $z = -2.35 \text{ cm}$ corresponding to the annular channel. In the channel, very intense emissions are observed, notably the ones at 823 nm, 828 nm,

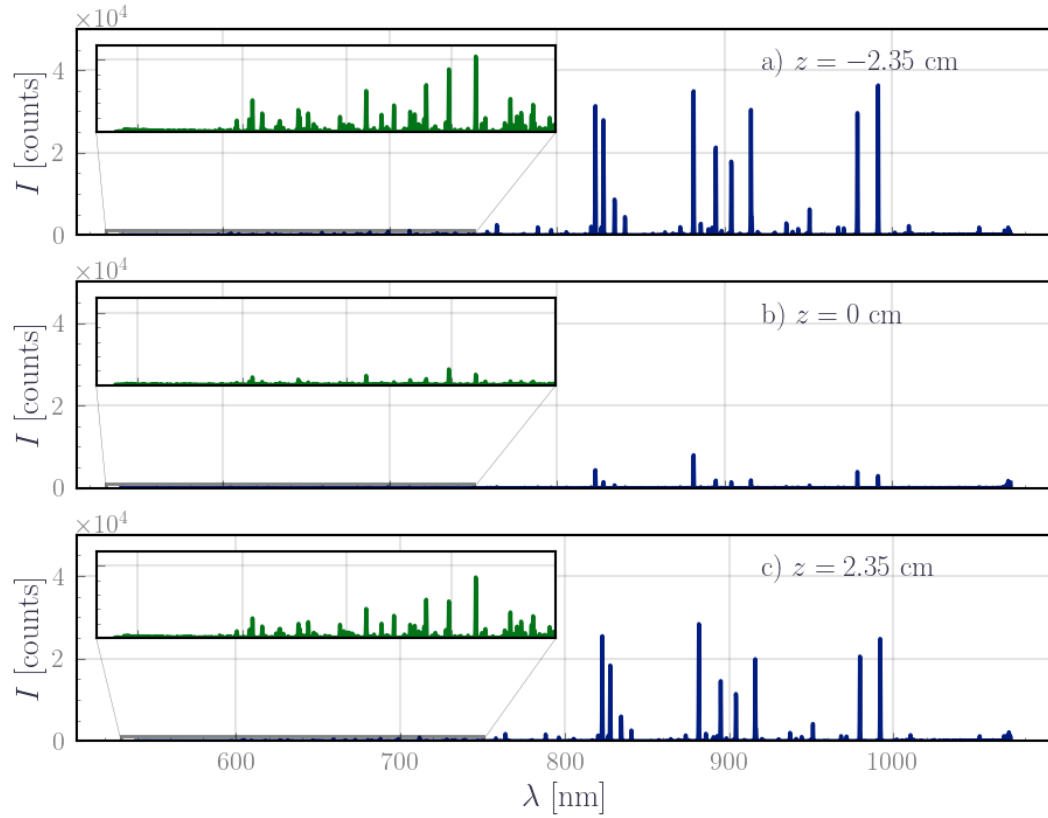


Figure 7.12: Emission spectra at different radial positions. The zoomed axes correspond to the 540 nm to 750 nm range containing several Xe^+ lines.

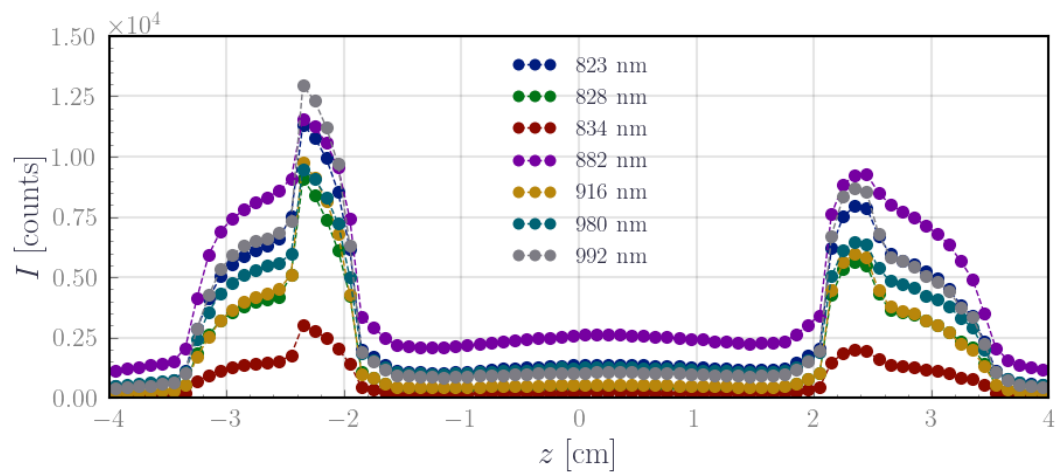


Figure 7.13: Spatial gradient of several neutral lines along the radial direction.

835 nm and 980 nm, especially when compared with the axial scan. The singly ionized xenon emission lines are also more intense within the channel, reflecting higher electron temperatures in the channel. However, the absence of the 540 nm line, apparent in the axial scan, is surprising, although the ion lines at 597 nm and 604 nm are identified. In the center of the thruster, the emission lines are systematically less intense.

Figure 7.13 shows the radial evolution of several neutral lines along the radial direction z , for $U_a = 110$ V and $q_a = 2.5$ mg.s⁻¹. The evolution of the line intensities is nearly symmetrical about $z = 0$ and mirrors the annular geometry of the channel. In particular, we observe an emission bulk between -3.5 cm to -2 cm and 2 cm to 3.5 cm. A secondary intensity peak near the internal wall at ± 2 cm might be attributed to the lateral gas injection positioned on the internal annular wall in SPT models. These features remain consistent across all operational conditions. The discrepancy between different operating parameters chiefly manifests in the line ratio reflecting changes in T_e for different operating conditions which is better explored using the CRM.

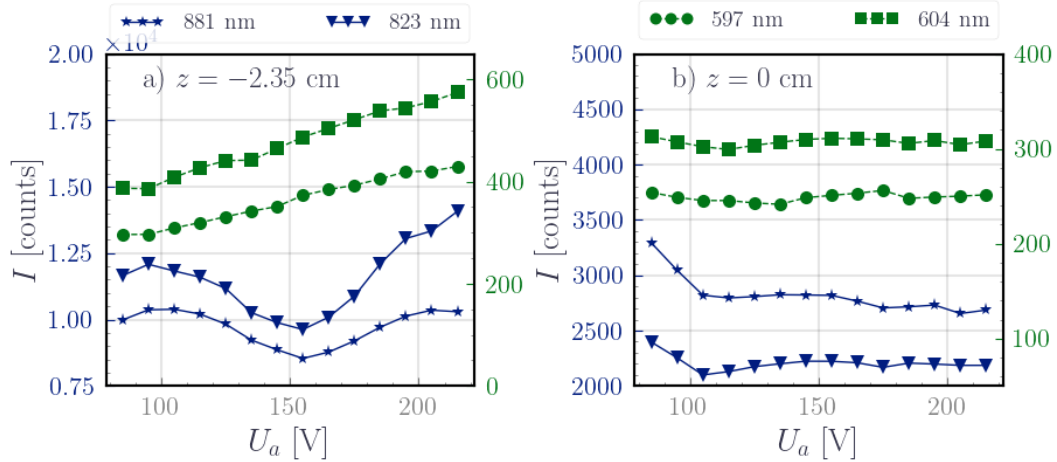


Figure 7.14: Intensity evolution of neutral and ionic lines at different radial positions, concerning the anode voltage: a) at $z = -2.35$ cm (inside the channel) and b) at $z = 0$ cm (center of symmetry of the thruster). In green are the 597 nm and 604 nm ion lines and in blue are the 881 nm and 823 nm neutral lines.

Impact of the voltage variations on radial emission spectra The radial evolution of the neutral emission lines is performed at a constant anode flow of $q_a = 2.5$ mg.s⁻¹ across Regime I, III, and IV. The fiber was pointed at two positions, $z = 0$ cm and $z = 2.35$ cm, and a voltage scan at the step of 10 V was performed to construct a clear voltage dependency in these regions. Figure 7.14 illustrates the evolution of the intensity of two neutral lines 823 nm and 881 nm (blue) and two ionic lines 597 nm and 604 nm in both the center of the thruster and in the channel.

In the channel at $z = 2.35$ cm, the neutral lines mimic the trends observed in the

thruster's $I - V$ characteristics, (Figure 6.5), indicating a relationship between the line intensities and the discharge current. This observation also suggests that the neutral lines from the channel are indicative of the operating regime of the thruster. On the other hand, the ions exhibit a consistent linear increase in intensity with the voltage. This reflects an increase of T_e with the voltage since the ionic lines are more sensitive to T_e . On the contrary, at the center of the thruster ($z = 0$ cm), the neutral lines exhibit a minor decrease before leveling off. The ion lines, however, remain constant across the voltage scan, indicating a different dependency on the voltage.

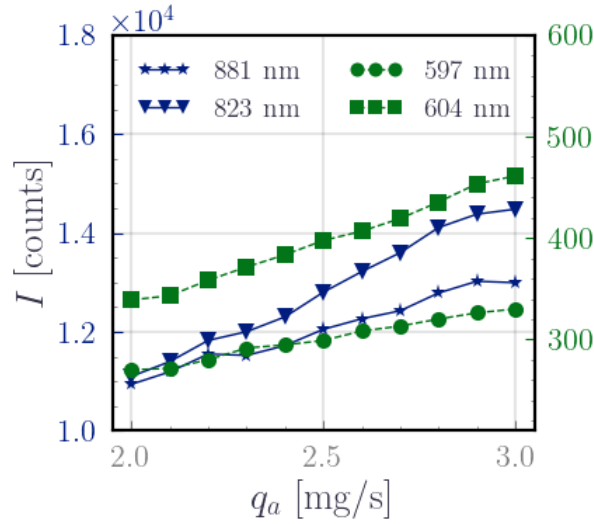


Figure 7.15: Intensity evolution of neutral and ionic lines in the channel, concerning the anode flow injection. In green are the 597 nm and 604 nm ion lines and in blue are the 881 nm and 823 nm neutral lines. Note the change in the line ratio which reflects the sensitivity to T_e .

Impact of the flow variations on radial emission spectra The same analysis is performed with a flow scan at a constant voltage $U_a = 105$ V (Figure 7.15). Lines intensities are linear with the injected flow in the channel. Note that the ratio of the two lines varies with the flow rate, probably because T_e varies.

7.3 Coupling the CRM with experimental spectra

The OES results were very difficult to interpret since the optical emission involves an interplay between all the plasma parameters. To extract a clear trend, we use the CRM to relate these observations to plasma parameters. In this section, we present how the measurements are related to the HET0D CRM to quantify the electron temperature and the electron density in the discharge in the lateral, axial,

and radial directions. The results of this coupling are reported in Section 7.4.

7.3.1 Relating the spectral measurement to CRM output

The CRM output and the measured spectra do not correspond to the same physical quantity. The CRM produces results that are homogenous to a radiant power in the unit $\text{W}\cdot\text{m}^{-3}$. In practice, the sensors on the spectrometers convert this quantity to irradiance, measured in $\text{W}\cdot\text{m}^{-2}$, corresponding to the energy flux detected. These quantities are related by geometrical parameters, including the distance from the source to the sensor, the sizes of both the source and the sensor, and the light path geometry. However, it is essential to note that all these geometrical factors can be eliminated when looking at line ratios or normalized line intensities.

Moreover, the spectrometer introduces some instrumental broadening effects to the spectra, impacting the spectral line intensity measurements. This broadening prevents the peak values from directly matching the CRM output, as they are not directly related to a radiant power but rather to a spectral density radiant power $\text{W}\cdot\text{m}^{-3}\cdot\text{m}^{-1}$. Given this, the choice leans towards determining spectral line intensity through integrated profiles rather than using the peak values.

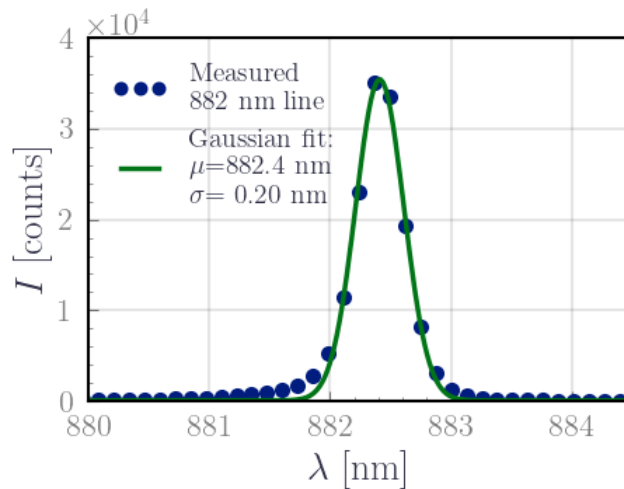


Figure 7.16: Gaussian profile fit of the 882 nm line

To this purpose, we fit each detected spectral line with a Gaussian profile. The instrument's resolution ensures that each line extends across approximately 5-6 pixels, providing greater reliability of the fit, as illustrated in Figure 7.16.

7.3.2 Relating spectral measurements to CRM inputs

Chapter 5 explored various methods to derive the electron temperature from synthetic emission spectra generated from PIC simulations. The analysis underscores the importance of accounting for the gradients in electron and gas density, n_e and n_g , to achieve sensible predictions of the electron temperature. Among the evaluated

methods, the 823/828 – 980/992 line ratios emerged as a promising candidate for predicting the temperature profiles, though its estimations in the plume were skewed high due to the overlooked neutral gas gradient. For the analysis of experimental spectra, we aim to improve the methodology by incorporating the gas density, thus expanding the set of investigated parameters in the parametric space to (n_e, T_e, n_g) .

The discussed methods in Chapter 5 can be formulated as optimization problems concerning one variable T_e when using line ratios curves, or two variables n_e and T_e in the case of the abacus method. Transitioning forward, the aim here is to formulate an optimization problem over the three variables (n_e, T_e, n_g) within the CRM:

$$\min_{(T_e, n_e, n_g)} E(I_{\lambda_{ij}}^{Exp}, I_{\lambda_{ij}}^{CRM}) \quad (7.3)$$

where E is the cost function involving the intensities of the CRM and the experimental OES and $I_{\lambda_{ij}}^{exp}$ and $I_{\lambda_{ij}}^{CRM}$ represent the observed and predicted line intensities, respectively, for each emission line under scrutiny.

Building upon the desired optimization framework, it is relevant to look first at the input variables defined in HET0D-CRM. Although initially presented with five input variables, Chapter 4 showed that the variables n_g , d , and T_g are dependent, with their impact being consolidated within a single parameter, $\kappa = n_g d \sqrt{M/2RT_g}$. Consequently, we can fix the optical length d to the line of sight's geometric length and assign the gas temperature to the typical PIC value, $T_g = 640$ K, leaving n_g as a free variable. In this description, n_g adopts the role of an "optical" gas density, including both the gas density variation and the optical length variation. This depiction is particularly apt given the non-cylindrical nature of the HET's plume and its varying optical depth along the axis. Such an interpretation of the varying n_g accounts for the spatial expansion of the plume and spatially dependent radiation trapping effects. All in all, the effective free parameters can be narrowed down to (n_e, T_e, n_g) within HET0D without any loss of generality.

The choice of the cost function E is instrumental in correlating the output of the CRM to the OES measurements. The chosen cost function E is the least square residual of the line intensities, normalized in $\|\cdot\|_2$. This is expressed as follows:

$$E(n_g, n_e, T_e) = \frac{1}{N} \sum_{\lambda_{ij}} \left(\frac{I_{\lambda_{ij}}^{Exp}}{\|I^{Exp}\|_2} - \frac{I_{\lambda_{ij}}^{CRM}}{\|I^{CRM}\|_2} \right)^2. \quad (7.4)$$

Now, the task is to determine the lines on which to perform the optimization. Aligning with [Karabadzak *et al.* 2006, Zhu *et al.* 2019] recommendations, our methodology uses multiple lines to foster robustness in the predictions. Initially, all lines in the NIR from the 6p levels will be included. The targeted xenon lines range from 764 nm to 1100 nm. This consists in 15 lines: 764.41 nm, 788.95 nm, 820.85 nm, 823.38 nm, 826.87 nm, 828.23 nm, 834.91 nm, 841.15 nm, 882.18 nm, 893.32 nm, 895.47 nm, 904.79 nm, 916.51 nm, 980.23 nm and 992.59 nm.

Finally, the minimization of the cost function between the observed experimental spectra to the model spectra extracts the most fitting plasma parameters

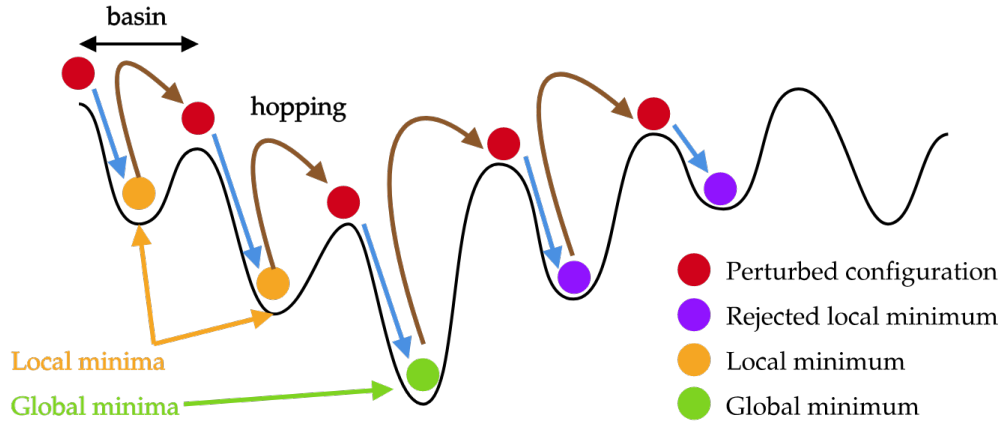


Figure 7.17: Schematic representation of the optimization process relating the CRM to the plasma parameters.

(T_e, n_e, n_g) . This is done by a stochastic basin-hopping optimization scheme to find the global minimum of the cost function over a given range of plasma parameters [Wales & Doye 1997]. It operates by combining a local minimizer, in this instance, a Nelder-Mead's simplex gradient descent algorithm, with stochastic jumps, "hopping" over basins to evade being trapped in local minima, such as it is illustrated in Figure 7.17, thereby enhancing the likelihood of locating the global minimum. Our implementation "hops" 100 times to enhance the likelihood of reaching the global cost function minimum. A successful result is registered when the same minimum is achieved in 10 consecutive iterations, indicating a reliable solution.

7.3.3 Relating Langmuir probes measurements to CRM predictions

To compare OES/CRM results with those obtained using Langmuir probes, one must account for the differences between these diagnostics. Specifically, OES/CRM integrates the plasma parameters along the line of sight, whereas Langmuir probes provide a local measurement. Achieving excellent agreement between these disparate techniques is usually challenging if not anecdotal [Boffard *et al.* 2018]. OES inherently tends to overestimate the electron temperature due to its sensitivity to higher excitation energies, while the Langmuir probe is more sensitive to low-energy electrons. Nevertheless, both diagnostics shall consistently reproduce the underlying trends in the plasma parameters.

To compare similar quantities, we define a "line-of-sight integrated" electron temperature T_e^{ls} . This quantity is derived by averaging the electron temperature along the line of sight weighed by the electron density, in such a way that the light collected from the detector, I_λ , can be expressed as:

$$I_\lambda = K [T_e^{ls}] n_e^{ls} n_{gs} \quad , \quad (7.5)$$

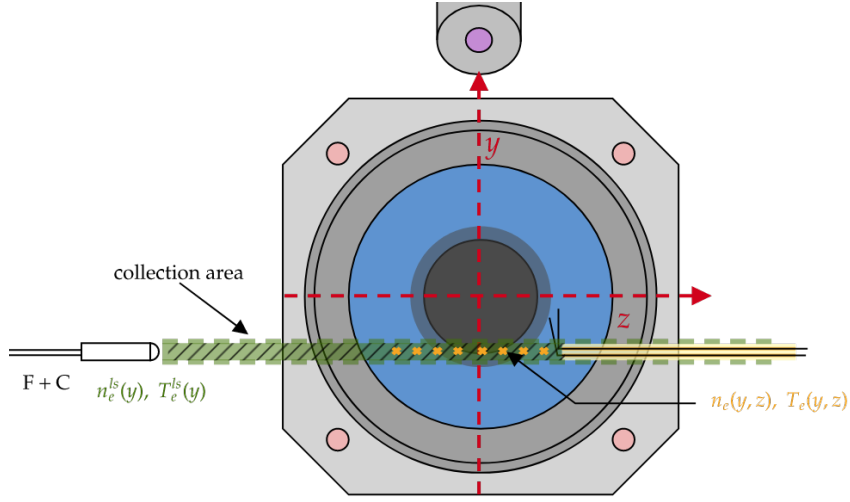


Figure 7.18: Illustration of the Langmuir measurement comparison to the OES. Each measurement with OES corresponds to 15 measurements (yellow) with a Langmuir probe along the line of sight (green).

where n_e^{ls} and n_{gs} are the volume averaged electron density and ground state density within the light collection volume.

To determine the expression of T_e^{ls} and for the sake of simplicity, we assume that the radiative levels are populated through electron impact excitation from the ground state and are depopulated radiatively. We also assume that the gas density is constant along the line of sight. A fiber is placed at an axial position (x, y) and is pointing at the tip of the Langmuir probe where measurements are conducted, as illustrated in Figure 7.18. The light collection area is assumed cylindrical thanks to the use of a collimator in Configuration 1 and we neglect the impact of absorption. Let an emission line originate from an excited level at the position (y, z) in the plume. At steady-state, the line intensity $I_\lambda(y, z)$ emitted at a position (y, z) can be expressed as:

$$I_\lambda(y, z) = K[T_e(y, z)] n_e(y, z) n_{gs}$$

where K is the electron impact excitation rate coefficient and n_{gs} is the ground state number density. In absence of absorption, the collected light intensity $I_\lambda(y)$ from the detector becomes :

$$I_\lambda(y) = \int_z K[T_e(y, z)] n_e(y, z) n_{gs} dz. \quad (7.6)$$

Upon assuming that the rate coefficient K follows the Arrhenius law $K = K_0 e^{-E_a/T_e}$ with E_a and T_e expressed in eV, and equating Eq. (7.6) with Eq. (7.5), we arrive at:

$$e^{-E_a/T_e^{ls}} = \frac{1}{n_e^{ls}} \int_z e^{-E_a/T_e(y, z)} n_e(y, z) dz.$$

Consequently, the "line-of-sight integrated" electron temperature T_e^{ls} can be expressed as:

$$T_e^{ls}(y) = \frac{E_a}{-\log\left(\frac{1}{n_e^{ls}} \int_z e^{-E_a/T_e(y,z)} n_e(y,z) dz\right)}. \quad (7.7)$$

Although our model considers a simple one-dimensional line of sight and a single excited level, it suggests that Eq. 7.7 offers a more accurate basis for comparison between Langmuir probes and OES/CRM than a straightforward arithmetic average. To account for multiple excited levels in our model, we adjust E_a to E_a^{ls} , the average excitation energies of the relevant levels.

7.3.4 Validating the CRM with Langmuir probe measurements

In this section, we apply this methodology to validate results from both the lateral OES scans and Langmuir probe measurements. Recall that these were conducted at the same operating conditions ($U_a = 110$ V, $q_a = 2.5$ mg.s⁻¹, and $q_c = 0.6$ mg.s⁻¹). The goal is to validate the CRM capabilities in reflecting the electron temperature.

The optimization was performed on the lateral scan data obtained from the OES. For the optimization, T_e varied between 1 eV and 7 eV, n_e varied between 1×10^{14} m⁻³ to 1×10^{18} m⁻³, and n_g varied between from 1×10^{17} m⁻³ and 1×10^{22} m⁻³, while d was fixed at 12.5 cm and T_g at 640 K.

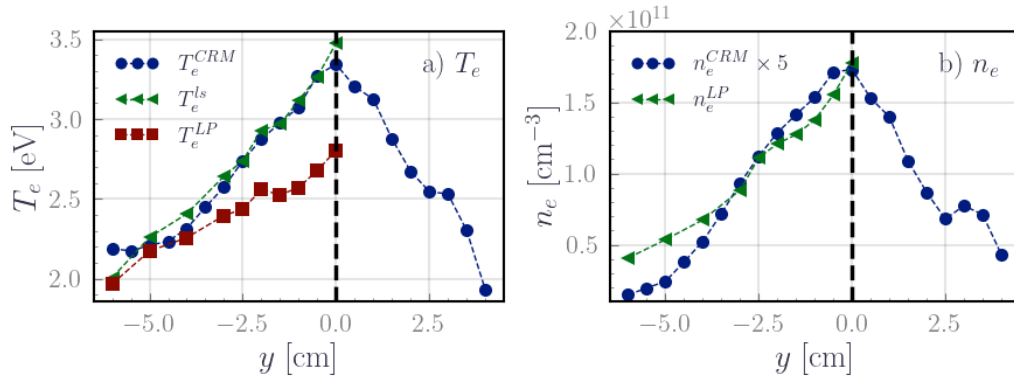


Figure 7.19: Lateral profiles of the electron temperature and density as determined by Langmuir probe measurements, alongside predictions from the CRM. In blue are the predictions of the CRM. In green are the line-of-sight plasma parameters derived from Langmuir probes using Eq. (7.7). In red is the arithmetic average along the line of sight. Note that in this graph, one spectra (blue data point) corresponds to the average of 15 Langmuir probe measurements (green or red points)

We observe a good agreement with the arithmetic average (in red) with the CRM prediction overestimating the temperature average by +18%. This overestimation is usually expected since OES is usually sensitive to a higher range of temperature as compared to Langmuir probes. Furthermore, the correspondence between the

predicted T_e and the line-of-sight integrated electron temperature, T_e^{ls} , is excellent as shown in 7.19 a). This justifies the need to adapt the average formulation to account for the integrated nature of OES as well as gradients in the plasmas parameters. When comparing the predicted n_e from the CRM with the volume averaged electron density, in 7.19 b), the trend is well reproduced; however, with a discrepancy by a factor of 5. The secondary peak at $y = 3$ cm is prominent in n_e profiles and marginally in T_e profile, confirming that the peak in the lateral intensity profile observed in Figure 7.6 is indeed linked to the cathode electron emission.

The interpretation of the gas density prediction is challenging due to the parameter n_g catering to both the variation in the optical depth and gas density i.e. $n_g \Leftrightarrow n_g \times d$. In Figure 7.20, the resultant gas density mean value was found to be 10 times higher than the gauge readings. An attempt to explain this variation led to the hypothesis that, owing to the annular shape of the chamber, a lower neutral density at the center of the plume might prevail, which increases as one moves away from the axis before falling again. This hypothesis finds corroboration in the axisymmetric simulation results [Domínguez Vázquez 2019], albeit with a lesser gradient than the one observed here.

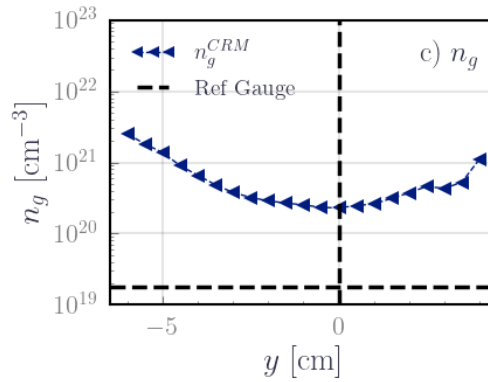


Figure 7.20: Lateral profiles of neutral gas density illustrating the comparison between CRM predictions and the pressure gauge reading (dashed horizontal line) converted into a density based on ideal gas law $P = nk_bT_g$: $P = 1.6 \times 10^{-3}$ mbar and $T_g = 640$ K (T_g is not measured on the setup and the value used here is the same used in the optimization for consistency).

All in all, the CRM predictions manifested consistency regarding T_e and n_e . Moving forward, n_g will be interpreted as an "optical" gas density describing the product $n_g \times d$.

7.4 CRM results

7.4.1 Axial scan of the plume

This section examines the axial profiles of the electron temperature, the electron density, and the gas density as predicted by the CRM across different voltages and flow rates reported in Table 7.1. The optimization was performed on the axial scans obtained from the OES. The optimization parameters are: T_e varied between 1 eV and 25 eV, n_e varied between $1 \times 10^{16} \text{ m}^{-3}$ to $1 \times 10^{20} \text{ m}^{-3}$, and n_g varied between $1 \times 10^{18} \text{ m}^{-3}$ and $1 \times 10^{22} \text{ m}^{-3}$, while d was fixed at 12.5 cm and T_g at 640 K. The CRM predictions are illustrated in Figures 7.21, 7.22 and 7.23.

The reported profiles of n_e and T_e decrease drastically at the exit plane of the thruster to the far plume. The profile of n_g , on the other hand, is decreasing at the exit plane of the thruster before monotonically increasing in the plume. The reported order of magnitude of these parameters is consistent with simulations and experiments.

Axial profile of the electron temperature T_e As depicted in Figure 7.21 a), an increase in the flow rate results in a decrease in the electron temperature at both the exit plane of the thruster and the far-field plume. This decrease can be attributed to an increase in the collision rate with neutrals in both mentioned regions, a fact corroborated by the gas density predictions illustrated in Figure 7.23 a). On the other hand, a voltage increase yields an increase in the electron temperature at the exit plane. However, within the far plume, the voltage's influence on the electron temperature is marginal, merely leading to a modest decline (≤ 0.1 eV) in T_e between 100 and 150 V, after which it stabilizes at 2.1 eV. Our investigations with Langmuir probes showed that the plume's radial expansion adheres to an isentropic model rather than an isothermal model. Nonetheless, considering the profile of T_e predicted with the CRM, adopting the isothermal assumption seems plausible, particularly beyond 5 cm but along the thruster axis.

Axial profile of the electron density n_e The electron density profiles, displayed in Figure 7.22, portray a rapid decay near the exit plane that slows down within the plume. Despite variations in voltage and flow rate, the decay rate remains slightly similar across the profiles. This can be explained by the nature of the prevailing operational regime (Regime III and IV). Typically, the parametric study in [Petronio 2023], in which the anode voltage was varied in PIC simulations, disclosed minor shifts in the electron profile for HET's typical operation voltages. Around $x = 2$ cm, coinciding with the cathode's position, we observe an increase in the electron density, confirming that the jump in the line intensity axial profiles in Figure 7.9 is due to the cathode electron emission. Moreover, this increase barely impacts the electron temperature, aligning with lateral scan observations regarding the energy of the electron emitted by the cathode in Figure 7.19. Decreasing the flow rate increases the electron density at the exit plane. In the far plume, the n_e

profile is slightly identical with a small decrease in n_e with the flow rate. However, note the pronounced drop in n_e especially under the 100 V condition (zoom-in axis in Figure 7.22). This sudden drop seems strange because it means that the ion density does the same and therefore the beam vanishes suddenly. This might be a bias from the optimization process being stuck in a local minimum and requires further refinement.

Axial profile of the gas density n_g The gas density exhibits a minor decrease at the thruster's exit plane, followed by an increase. The predicted densities within $x = 2$ cm to $x = 5$ cm range exhibit an exponential increase and are unaffected by the voltage changes. In the far plume, higher flow rates correspond to elevated densities. This pattern mirrors the observed behavior concerning plume extension. During under-ionized regimes, the CRM-predicted gas density plateaus around $x = 6$ cm, whereas a well-developed plume sees a continuing rise in the profile, surprisingly with a change of slope. This may be tied to facility effects and the residual pressure within the vacuum chamber. To elucidate these findings, a neutral plume model will be developed to extract the contribution of the optical length variation from the neutral gas variation during the axial expansion of the plume. However, the gas density levels predicted from the CRM are higher than the pressure reading in the tank, assuming a temperature $T_g = 640$ K indicated by the dashed horizontal lines in Figure 7.23.

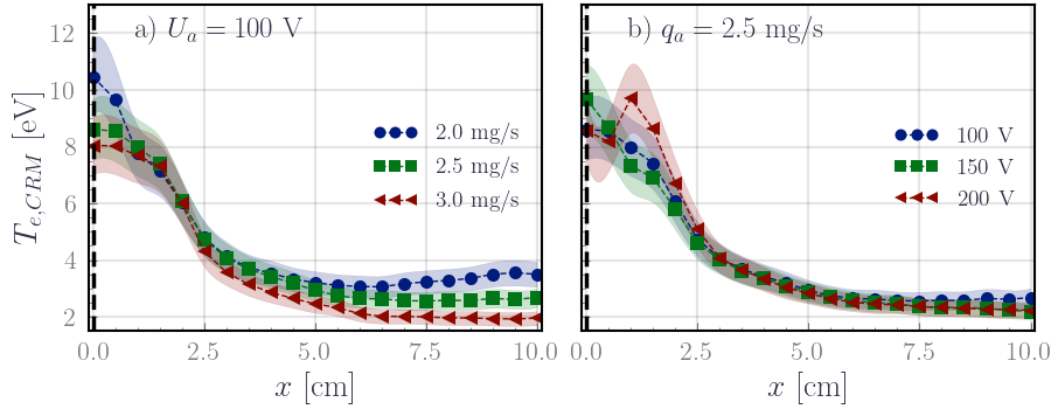


Figure 7.21: Axial profiles of CRM-predicted electron temperature for different operational conditions.

7.4.2 Radial scan of the plume

This section examines the radial profiles of the electron temperature, the electron density, and the gas density as predicted by the CRM across different voltages and flow rates reported in Table 7.2. The optimization parameters are: T_e varied between 1 eV and 40 eV, n_e varied between $1 \times 10^{16} \text{ m}^{-3}$ to $1 \times 10^{20} \text{ m}^{-3}$, and n_g varied between from $1 \times 10^{18} \text{ m}^{-3}$ and $1 \times 10^{22} \text{ m}^{-3}$, while d was fixed at 12.5 cm

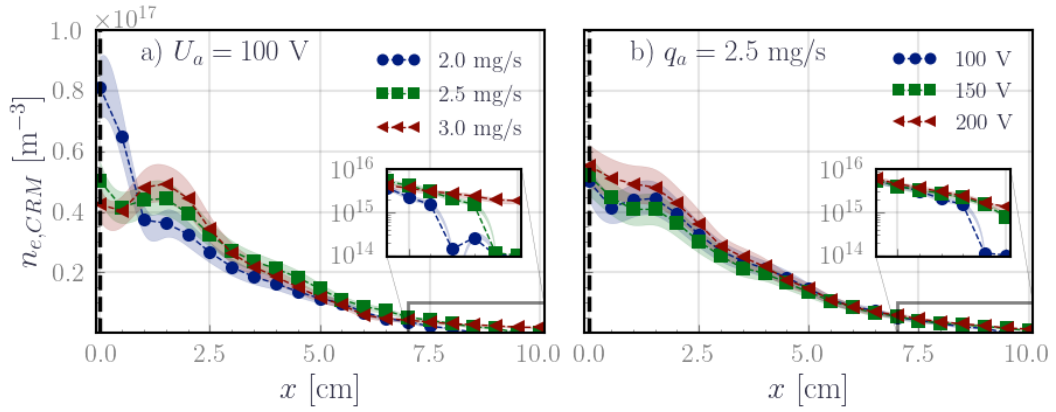


Figure 7.22: Axial profiles of CRM-predicted electron densities for different operational conditions.

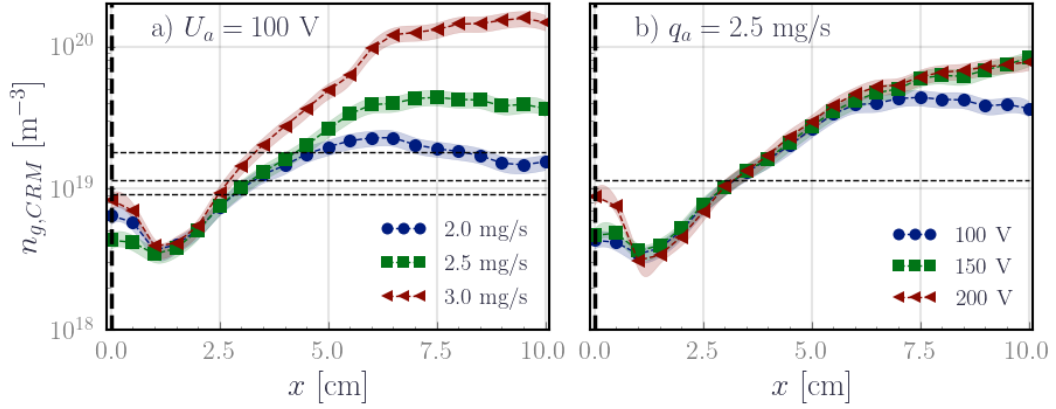


Figure 7.23: Axial profiles of CRM-predicted gas densities for different operational conditions.

and T_g at 640 K. The CRM predictions are illustrated in Figures 7.24, 7.25 and 7.26.

The profiles of T_e , n_e , and n_g are symmetrical about the thruster axis, despite the slight asymmetry observed in the light profiles in Figure 7.13. Therefore, only the profile for positive z is displayed in the next analysis. The most pronounced variations are primarily noticed in T_e , while n_e and n_g manifest modest variations across the investigated operational conditions.

Radial profile of the electron temperature T_e Figure 7.24 shows that the temperature profile has a maximum in the channel, with a peak ranging between 30 and 40 eV, while the wings and center of the channel maintain constant temperatures around 7-8 eV. The maximum of the predicted temperature in the channel increases linearly with the voltage and flow rate as denoted by Figures 7.27 a) and 7.28 a); however, the impact of the flow is moderate. The linear trend for the voltage is

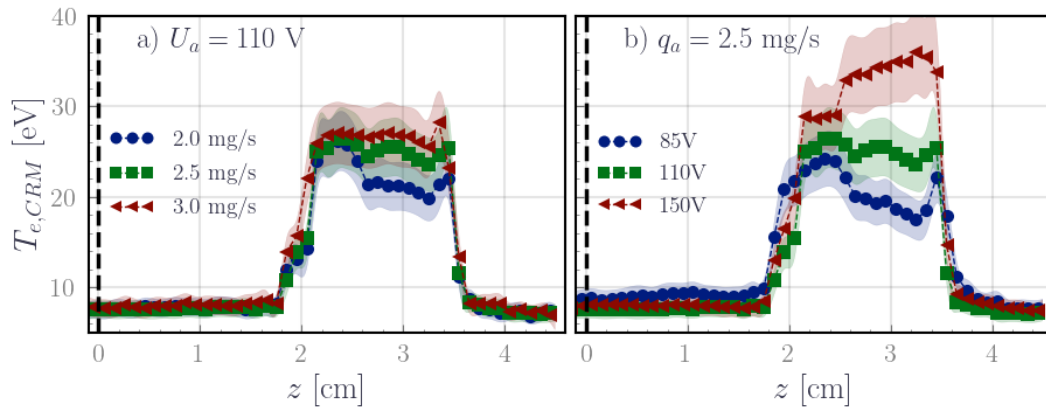


Figure 7.24: Radial profiles of CRM-predicted electron temperature for different operational conditions.

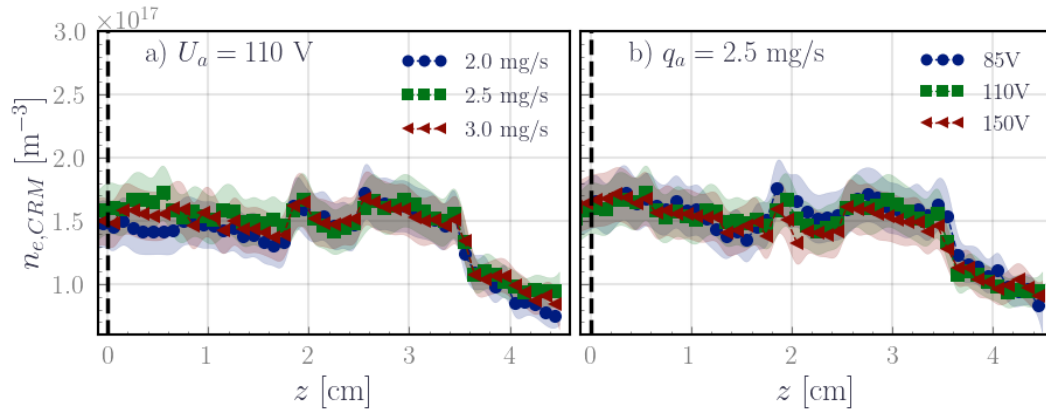


Figure 7.25: Radial profiles of CRM-predicted electron densities for different operational conditions.

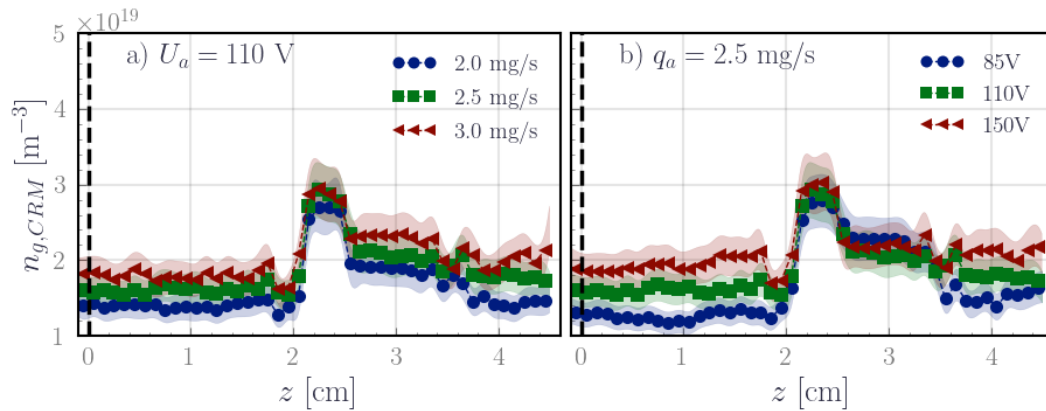


Figure 7.26: Radial profiles of CRM-predicted gas densities for different operational conditions.

consistent during Regime III and Regime IV. For elevated voltages in Regime IV, the electron temperature seems to plateau at approximately 29 eV after 180 V. The shape of the electron temperature gradient within the channel is interesting since it is systematic across all flow rate conditions with the location of the maximum of T_e seeming dependent on the operating regime:

- Regime II $U_a = 85$ V: The maximum of T_e is located near the inner wall, where the maximal radial magnetic field is reached. T_e varies between 17 eV and 25 eV for $q_a = 2.5$ mg.s⁻¹.
- Regime III $U_a = 110$ V: The electron temperature profile remains nearly constant, around 25 eV for $q_a = 2.5$ mg.s⁻¹.
- Regime IV $U_a = 150$ V: The maximum of T_e is located near the outer wall, varying between 29 eV and 35 eV for $q_a = 2.5$ mg.s⁻¹.

These profiles seem to be dependent on the thruster operating regime. This might be related to several factors: changes of the secondary electron emission with the voltage, or perhaps the acceleration of the ions, requiring further investigation.

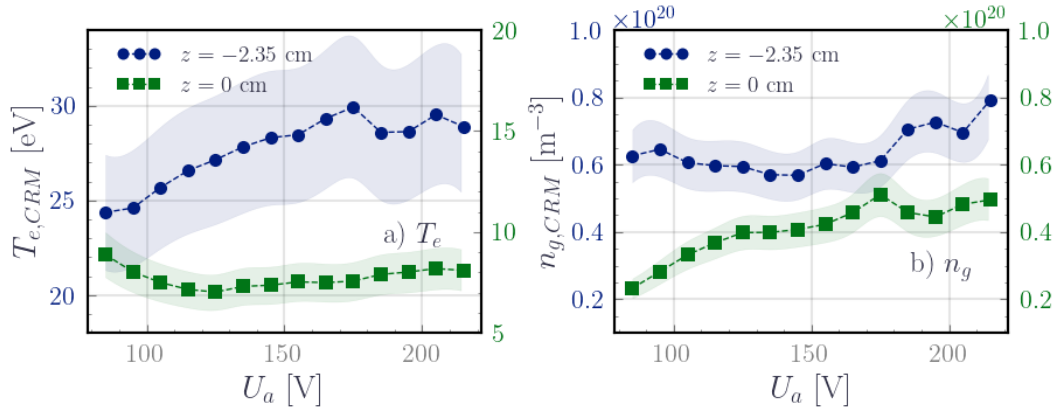


Figure 7.27: Dependence on the anode voltage of T_e and n_g predicted from the CRM a $z = -2.35$ cm (the thruster channel) and $z = 0$ cm (the thruster center) for a flow rate at 2.5 mg.s⁻¹.

Radial profile of the electron and gas densities n_e and n_g The CRM-predicted electron and gas density profiles in Figures 7.25 and 7.26 show a modest increase in the channel. The predicted electron density profiles remain independent of the flow and unexpectedly are weakly dependent on the applied voltage. The profiles of the gas densities within the channel remain independent of the voltage, while linearly dependent on the flow rate in the center as illustrated by Figure 7.27 b). It is notable finally that for all the investigated conditions, the gas density seems to slightly accumulate adjacent to the inner ceramic channel where the gas injection is positioned in SPT models.

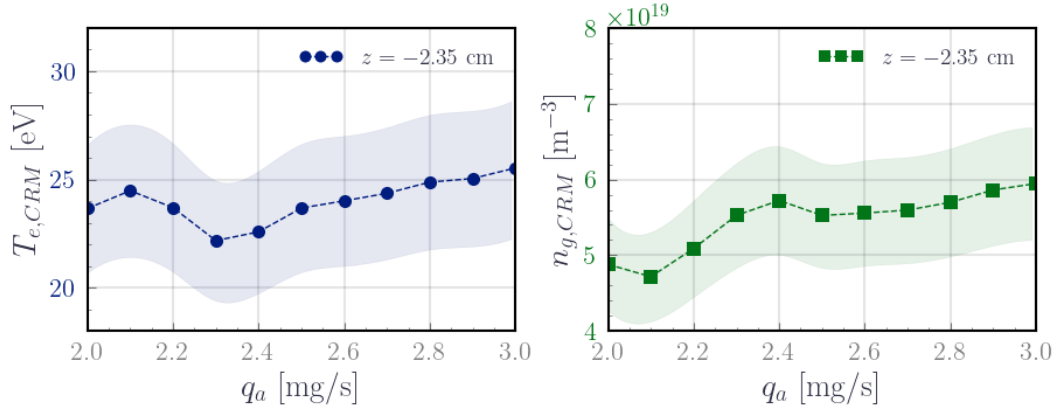


Figure 7.28: Dependence on the rate flow of T_e and n_g predicted from the CRM at $z = -2.35$ cm (the thruster channel) and $z = 0$ cm (the thruster center) for a voltage at 105 V.

7.5 Discussion

7.5.1 Impact of the optimization method

Impact of the choice problem parameters Chapter 5 argued that to retrieve all the correct trends for the plasma parameters, it is important to optimize over n_e , T_e and n_g . The axial scans show that the plume exhibits also a gradient in the optical length d . This suggests that we should account for all four inputs in the CRM, despite the reduction to only 3 parameters (n_e, T_e, n_g), by consolidating the variable n_g and d into one variable. We recalculated the profiles for all the previous scans with the full CRM input, and we obtained the same profile for T_e and n_e , which gives us more confidence in the n_e and T_e predictions of the CRM. However n_g and d were fluctuating, as illustrated in Figure 7.29. The reason might be related to the relation $n_g d = cte$, leading to a non-unique solution for n_g and d , so that the optimizer is stuck often in a local minimum.

Impact of the cost function The cost function defines the parametric surface whose extrema are to be found by the algorithm. Therefore, it has indeed a significant impact on the prediction. The χ^2 cost function Eq. (7.4) though is biased since it favors fitting the most intense lines. Alternatively, the following cost function can be used:

$$\min_{(T_e, n_e, n_g)} E(n_g, n_e, T_e) = \frac{1}{N} \sum_{\lambda_{ij}} \left(\frac{I_{\lambda_{ij}}^{CRM}}{I_{\lambda_{ij}}^{Exp}} - 1 \right)^2 \quad (7.8)$$

This cost function equalizes the weight across all lines since its gradient involves a normalization with the experimental intensities. We made the predictions with the CRM with both cost functions for the axial scans and the results for T_e are reported in Figure 7.30. We can see interestingly that the order of magnitude is

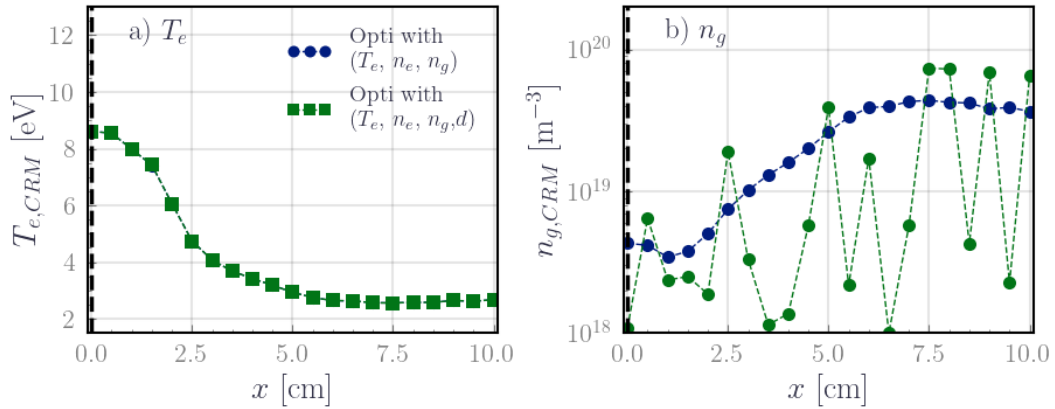


Figure 7.29: Comparison between a 3-variable and a 4-variable formulation of the CRM optimisation problem. The blue circles are superposed to the green squares on the left Figure a). On the right Figure b), we can see that the n_g prediction between the two formulations is very different. The 4-variable formulation exhibit a fluctuating profile compared to the smooth profile for the 3-variables formulation.

the same between the results from the two cost functions (Figure 7.21 and Figure 7.30). We observe the temperature gradient which is less prominent with the second Eq. (7.8). The sensitivity over the operational parameters looks very low and only the general trend is reproduced. For this reason, Eq. (7.4) seems like a better choice to keep the model's sensitivity to the input variables. Typically, Eq. (7.4) formulation considers the normalized intensity of each line as compared to the other lines, and therefore it reflects the big picture even though it is driven by the more intense lines. However, since the prediction using Eq. (7.4) are relatively high for some operational conditions (the 85 V in the radial scan for instance), the results of Eq. (7.4) suggest that our current formulation of the CRM might overestimate the plasmas parameters and that considering a formulation close to Eq. (7.8) might improve the quality of the predictions.

7.5.2 Gas density variation

We emphasized in the methods that the CRM-predicted gas density ought to be interpreted as an "optical" gas density. In the case of the radial scan, the plasma thickness along the line of sight can be considered in the order of the depth of field of the setup (Appendix G) since the photons are collected from the focal point coinciding with the exit plane of the thruster where the most intense emission is, thereby allowing the results for the radial scan on the gas density to be considered well representative of the neutral density changes in the channel.

Interpreting the "optical" gas density from the axial/lateral scans is more complex, due to the axially expanding plume implying an increase in optical length in this direction. Rigorous treatment of this would necessitate a comprehensive radiative transfer model that accounts for both neutral dynamics and optical depth

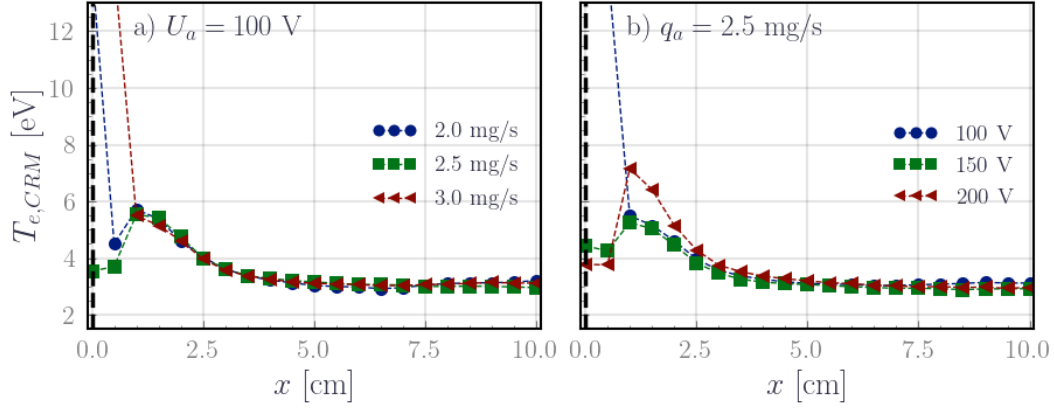


Figure 7.30: Axial profiles of CRM-predicted electron temperature for different operational conditions using the cost function from Eq. (7.8). The trends are similar to the results reported in Figure 7.21. However, the values are smaller.

variation. We propose a simplified model aimed at extracting/validating the trends of the optical length variation. Within HET, given the annular shape, the neutral distribution in the plume may be modeled as isotropic emission from an annular disc, as a first approximation [Goebel & Katz 2008]. Considering a disk of diameter R at $z = 0$ emitting gas uniformly in all directions at a surface emission rate q , and a point P located at (x, y, z) (with cylindrical symmetry allowing us to set y to 0), the gas emitted by a surface element will travel a distance

$$d = \sqrt{(x - r \cos \theta)^2 + r^2 \sin^2 \theta + z^2}.$$

Given the isotropy of the emission, the infinitesimal flux of particles dF received at P is given by Eq. 7.9:

$$F_{n_g} = \iint_{r,\theta} \frac{q}{4\pi d^2} r dr d\theta. \quad (7.9)$$

The emission from an annulus disk can be described by subtracting the emission from a disk of radius R_2 from that of a disk with radius R_1 ($R_1 \geq R_2$). Taking $R_1 = 5.2$ cm and $R_2 = 3.2$ cm, we derive the following map of neutral density in the plume, illustrated in Figure 7.31. Figure 7.31 b) relates well to the lateral profile of the gas density.

Figure 7.31 c) relates well with the decrease in the neutral density around the exit plane in the axial scans. However, we expect a monotonous decrease in the neutral density along the plume at a rate of $1/r$, which suggests that the observed increase in Figure 7.23 is associated with the plume expansion and the increase in the optical length d . Since

$$n_g^{CRM} = n_g(x) \times d(x),$$

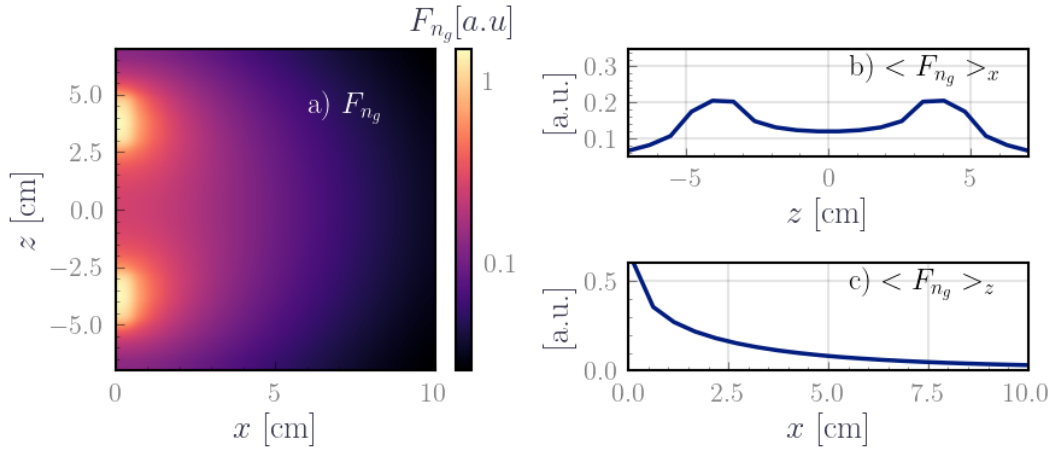


Figure 7.31: Model-derived map of neutral density in the plume.

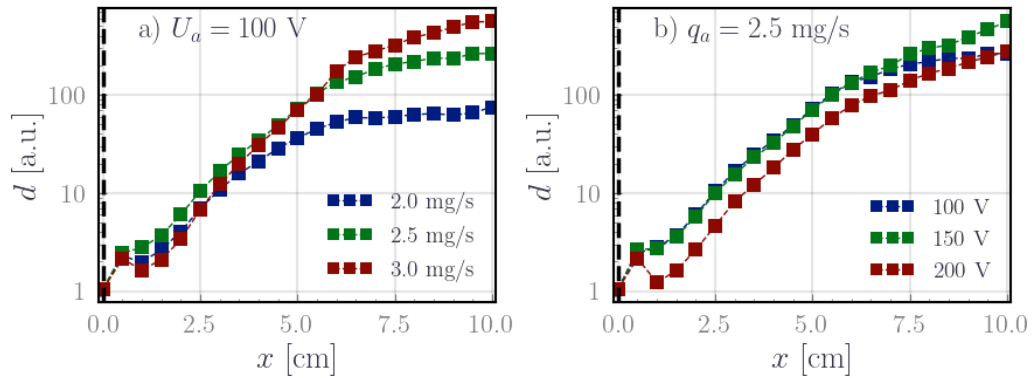


Figure 7.32: Normalized neutral density, illustrating optical length evolution in the plume.

normalizing by the model-predicted theoretical density evolution allows the extraction of the optical length evolution d . The theoretical evolution is integrated along the line of sight z and the value at the exit plane is set at the predicted value from the CRM. The results are displayed in Figure 7.32. This reveals that the optical length increases axially with the expansion of the plume, with the voltage dependency indicating a decrease in the optical length at higher voltages, potentially reflecting a more focused ion beam and, consequently, a less divergent plume as expected [Baird *et al.* 2021].

We draw the attention that these are qualitative trends and not absolute comparisons. Our method uses n_g and d as adaptive parameters to more accurately fit experimental spectra, necessitating the reproduction of trends but complicating absolute value extraction. Moreover, the pumping speed of the chamber is finite and there is a neutral backflow, in addition to heating, pressure, collisions, etc ... Therefore, the preceding neutral density analysis should be interpreted with caution.

7.5.3 Electron temperature dynamics

The shift in the location of the maximum electron temperature (Figure 7.24) needs more scrutiny, since to our knowledge it has not been reported in previous simulations (radial-azimuthal [Tavant *et al.* 2018], axial-radial [Domínguez Vázquez 2019], and axial-azimuthal [Charoy 2020, Petronio 2023] directions) mainly due to the absence of a parametric study with voltage variations. One initial hypothesis to explain these observations is to consider the impact of secondary electron emission. However, this hypothesis is not substantiated by the work of [Tavant *et al.* 2018]. Specifically, alterations in the secondary emission model did not induce any asymmetry in the temperature profile, and the plasma parameters retained their bell-shaped characteristics, concerning the inner and outer wall sheaths.

Nevertheless, the preceding simulation made a critical assumption regarding the uniformity of the magnetic field in the radial direction, which is not supported by the magnetic field profile illustrated in Figure 6.3. Consequently, the observable displacement could plausibly be attributed to the radial gradient of the magnetic field, although the exact mechanisms of such an effect remain uncertain. The simulations also omitted consideration for the chamber's curvature, thereby assuming a uniform particle flux throughout the simulation radial-azimuthal domain instead of the more plausible scenario of a radially decreasing particle flux as one moves toward the outer wall. This would impact the position of the peak in the electron density and temperature in the absence of the magnetic field as supported by the calculation of radial transport terms in an annular configuration by [Zhang *et al.* 2015] where it was observed that the peak was located towards the inner wall instead of mid the annular geometry. Further investigation in this direction will be performed in the future, especially to include the magnetic field and understand the peak position dependency on the voltage. These questions can be investigated on two levels. First using axisymmetric simulations and performing a parametric study on the voltage variation. Second, using the CRM by performing scans inside of the channel which can be rendered possible by introducing a small slit in the ceramics to acquire radiative emission from the thrusters channel, similarly to [Zhu *et al.* 2019].

7.5.4 Preliminary insights from PIC simulations vs. experimental results

We can compare synthetic profiles from 2D axial-azimuthal PIC simulations vis-à-vis experimental results. Several simulation cases were executed under conditions approximating our experimental setup. This investigation underscored the sensitivity of simulations to experimental conditions. The PIC simulation ran under various conditions, incorporating diverse circuit values, neutral flow rates, and neutral injection speeds, yet none achieved a discharge current closely resembling the experimental observations. The pivotal aspect discovered was the acute sensitivity of the PIC simulation to the neutral injection speed and background pressure, reflecting the complex dynamic between the plasma, and the neutrals, and the limitation of a

unidimensional neutral dynamics description. While the exact reproduction of the experimental conditions remains a subject of ongoing investigation, the study will focus on a simulation case that has a sustained discharge with a voltage and a flow rate closest to the experiment. The general PIC framework was detailed in Chapter 5, and here we only change the voltage drop to 300 V and the flow rate 2 mg.s^{-1} . The simulation parameters are reported in Table 7.3.

Table 7.3: Simulation parameters for the PIC simulation used for the comparison with the CRM.

Parameter	Value
Δt	$2 \times 10^{-12} \text{ s}$
Δx	$2 \times 10^{-5} \text{ m}$
q_a	2 mg.s^{-1}
V	300 V
Scaling factor	64
T_e cathode	0.1 eV
R	120Ω
L	4 mH
C	15 nF
Cathode model	Quasi-Neutrality
Collisions	Yes
Neutral dynamics	Yes
Anode ion recombination	Yes
External Circuit	Yes

In Figure 7.33 a), the temperature profile T_e is compared between the PIC simulation ($q_a = 2 \text{ mg.s}^{-1}$ and a measured voltage drop $U_a = 300 \text{ V}$) and CRM results for a xenon flow at the anode ($q_a = 2 \text{ mg.s}^{-1}$ and a measured voltage drop $U_a = 200 \text{ V}$). The profile averaged over $12 \mu\text{s}$ upon reaching a steady state, reveals that despite a higher voltage drop in the simulation, the temperature predictions from the CRM slightly surpass those from the simulation but yield the correct order of magnitude and variations, in particular the inflection point at the exit plane.

Figure 7.33 b) shows a comparative analysis of the experimental spectra. In blue is the synthetically-generated and azimuthally-averaged spectra from the PIC simulation obtained via the coupling with the CRM at an axial position $x = 1 \text{ cm}$ from the thruster exit plane and using PIC EEDF. The method is detailed in Chapter 5. In green are the best-fit spectra suggested by the CRM to the experimental spectra at $x = 1 \text{ cm}$ via basin hopping optimization and assuming a Maxwellian EEDF. In red is the experimental spectra at $x = 1 \text{ cm}$ from the thruster exit plane

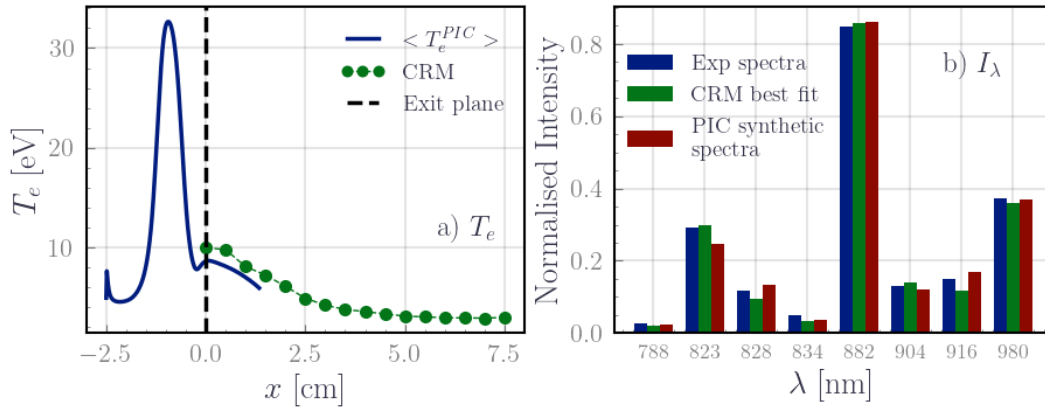


Figure 7.33: Comparison between PIC simulations and CRM predictions at $U_a = 200$ V and $q_a = 2 \text{ mg}\cdot\text{s}^{-1}$ for the experiment and $U_a^{PIC} = 300$ V and $q_a^{PIC} = 2 \text{ mg}\cdot\text{s}^{-1}$ a) Comparative overview of CRM predicted and PIC T_e profiles b) Comparative overview of experimental, CRM-predicted, and PIC-resultant synthetic spectra at $x = 1$ cm.

in Configuration 1 for $q_a = 2.0 \text{ mg}\cdot\text{s}^{-1}$ and $U_a = 200$ V. The normalized ($\|\cdot\|_2$) intensity of the strong lines 823 nm, 882 nm and 980 nm is effectively rendered and slight differences are observed on less intense lines 788 nm, 834 nm and 904 nm, still showcasing substantive agreement with the experimental spectra.

This agreement is encouraging on both the validity of the CRM and PIC simulation, but still is not definite due to the challenges in finding a systematic alignment between the experiment and the simulation, without resorting to assumptions and simplifications, in particular on the neutral dynamics. This observation increasingly underscores the validity of the virtual diagnostics approach. They effectively introduce experimental insights into simulations and bring up deviations emerging either from a local versus an integrated experimental signal or the signal processing leading from one to the other. For instance, the OES line-of-sight integrated nature reveals that spatial gradients along the line of sight are not detected, leading to the need to compare the results to line-of-sight integrated parameters as suggested in Eq. (7.7). The investigations with the Langmuir probe showed that within the xenon first excitation energy range, the Maxwellian approximation is a fitting initial approximation, particularly in the plume's periphery. In contrast, the core of the plume significantly deviates from the Maxwellian hypothesis. These features cannot be detected along the line of sight since OES is unable to discriminate the spatial extension of these regions and thereby delimitate between Maxwellian and non-Maxwellian regions. This was also observed in Section 5.5, based on the virtual diagnostic approach where we concluded that the Maxwellian and the non-Maxwellian hypothesis do not reflect distinctively on the neutral lines emissions. The takeaway message is ultimately that simulation and experiment comparisons are never straightforward given the multifaceted variables on both sides and the implementation of synthetic diagnostics paves the way to more rigorous comparisons.

Chapter conclusions

The previous analysis extensively examined the evolution of the intensity of the neutral lines, drawing insights into the thruster and its operational regimes. A future perspective is introducing ionic lines in the analysis since, as highlighted by the 541 nm, 597 nm and 604 nm lines emission, these lines reflect a different facet of the EEDF. The work of [Leray & Bretagne 1997] showed that by integrating helium into the system and using the line ratio method between helium lines and ionized xenon lines, it is feasible to probe the energetic tail of the EEDF. Integrating ionic lines could potentially augment the energy range in the diagnostic, granting perhaps the capability to discern the non-Maxwellian shape of the EEDF due to the depletion of high-energy electrons. Indeed, the coupling with PIC showed that only relying on neutral lines fails to visibly mirror the deviation from the Maxwellian EEDF. Consequently, the incorporation of ionic line surfaces is a crucial factor in the study as demonstrated by [Konopliv *et al.* 2021]. However, this will not allow us to go past the lack of spatial resolution parallel to the line-of-sight which is inherent to OES as stated in the previous subsection.

The limitations, the multiple variables, and the sensitivity to the optimization parameters in the model engender a baseline uncertainty on the predictions that potentially surpasses the conservative 20% threshold delineated in Chapter 3 and that was used throughout this chapter as the uncertainty on the CRM predictions. Nonetheless, the discerned trends from radial, axial, and lateral scans are robust and the order of magnitude is consistent. These observations underscore that a CRM, reduced to the discharge dominant mechanisms, such as HET0D for HET, suffices in portraying the intricate physics inherent in HET from merely the light emission. The CRM validation in high-pressure conditions, ostensibly a worst-case scenario, fosters an expectation of better performance in optimal vacuum conditions. It is also paramount to note that the CRM validation was performed for a singular operating condition, albeit validated across various positions within this condition. This assures, to some degree, that the CRM can extract trends of plasma parameters, albeit perhaps not their absolute values. Typically the CRM-predicted electron temperature reflects mainly the energy of the electrons contributing to the excitation of the neutrals, usually called excitation temperature. However, the variation of this temperature reflects the trends of the electron temperature, hence ensuring that the CRM can reflect the physics.

Exploring the scalability of detected trends to different thruster sizes and power levels remains vital. First, our analysis was rooted in regime-specific observations and relied on the understanding of the light emission trends within the operational context of the HET. The CRM was able to detect the changes in the regimes and specifically highlighted some non-monotonic variations of the plasma parameters across the voltage changes. For that reason, we recommend for future work to conduct diagnostics while specifying the thruster's operational regime and its characteristics to ensure that the results are comparable across the different sizes and powers, especially. Moreover, during this Ph.D., HET0D was also developed in

argon and was applied to different thruster designs, such as the PEGASES thruster, and was also deployed on the PPS-1350 model on xenon. Although the results are not reported here, they exhibited consistency in orders of magnitude and trends of T_e , affirming again that HET0D is scalable and can track the evolution of the electron temperature across varied thruster models.

Finally, light emerges as a common denominator amongst these thrusters, enabling the detection of different phenomena without necessitating invasive diagnostics, thus further reinforcing the argument for its usage as an in-orbit monitoring tool for thrusters. Our implementation does encounter a challenge in its incompatibility with time-resolved diagnostics. The optimization process, being inherently time-intensive, results in the plasma altering its state between two consecutive measurements. Nevertheless, the simplicity of data acquisition remains appealing, and the potential acceleration of the process might be realized through reliance on data-driven models and machine learning.

Enhancing CRM Predictions using Machine Learning

*May it be a light to you in dark places, when all other lights
go out.*

J.R.R. Tolkien, *The Fellowship of the Ring*

Contents

8.1	Machine learning methodology	175
8.1.1	Presentation of ANNs	175
8.1.2	The learning process	177
8.1.3	Hyperparameter tuning and cross validation	179
8.1.4	Practical workflow to developing ANN	180
8.2	Accelerating predictions with the collisional radiative model	182
8.2.1	Data collection and integration approach	182
8.2.2	Results	184
8.3	Learning macroscopic parameters	186
8.3.1	Experimental setup, data acquisition and cleaning	186
8.3.2	Model development	190
8.3.3	Results and insights	192
8.4	Machine learning control with PID	197
8.4.1	Control strategy and implementation of the Proportional- Integrator-Derivative controller (PID)	198
8.4.2	Control simulation results	199
8.4.3	Enhancing control and monitoring: PID and varied magnetic configurations	202
8.5	Chapter conclusions	203

Introduction

The prediction method with the CRM, relied on a time-consuming stochastic optimization over multiple parameters (≈ 1 min per data point), making real-time monitoring challenging. In recent years, Machine Learning (ML) algorithms have emerged as a promising solution for predicting complex systems' state variables, offering the possibility to replace complex models and the advantage of rapid predictions. Time-resolved OES is a well-established technique for low-temperature plasma [Orlikovskii & Rudenko 2001]. By analyzing optical emissions from excited species, we can identify atomic or molecular species, estimate their temperature, and study the plasma kinetic processes in real time. This approach has found applications in plasma etching, thin-film deposition [Schiller *et al.* 1982, Bartkowiak 2010, Song *et al.* 2012, Song & Mazumder 2012], and even as a control feedback loop to monitor and manage deposition processes cost-effectively [Koo *et al.* 2017, Bartkowiak 2010, Chang & Yang 2018]. However, all these implementations required the implementation of a correlation between the light intensity and the control parameter of the plasma process of interest, which can be achieved by creating an optical footprint [Song & Mazumder 2012], either by recording the optical signal for different control parameters in the form of a calibration curve or by teaching this optical footprint to an artificial intelligence or a ML model.

The integration of ML in OES presents a paradigm shift in spectroscopy and plasma diagnostics. Previous work introduced the foundations of Deep Learning Spectroscopy (DLS) and has demonstrated ML's potential in predicting mechanical properties [Ward *et al.* 2016], recognizing band gaps [Pilania *et al.* 2016], detecting functional groups [Fine *et al.* 2020], simulation of excitation spectra [Ghosh *et al.* 2019], and even exploring molecular design [Raccuglia *et al.* 2016, Joung *et al.* 2021, Xue *et al.* 2016], drastically reducing the time and cost associated with these analyses.

From an engineering standpoint, the application of ML to OES and CRM to achieve time-resolved measurements holds practical significance. It enables real-time implementation of optical ML control loop systems to manage the discharge parameters (voltage and flow rate) and, consequently, adjust plasma parameters like the electron temperature T_e or the electron density n_e . Moreover, optical ML controllers might also come in handy to control the thrust and the specific impulse using the PPU according to the different types of control modes required by the mission profile. This provides flexibility on the control mode and reduces the number of required controllers as light emission allows compounded control over all the discharge parameters.

This chapter represents a pioneering step in applying DLS to HET. The goal is to construct an optical footprint of an HET using ANNs, that allows probing the discharge at two levels: microscopic level by enhancing the CRM optimization on T_e and n_e and macroscopic level by predicting from optical emission the voltage, the discharge current and the magnetic field. Finally, we will develop a PID controller

based on the latter footprint, akin to applications in plasma etching and deposition, to control the voltage and flow rate on a simulated HET emission. Section 8.1 provides a detailed overview of the methodology used, including data collection, preprocessing, model selection, and evaluation. Section 8.2 discusses how machine learning accelerates predictions by integrating the CRM into the model. Section 8.3 focuses on predicting macroscopic parameters under varying operating conditions using machine learning. Section 8.4 explores the implementation of machine learning for control, including PID design with adaptive coefficients. The chapter concludes by summarizing the implications of the findings and suggesting future research directions.

8.1 Machine learning methodology

8.1.1 Presentation of ANNs

ANNs are a machine learning model designed to artificially mimic the brain structure and wiring of the information. It consists of multiple layers of interconnected artificial neurons that can optimize their behavior to learn complex functions from large amounts of data.

From the perceptron to neural networks The basic building block of an ANN is the perceptron, i.e. the artificial equivalent of a biological neuron. Similar to its biological counterpart, a perceptron receives different inputs from its neighbors on which it performs a transformation to produce an output that is then passed to the other perceptrons. The critical distinction is that the transformation performed by a perceptron is purely mathematical. Typically, the inputs $\mathbf{X} = (x_i)$ are weighed

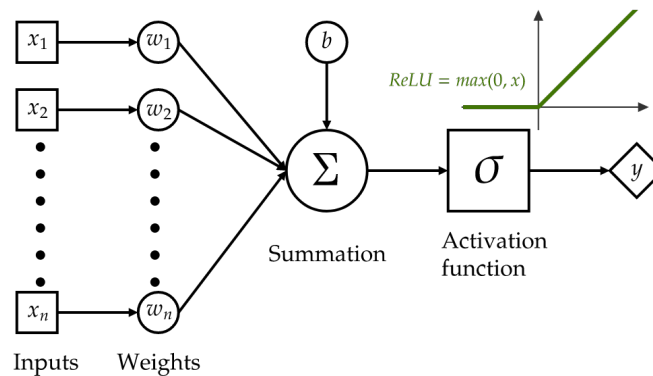


Figure 8.1: Representation of the perceptron with n inputs x_i . Each is weighed with w_i before being summed with the summation operator Σ . A bias b is added to the result before passing the result to the activation function σ to yield the output y .

by $\mathbf{w} = (w_i)$ depending on their importance, summed then passed to a non-linear function σ called the activation function to produce the output y . This process is

illustrated in Figure 8.1 and is represented by the equation:

$$y = \sigma(\mathbf{X}^T \mathbf{w} + b) \tag{8.1}$$

where \cdot^T is the transpose operator. Numerous activation functions are possible, with σ being any real-valued function. For instance, using a linear activation function will result in a network describing only linear functions. In that sense, we understand that these activation functions introduce non-linearity into the network, enabling it to capture complex relationships within the data. Common activation functions include the sigmoid function $\sigma(x) = \frac{1}{1+e^{-x}}$, hyperbolic tangent $\sigma(x) = \tanh(x)$, Rectified Linear Unit (ReLU) $\sigma(x) = \max(0, x)$, and variants like Leaky ReLU. The choice of the activation function is usually guided by theoretical or empirical considerations, with ReLU often being a practical starting point. The output y from one perceptron can then serve as input for multiple other perceptrons, including itself, allowing for recursive feedback loops. These perceptrons are organized into different layers, as illustrated in Figure 8.2, resulting in the formation of a neural network. Conventionally, the input layer contains the initial data, the output layer contains the final results, and the intermediate layers are referred to as hidden layers.

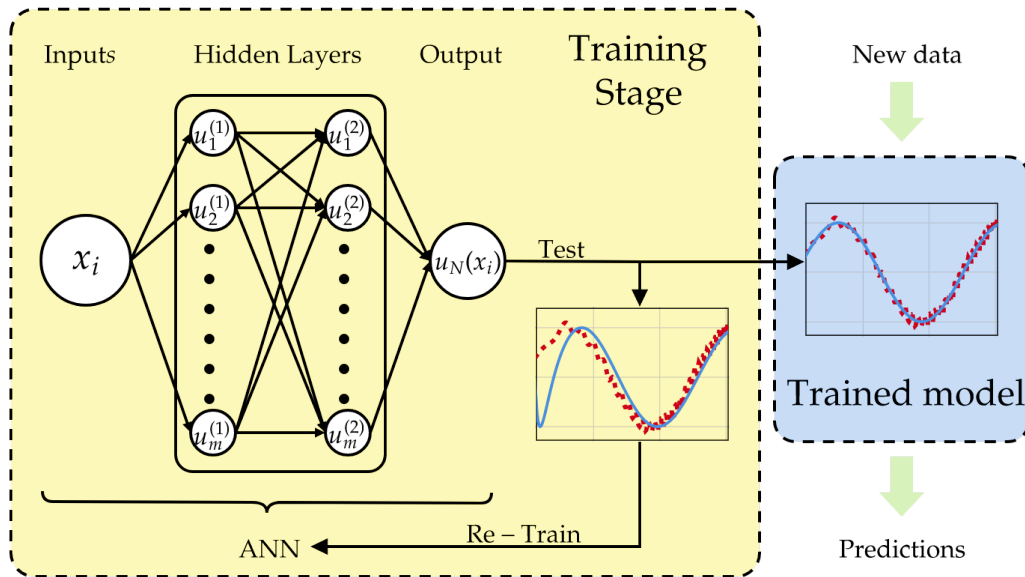


Figure 8.2: Canonical illustration of the general architecture of an ANN. The ANN here consists of 2 hidden layers. The inputs are forward propagated from one layer to another. The resulting output is tested against the validation data during the Training stage. If the ANN prediction is not satisfactory, then the ANN is re-trained. Otherwise, the trained model is deployed on new data.

8.1.2 The learning process

The learning consists of the network iteratively refining its weights through training data to minimize the prediction error on the target features, making it capable of generalizing and making predictions on new, unseen data. This is achieved using a gradient descent algorithm in which the steepest descent direction with respect to the weights is calculated using a process called backpropagation. In this manner, the weights are modified along the steepest descent direction, and the error is minimized efficiently.

Forward propagation This process is akin to the transmission of information through the network from one layer to another, leading to the computation of the output. Let us consider the neural network shown in Figure 8.3, featuring one

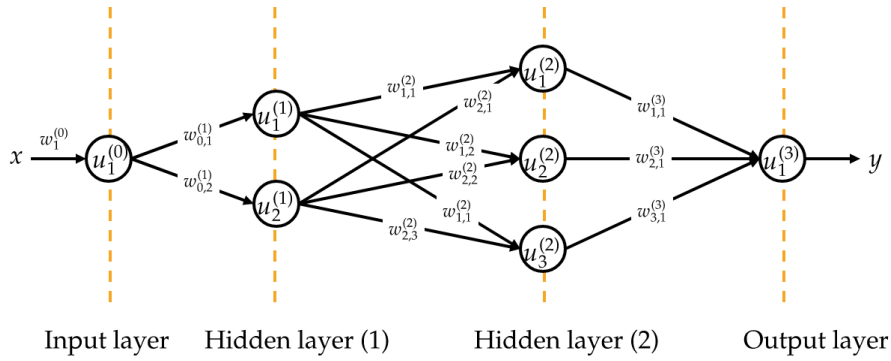


Figure 8.3: Example ANN with 2 hidden layers, an input layer, and an output layer. Each perceptron is indicated by $u_i^{(j)}$ with j as the rank of the layer and i as the rank of the perceptron within the layer. The weights are indicated with $w_{i,k}^{(j)}$ representing the weight from the perceptron i to k at the input of the layer j . The activation function is not indicated here and is assumed constant across the ANN.

input, one output, and two hidden layers. Assuming all perceptrons share the same activation function, σ , we can express the information flow through the second hidden layer as:

$$\mathbf{y}^{(3)} = \sigma \left(\begin{bmatrix} \sum_{j=1}^2 w_{j,1}^{(2)} y_j^{(2)} + b_1^{(3)} \\ \sum_{j=1}^2 w_{j,2}^{(2)} y_j^{(2)} + b_2^{(3)} \\ \sum_{j=1}^2 w_{j,3}^{(2)} y_j^{(2)} + b_3^{(3)} \end{bmatrix} \right) = \sigma \left(\mathbf{W}_{2,3} \mathbf{y}^{(2)} + \mathbf{b}^{(3)} \right) \quad (8.2)$$

Here, $\mathbf{W}_{2,3}$ represents the weight matrix connecting the first hidden layer to the second hidden layer, and $\mathbf{b}^{(3)}$ is the bias vector associated with the perceptrons in the second hidden layer. Reiterating this for all the layers in the network, the total output of the network is expressed as:

$$y = \sigma \left(\mathbf{W}_{3,4} \sigma \left(\mathbf{W}_{2,3} \sigma \left(\mathbf{W}_{1,2} \sigma \left(w_1^0 x + \mathbf{b}^{(1)} \right) + \mathbf{b}^{(2)} \right) + \mathbf{b}^{(3)} \right) + \mathbf{b}^{(4)} \right) \quad (8.3)$$

Backpropagation Backpropagation is the subsequent phase in the learning process and consists of calculating the gradient of the output with respect to the weights and biases of the network, to be used for the gradient descent algorithm. The heart of backpropagation lies in the clever use of the Leibniz chain rule for calculating derivatives. Let us introduce the sensitivity—the network’s output’s responsiveness to information transmitted among perceptrons, which is expressed as follows:

$$\delta_j^i = \frac{\partial y}{\partial z_j^i}$$

Here, $z_k^{(i)} = \sum_l w_{l,k}^{(i-1)} y_l^{(i-1)} + b_k^{(i)}$ represents the output of k^{th} perceptron in the i^{th} layer before applying the activation function. The sensitivity is propagated backward through the network, using the chain rule such as, for instance:

$$\delta_1^{(2)} = \frac{\partial y}{\partial z_1^{(2)}} = \left[\frac{\partial y}{\partial z_1^{(3)}} \frac{\partial z_1^{(3)}}{\partial y_1^{(2)}} + \frac{\partial y}{\partial z_2^{(3)}} \frac{\partial z_2^{(3)}}{\partial y_1^{(2)}} + \frac{\partial y}{\partial z_3^{(3)}} \frac{\partial z_3^{(3)}}{\partial y_1^{(2)}} \right] \frac{\partial y_1^{(2)}}{\partial z_1^{(2)}} \quad (8.4)$$

$$= \left[\delta_1^{(3)} w_{1,1}^{(2)} + \delta_2^{(3)} w_{1,2}^{(2)} + \delta_3^{(3)} w_{1,3}^{(2)} \right] \sigma'(z_1^{(2)}) \quad (8.5)$$

This allows us to compute the gradients with respect to the weights and biases efficiently, as compared to finite differences, since the gradients are expressed analytically, for instance:

$$\frac{\partial y}{\partial w_{1,1}^{(3)}} = \frac{\partial y}{\partial z_1^{(4)}} \frac{\partial z_1^{(4)}}{\partial w_{1,1}^{(3)}} = \delta_1^{(4)} y_1^{(3)}, \quad \frac{\partial y}{\partial w_{2,3}^{(2)}} = \frac{\partial y}{\partial z_3^{(3)}} \frac{\partial z_3^{(3)}}{\partial w_{2,3}^{(2)}} = \delta_3^{(3)} y_2^{(2)}$$

Gradient descent After computing the gradients via backpropagation, we use the gradient descent algorithm to iteratively find the optimal weights for the given network architecture. In this process, the network adjusts its weights in the direction of the steepest gradient to minimize the cost function J or error, effectively "learning" from the data. The optimization process can be represented as:

$$\mathbf{w}^{i+1} = \mathbf{w}^i - \alpha \nabla_{\mathbf{w}} J(\mathbf{w}), \quad (8.6)$$

Here, \mathbf{w}^i represents the previous value of the network’s weights, \mathbf{w}^{i+1} represents the updated weights, $\nabla_{\mathbf{w}}$ signifies the gradient with respect to the network weights calculated using backpropagation, and $J(w)$ is the error function that quantifies the discrepancy between the network’s output and the target feature. Various gradient descent strategies are available, and one classical starting point is the Adaptive Moment (ADAM) optimization method. The ADAM method combines the benefits of momentum to smooth out gradients and adaptive learning rates to achieve efficient optimization. ADAM introduces two key parameters:

- α : The learning rate controls the step size in the update of the gradients with respect to the weights. It determines how large or small the changes to the weights are for each iteration. Choosing an appropriate learning rate is essential for convergence and stability.

- β_1 and β_2 : These coefficients, often close to 1, describe the exponential decay rates for moving averages of past gradients for β_1 and past squared gradients for β_2 . They influence the momentum of the optimization process, helping the algorithm converge efficiently.

More details about this method are available in the appendix H and can be found in the original work of [Kingma & Ba 2015].

Finally, the choice of cost or loss function J can vary depending on the problem at hand. Two common cost functions are used:

- Mean Squared Error (MSE): $J(\mathbf{w}) = \frac{1}{2m} \sum_{i=1}^m (y_i - \hat{y}_i)^2$, where y_i represents the target values, \hat{y}_i represents the predicted values, and m is the number of training examples.
- Mean Absolute Error (MAE): $J(\mathbf{w}) = \frac{1}{m} \sum_{i=1}^m |y_i - \hat{y}_i|$, which measures the average absolute difference between predicted and actual values.

Note that the choice of the activation function, the architecture of the network, the gradient descent method, the learning rate, the cost function, and associated parameters are not learned from the data but are defined before training begins. That is why they are termed hyperparameters. These parameters greatly influence the training and convergence of an ANN. The proper tuning of these components is then crucial.

8.1.3 Hyperparameter tuning and cross validation

The selection of the hyperparameters often involves an iterative process of testing and evaluation. It is performed through techniques such as grid search, random search, or Bayesian optimization. These involve training and evaluating the model with different combinations of hyperparameters to find the set that yields the best performance on the validation dataset. *Grid search* involves defining a set of values for each parameter and systematically testing all combinations to determine the best combination. *Random search* involves selecting values randomly for each parameter and evaluating the model's performance with each combination. *Bayesian optimization* involves using probability models to guide the search for the optimal parameters.

In this process, cross-validation [Stone 1974] is also commonly used to assess how well the model can generalize to unseen data, helping to avoid overfitting the prediction to the used training data. The technique consists of a resampling method used to split the dataset into multiple subsets, typically training and validation sets, and evaluate the model performance by changing the pair training and validation sets. This process helps mitigate the risk of the model performing well on the training data but poorly on unseen data. By systematically varying hyperparameters and evaluating the model's performance on different validation sets, the network aims to achieve the best trade-off between under-fitting and over-fitting, ultimately leading to more robust and generalizable models.

8.1.4 Practical workflow to developing ANN

In practice, the typical workflow for developing an ANN encompasses establishing a dataset, cleaning and prepping the data, developing and validating the model via hyperparameters tuning and cross-validation, and finally deploying the model into its dedicated application. These steps are illustrated in Figure 8.4. In the following, we describe the general steps followed to develop the models used in sections 8.2 and 8.3 for HET. For a more in-depth understanding of these steps, readers are encouraged to refer to specialized literature [Géron 2019]. In practice, we used the Scikit-learn library to wrap all these steps in a pipeline [Pedregosa *et al.* 2011].

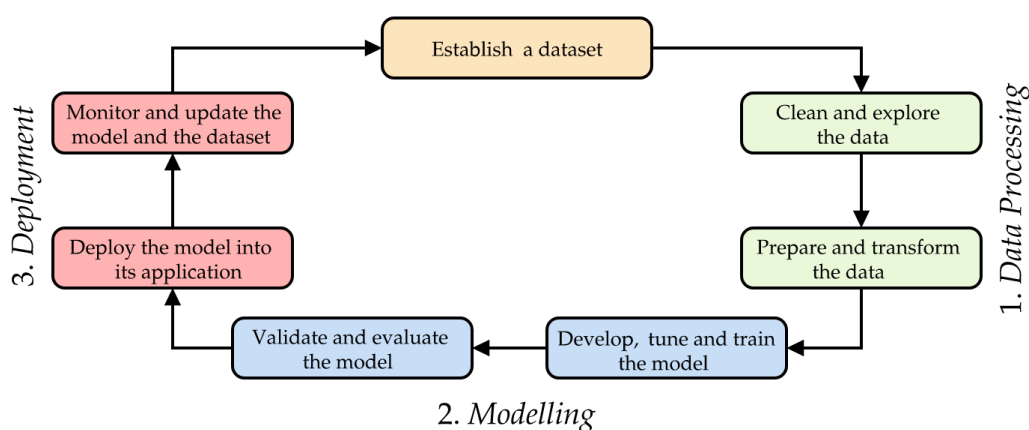


Figure 8.4: Typical workflow for developing ANNs

Establishing a dataset The development of a neural network model begins with careful data collection and preprocessing for the desired application. Typically, in our case, this includes spectral line intensities, either from the CRM for Section 8.2 or from experiments at different operating conditions for section 8.3, with a focus on maintaining data relevance and representativeness. Previous studies in other fields insisted that the quality of the predictions in DLS depends a lot on the quality and size of the spectroscopic data, as well as the complexity of the learning algorithm, specifically preconizing large datasets for experimental applications [Ghosh *et al.* 2019].

Data processing Next, the data is preprocessed to refine it for ML. This critical phase encompassed key steps:

- Data cleaning consists of identifying and removing outliers and erroneous data points to ensure dataset integrity and enable the network to focus on meaningful data patterns without undue influence from anomalies. This avoids, for instance, the over-representation of a specific operation condition, due to the way measurements are taken or how the sampling is performed.

- Feature selection consists of reducing the number of inputs to train the model by selecting the most "relevant" features from raw data. Feature selection allows for streamlining and accelerating the learning while mitigating overfitting risks. In this work, feature selection is especially important due to the large number of features— all spectral lines in the visible range.
- Normalization consists of achieving uniform scaling to prevent some features from dominating the learning process because of their magnitude. This is performed through the application of normalization techniques. Throughout this work, all input and target variables were normalized within the $[0, 1]$ range using a MinMax scaler.

Modelling The next stage involves the model development which starts with the ML model selection. Indeed, different learning models yield varying performances on experimental data, as shown in the work of [Joung *et al.* 2021], where ANN outperformed Random Forest classifiers in predicting functional groups in organic molecules. In this chapter, we focus only on ANN as our chosen models due to their inherent flexibility, serving as an apt starting point.

Data splitting is the next step which involves dividing the dataset into training and testing/validation subsets. This division enables the model training on one subset while *independently* evaluating its predictions on another. In this chapter, the features dataset is split into a 2:1 ratio, with two-thirds allocated for training and one-third for testing. Additionally, data splitting is often combined with cross-validation techniques to assess the impact of specific training and testing set pairings. In this chapter, we employed a Monte Carlo cross-validation approach, which involves randomly splitting the dataset into training and testing sets.

The next step is the hyperparameter tuning. In this chapter, the hyperparameters considered included α , β_1 , and β_2 for ADAM gradient descent, the number of layers, the number of perceptrons per layer, and the learning rate α initialization. Note that the number of perceptrons was kept constant across the layers as it should not have a major impact [Géron 2019] and that various activation functions were also tested before ultimately selecting the ReLU function since no significant impact on the learning quality was observed on the performance of the network. The optimal hyperparameters were determined through a Random Grid Search.

Finally, the trained model is validated to ensure the model's generalization ability. We use again a Monte-Carlo cross-validation approach but with more extensive pairing of the training and testing subsets. This allows the model performance to be consistent along the pairing. In this chapter, the performance is evaluated using two different cost functions MAE and MSE.

Deployment Finally is the model integration into real-world applications. Yet, in this chapter, we concentrate on the preceding stages of model development and validation. The deployment of the models into practical applications may be explored in future work.



Figure 8.5: Schematic representation of the learning process for inverting the HETOD CRM. This figure illustrates the development of ANNs to predict the electron temperature T_e based on optical emission data.

8.2 Accelerating predictions with the collisional radiative model

In this section, we explore the potential of replacing the CRM with an ANN. Such a substitution promises a notable acceleration in computation, as ANNs are a function evaluation compared to the basin hopping optimization implemented in the current CRM. Our primary objective is to construct an ANN capable of estimating the electron temperature by learning from the CRM specifically how T_e relates to the output optical emission of the CRM, as illustrated in Figure 8.8. It is worth noting that we solely focus on estimating T_e , as it is a key parameter of the plasma.

8.2.1 Data collection and integration approach

To train and validate our ANN, we directly generate training data from the CRM within the parameter range outlined in Table 8.1, maintaining a constant optical length $d = 15$ cm.

Table 8.1: Range of plasmas parameters used to generate the synthetic spectra with the CRM

Parameter	Minimum	Maximum
T_e [eV]	0.1	25
n_e [m ⁻³]	10 ¹⁶	10 ²⁰
n_g [m ⁻³]	10 ¹⁸	10 ²²

Our database comprises 50000 entries, generated through random grid sampling. Instead of using individual line intensities, the ANN's input is composed of intensity ratios. The intensity ratio $r_{i,j}$ is calculated as:

$$r_{i,j} = \frac{I_{ij}}{\sqrt{\sum_{\lambda_{ij}} I_{ij}^2}} \quad (8.7)$$

We focus on lines within the visible and near-infrared range. This selection re-

sults in a dataset encompassing 15 lines, which aligns with the set of lines used for optimization in Chapter 7:

- 764.41 nm, 788.95 nm, 820.85 nm, 823.38 nm, 826.87 nm, 828.23 nm, 834.91 nm, 841.15 nm, 882.18 nm, 893.32 nm, 895.47 nm, 904.79 nm, 916.51 nm, 980.23 nm and 992.59 nm

Model development

In Section 8.1.4, we discussed the general framework for the development of the ANN. In this subsection, we list the parameters used in hyperparameter tuning to achieve the desired speed-up of the CRM. The generated dataset was divided into a training set (2/3 of the data) and a testing set (1/3 of the data). Hyperparameter tuning involved the exploration of 10000 different combinations of different hyperparameters using a random Grid Search. The hyperparameters considered in this tuning process included α , β_1 , and β_2 for the ADAM optimizer, the number of hidden layers, the number of perceptrons per layer, and the initialization of the learning rate. The number of perceptrons remained constant across the layers, and we employed the Rectified Linear Unit (ReLU) activation function.

Table 8.2 presents the ranges and distributions of the explored hyperparameters. To assess the performance of each model during the tuning process, we conducted a preliminary partial four-fold cross-validation. For the preliminary model training and exploration, we employed the Monte Carlo cross-validation approach. This technique randomizes the dataset splitting into training and testing sets, reducing the impact of specific pairings. In each step of the hyperparameter tuning, we evaluated model performance using three scoring metrics: the coefficient of determination R^2 , MAE, and MSE. The model that exhibited the best scores for all three metrics was selected.

Table 8.2: Range and distribution of the hyperparameters explored in the random grid search for tuning of the ANN

Parameter	α	β_1	β_2	Layers	Perceptrons
Range	1×10^{-7} – 1×10^{-3}	0.95–0.96	0.98–1	1–56	1–50
Distribution	Log-uniform	Uniform	Uniform	Uniform	Log-uniform

For cross-validation, we executed 1000 random splits of the dataset into training and testing sets, and the model’s performance was assessed using the aforementioned three metrics. The results from each split were plotted as histograms to visualize the distribution of model scores.

It is important to underline that the ANN was trained and tested exclusively on the CRM input-output data. The performance of the network was evaluated hence, on synthetic spectra from the CRM, rather than experimental spectra. Comparison

of predictions to experimental results from the basin hopping optimization is carried out using experimental data from the optimization process in Configuration 1, specifically from the axial scans.

8.2.2 Results

Best-performing models

Table 8.3 reports the hyperparameter tuning results and presents the best-performing model for predicting the electron temperature T_e from the CRM synthetic spectra. Figure 8.6 a) displays the distribution of R^2 scores obtained from cross-validation, which showcases the robustness of the model across 1000 random dataset splits. The developed ANN is inverting the CRM.

Table 8.3: Hyperparameters of the best-performing model from the cross-validation results

Parameter	T_e model
α	9.94×10^{-5}
β_1	0.95548
β_2	0.99585
Hidden Layers	2
Perceptrons	43
Initial Learning Rate	2.22×10^{-3}
R^2 Score	$95\% \pm 2$

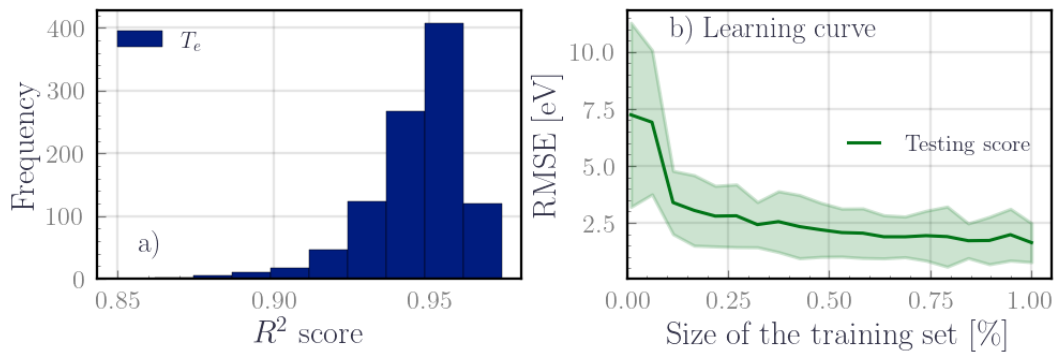


Figure 8.6: Performance of the selected ANN model learning the CRM. a) shows the distribution of R^2 testing scores in cross-validation across the 1000 train-test pairing. b) shows the evolution of the R^2 score with the size of the training set. The testing set was unchanged and corresponded to a third of the dataset.

The results of testing and validation on data generated by the CRM exhibit a good performance with an R^2 score of $95\% \pm 2$. Examining the learning curve in Figure 8.6 b), we observe that the learning process converges effectively to an

average RMSE of 2 eV, yielding an order of magnitude of the uncertainty on the predictions. Keep in mind that this error is an average error on the parametric space described in Table 8.1.

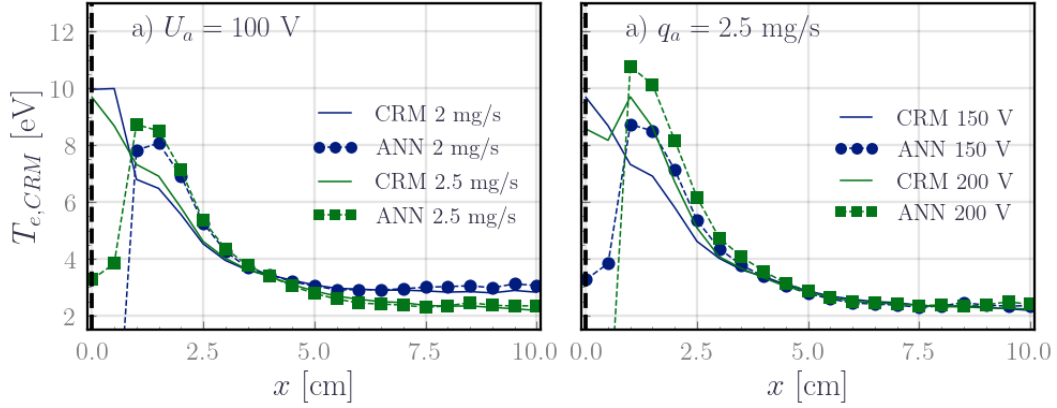


Figure 8.7: Comparison between the results from the CRM via a basin hopping least square optimization (fine solid lines) with the results from the ANN predictions (scatter plot with dashed lines). This comparison involves experimental spectra from the axial scans in Chapter 7.

To evaluate how learning on synthetic spectra relates to experimental spectra, we apply the developed ANN to experimental intensity ratios obtained from the axial scans from Chapter 7. Figure 8.7 presents a comparison between the optimization results from the CRM (solid lines) and the predictions generated by the ANN (scatter plot), for a constant voltage of 100 V and two values of the xenon flow rates $2 \text{ mg}\cdot\text{s}^{-1}$ and $2.5 \text{ mg}\cdot\text{s}^{-1}$ on Figure 8.7 a) and a constant xenon flow rate of $2.5 \text{ mg}\cdot\text{s}^{-1}$ and two anode voltage 150 V and 200 V on Figure 8.7 b). The overall agreement between the two sets of results is promising, capturing trends and features of the plasma plume accurately. Notably, the ANN predictions align well with the CRM predictions in the far plume region. However, at the exit plane of the thruster, while the agreement remains good, there is a slight deviation between the ANN predictions and the CRM results.

While these initial results are encouraging with the required time for the prediction of the plasma temperature reduced from several $\approx \text{min}$ with the basin hopping optimization to several $\approx 10 \text{ ms}$, further investigation is warranted. It is important to note that the testing results on the CRM data consistently performed well. In contrast, predictions on experimental data, especially near the thruster's exit plane, showed more variability. Notably, the trends were not impacted, whereas the values shifted by $\pm 2 - 3 \text{ eV}$, depending on the train-test set pairing. This underscores that the synthetic spectra do not relate systematically to experimental spectra which is likely due to the inherent differences between optimizing the likelihood between experimental and synthetic spectra and learning the CRM model itself which is akin to interpolating over 15 variables. To address this, future work should consider building a comprehensive database that includes spectral data and corresponding

T_e values for a more accurate and holistic approach. The first steps of such a work are laid in the next section 8.3.

8.3 Learning macroscopic parameters

This section presents the initial steps in the application of DLS to HET, aiming to determine the thruster’s macroscopic parameters. The primary objective is to construct an optical footprint of the HET using ANNs capable of predicting operational parameters such as the anode voltage U_a , discharge current I_d , anode flow rate q_a , and coil current I_b . The ultimate goal is to deploy this model into a PID controller, which will actively monitor and regulate these operational parameters based on optical emission data. We have chosen to develop four separate ANNs, each tailored to predict one of the target parameters: q_a , I_b , U_a , and I_d . This deliberate separation allows for consistent assessments of the uncertainties on each parameter across a homogeneous unit scale. This approach becomes particularly crucial due to the inherent differences in voltage and flow rate ranges, which can span orders of magnitude.

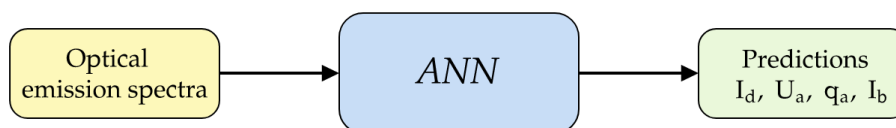


Figure 8.8: Schematic representation of the learning process for macroscopic parameters in HET. This figure illustrates the development of ANNs to predict the anode voltage U_a , discharge current I_d , anode flow rate q_a , and coil current I_b based on optical emission data.

8.3.1 Experimental setup, data acquisition and cleaning

In this section, we detail the experimental approach for acquiring and preparing the dataset before developing the ANN.

Experimental setup

The emission spectra were captured within the cryogenic vacuum chamber of the PIVOINE 2G test facility, during a *Safran* test campaign. A laboratory model Hall Thruster was placed inside this stainless steel vacuum chamber, with dimensions of 4 m in length and 2.2 m in diameter. The chamber was maintained at a pumping speed of $70\,000\text{ L}\cdot\text{s}^{-1}$ for xenon, resulting in a background pressure of approximately 5×10^{-6} mbar for a xenon flow rate of $1\text{ mg}\cdot\text{s}^{-1}$. Multiple viewports allowed optical access to the thruster’s plasma plume during the experiment. Emission spectra

were collected using a collimated optical fiber positioned approximately at $x \approx 2$ cm from the thruster's exit plane, as illustrated in Figure 8.9. The emission was then collected to an Avantes *AvaSpec-Dual* spectrometer. This is the same configuration as Configuration 1 used in Chapter 6.

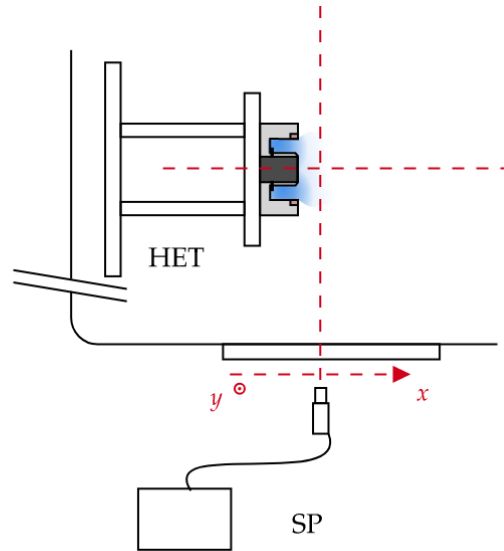


Figure 8.9: Experimental setup in PIVOINE 2G vacuum chamber. The collimated optical fiber is pointing at the thruster's exit plane perpendicular to the thruster's axis. The origin of the x axis is placed at the exit plane of the thruster.

Procedure to change the operating parameters

The control of the operating parameters of the thruster, i.e. the anode voltage U_a , the coil current I_b , and the gas flow rate at the anode q_a , was achieved using a LabVIEW interface. A systematic protocol was adopted to change the operation parameters, wherein, for a given flow q_a at the anode, a step increment of $\delta I_b = 0.2$ A was used to adjust the coil current, then, for each new value of the coil current I_b , the anode voltage U_a followed a ramp pattern within a specified voltage range at increments of 5 V every 0.5 s and returned to the nominal value of $U_{\text{nom}} = 300$ V at the end before passing to the next coil current value. The xenon flow rate at the anode varied between $1 \text{ mg}\cdot\text{s}^{-1}$ and $3.75 \text{ mg}\cdot\text{s}^{-1}$, with the cathode flow rate adjusting proportionally. An example of a measurement cycle is illustrated in Figure 8.10. Table 8.4 sums up the range of operating conditions explored during the experiment.

Spectral data acquisition and cleaning

The acquisition of the emission spectra and the changes in the operating parameters were synchronized to ensure simultaneous data acquisition at a uniform temporal resolution of 0.5 s. Spectra were acquired at 0.5 s intervals and averaged over eight

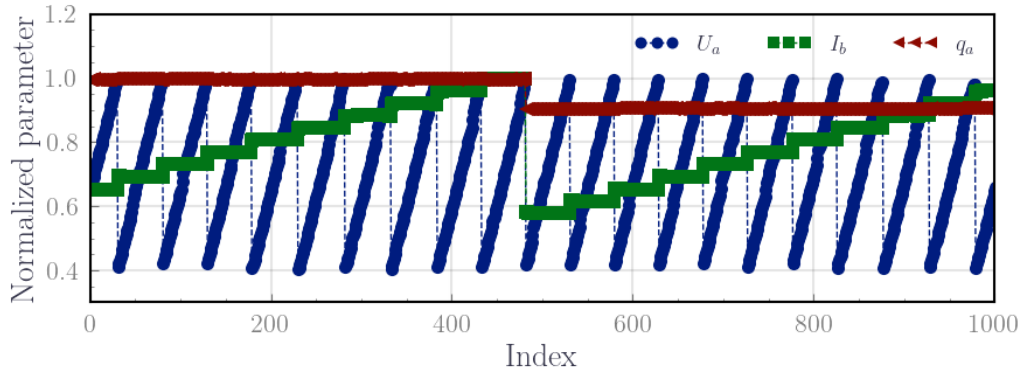


Figure 8.10: Time evolution of the normalized values of the operation parameters during the acquisition of the spectra. For a given flow rate q_a , the coil current I_b was changed at increments of $\delta I_b = 0.2$ A and the anode voltage U_a described a ramp.

Table 8.4: Range of the explored operating conditions of the thruster during the acquisition of the spectra.

Parameter	Min	Max
q_a [ms]	1.00	3.75
I_b [A]	3.0	5.4
U_a [V]	200	500

spectra, integrated over 25 ms. Each captured spectrum corresponded to a distinct operational condition defined by q_a , U_a , I_b , and I_d . Post-processing was subsequently carried out to eliminate any bias associated with the discharge extinction. Data points associated with nominal operating conditions at $U_{\text{nom}} = 300$ V before and after each cycle were particularly removed. Figure 8.11 illustrates the distribution of the parameters in the data set before and after data cleaning.

The cleaned database accounts for both neutral and singly ionized xenon lines. The emissions were processed using the same procedure specified in Chapter 6. Specifically, after removing the continuous background spectra with a Savitzky-Golay filter, we defined a noise threshold of 50 counts, and lines with intensities below this threshold were discarded, maintaining a signal-to-noise ratio of 2 across the data set. Line identification was performed manually and relied on a wavelength list obtained from NIST. A total of 21 neutral lines and 5 ionic lines were identified.

- xenon I lines : 688 nm, 712 nm, 728 nm, 733 nm, 758 nm, 764 nm, 788 nm, 797 nm, 820 nm, 823 nm, 826 nm, 828 nm, 834 nm, 841 nm, 882 nm, 895 nm, 904 nm, 916 nm, 951 nm, 980 nm and 992 nm.

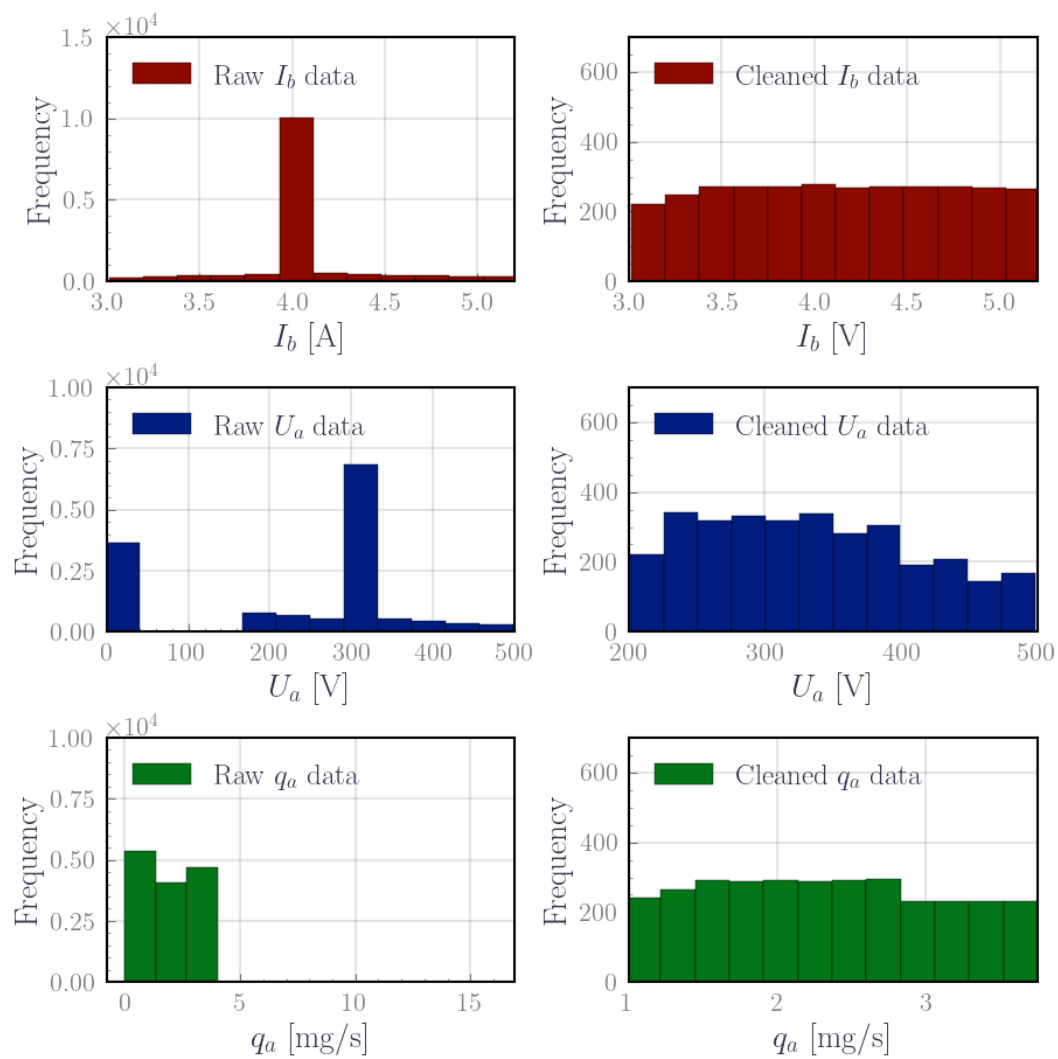


Figure 8.11: Histograms for the explored operation parameters before and after data cleaning. After the cleaning, the data is uniformly distributed.

- xenon II lines : 542 nm, 605 nm, 659 nm, 699 nm and 716 nm.

The resulting dataset consisted of an array of 6469×26 intensity lines, each representing a distinct operational parameter. This dataset serves as the foundation for the subsequent development of ANN to predict q_a , I_b , U_a , and I_d from the spectral data. Per the workflow in Figure 8.4, the next subsection will present the development of the ANN and the settings for feature selection, hyperparameters tuning, and cross-validation.

8.3.2 Model development

Feature selection

The goal was to reduce the number of learning spectral lines to the most informative ones. The feature selection methods included correlation coefficients measured as F-scores and mutual information tests from the Sci-kit learn library.

Correlation coefficient The correlation coefficient quantifies the linear dependence between two groups of data, which are the spectral line intensities and the target variables (q_a , I_b , U_a , I_d) in this work. For each spectral line I_i , its correlation coefficient with each target parameter Y_j is computed using:

$$\sigma(I_i, Y_j) = \frac{\text{cov}(I_i, Y_j)}{\sigma_{I_i} \sigma_{Y_j}}, \quad (8.8)$$

Here, $\text{cov}(I_i, Y_j)$ represents the covariance between line I_i intensity and target parameter Y_j , while σ_{I_i} and σ_{Y_j} denote the standard deviations of I_i and Y_j respectively. The F-score is derived from the correlation coefficient as follows:

$$F = \frac{\sigma^2(I_i, Y_j)}{1 - \sigma^2(I_i, Y_j)} \quad (8.9)$$

Based on F-scores, the top four spectral lines showing high association with a particular target parameter were included in the model.

Mutual information The Mutual Information (MI) score measures the information shared between features and target variables. High MI scores indicate the importance of a spectral line for prediction. The MI score between variables I_i , Y_j is defined as:

$$I(I_i, Y_j) = \int_{x,y \in I_i \times Y_j} \mu_{I_i, Y_j}(x, y) \log\left(\frac{\mu_{I_i, Y_j}(x, y)}{\mu_{I_i}(x) \mu_{Y_j}(y)}\right) \quad (8.10)$$

where $\mu_{X,Y}(x, y)$ is the joint probability distribution and $\mu_X(x)$ and $\mu_Y(y)$ are the marginal probability distributions. This integral was estimated using the nearest neighbor methods [Kraskov *et al.* 2004, Ross 2014]. The top four spectral lines with the highest MI scores were selected for the model.

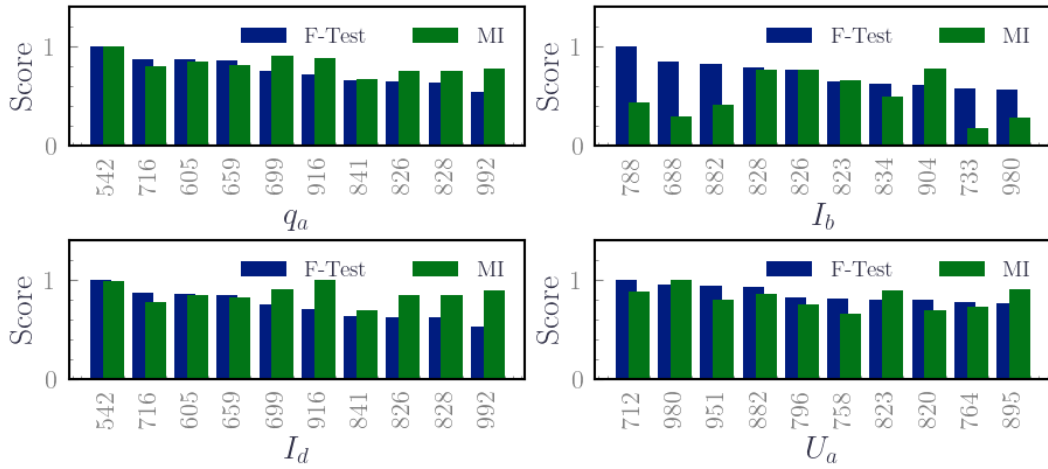


Figure 8.12: Spectral Line Selection for Target Parameters. The figure shows the histogram with the normalized scores of the 8 best-scoring features based on the F-Test (blue) and MI test (green).

Feature selection results

Figure 8.12 and Table 8.5 report the best scoring lines for each target parameter. Notably, ionic lines demonstrate greater relevance in predicting flow rate and discharge current, while neutral lines exhibit stronger relevance for coil current and voltage. This resonates with the observations in Chapter 7, Figures 7.14, and 7.15. Additionally, many significant neutral lines stem from energy levels with a core angular momentum of $j_c = 3/2$, ($2p5 - 2p10$ levels). This supports and complements the previous observations from Chapters 4 and 5 and the work of [Karabadzhak *et al.* 2006] on the relevance of these lines for OES for HETs. Specifically, the coupling with PIC showed that the lines from $2p5 - 2p10$ yield the line ratios that are most relevant to predict T_e and n_e and here it is shown that they also reflect the operation parameters of the thruster. These aspects will be discussed later in the chapter. Henceforth, the learning lines consist of the set of lines in Table 8.5 except for 659 nm and 951 nm lines. These were excluded from the final selection due to missing diagnostic data in the NIST database. The learn feature set consists of 15 spectral lines.

Training and validation

The high-level process of developing the ANN for each target parameter has been presented in Section 8.1.4. In this subsection, we explicit the range of parameters of the exploration. First, the dataset was divided into a 2/3 training set and a 1/3 testing set. The hyperparameters tuning was conducted using random Grid Search, exploring 10000 different combinations of the hyperparameters. As mentioned before, the hyperparameter included α , β_1 , and β_2 , the number of layers, the number of perceptrons per layer, and the learning rate initialization. The number of perceptrons remained constant across the layers. The activation function

Table 8.5: List of the four best scoring lines selected based on the F-scores and MI scores for each of the four target parameters. The ionic lines are put in bold

Parameter	q_a	I_b	I_d	U_d
F-score	542 nm	788 nm	542 nm	712 nm
	716 nm	688 nm	716 nm	980 nm
	605 nm	882 nm	605 nm	951 nm
	659 nm	828 nm	659 nm	882 nm
MI score	542 nm	916 nm	916 nm	980 nm
	916 nm	992 nm	542 nm	895 nm
	699 nm	904 nm	699 nm	823 nm
	605 nm	826 nm	992 nm	712 nm

was fixed to ReLU. Table 8.6 lists the hyperparameter ranges for the random grid search. For each explored model during the tuning, a four-fold cross-validation was performed, as a preliminary validation. For model validation, we used the Monte Carlo cross-validation approach. At each step, model performance was evaluated

Table 8.6: Range of hyperparameters explored in the random grid search for tuning the ANN predicting the operation parameters of the thruster.

Parameter	α	β_1	β_2	Layers	Perceptrons
Range	$1 \times 10^{-7} - 1 \times 10^{-2}$	0.95 – 0.96	0.98 – 1	1 – 5	1 – 100
Distribution	Log-uniform	Uniform	Uniform	Uniform	Log-uniform

by three scoring metrics: the coefficient of determination R^2 , MAE, and MSE. The model with the best score for the three metrics was selected. For cross-validation, we performed 10000 random splits of the dataset into a training set and a testing set. The performance was evaluated using the three metrics specified earlier. The results from each split were plotted into a histogram to inspect the distribution of the model scores.

8.3.3 Results and insights

Model performance evaluation

Table 8.7 summarizes the best-performing models obtained after hyperparameter tuning and cross-validation. Figure 8.13 displays the distribution of R^2 scores from cross-validation across 10000 random dataset splits. All models perform well, with I_b achieving the lowest average R^2 score at approximately 84%, while q_a and I_d models achieve high scores of around 99%. For the flow rate and the discharge current, the linear relationship with emission intensity accounts for the models' performance.

The possibility of using simpler linear models for these parameters will be discussed later.

Table 8.7: Hyperparameters of the best models for each operation parameters obtained from the cross-validation results

	U_a Model	I_d Model	I_b Model	q_a Model
α	3.36×10^{-6}	1.80×10^{-5}	2.51×10^{-4}	8.15×10^{-7}
β_1	0.95472	0.95661	0.95837	0.95792
β_2	0.98549	0.98006	0.99850	0.98145
Layers	4	4	3	3
Perceptrons	90	99	92	92
Initial Learning Rate	2.42×10^{-3}	2.17×10^{-3}	3.32×10^{-3}	2.38×10^{-3}
R^2 Score	$95\% \pm 3\%$	$99\% \pm 0.1\%$	$84\% \pm 5\%$	$99\% \pm 0.1\%$

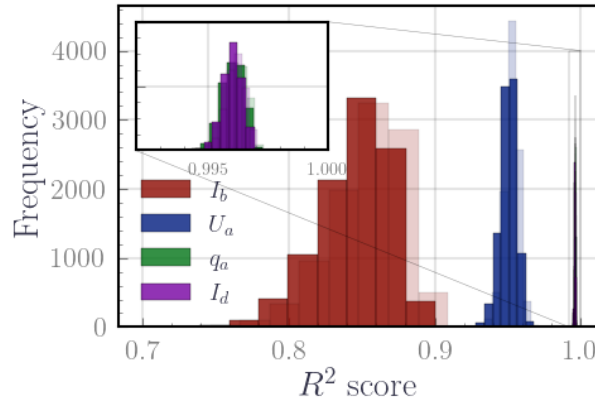


Figure 8.13: Distribution of R^2 scores for the selected models for each operation parameter from cross-validation across 10000 models. Opaque colors correspond to test scores when evaluating the model on the test data and transparent color is the training score when evaluating the model on the training data.

Examining the error distributions in Figure 8.14, both MAE and MSE are relatively small, indicating reasonable prediction uncertainty (approximately 10%). A "confidence envelope" within three times the average square root of the MSE is reasonable. Notably, MSE for I_b and U_a is twice the MAE, suggesting outliers in predictions. This is evident in Figure 8.15 where predicted vs. target values for U_a and I_b show points outside the $y = x$ line, while q_a and I_d align closely. Nevertheless, Figure 8.15 still highlights the capability of ANN to capture non-linear relationships in predicting voltage and magnetic configuration, primarily driven by the electron temperature.

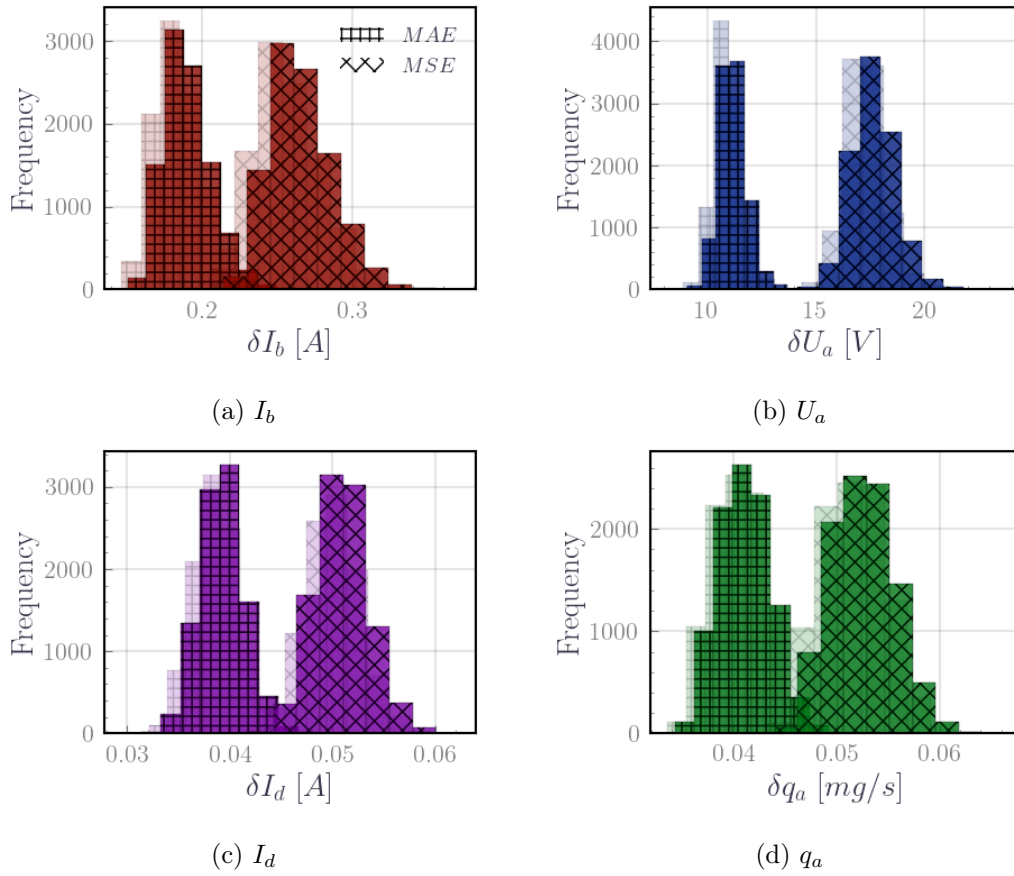


Figure 8.14: Distribution of MAE and the root of the MSE scores for the selected models for each operation parameter from cross-validation across 10000 models. Opaque colors correspond to test scores when evaluating the model on the test data and transparent color is the training score when evaluating the model on the training data.

Reduction of the number of learning lines

The process of feature selection has effectively reduced the number of lines from 26 to 15, primarily based on statistical significance rather than physical arguments. Interestingly, we suggest some hypotheses to link statistical relevance to physical grounding. Firstly, the selected lines exhibit high radiative characteristics, marked by high Einstein coefficients. Secondly, in alignment with the KCD model, lines originating from the $j_c = 3/2$ energy levels are significant for the diagnostic, along with the use of 823 nm and 828 nm wavelengths. Furthermore, the common use of 980 nm and 916 nm xenon lines in low-pressure plasma diagnostics further supports the results of feature selection.

On the other hand, ionic lines were relevant for predicting current and flow rates based on the feature selection results. It is expected that the radiative emission, both neutral and ionic, is dependent on these two parameters in such a way that an

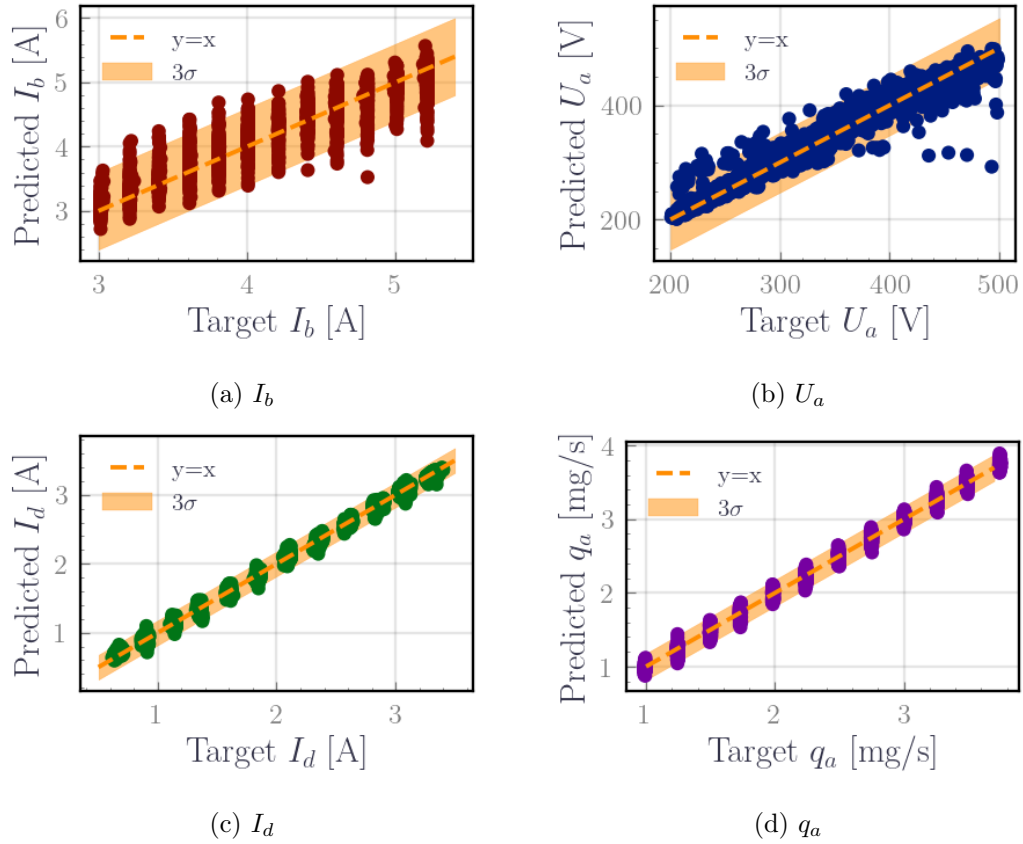


Figure 8.15: predicted vs. target values for four parameters. The orange line corresponds to the line $y = x$. The predictions align around this line, illustrating the performance of the model. The uncertainty envelope is a 3σ envelope based on the root of the average MSE score.

increase in the flow rate leads to enhanced emission in the plume. This aligns with the observations made in the previous chapter and the observation on the optical emission in the work by [Hara & D.Boyed 2013]. The higher scores of ionic lines might probably reflect their higher sensitivity to the electron temperature when the flow rate changes compared to neutral lines. Moreover, neutral lines were more relevant for predicting the magnetic field topology imposed by I_b and the anode voltage U_a based on the feature selection results. This might be attributed to the relationship between the magnetic field within the HET channel and the ionization source term. Typically we observe a decrease in the neutral lines emission with an increasing voltage and magnetic current.

While statistical tests may not inherently provide physical explanations, they effectively demonstrate that statistical screening complements physical intuition in selecting pertinent lines for models and parameter exploration.

ANN vs. other learning models

The ANN's performance in predicting the four parameters suggests that it may be an overly complex tool for predicting the flow rate and the discharge current, in particular, with a 99% R^2 score. This stems from the linear relationship between these parameters and the optical emission. Therefore, simpler linear models such as Ridge regression or Lasso may be more suitable for these parameters.

Figure 8.16 compares the R^2 scores of three linear models with ANN for individual prediction of I_b , U_a , q_a , and I_d : linear regression, Lasso, and Ridge regression. ANN slightly outperforms linear models for flow rate and discharge current. However, for predicting anode voltage and magnetic configuration, ANN significantly outperforms linear models due to non-linear relationships influenced by electron temperature. When aiming for a single model predicting all four parameters simultaneously, ANN outperforms linear models by being able to accommodate both the linear trends of I_d and q_a and the non-linear trends of U_a and I_b . This highlights that the model's choice should reflect the problem complexity and that for multi-target prediction, ANN provides sufficient flexibility.

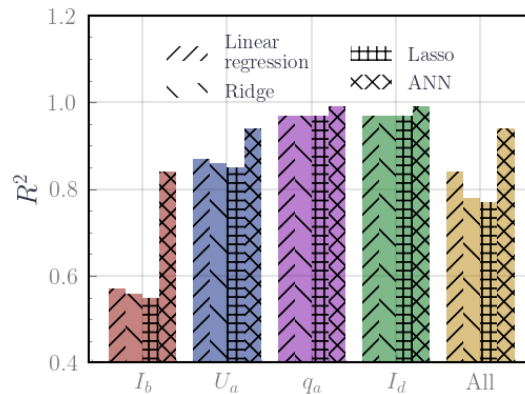


Figure 8.16: Comparison of the performance of different learning models. Linear models have a competitive performance on q_a and I_d , while ANN outperforms these models for U_a and I_b .

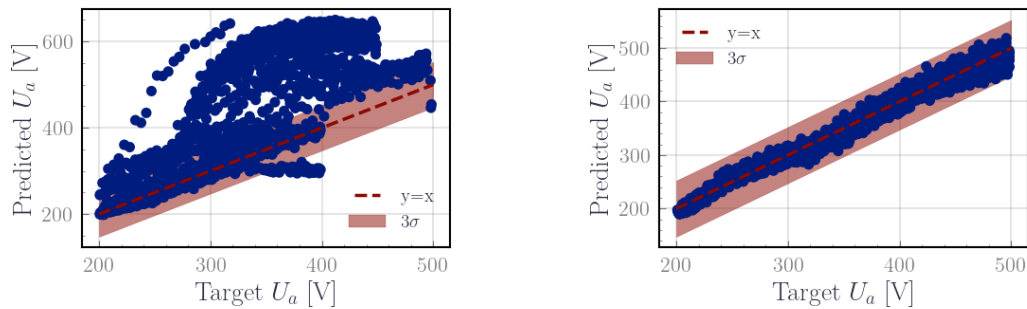
Generalization and limitations

The validation and the training of the model were subjected to cross-validation using Monte Carlo sampling on the database. Given the size of the database, the training set covered a wide range of operating conditions. This provided a well-trained model with a good level of confidence in its predictions. The choice of Monte Carlo sampling was motivated by the need to mitigate potential biases introduced by consecutive voltage ramp patterns in the data collection method, ensuring that the model learned from a representative dataset.

Imagine now that the model was trained on a dataset that represents only a part of the operating conditions. For instance, the model is trained on low flow rates

and then tested on high flow rate values or vice versa. Preliminary results shed light on this matter. When the model predicting the anode voltage was trained on nominal flow rates (ranging from 1.25 to 3.25 $\text{mg}\cdot\text{s}^{-1}$) and subsequently tested on extreme flow rate values (3.25 to 3.75 $\text{mg}\cdot\text{s}^{-1}$ and 1 to 1.25 $\text{mg}\cdot\text{s}^{-1}$), it exhibited poor predictive capabilities, as illustrated in Figure 8.17a. This poor performance can be attributed to the limited variability of the thruster's operational regime within the nominal flow rate range. Notably, significant changes in the $I - V$ curves of the thruster were observed at extreme flow rate values, indicating a pronounced shift in the operational regime and the discharge kinetics.

Conversely, when the model was trained on extreme conditions (1 to 1.75 $\text{mg}\cdot\text{s}^{-1}$ and 3 to 3.75 $\text{mg}\cdot\text{s}^{-1}$) and subsequently tested within the nominal flow rate range (1.75 to 3 $\text{mg}\cdot\text{s}^{-1}$), it yielded more competitive predictive results, as illustrated in Figure 8.17b. This suggests that the model can learn more effectively from situations characterized by significant deviations from nominal conditions. These findings underscore the critical importance of incorporating data from extreme experimental conditions in the model training process. By doing so, the model gains the ability to handle and generalize to a broader range of operational scenarios. This is particularly valuable for robust and accurate modeling in real-world applications.



(a) Training on nominal values and testing on very high and very low flow rate values

(b) Training on very high and very low flow rate values and testing on nominal values

Figure 8.17: Impact of learning on a specific range of flow rate instead of training on random sampling.

8.4 Machine learning control with PID

The goal of this section is to discuss the implementation of PID controllers with the DLS ANN developed in the previous section for controlling both the flow rate q_a and the voltage U_a from the optical emission generated by the plume of HET.

8.4.1 Control strategy and implementation of the PID

PID controllers are fundamental in control theory, finding wide application across various industries. They leverage the interaction between proportional (P), integral (I), and derivative (D) error components. Mathematically, a PID controller is represented as:

$$u(t) = k_p e(t) + k_i \int_0^t e(\tau) d\tau + k_d \frac{de(t)}{dt} \quad (8.11)$$

Here, $e(t)$ is the error signal, $u(t)$ is the control signal, and k_p , k_i , and k_d are the proportional, integral, and derivative coefficients, respectively. The P term ensures the control output is proportional to the error, the I term corrects accumulated error over the past, and the D term adjusts for the error's rate of change accounting for future dynamics of the system. Choosing the appropriate PID coefficients for a specific application is the challenging part of implementing PID due to their interdependence. Various methodologies have been developed from the work of [Ziegler & Nichols 1942] and [Åström & Hägglund 1984] to tune PID controllers.

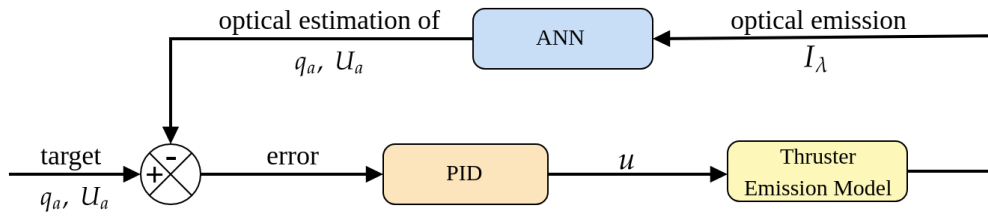


Figure 8.18: Block diagram for the PID controller.

The control strategy proposed here consists of a traditional closed-control loop, consisting of the PID controller, the thruster, and a sensor, which is here an ANN optical sensor (Figure 8.18). The control loop involves:

1. Define the thruster's target flow and voltage values q_a^T and U_a^T .
2. Estimate the current values of the anode flow rate and the anode voltage q_a^c and U_a^c via the ANN's prediction from the plume emission spectra.
3. Calculate the error vector $e = (q_a^c - q_a^T, U_a^c - U_a^T)$.
4. Calculate the control action u via the PID using Eq. (8.11)
5. Adjust the applied flow and voltage in the thruster based on the value of the control action from step 4.
6. Measure the optical emission from the thruster and repeat step 2 until converging to the target values.

To *simulate plasma emission at a fixed magnetic configuration*, we linearly interpolated the experimental intensity of the 15 spectral lines over the mesh grid of U_a and q_a . Gaussian noise, with standard deviations of $\sigma = 3$ and $\sigma = 10$, was added to emulate experimentally observed noise levels at different strengths. These values are based on the estimation of the noise level from the experimental spectra after the subtraction of the continuous background.

The PID controller uses constant coefficients and the optimal coefficients were manually tuned using Ziegler's method [Ziegler & Nichols 1942]. The chosen coefficients are reported on Table 8.8. Note that a maximum control action u_{max} was included in the controller to prevent drifting. Specifically, if the calculated control action u is greater than u_{max} , the controller will systematically return u_{max} .

Table 8.8: Coefficients of the PID Controller

	K_p	K_i	K_d	u_{max}
Flow Controller	1	10	0.0001	0.5 mg.s^{-1}
Voltage Controller	1	1	0.0001	100 V

Three control scenarios were simulated in this setup:

Control of the anode flow rate at a fixed anode voltage rate: The voltage at the anode was fixed at 300 V. The initial flow rate was set to 2 mg.s^{-1} , with the target value switching every 3 s between 1.5 mg.s^{-1} and 3 mg.s^{-1} .

Control of the anode voltage at a fixed anode flow rate: The flow rate at the anode was fixed at 3.5 mg.s^{-1} , with the initial voltage at 280 V. Target anode voltages switched every 3 s between 250 V and 300 V.

Simultaneous control of the anode voltage and the anode flow rate: Initial conditions: $U_a = 250 \text{ V}$ and $q_a = 1.5 \text{ mg.s}^{-1}$. Various combinations of the variation of the voltage and the flow rate targets were tested in cycles of 3 s (increasing voltage with increasing flow rate, increasing voltage with decreasing flow rate, etc ...). These combinations are reported on Table 8.9.

Table 8.9: The target values for the third simulation

Target values	1 st cycle	2 nd cycle	3 rd cycle	4 th cycle	5 th cycle
q_a^T [mg.s^{-1}]	2.25	3.00	2.25	1.50	2.25
U_a^T [V]	350	250	350	250	250

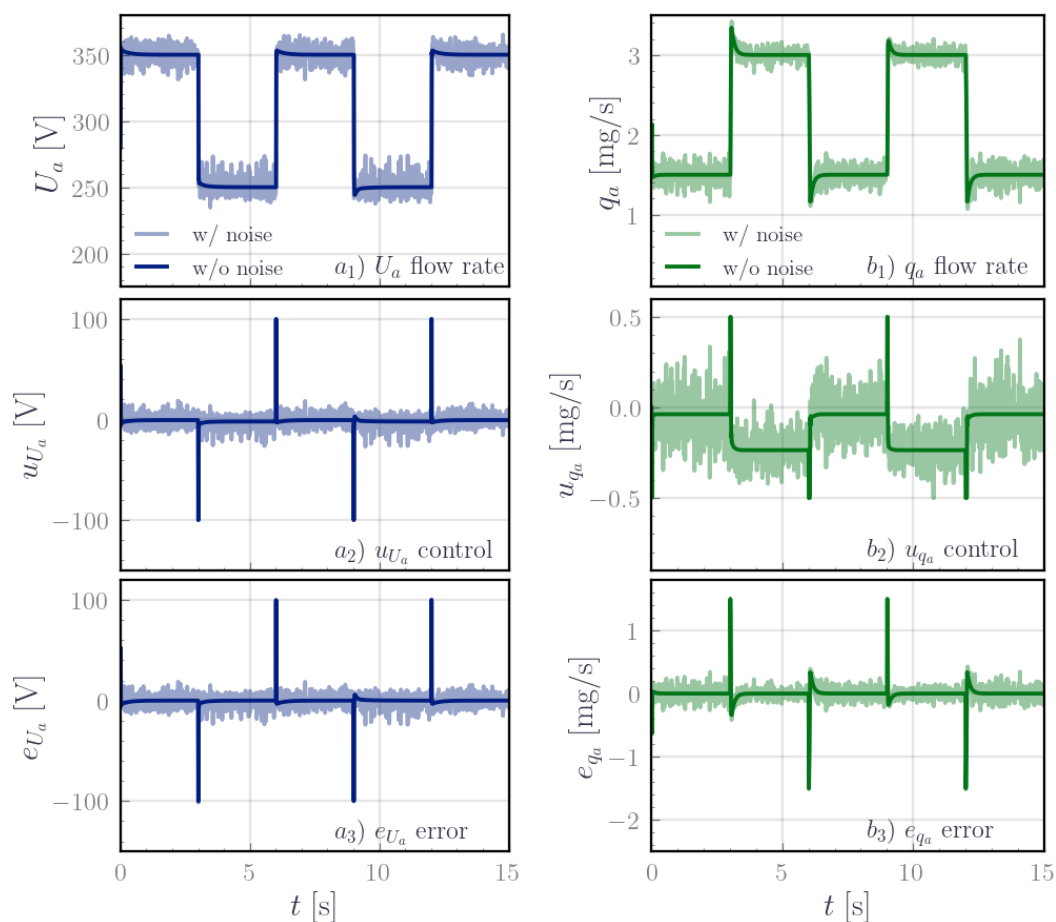
In all these scenarios, the PID controller's frequency was fixed to 100 Hz.

8.4.2 Control simulation results

The simulation results for the three control scenarios illustrate that the actual system outputs closely align with the target values (Figures 8.19 and 8.20) with a coils'

current $I_b = 4$ A. This demonstrates the successful interfacing of the PID with the ANN. Notably, the control law exhibits a rapid stabilization, with a minor initial overshoot when transitioning from the initial state to the desired setpoint. Subsequently, the system converges to an error level close to zero.

Individual control of the anode voltage and the anode flow Rate



(a) U_a individual controller results

(b) q_a individual controller results

Figure 8.19: Control results from the first and second studies. Voltage and flow rate are controlled at a fixed flow rate and a fixed voltage respectively.

Figures 8.19 present the outcomes of individual control experiments, where we separately regulate the voltage and flow rate. In the case of the anode voltage control, we observe a slight initial overshoot of approximately 3% (equivalent to 5 V) from the target voltage value. Conversely, in the case of the anode flow rate control, we observe a more significant overshoot, amounting to 10% ($0.3 \text{ mg}\cdot\text{s}^{-1}$). This reflects the higher sensitivity of the optical emission on the flow rate compared to the voltage. This has been also observed during the PID coefficient tuning. During this

process, the control of the mass flow was particularly sensitive to variations/noise in the emission intensity levels. This required the flow rate to be adjusted in very small increments and setting a small upper control limit $u_{max} = 0.5 \text{ mg}\cdot\text{s}^{-1}$ to avoid drifting. In contrast, the anode voltage control demonstrated greater stability, even when larger control values were applied. The settling time for both the voltage and the flow rate remained relatively small, ranging between 1 to 1.5s across all experimental scenarios. Furthermore, the control system exhibited a linear response to noise, centered around the target values. This can be improved in the future by including an upperband filter in the optical sensors to reduce the fluctuations in the emission intensity.

Simultaneous control of voltage and flow rate

In Figure 8.20, we showcase the results of the simultaneous control of both voltage and flow rate. We obtain similar promising results with effective control over the different voltage, and flow rate combinations. The overshoot levels in this scenario remain comparable to those observed in the previous individual control simulation. However, the settling time is notably reduced, halving the duration required for the system to stabilize.

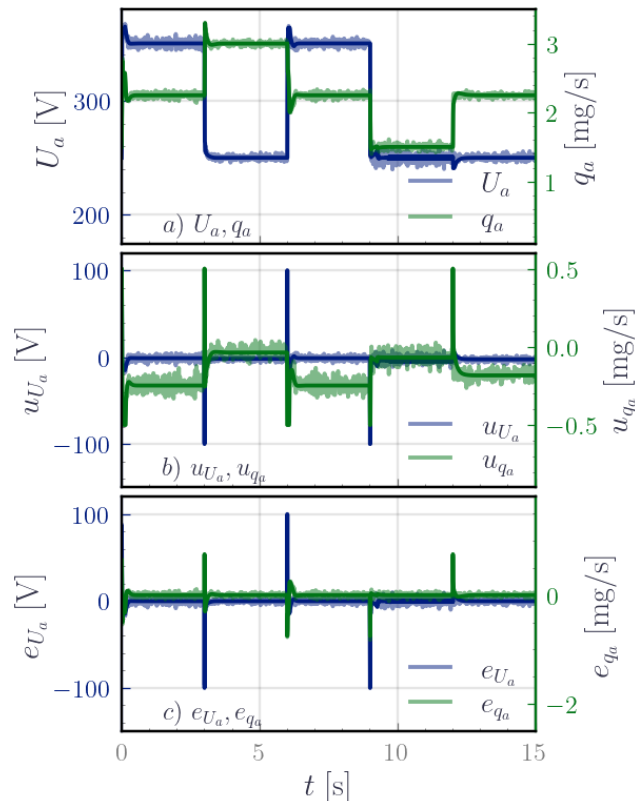


Figure 8.20: Control results from the third study. Voltage and rate flow are controlled simultaneously.

8.4.3 Enhancing control and monitoring: PID and varied magnetic configurations

The control simulations demonstrated that the PID controller can effectively operate the thruster at a fixed magnetic configuration with $I_b = 4$ A based on its optical emission. However, when the magnetic configuration is changed to other coil currents, the PID controller performs less efficiently since it was tuned for the $I_b = 4$ A condition. While the overshoot level and settling time remain relatively unchanged in most simulation scenarios when the coil current is altered, some conditions result in oscillations in the control signal, indicating difficulties in stabilizing the system, as illustrated in Figure 8.21 for $I_b = 4.4$ A. These oscillations are attributed to high values of the proportional gain K_p for those specific conditions.

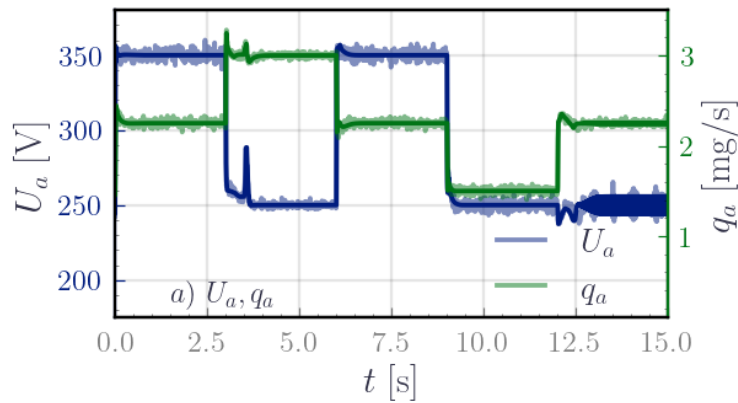


Figure 8.21: Impact of changing the magnetic configuration on the stability of the control. Oscillations appear at 12.5 s.

To address the challenge posed by varying the magnetic configurations, one potential approach is to re-tune the PID coefficient to the new magnetic topology, ensuring that the control system can maintain stability and effectiveness. This might be viable if the thruster is designed to work on a limited values of the coil currents. However, some mission requirements might need to change the coil's current. In this case, the use of a PID controller based on the optical emission with predefined coefficients, would exhibit reduced efficiency. A potential improvement is the implementation of an adaptive PID coefficient which might be achieved with an Adaptive Neural Network PID (ANN-PID) controller [Kang *et al.* 2014]. In an ANN-PID controller, an additional neural network dynamically adjusts the PID coefficients in real time based on the system's feedback. This adaptive approach might allow for better feedback control even amidst shifting the magnetic field. This will be the subject of future investigations.

8.5 Chapter conclusions

In this study, we looked at OES, CRM in tandem with ANN to investigate and control HET. This approach proved fruitful, allowing us to leverage OES and have one diagnostic bridging the gap between the macroscopic and the microscopic aspects of the plasma discharge in HET. The ANN-enhanced optimization process expedited and facilitated real-time monitoring of thruster performance, offering a practical avenue for in-orbit implementation of the diagnostic. Moreover, the simplicity and non-invasive nature of optical data collection presented exciting opportunities for crafting optical control strategies, offering adaptability and flexibility. However, ongoing work is required to ensure model consistency and validation. The precision and consistency of the ANN CRM in predicting plasma parameters require further refinement. Practical challenges related to the implementation of the required optics in space, such as deposition due to the divergence of the plasma plume, stray light correction from the satellite activities/operations, and the sensor placement with regards to the thruster, must be addressed. The potential for adaptive tuning strategies as the magnetic configurations change is also a promising direction. Foremost, this study underscores the value of ML, particularly ANN, in studying and engineering HET. Future research can further refine machine learning models, explore alternative control strategies, and enhance light-based control methods for HET systems. In essence, this research lays a foundation for new venues in electric propulsion diagnostics in the future where ML and OES hold pivotal roles.

Summary

Pourtant, le matin parut. Il approcha comme à l'ordinaire. Les étoiles s'éteignirent. A la limite du ciel et de l'eau se glissa un filet trouble. Puis un sorte de reflet d'incendie marqua l'horizon. Et le soleil émergea de la mer. Le ciel était radieux, le jour d'une limpidité merveilleuse. Philippe eût le sentiment d'une résurrection.

Joseph Kessel, *Fortune Carrée*

In this manuscript, we have investigated **HET** through the integration of virtual diagnostics, numerical simulations, optical diagnostics, and machine learning. The primary goal was to lay the foundations for an embedded optical diagnostic able to monitor the thruster in orbit. Throughout this work, we have demonstrated the potential of **OES** as a valuable in-orbit diagnostic tool for **HET**. By examining the optical emission, using a **CRM** and by implementing an **ANN**, we can gain insights not only into the plasma parameters within the thruster's plume and channel but also into its operational parameters. We have explored the interplay between **CTS**, **OES**, and **PIC** simulations, showing how virtual diagnostics can enhance our understanding of both the experimental diagnostic assumptions and simulation limitations. In this concluding chapter, we highlight the contributions, summarize the key findings, and outline future perspectives.

9.1 General recommendations

The recommendations of this manuscript can be summarized as follows:

Impact of the collection area on optical diagnostics

One crucial aspect that emerged from the comparative studies between **OES**, **CTS**, Langmuir probe, and **PIC** is the impact of the finite collection area on measurements from different diagnostic techniques. This observation holds particular relevance for **CTS/PIC**, **OES/PIC**, and **OES/Langmuir** probes comparisons, and we recommend carefully considering this factor when comparing data. In the case of **CTS**, the starting point was the difference in the electron density fluctuation rate between **PIC** simulations and **CTS** measurements. The virtual diagnostic approach highlighted the strong axial variation of the electron density fluctuation rates. Adjusting the

expression of the fluctuation rates was emphasized to accurately reflect the electron density within the total scattering volume defined by the intersection of the two laser beams. Furthermore, the evaluation of the root-mean-square electron density was shown to be influenced by the size of the laser beam waist, particularly in regions characterized by substantial electron density gradients. To ensure coherent comparisons between PIC simulations and CTS experiments, accounting for these spatial variations and beam characteristics is recommended. In the context of OES, the collection area poses a unique challenge, especially when the geometry of the setup is complex. In simple, collimated configurations, the comparison between OES and Langmuir probes, for instance, is relatively straightforward, by adjusting the formula of the mean to account for the gradient of the electron density and temperature along the line of sight. However, when the optical system involves lenses or other optical components, estimating the precise collection area becomes more intricate. In the simple case, the coupling with PIC suggests that the collection area extension can lead to a slight underestimation of the plasma parameters, with the impact becoming more pronounced as the collection area extends. While these limitations are inherent to the diagnostic themselves, they should not be perceived as hindrances. Instead, they should be acknowledged when comparing or validating models against experimental data. Developing adaptation techniques or averaging methods that account for the collection area may lead to more meaningful comparisons.

Dynamic scales and instabilities

The investigation has also highlighted the strengths of CTS and OES to investigate dynamic scales and instabilities. This recommendation encompasses an understanding of the observed instabilities, the frequency ranges at which each diagnostic operates, and the necessity for dynamic coupling between plasma dynamics and light emission in modeling. Using virtual CTS, we identified two distinct modes propagating along the thruster axis. These modes displayed dynamic behavior as they were convected by ions within the plasma. Notably, when ion convection became significant, changes in the direction of the mode propagation coincided with alterations in their amplitudes. The dispersion relations (f, k) computed using this approach within the ionization zone and the acceleration zone closely matched observations from CTS experiments. These findings underscore the dynamic nature of instabilities within HET and emphasize the capabilities of CTS as a spatially-resolved, time-resolved, and directional diagnostic. Furthermore, the same study was performed with virtual OES to detect instabilities within the simulation. While both diagnostics demonstrated the capacity to observe instabilities, certain considerations came to light. Though time-resolved, OES pertains spatial resolution only in the direction perpendicular to the line of sight. Also, the diagnostic is not directional and the choice of the view angle significantly influences the observability of the instabilities. Side views were more conducive to detecting axially propagating instabilities, whereas front views were better suited for observing azimuthally propagating ones. Another crucial aspect to consider is the frequency range of each

diagnostic. **CTS** is better suited for studying high-frequency, millimeter-scale instabilities compared to **OES**. The limitations of **OES** in this context stem from two primary factors. First, it is line-of-sight integrated as mentioned earlier. Second, it has a bandwidth limit related to the characteristic lifetime of the excited levels, typically with a cutoff at approximately the hundredth of kHz as highlighted from the coupling with **PIC** simulations. This constraint limits their ability to capture high-frequency dynamics within the plasma.

Importance of accounting for gradients in the plasma parameters

The study highlighted the importance of accounting for the gradients in the plasmas parameters in **HET**. Either for **CTS** or **OES**, gradients are smoothed by the collection volume leading to a large difference between the local values and the measurements if the collection volume is very large. Moreover, the use of the **CRM** with **OES**, highlighted that accounting for these gradients by keeping T_e , n_e , and n_g as free variables in the optimization cost function, is necessary to capture the trends in the plasmas parameters. The coupling with **PIC** simulation showed that line ratio curves overestimate T_e to compensate for the lack of n_e and n_g gradients. The abacus method compensates the non-inclusion of n_g by lowering the estimation of the n_e . Only having T_e , n_e , and n_g in the model yielded decent profiles.

Evaluation of the **CRM** assumption

Our investigation into the **CRM** assumptions within the context of **HET** simulations has yielded valuable insights into the reliability and limitations of this approach. Initially, we employed a steady-state coupling approach with **PIC** simulations to approximate optical emissions from **HET** plasmas. It was observed that the negligible transport assumption, as well as the often-critical Maxwellian assumption for the **EEDF**, had a minimal impact on $6p$ tier emissions, particularly in the mid-channel and near-field plume regions of the thruster. This finding challenges conventional thinking and suggests that deviations from idealized assumptions may not significantly affect emission predictions, and even if it does it might be indiscernible from the measurement noise, in our working conditions. Our investigation into the impact of gradients in electron density and neutral gas density on plasma emissions underscored the need to account for these gradients when applying the line ratio method within **CRM** for **HETs**. We identified certain line ratios, such as 823/828 and 980/992, as robust candidates for determining electron temperature. These ratios proved to be effective in estimating the electron temperature even though their use in estimating electron density was comparatively limited.

Practical recommendations for developing a **CRM**

Chapters 2 and 3 provided a comprehensive exploration of cross-sections, radiative coefficients, sensitivity analysis, and parametric study on the **CRM**. They have shed light on the challenges in building **CRMs** and have raised critical questions regarding

the validation and verification processes. For future CRM developers, first and foremost, we emphasize the paramount importance of establishing a solid foundation for atomic and molecular models used in CRM development. This entails close collaboration with atomic physicists and spectroscopists, especially when working with species for which data may be incomplete or uncertain. The choice of data sources and cross-section datasets must accurately reflect the energy levels and transitions of the particles under consideration. It is also crucial to recognize that cross-section data, even though some are perceived to be well-understood or complete, are valid in a certain range of energy and pressure. Therefore, we recommend extending the effort to validate and refine cross-section data for simple atoms like argon, krypton, xenon, and other common species used in plasma modeling, on a wide pressure range. Benchmarking, reviewing, and clarifying the available data in the literature are essential steps to model validation. Next, it is important to systematically perform a sensitivity analysis of the model to gauge its robustness and limitations. It is noteworthy that even models with a seemingly high level of complexity can exhibit uncertainties on the order of 20%. This observation underscores the importance of sensitivity analysis, which can provide insights into whether further complexity or optimization of cross-section data is necessary. It is both enlightening and, at times, frustrating to note that some models in the literature, with thousands of reactions, exhibit uncertainties similar to those of simpler models with far fewer reactions. Therefore, sensitivity analysis remains paramount in assessing the model's performance and in finding the trade-off between the model's complexity and interpretability. Furthermore, conducting a comprehensive parametric study is very helpful. Such a study can help determine the dominant kinetic mechanisms within the model and establish a validation range for specific pressure conditions. However, we acknowledge the complexity of this task, as it often requires experimental comparisons and an a priori assessment of reaction rates to characterize the chemistry under consideration. Lastly, the impact of the choices made during the model development process shall not be underestimated. Each choice introduces a potential bias, whether justified or arbitrary. Factors such as the choice of the cost function, the inclusion of specific lines, and other modeling decisions can significantly influence the model's predictions. Awareness of these choices and their implications is key to producing reliable results and relating them to different models.

9.2 Key findings

Taking several steps back, we have come across several high-level findings, throughout the course of this research:

Comparison between experiments and simulations via virtual diagnostics

First among our contributions is the introduction of virtual diagnostics as a framework to compare experimental and simulation results. Chapter 2 and 5 have delved deep into the interface between PIC simulations and both CTS and OES. It has

showcased how the virtual diagnostic approach can enhance our comprehension of the diagnostics and the simulation and bring new elements to the understanding of HET. Bridging the debate by overcoming the 3D argument and examining the limitations both from the simulation and the experiments side. Specifically, this work highlighted several possible improvements to PIC simulations mainly the impact of the cathode boundary condition on the results, the improvement of the model neutral dynamics, and the inclusion of the curvature and radial gradients in the magnetic field. This work also highlights how experiments act like convolution kernels smoothing out gradients, due to the impact of the finite diagnostic volume on the observed quantities and the importance of accounting for the gradient of the plasma parameters in both OES and CTS. Finally, this virtual approach holds the promise of facilitating the comparison between experiments and simulation by encouraging modelers to express the simulation results in measurable quantities and inciting experimentalists to identify the transformation in their measures.

Revaluating optical emission spectroscopy

Second among our contributions is the establishment of OES as the conductor of an enriching dialog between multiple fields: atomic physics, plasma physics, numerical and experimental methods, and machine learning. OES, thanks to its simplicity and flexibility, is capable of easily harnessing the power of CRM, the capabilities of PIC, and the opportunities of ML. We have demonstrated the capacity of OES to furnish invaluable insights about HET on different levels of complexity. From the plasma parameters, the dominant kinetic mechanisms to the operation parameters. It also offers a framework to re-establish the link between atomic physics and plasma physics, through discussions on unifying/benchmarking cross-sections and radiative data for simulations. This journey relied a lot on the work of [Karabadzhak *et al.* 2006] and [Boffard *et al.* 2004], to re-contextualize OES in the middle of the new tools available today.

Proof of concept for OES for in-orbit HET diagnostics

The seminal contribution of this work is the establishment of a proof of concept for the use of OES as a potent in-orbit diagnostic tool for HET. Different implementation methods via a CRM were explored either by using line ratios/abacus in Chapter 5, an optimization loop in Chapter 7 or an ANN in Chapter 8, and all have provided compelling evidence that OES can be harnessed to glean information about the electron temperature within the thruster as well as its operation parameters. The extraction of other plasma parameters was deemed more difficult and we demonstrated that it required accounting for the inherent gradients to the thruster's plume. The use of ANN offered more flexibility in terms of applications allowing not only to monitor the thruster micro/macroscopic states but also control its operation. These breakthroughs offer fresh avenues for characterizing and mitigating ground facility effect on HET performance in space.

9.3 Future perspectives

At last, several opportunities for further research and development come into view:

Implementation of the in-orbit diagnostic

Future work should prioritize the practical design and implementation of the diagnostic, especially for space missions, leading to a functional prototype of CRM-ANN. Overcoming challenges in the used optics in space, including concerns like deposition due to the divergent plume, stray light, the sensor placement with regards to the thruster, the thermal tolerance of optical sensors, and the required power budget will be crucial to enhancing the consistency and relevance of such a diagnostic for in-orbit monitoring of HET. Additionally, we should explore the development of adaptative tuning strategies that can adapt to changing magnetic configurations, ensuring robust and flexible control under varying conditions.

Machine learning advancements

Continuing the effort with ML, particularly through the use of ANNs, holds significant promise in enhancing diagnostic capabilities. Our work investigated supervised learning technics where the data set is fixed. Future work should explore unsupervised learning models to have learning models interactively update their learning with new incoming feeds of data.

Enhancement of the HET0D Model

Enhancements should focus on incorporating ionic lines into the diagnostic. Though their impact on the kinetics of the neutral excited species is negligible, ionic lines can potentially reveal non-Maxwellian characteristics of the EEDF, giving their sensitivity to higher T_e . Moreover, the validation with the KCD model and the coupling with PIC revealed that while the dominant kinetic mechanisms are consistent for the $6p$ tier, some processes are missing for the $6p'$ tier. An improvement will consist of incorporating the $5d$ levels into the model given their proximity to the $6p'$ manifold. The absorption model so far relied on the Mewe approximation, which assumes a homogeneous distribution of the excited species densities. Future work should investigate the improvement of this approximation to consistently account for the radiation field and the gradients.

Adapting to different conditions and gases

We should explore the scalability and adaptability of HET0D to different HET sizes, power levels, and configurations. Preliminary work was initiated during this Ph.D. by using the CRM on the PPSX00-CHEAP, the PPS-1350 and the PEGASES ion gridded thruster operating with argon. Adapting the CRM to other gases, such as krypton and iodine, represents a valuable direction for future research. This expansion requires continuous improvement of atomic and molecular data through

collaboration with atomic physicists and spectroscopists. Currently, the xenon CRM and the previous methodology can be used with these gases using Trace rare gases optical emission spectroscopy, where xenon is injected in small quantities into the discharge.

Broadening the validation of the CRM to cover a wider range of pressure conditions is essential for the continuity of the code at LPP. Future work should also explore the integration of other kinetic processes into the CRM to accurately model transient and non-equilibrium plasmas, in particular, the diffusion to the walls and anode recombination to allow more accurate investigation in the channel. Moreover, developing hybrid models that combine the CRM that include ionic emission with kinetic PIC simulations can eventually capture phenomena like the tail of the electron energy distribution functions and their non-Maxwellian behavior. This can be reached by improving the coupling between the CRM and the PIC by increasing the level of details in the PIC with the addition of well-chosen excited levels and by improving the accuracy of the CRM in dealing with ionization and absorption.

User-friendly interface for HET0D

A great effort was made during this work to make HET0D as user-friendly as possible. To promote broader adoption of HET0D CRM within the LPP, a user-friendly interface should be developed. This should allow other users to input their specific thruster parameters and generate synthetic spectra for comparison with experimental data, making HET0D more accessible.

Integration of advanced diagnostics and alternative propellants

The integration of advanced plasma diagnostics into CRM development and validation processes offers a promising path forward. The test bench implemented during this PhD has been upgraded with a new thruster to explore alternative propellants, mainly iodine and krypton. Experiments that provide detailed spatial and temporal information on plasma parameters, such as electron density and temperature, will enable more accurate model validation. Techniques like Tunable Diode Laser Absorption Spectroscopy, Laser-Induced Fluorescence and Thomson Scattering can provide valuable experimental data for comparison with CRM predictions, aiding in the refinement and validation of these models while operating on different gases. This might help shed more light on some open questions raised by this work, mainly the impact of the background pressure, the radial displacement of the maximum electron temperature T_e with the voltage and the neutral dynamics in the plume.

9.4 In closing

In summary, this manuscript has been an exploratory journey with a particular focus on HET. The blending of optical diagnostics, numerical simulations, and machine learning techniques has opened up new avenues for the exploration and

control of these systems. As we embark on the path ahead, there are promises of new developments in the field of [EP](#). Although challenges remain, the possibilities are limitless.

Appendices

APPENDIX A

Appendix Example

A.1 General Notes

Racah and Paschen Notations

Racah and Paschen's notations are commonly used to represent energy levels in noble gases. Racah coupling is suitable when multiple electrons are grouped within a partially filled electronic layer, while an external electron resides in a distant layer. This is particularly applicable to xenon, where the first excited levels are at 8 eV.

The core electrons Hamiltonian is dominated by the core spin-orbit coupling between their angular momenta L_c and spin S_c . Thanks to the rotational invariance, the eigenvalues of the core Hamiltonian are then the eigenvalues of the total core angular momentum j_c such as $j_c = L_c + S_c$. For noble gases, given the configuration of the core, L_c is equal to 1 and S_c is equal to $\frac{1}{2}$ in such a way that j_c can take two values $\frac{1}{2}$ and $\frac{3}{2}$. Adding the electrostatic interaction between the core and the external electron, j_c couples with the electron orbital momentum l_e in such a way that the eigenvalues of the Hamiltonian are the eigenvalues of $K = j_c + l_e$. Then, K couples with the electron spin s_e so that at the end the eigenvalues of the Hamiltonian are given by the eigen values of the total angular momentum quantum number $J = K + s_e$.

The previous scheme is illustrated in Figure B.1. As per the angular momentum addition rules, the quantum number K can take values ranging from $|j_c + l_e|$ to $|j_c - l_e|$. The eigenvalues, i.e energy levels, are denoted using the expression

$$nl_e[K]_J,$$

where n is the principal quantum number of the excited electron layer, l_e its orbital quantum number with a prime sign if $j_c = \frac{1}{2}$.

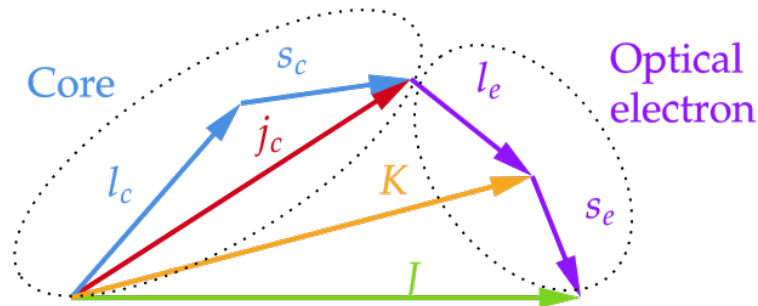


Figure B.1: Illustration of the angular momentum coupling between the core and the optical electron relevant to Racah's coupling scheme

Racah's notation is very practical for rare gases since it highlights the atomic structure. However, for spectroscopic investigation and computational modeling, a more simple and sequential encoding is preferred which is Paschen notation. Paschen notation simply orders the quantum states in decreasing energy for a given state of the optical electron. For instance, if the external electron is in an p layer, levels will be encoded from 1 to 10 in decreasing energies. There is an exception for s layers where the order starts from 2 to 5.

Comparison Between Numerical and Experimental Cross Section

Contents

C.1 From the ground state to the $6s$	219
C.2 From the ground state to the $6p$	221
C.3 From the $6s$ to the $6p$	224
C.4 From $6s$ to $6s$	226
C.5 From $6p$ to $6p$	226
C.6 Energy levels and radiative data	228

C.1 From the ground state to the $6s$

The cross sections from the ground state to the metastable levels are shown in figure C.1. These cross-sections are available in the BSR, Biagi, and Priti datasets. Priti's calculations agree with the BSR calculations and are not presented here. Several features can be observed in the cross sections. First, the excitation cross sections to the upper tier $6s'$ group are slightly smaller compared to the $6s$ tier. This difference is again a result of the strong core splitting in xenon atoms, which favors transitions that preserve the core angular momentum.

The cross sections for optically allowed transitions ($1s2$ and $1s4$) exhibit broader peaks consistent with the empirical decay behavior of $\log E/E$ proposed by Darwin. In contrast, the cross sections for metastable transitions display narrower peaks. It is important to note the discrepancies of at least a factor of 2 between the BSR and Biagi datasets, which can be attributed to the neglect of coupling in the ionization continuum in the calculations. At the low-energy threshold, BSR shows resonance structures with extremely high peaks that Biagi does not exhibit. Overall, the datasets are qualitatively in agreement but quantitatively different. Figure C.2 compares the total excitation from the ground state to the $1s$ level, demonstrating that the values are within 15% of each other.

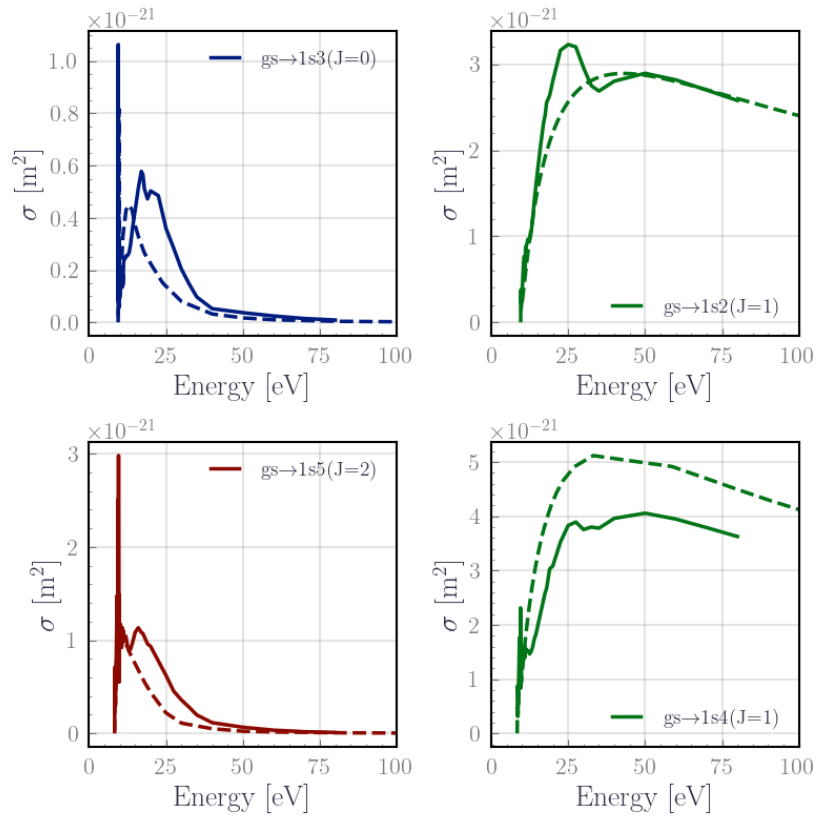


Figure C.1: Excitation cross-section from the ground state to the 6s levels from the BSR dataset (solid line) and BIAGI dataset (dashed lines).

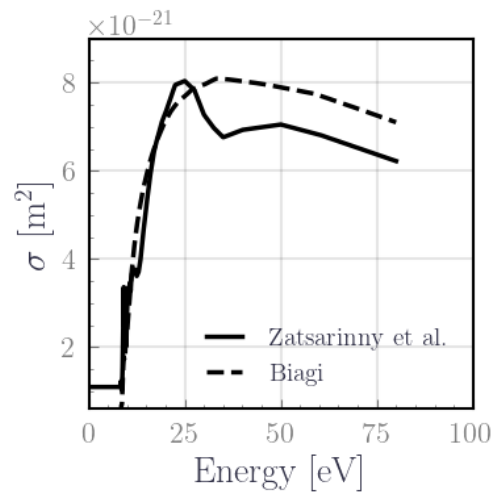


Figure C.2: Comparison of the total excitation cross-section from the ground state to the 6s levels from the BSR dataset (solid line) and BIAGI dataset (dashed lines).

C.2 From the ground state to the $6p$

Figure C.3 illustrates the direct cross-section from Biagi, BSR, and Fons & Lin datasets. These cross sections display sharp narrow peaks with varying degrees of decline at higher energies, consistent with the qualitative expectation of an E^{-J} decline in the Bethe-Born approximation. Similar trends can be observed in the direct excitation cross sections. Notably, the excitation cross sections for non-core preserving transitions are distinctly smaller for the $6p'$ group compared to the $6p$ group, except for the cross-section from the ground state to the $2p6$ level from Biagi, which is slightly smaller.

The discrepancies between the datasets are more pronounced for the $2p$ levels, with factors ranging between 3 and 7. The reasons for such discrepancies are not clear in the literature. It could be attributed to differences in calculation methods, as mentioned before, the coupling with the ionization continuum, which might be neglected in some cases. The experimental cross-sections also do not provide conclusive results, and the reasons for these differences are still unknown. The reported factors range from 0.3 to 1.3 compared to measurements by Feltsan [Feltsan 1967] and factors of 1-2 compared to measurements by Filipovic [Filipović *et al.* 1988].

Finally, figure C.4 presents the apparent and direct cross sections from Fons & Lin measurements. The difference between the dotted dot-dashed curves corresponds to the cascade contribution, which correlates well with the total angular momentum number. It is worth noting that the radiative cascade contributes as much as a factor of 2 to the apparent cross section for some levels.

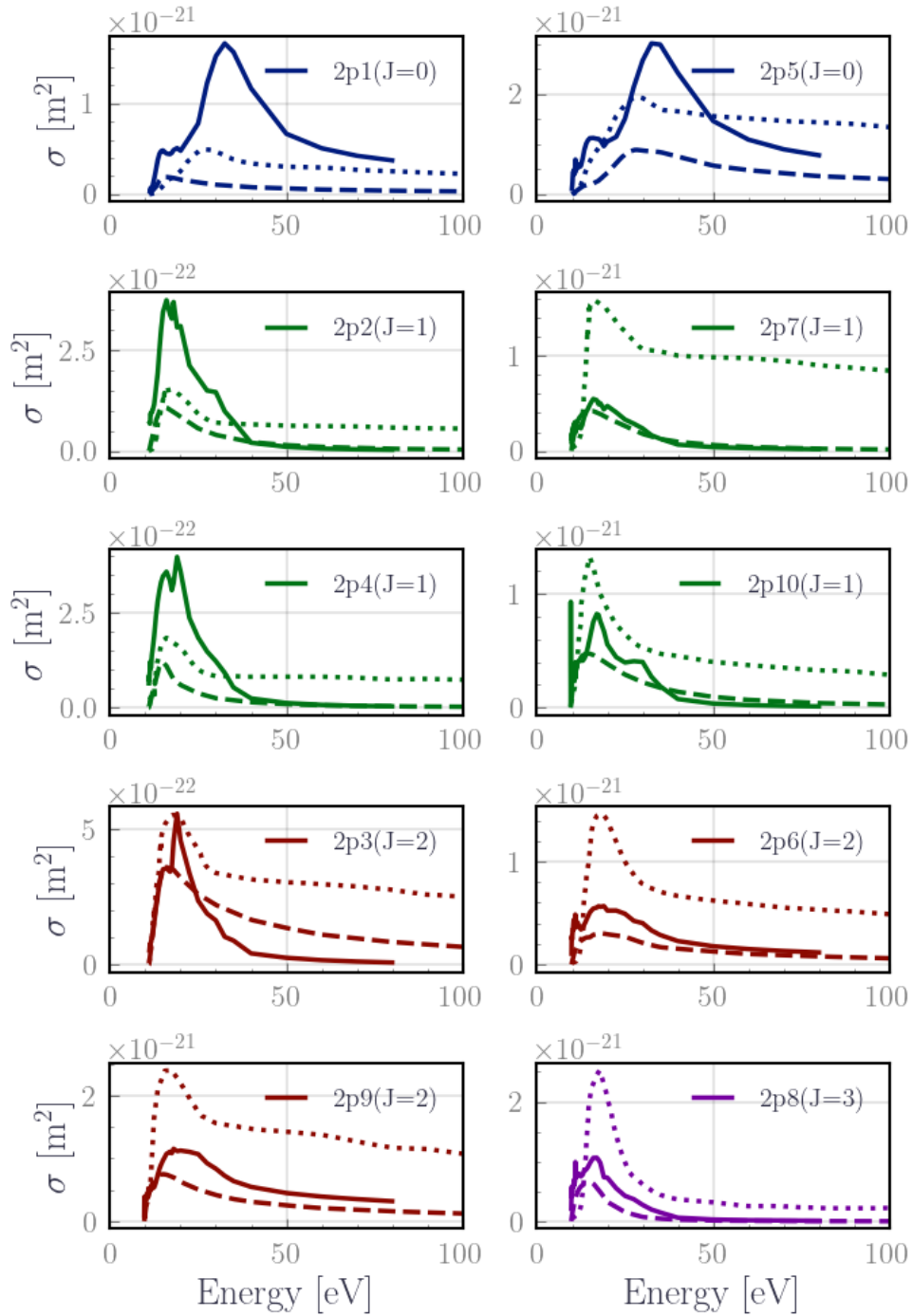


Figure C.3: Comparison of the total excitation cross-section from the ground state to the 6p levels from BSR dataset (solid line) and BIAGI dataset (dashed lines), Fons & Lin measurements (dotted line).

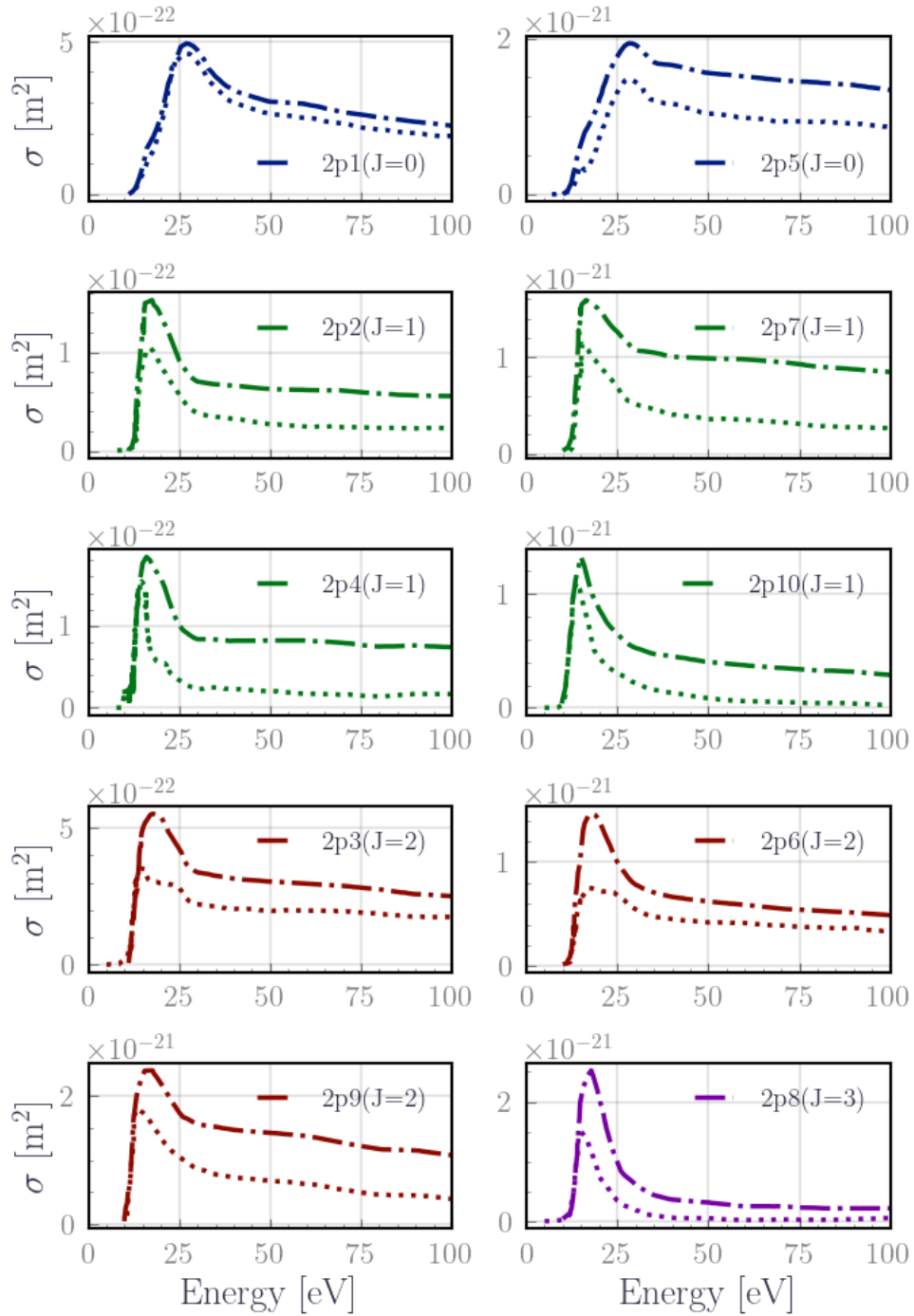


Figure C.4: Comparison apparent and direct section from the ground state to the $6p$ levels from Fons & Lin measurements.

C.3 From the $6s$ to the $6p$

Only Priti and BSR allow an extensive comparison between the excitation functions of these transitions and the cross sections are illustrated in Figure C.6. Again we observe that core-preserving transitions are favored against non-core-preserving transitions. However, a notable difference between Priti and BSR is observed for transitions from the $6s'$ levels ($1s2$ and $1s3$) to the $6p$ level which is higher in BSR than in Priti. Looking into the xenon energy diagram, these transitions exhibit a near resonance configuration at an energy difference of 0.11 eV, which gives more credit to the cross-section calculations of BSR.

The work by Karabadzahk [Karabadzahk *et al.* 2006] highlights the significant role of excitations from $1s5$ to $6p$ in the kinetics of low-pressure xenon. Therefore a consistent evaluation of the excitation cross section is necessary to ensure the right kinetic in the model. Specifically, for the $1s5$ level, a difference of a factor of 10-50 is observed between Priti and BSR datasets. Comparing these values to experimental measurements from Jung *et al.* [Jung *et al.* 2005] in Figure C.5, the BSR database shows better agreement for transitions from $1s5$ to higher level tiers, such as $6p$. These observations align well with measurements of oscillator strengths also discussed in [Boffard *et al.* 2007].

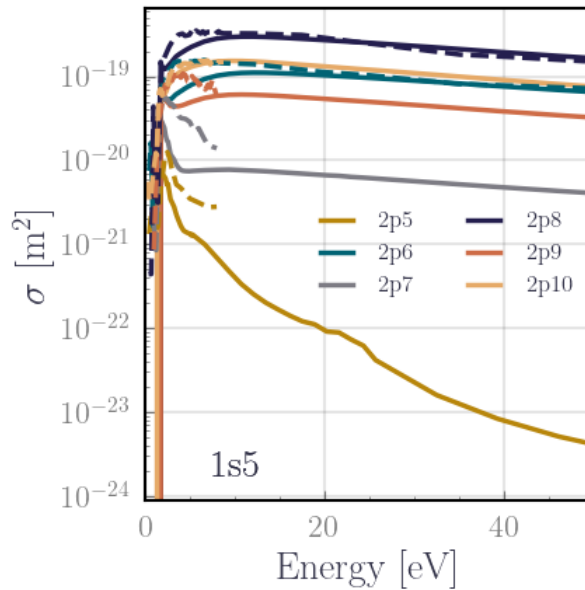


Figure C.5: Comparison of direct excitation cross-section from the $1s5$ to $6p$ from BSR dataset (solid line) and FONS dataset (dashed lines).

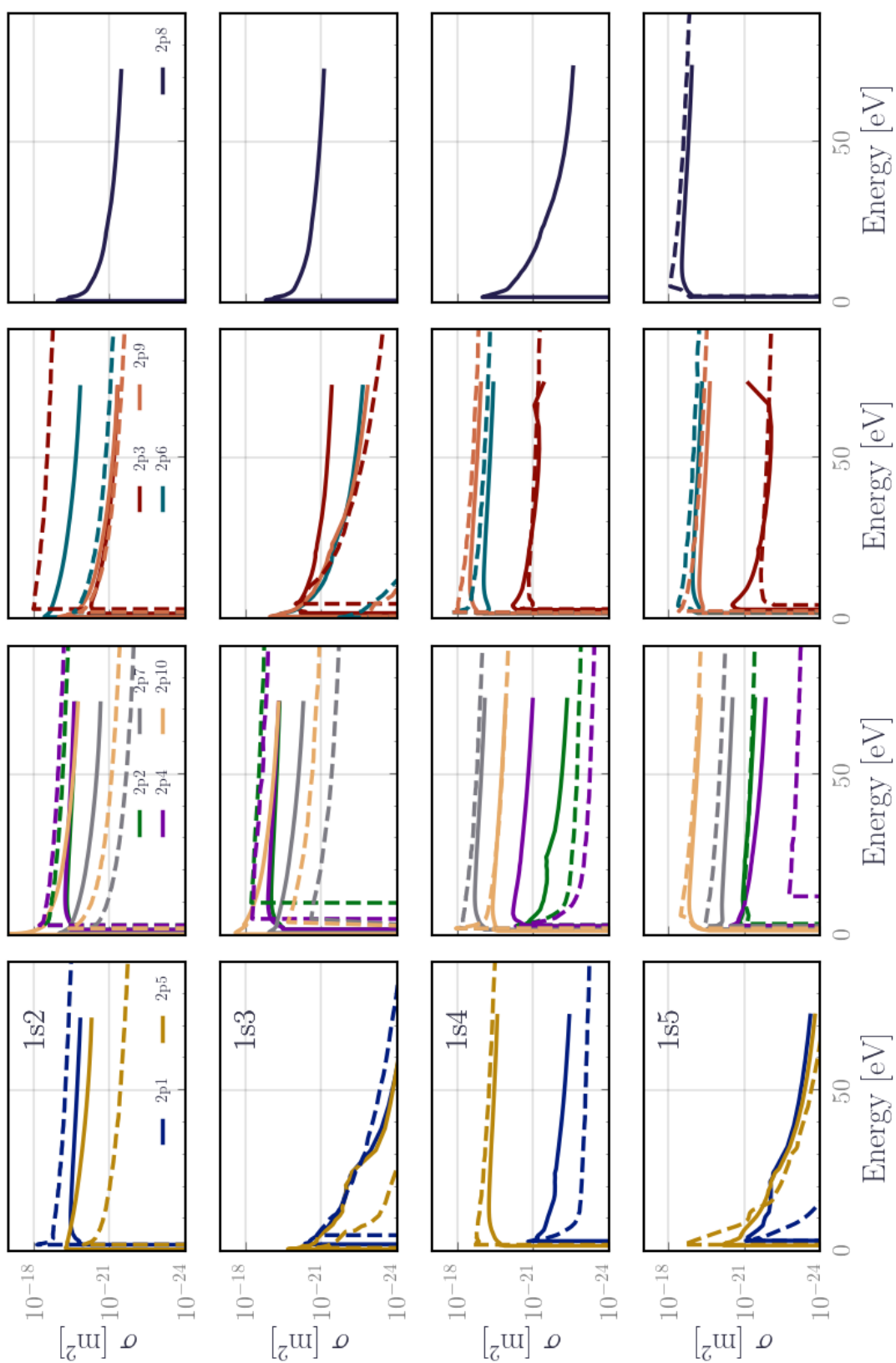


Figure C-6: Comparison of direct excitation cross-section from the 6s to the 6p levels from BSR dataset (solid line) and Pritri dataset (dashed lines).

C.4 From $6s$ to $6s$

For the $6s$ collisional mixing, Figure C.7 shows a comparison between BSR and Priti calculations, with the measures from the work [Dressler *et al.* 2009]. We have similar observations with BSR yielding a better agreement with measurements.

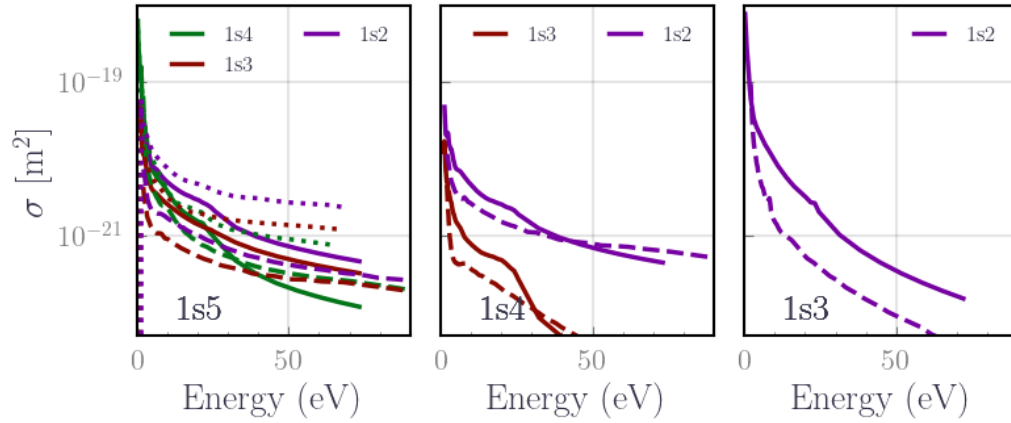
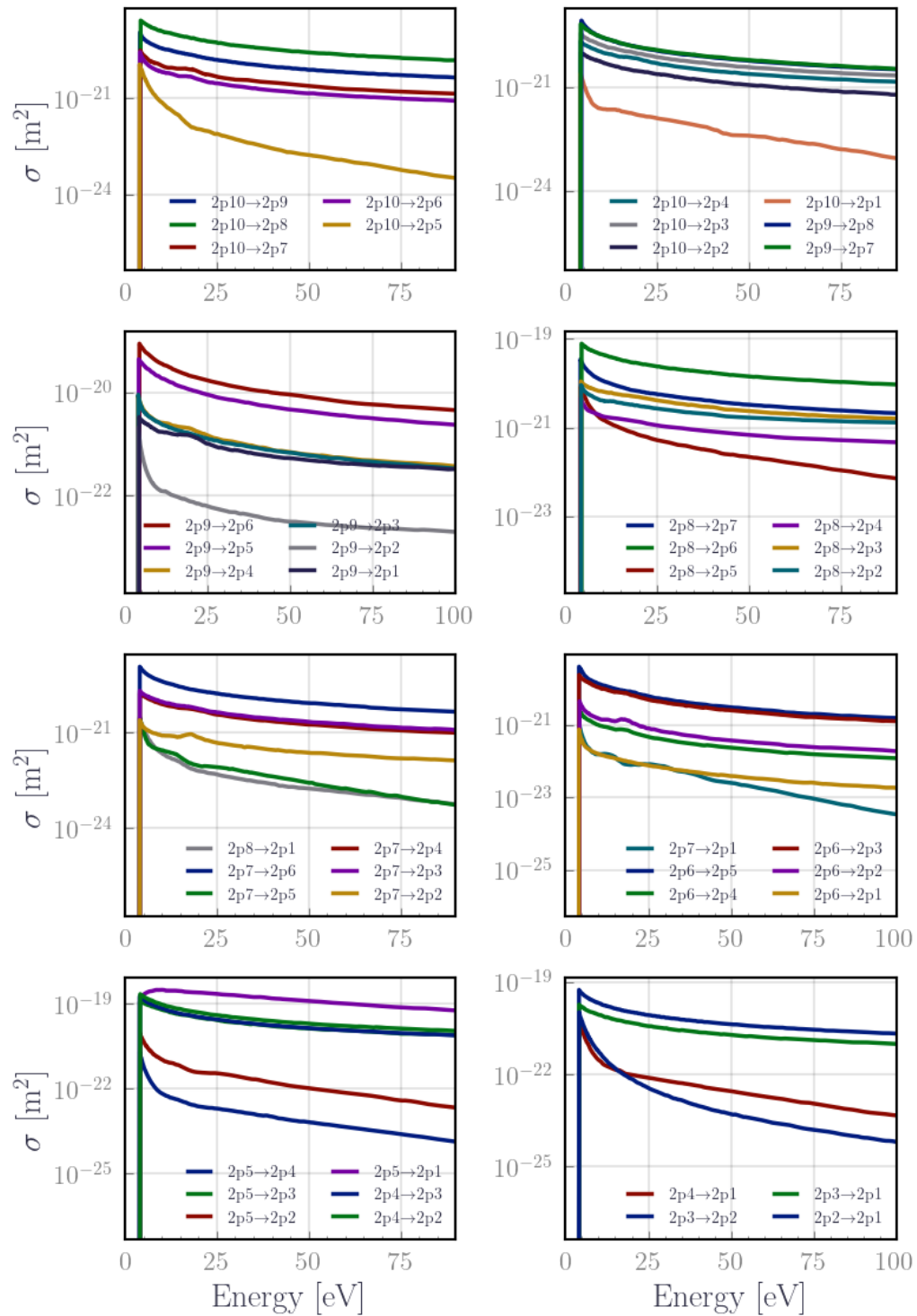


Figure C.7: Comparison of the direct excitation cross-section from the $6s$ levels to the $6s$ levels from the BSR dataset (solid line) and PRITI dataset (dashed lines) and the FONS dataset (dotted line).

C.5 From $6p$ to $6p$

For $2p$ collisional mixing, data is available only in Priti's data set in Figure C.8

Figure C.8: Excitation cross section for the collisional mixing inside the $6p$ levels.

C.6 Energy levels and radiative data

An additional practical way to check calculated cross-sections is to compare the energy levels and the Einstein coefficient. Figure C.9 illustrates the errors in xenon energy levels calculated using the R-matrix and RDW formulation. The BSR data demonstrates a close agreement with the experimental data from NIST, particularly for low energy levels. However, the discrepancy becomes slightly larger at higher energy levels ≈ 0.05 eV. In contrast, the Priti et al. data exhibits consistently a significant scattering of errors across different energy levels.

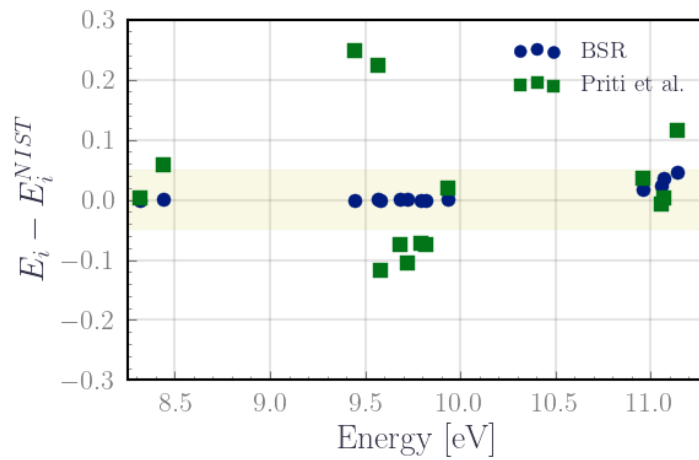


Figure C.9: Difference in the energy of the excited species provided by the NIST to those BSR and those of PRITI. The light green region indicates an overall deviation that is less than 0.05 eV

The spontaneous emission in xenon is governed by Einstein coefficients. Currently, the most reliable and up-to-date source of measured xenon Einstein coefficients is NIST [Kramida & Ralchenko 1999]. They can also be calculated using the BSR [Zatsarinny & Bartschat 2009] and RDW [Priti *et al.* 2019a] formulations. While BSR provides both the Einstein coefficient and the oscillator strength, the work of [Priti *et al.* 2019a] provides only oscillator strengths, Therefore, Einstein coefficients were calculated using the following formula :

$$A_{ij} = \frac{8\pi^2 e^2}{\epsilon_0 m_e \lambda_{ij}^3 c} \frac{g_i}{g_j}. \quad (C.1)$$

Figure C.10 compares the calculated Einstein coefficients to the experimental NIST coefficients. There is a significant dispersion in the Priti data, despite good agreement in oscillator strength values. On the other hand, the BSR database exhibits less scattering of the data and is consistent for both the oscillator strength and the dispersion of Einstein coefficients.

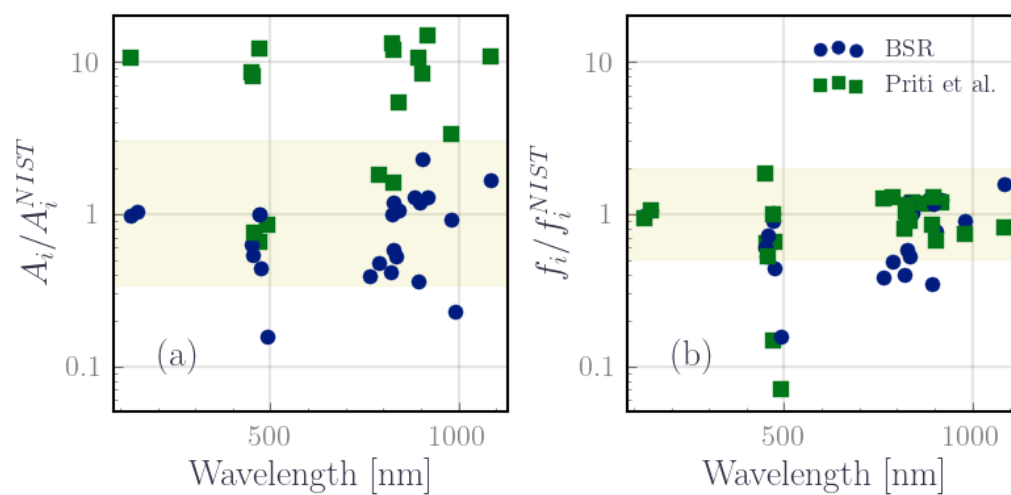


Figure C.10: Ratio of the Einstein coefficients and oscillators strength provided by the NIST to those of BSR and those of PRITI. The light green region indicates a deviation that is less than a factor of 2

Estimation of Uncertainties for Rate Coefficients

Let a cross-section measurement with N measurement points modeled here with a set of random variables $(X_i)_{i \in [1, N]}$. We assume that each random variable follows a normal distribution with $N(x_i, s_i)$, where μ_i represents the measure and $s_i = \frac{Ux_i}{2}$ with U_i is the uncertainty expressed as a percentage of the mean value. Implicitly we are assuming that the uncertainty is defined at $2s$ for a normal distribution. For simplicity, we also assume that all U_i are equal to U .

The rate coefficient K is expressed based on Eq. (3.14), which we re-write here for the sake of clarity :

$$K = \sqrt{\frac{2}{m_e}} \int_0^\infty \sigma \sqrt{E} \hat{f}_e(E) dE. \quad (\text{D.1})$$

In HETOD, K is calculated numerically using a simple trapeze scheme, in such a way that the previous integral is estimated with \bar{K} expressed as follows:

$$\bar{K} \approx \sqrt{\frac{2}{m_e}} \frac{L}{N} \left(\frac{x_0 \sqrt{E_0} \hat{f}_e(E_0)}{2} + \sum_{i=1}^{N-1} x_i \sqrt{E_i} \hat{f}_e(E_i) + \frac{x_N \sqrt{E_N} \hat{f}_e(E_N)}{2} \right), \quad (\text{D.2})$$

where L is the energy range of the measurements. The previous expression establishes that K is also a random variable and it can be expressed as a linear combination of the X_i . Let $\alpha_i = \sqrt{E_i} \hat{f}_e(E_i)$ so that K can be easily expressed as in terms of :

$$K = \sqrt{\frac{2}{m_e}} \frac{L}{N} \left(\frac{X_0 \alpha_0}{2} + \sum_{i=1}^{N-1} X_i \alpha_i + \frac{X_N \alpha_N}{2} \right), \quad (\text{D.3})$$

Since the family of normal distributions is closed under linear transformations, we establish that K follows also a normal distribution $N(\bar{K}, s_k)$ where s_k is expressed as follows :

$$s_k^2 = \frac{2}{m_e} \frac{L^2}{N^2} \left(\frac{s_0^2 \alpha_0^2}{4} + \sum_{i=1}^{N-1} s_i^2 \alpha_i^2 + \frac{s_N^2 \alpha_N^2}{4} \right) \quad (\text{D.4})$$

Upon plugging the expression of s_i with respect to U :

$$\begin{aligned}
 s_k^2 &= \frac{2}{m_e} \frac{L^2}{N^2} \left(\frac{s_0^2 \alpha_0^2}{4} + \sum_{i=1}^{N-1} s_i^2 \alpha_i^2 + \frac{s_N^2 \alpha_N^2}{4} \right) \\
 &= \frac{2}{m_e} \frac{L^2}{N^2} \left(\frac{U x_0^2 \alpha_0^2}{4} + \sum_{i=1}^{N-1} \frac{U x_i^2}{2} \alpha_i^2 + \frac{U x_N^2 \alpha_N^2}{4} \right) \\
 &= \frac{U^2}{4} \frac{2}{m_e} \frac{L^2}{N^2} \left(\frac{x_0^2 \alpha_0^2}{4} + \sum_{i=1}^{N-1} x_i^2 \alpha_i^2 + \frac{x_N^2 \alpha_N^2}{4} \right) \\
 &\leq \frac{U^2}{4} \frac{2}{m_e} \frac{L^2}{N^2} \left(\frac{x_0 \alpha_0}{2} + \sum_{i=1}^{N-1} x_i \alpha_i + \frac{x_N \alpha_N}{2} \right)^2 \\
 &\leq \frac{U^2}{4} \bar{K}^2
 \end{aligned}$$

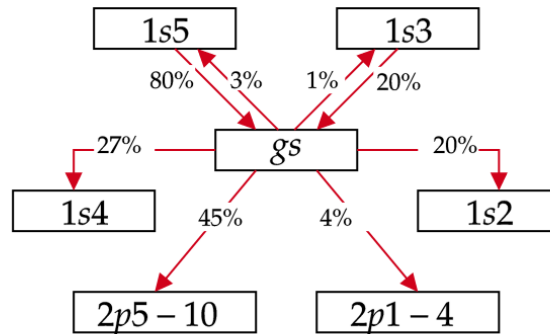
which we can write as follows:

$$U_K = \frac{2s_k}{\bar{K}} \leq U \tag{D.5}$$

This demonstrates that the uncertainty in the rate coefficients, expressed as a percentage of the mean value, is generally smaller than the uncertainty in the cross-sections when considering the same level of uncertainty. A finer estimation of the uncertainties would require more detailed information about the shape of the EEDF and its behavior at high electron energies. However, for uncertainty quantification in our model, this conservative upper bound is sufficient.

Kinetics Diagrams of Xenon Excited Species at Typical HET Conditions

Here we report the detailed kinetic mechanisms characteristic to subregion II*d* in Figures E.1, E.2, E.3 and E.4. The contributions are calculated using Eq. (4.5) for each level. The following diagrams are obtained with the following input parameters in HETOD: $T_e = 20$ eV, $n_e = 4 \times 10^{15} \text{ m}^{-3}$, $n_g 1 \times 10^{20} \text{ m}^{-3}$ and $T_g = 300$ K, $d = 15$ cm and a Maxwellian EEDF.



Radiative decay e^- impact

Figure E.1: Kinetic diagram for Xe ground state. The number on the line is the percentage contribution of the process to production or depopulation of the level. These contributions were estimated using HETOD with the following parameters: $T_e = 20$ eV, $n_e = 4 \times 10^{15} \text{ m}^{-3}$, $n_g 1 \times 10^{20} \text{ m}^{-3}$ and $T_g = 300$ K, $d = 15$ cm and a Maxwellian EEDF

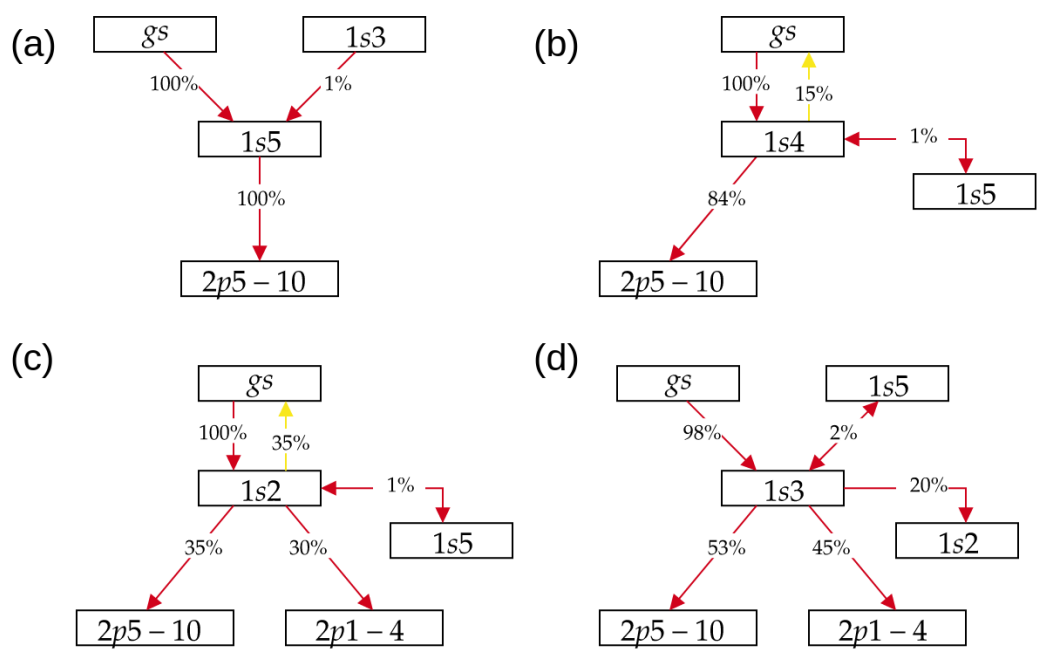


Figure E.2: Kinetic diagram for Xe(1s) states.

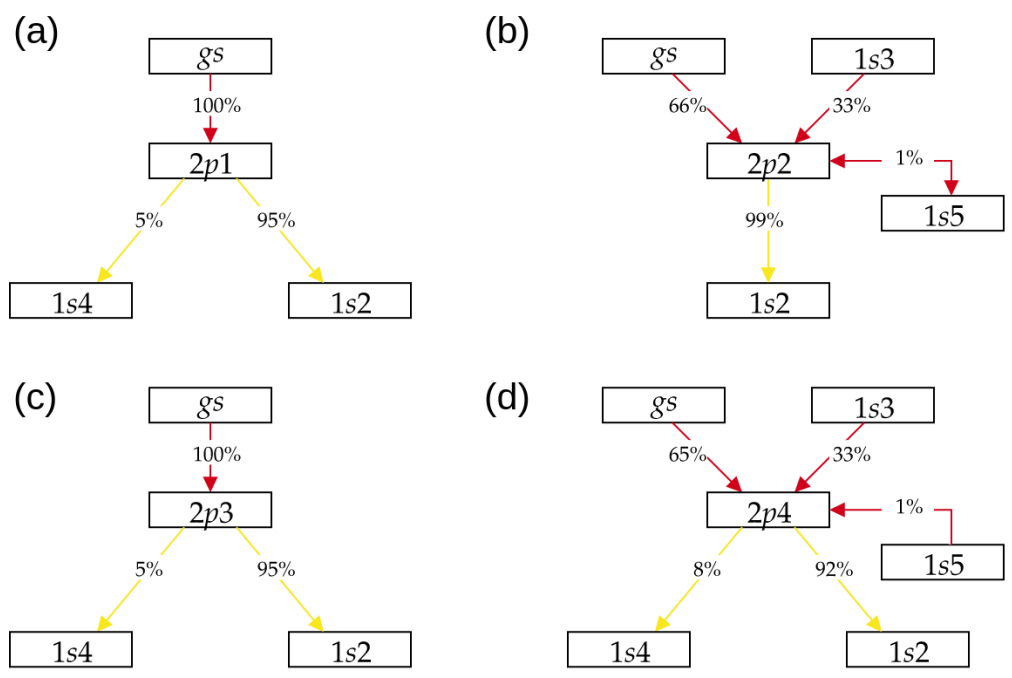
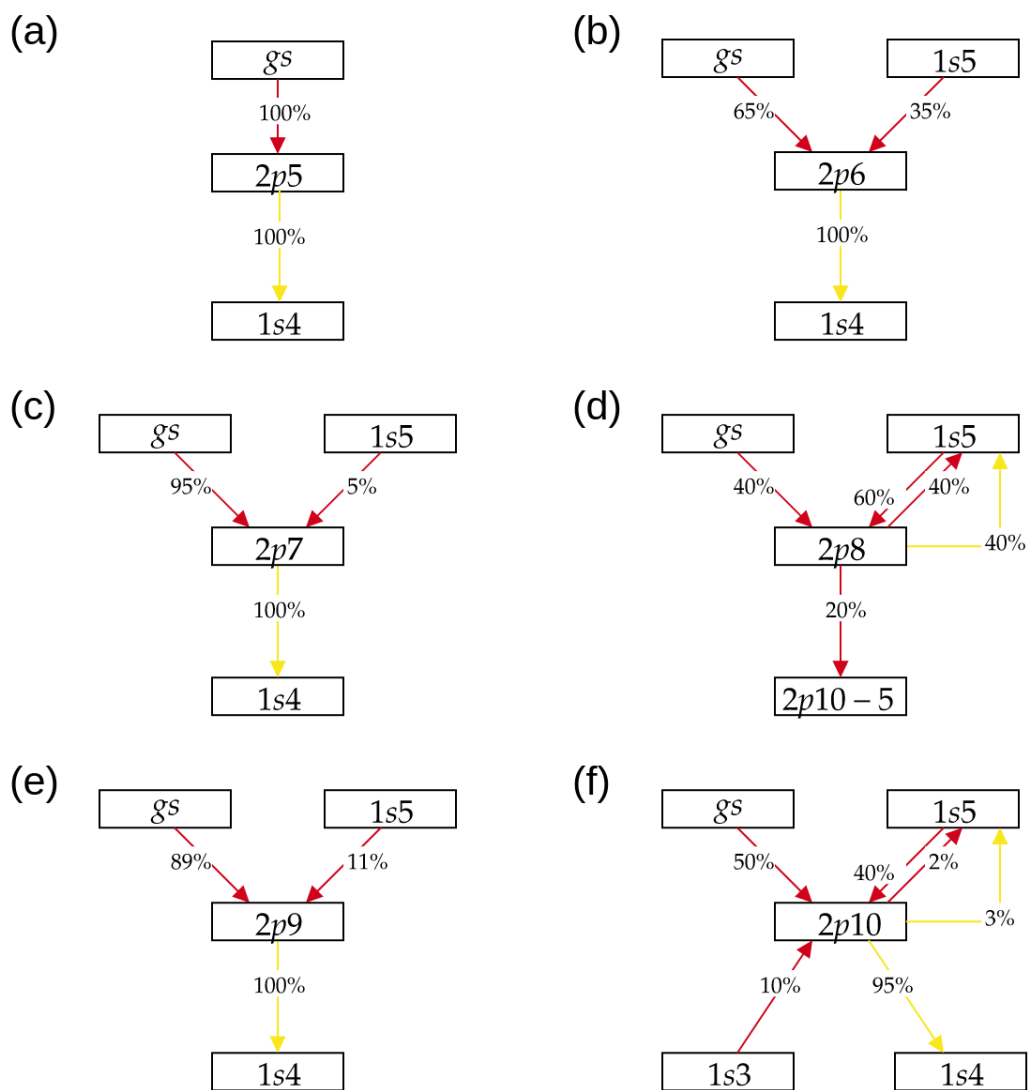


Figure E.3: Kinetic diagram for Xe(6p') states.

Figure E.4: Kinetic diagram for Xe($6p$) states.

Line broadening

Three principal bound-bound optical processes occur in plasmas: spontaneous emission, absorption, and stimulated emission. In the case of spontaneous emission, a particle in an excited state p transitions to a lower state q by emitting a photon. Absorption occurs when an incoming photon excites an atom from state q to p . In contrast, stimulated emission ensues when a photon induces an already excited particle to transition to a lower energy level, emitting an additional photon. The rate R_{pq} for these processes can be ascertained by solving the time-dependent Schrödinger equation for transitions between states p and q . These rates are subsequently expressed in terms of Einstein coefficients A_{pq} , B_{pq} , and B_{qp} as shown in Table F.1.

Process	Incoming	Outgoing	Rate
Spontaneous Emission	X_p	$X_q + h\nu_{pq}$	$R_{pq} = A_{pq}n_p$
Absorption	$X_q + h\nu_{pq}$	X_p	$R_{qp} = n_q B_{pq} \bar{J}_{\nu_0}^\phi$
Stimulated Emission	$X_p + h\nu_{pq}$	$X_q + 2h\nu_{pq}$	$R_{pq} = n_p B_{pq} \bar{J}_{\nu_0}^\psi$

Table F.1: Radiative Rates [Rutten 2003]

Here, ϕ and ψ denote the line profiles for absorbed and stimulated photons, respectively. Meanwhile, $\bar{J}_{\nu_0}^f$ represents the average radiative intensity J_ν over a given line profile f .

To characterize the line profiles, models adopt the notion of *complete redistribution in frequency* for the sake of simplicity. This implies that the atoms have no "memory," making the absorption and emission line profiles identical ($\phi = \psi = \chi$). This results in broadening mechanisms affecting all lines similarly.

Natural Broadening A fundamental factor influencing the line profile is natural broadening, which arises due to the finite lifetime of the excited state. Utilizing the Einstein A_{pq} coefficient, which outlines the probability of spontaneous emission per second per particle, the lifetime of the excited state p can be expressed as A_p^{-1} where $A_p = \sum_q A_{pq}$. The electric field due to spontaneous emission from the state p decays as $\mathbf{E}(t) = \mathbf{E}(0) \exp(-A_p t/2)$. The factor 2 comes from the fact that the intensity decays actually in A_p^{-1} and is proportional to the square of the electric field. Taking the Fourier Transform of the electric field, yields the following variation in the frequency domain:

$$E(\nu) = \frac{1}{A/2 + i(\nu - \nu_0)},$$

which translates, by taking the modulus into a Lorentzian profile of the intensity.

$$f_L(\nu) = \frac{A_u/4\pi^2}{(A_u/4\pi)^2 + (\nu - \nu_0)^2} \quad (\text{F.1})$$

Doppler Broadening A second contributing factor is Doppler broadening, instigated by the thermal motion of particles in the plasma, resulting in a Doppler shift of the emitted frequency. The broadening depends on the frequency of the spectral line, the mass of the particle, and its kinetic temperature. Non-relativistic Doppler shift provides the relationship between the frequency of the radiation ν as observed by an observer and the one in the frame of reference of the emitter ν_0 :

$$\nu = \nu_0 \left(1 + \frac{v}{c}\right)$$

Assuming the emitting particles exhibit an isotropic Maxwellian velocity distribution, denoted as f_v , this distribution is defined by the proportionality:

$$f_v \propto \exp\left(-\frac{Mv^2}{2kT}\right)$$

Here, T represents the kinetic temperature of the particle and M stands for the mass of the atom. By substituting the velocity v using the Doppler shift expression, we can derive the expression for the Doppler line profile. Upon normalizing this profile, we obtain the ultimate form of the Doppler line profile:

$$f_D(\nu) = \sqrt{\frac{Mc^2}{2\pi k_B T f_0^2}} \exp\left(-\frac{Mc^2(\nu - \nu_0)^2}{2k_B T \nu_0^2}\right) \quad (\text{F.2})$$

Voigt Profile When both natural and Doppler broadening mechanisms are at play, the resultant line profile is a convolution of the Lorentz and Doppler profiles, known as the Voigt profile:

$$f_V(\nu) = \int f_L(\nu) f_D(\nu - \nu') d\nu' \quad (\text{F.3})$$

Estimation of the Depth of Field of the Lens Setup

The depth of field (DoF) can be calculated using the following formulas:

1. **Near Limit (Dn) and Far Limit (Df) of the depth of field:**

$$D_n = \frac{H \times s}{H + (s - f)} \quad (\text{G.1})$$

$$D_f = \frac{H \times s}{H - (s - f)} \quad (\text{G.2})$$

Where:

- H = Hyperfocal distance
- s = Distance from the lens to the object (subject distance) = 100 cm
- f = Focal length of the lens = 50 cm

2. **Hyperfocal distance (H):**

$$H = \frac{f^2}{N \times c} + f \quad (\text{G.3})$$

Where:

- N = F-number (aperture), which is derived from $N = \frac{f}{D}$
- D = Diameter of the entrance pupil = 0.4 mm = 0.04 cm
- c = Circle of confusion = 0.1 mm = 0.01 cm

Plugging in the values we have:

$$N = \frac{50 \text{ cm}}{0.04 \text{ cm}} = 1250 \quad (\text{G.4})$$

Now, for the hyperfocal distance:

$$H = \frac{50^2 \text{ cm}^2}{1250 \times 0.01 \text{ cm}} + 50 \text{ cm} \quad (\text{G.5})$$

$$= \frac{2500 \text{ cm}^2}{12.5 \text{ cm}} + 50 \text{ cm} \quad (\text{G.6})$$

$$= 250 \text{ cm} \quad (\text{G.7})$$

240 Appendix G. Estimation of the Depth of Field of the Lens Setup

Using this H , we can calculate D_n and D_f :

$$D_n = \frac{250 \text{ cm} \times 100 \text{ cm}}{250 \text{ cm} + (100 \text{ cm} - 50 \text{ cm})} \quad (\text{G.8})$$

$$= 83.33 \text{ cm} \quad (\text{G.9})$$

$$D_f = \frac{250 \text{ cm} \times 100 \text{ cm}}{250 \text{ cm} - (100 \text{ cm} - 50 \text{ cm})} \quad (\text{G.10})$$

$$= 125 \text{ cm} \quad (\text{G.11})$$

The depth of field is:

$$\text{DoF} = D_f - D_n \quad (\text{G.12})$$

$$= 41.67 \text{ cm} \quad (\text{G.13})$$

So, the depth of field for the given setup is approximately 41.67 cm.

ADAM Optimization

ADAM is a popular gradient descent optimization algorithm that combines the advantages of both momentum and RMSprop. **ADAM** combines the benefits of momentum (smooths out gradient updates) and RMSprop (adaptive learning rates) to achieve efficient optimization. Its adaptive nature makes it well-suited for various deep-learning tasks. Here's how **ADAM** works where t represents the current iteration:

- Compute the gradient $\nabla_{\mathbf{w}}J(\mathbf{w})_t$
- Update the biased first and second moment estimates m and v as follows:

$$\begin{aligned} m^t &= \beta_1 m^{t-1} + (1 - \beta_1) \nabla_{\mathbf{w}}J(\mathbf{w})_t, \\ v^t &= \beta_2 v^{t-1} + (1 - \beta_2) (\nabla_{\mathbf{w}}J(\mathbf{w}))_t^2, \end{aligned}$$

where β_1 and β_2 are the decay rates for the first and second moments, typically close to 1.

- Correct the biased first and second moment estimates to obtain the corrected biased first and second moment estimates \hat{m} and \hat{v} as follows:

$$\begin{aligned} \hat{m}^t &= \frac{m^t}{1 - \beta_1^t}, \\ \hat{v}^t &= \frac{v^t}{1 - \beta_2^t}, \end{aligned}$$

- Update weights: Finally, update the network weights using the corrected estimates:

$$\mathbf{w}^t = \mathbf{w}^{t-1} - \frac{\alpha}{\sqrt{\hat{v}^t} + \varepsilon} \hat{m}^t, \tag{H.1}$$

where α is the learning rate, and ε is a small constant (usually very small, e.g., 10^{-7}) to prevent division by zero.

Bibliography

- [A. Bretti 2022] Michael A. Bretti. *Progress and Developments of Ultra-Compact 10 Watt Class Adamantane Fueled Hall Thrusters for Picosatellites*. In Proceedings of 37th International Electric Propulsion Conference, 2022. (Cited on page 3.)
- [Abrantes & Martin 2021] Richard J. E. Abrantes and Robert S. Martin. *Reduced-order modeling of plasma ionization due to multifluid, collisional-radiative effects*. Physics of Plasmas, vol. 28, no. 2, page 022104, 2021. (Cited on page 126.)
- [Adam *et al.* 2004] J. C. Adam, A. Héron and G. Laval. *Study of stationary plasma thrusters using two-dimensional fully kinetic simulations*. Physics of Plasmas, vol. 11, no. 1, pages 295–305, 2004. (Cited on pages 5, 10 and 11.)
- [Akatsuka 2019] Hiroshi Akatsuka. *Optical Emission Spectroscopic analysis for diagnostics of electron density and temperature in non-equilibrium argon plasma based on collisional-radiative model*. Advances in Physics: X, vol. 4, no. 1, page 1592707, 2019. (Cited on page 36.)
- [Allan *et al.* 2006] M. Allan, O. Zatsarinny and K. Bartschat. *Near-threshold absolute angle-differential cross sections for electron-impact excitation of argon and xenon*. Phys. Rev. A, vol. 74, no. 3, page 030701, 2006. (Cited on page 33.)
- [Andrenucci *et al.* 2005] Mariano Andrenucci, Francesco Battista and Pietro Piliero. *Hall Thruster Scaling Methodology*. In Proceedings of 29th International Electric Propulsion Conference, 2005. (Cited on page 4.)
- [Andreussi *et al.* 2022] T. Andreussi, E. Ferrato, C. A. Paissoni, A. Kitaeva, V. Giannetti, A. Piragino, S. Schäff, K. Katsonis, Ch. Berenguer, Z. Kovacova, E. Neubauer, M. Tisaev, B. Karadag, A. Lucca Fabris, M. Smirnova, A. Mingo, D. Le Quang, Z. Alsalihi, F. Bariselli, P. Parodi, P. Jorge and T. E. Magin. *The AETHER project: development of air-breathing electric propulsion for VLEO missions*. CEAS Space Journal, vol. 14, no. 4, pages 717–740, 2022. (Cited on page 3.)
- [Baird *et al.* 2021] Matthew Baird, Thomas Kerber, Ron McGee-Sinclair and Kristina Lemmer. *Plume Divergence and Discharge Oscillations of an Accessible Low-Power Hall Effect Thruster*. Applied Sciences, vol. 11, no. 4, 2021. (Cited on page 167.)
- [Bartkowiak 2010] Konrad Bartkowiak. *Direct laser deposition process within spectrographic analysis in situ*. Physics Procedia, vol. 5, pages 623–629, 2010. (Cited on page 174.)

- [Bartschat *et al.* 2004] K. Bartschat, A. Dasgupta and D. H. Madison. *Close-coupling and distorted-wave calculations for electron-impact excitation of the ($5p^56p$) states of xenon*. Phys. Rev. A, vol. 69, no. 6, page 062706, 2004. (Cited on page 33.)
- [Bates *et al.* 1962] David Robert Bates, A. E. Kingston and R. W. P. McWhirter. *Recombination between electrons and atomic ions, I. Optically thin plasmas*. Proceedings of the Royal Society of London. Series A. Mathematical and Physical Sciences, vol. 267, no. 1330, pages 297–312, 1962. (Cited on page 26.)
- [Ben Slimane *et al.* 2022a] Tarek Ben Slimane, Thomas Charoy, Leduc Alexandre, Loic Schiesko, Anne Bourdon and Pascal Chabert. *Comparison of PIC simulation results of Hall Effect Thrusters against OES measurement using a xenon Collisional Radiative Model*. In Proceedings of 37th International Electric Propulsion Conference, 2022. (Cited on page 38.)
- [Ben Slimane *et al.* 2022b] Tarek Ben Slimane, Cyrille Honoré, Thomas Charoy, Anne Bourdon and Pascal Chabert. *Analysis of small scale fluctuations in Hall effect thrusters using virtual Thomson scattering on PIC simulations*. Physics of Plasmas, vol. 29, no. 2, page 023501, 2022. (Cited on page 9.)
- [Bhatia & Kastner 2000] A.K. Bhatia and S.O. Kastner. *Global and local Doppler-profile escape factors for plane-parallel geometry*. Journal of Quantitative Spectroscopy and Radiative Transfer, vol. 67, no. 1, pages 55–63, 2000. (Cited on page 43.)
- [Biagi 1988] S.F. Biagi. *Accurate solution of the Boltzmann transport equation*. Nuclear Instruments and Methods in Physics Research Section A: Accelerators, Spectrometers, Detectors and Associated Equipment, vol. 273, no. 2, pages 533–535, 1988. (Cited on page 33.)
- [Biagi 2022] S.F. Biagi. *Biagi Database V8.97 Fortran program, MAGBOLTZ*, www.lxcat.net, 2022. (Cited on page 33.)
- [Boccelli *et al.* 2019] Stefano Boccelli, Federico Bariselli, Bruno Dias and Thierry E Magin. *Lagrangian diffusive reactor for detailed thermochemical computations of plasma flows*. Plasma Sources Science and Technology, vol. 28, no. 6, page 065002, 2019. (Cited on page 117.)
- [Boeuf & Garrigues 2018] J. P. Boeuf and L. Garrigues. *$E \times B$ electron drift instability in Hall thrusters: Particle-in-cell simulations vs. theory*. Physics of Plasmas, vol. 25, no. 6, page 061204, 2018. (Cited on pages 12 and 13.)
- [Boeuf 2017] Jean-Pierre Boeuf. *Tutorial: Physics and modeling of Hall thrusters*. Journal of Applied Physics, vol. 121, no. 1, page 011101, 2017. (Cited on page 11.)

- [Boffard *et al.* 2004] John B Boffard, Chun C Lin and Charles A DeJosephJr. *Application of excitation cross sections to optical plasma diagnostics*. J. Phys. D: Appl. Phys., vol. 37, no. 12, pages R143–R161, 2004. (Cited on pages 34, 36, 37, 69, 109 and 209.)
- [Boffard *et al.* 2007] John B. Boffard, R.O. Jung, L.W. Anderson and C.C. Lin. *Electron-Impact Excitation of Rare-Gas Atoms from the Ground Level and Metastable Levels*. In Advances In Atomic, Molecular, and Optical Physics, volume 54, pages 319–421. 2007. (Cited on pages 34 and 224.)
- [Boffard *et al.* 2010] John B Boffard, R O Jung, Chun C Lin and A E Wendt. *Optical emission measurements of electron energy distributions in low-pressure argon inductively coupled plasmas*. Plasma Sources Sci. Technol., vol. 19, no. 6, page 065001, 2010. (Cited on page 36.)
- [Boffard *et al.* 2018] John B. Boffard, Chun C. Lin and Amy E. Wendt. *Application of Excitation Cross-Section Measurements to Optical Plasma Diagnostics*. In Advances In Atomic, Molecular, and Optical Physics, volume 67, pages 1–76. 2018. (Cited on pages 36, 40, 43 and 155.)
- [Bordage *et al.* 2013] M. C. Bordage, S. F. Biagi, L. L. Alves, K. Bartschat, S. Chowdhury, L. C. Pitchford, G. J. M. Hagelaar, W. L. Morgan, V. Puech and O. Zatsarinny. *Comparisons of sets of electron–neutral scattering cross sections and swarm parameters in noble gases: III. Krypton and xenon*. J. Phys. D: Appl. Phys., vol. 46, no. 33, page 334003, 2013. (Cited on page 33.)
- [Brown & Jorns 2019] Zachariah A. Brown and Benjamin A. Jorns. *Spatial evolution of small wavelength fluctuations in a Hall Thruster*. Physics of Plasmas, vol. 26, no. 11, page 113504, 2019. (Cited on pages 5 and 10.)
- [Buckman *et al.* 1983] S. J. Buckman, P. Hammond, G. C. King and F. H. Read. *High-resolution electron impact excitation functions of metastable states of neon, argon, krypton and xenon*. J. Phys. B: Atom. Mol. Phys., vol. 16, no. 22, page 4219, 1983. (Cited on page 32.)
- [Bugrova *et al.* 2012] A. I. Bugrova, G. E. Bugrov, V. K. Kharchevnikov, M. I. Shaposhnikov and S. Mazouffre. *Effect of deposited RF power on stationary plasma thruster characteristics*. Technical Physics Letters, vol. 38, no. 4, pages 344–346, 2012. (Cited on page 3.)
- [Byrne & Hindmarsh 1975] G. D. Byrne and A. C. Hindmarsh. *A Polyalgorithm for the Numerical Solution of Ordinary Differential Equations*. ACM Transactions on Mathematical Software (TOMS), vol. 1, no. 1, pages 71–96, 1975. (Cited on page 48.)
- [Cavalier *et al.* 2013] J. Cavalier, N. Lemoine, G. Bonhomme, S. Tsikata, C. Honoré and D. Grésillon. *Hall thruster plasma fluctuations identified as the $\mathbf{E} \times \mathbf{B}$*

- electron drift instability: Modeling and fitting on experimental data.* Physics of Plasmas, vol. 20, no. 8, page 082107, 2013. (Cited on page 10.)
- [Chang & Yang 2018] Chi-Lung Chang and Fu-Chi Yang. *Synthesis and characteristics of nc-WC/a-C:H thin films deposited via a reactive HIPIMS process using optical emission spectrometry feedback control.* Surface and Coatings Technology, vol. 350, pages 1120–1127, 2018. (Cited on page 174.)
- [Charoy *et al.* 2019] T Charoy, J P Boeuf, A Bourdon, J A Carlsson, P Chabert, B Cuenot, D Eremin, L Garrigues, K Hara, I D Kaganovich, A T Powis, A Smolyakov, D Sydorenko, A Tavant, O Vermorel and W Villafana. *2D axial-azimuthal particle-in-cell benchmark for low-temperature partially magnetized plasmas.* Plasma Sources Science and Technology, vol. 28, no. 10, page 105010, 2019. (Cited on pages xiii, 6, 7, 10, 11, 12, 13, 15 and 23.)
- [Charoy 2020] Thomas Charoy. *Numerical study of electron transport in Hall thrusters.* These de doctorat, Institut polytechnique de Paris, 2020. (Cited on pages 6, 90, 91, 92, 95 and 168.)
- [Chiu *et al.* 2006] Yu-hui Chiu, Brad L. Austin, Skip Williams, Rainer A. Dressler and George F. Karabadzhak. *Passive optical diagnostic of Xe-propelled Hall thrusters. I. Emission cross sections.* Journal of Applied Physics, vol. 99, no. 11, page 113304, 2006. (Cited on pages xxix, 36, 80, 81 and 83.)
- [Choueiri 2001] E. Y. Choueiri. *Plasma oscillations in Hall thrusters.* Physics of Plasmas, vol. 8, no. 4, pages 1411–1426, 2001. (Cited on page 130.)
- [Choueiri 2009] Edgar Y. Choueiri. *New Dawn for Electric Rockets.* Scientific American, vol. 300, no. 2, pages 58–65, 2009. (Cited on page 1.)
- [Clark *et al.* 2013] Stephen D Clark, Mark S Hutchins, Ismat Rudwan, Neil C Wallace, Javier Palencia and Howard Gray. *BepiColombo electric propulsion thruster and high power electronics coupling test performances.* In Proceedings of 33th International Electric Propulsion Conference, 2013. (Cited on page 2.)
- [Claude 1967] Breton Claude. *Etude de l'ionisation de l'hydrogène dans une décharge puisée.- Saclay (Essonne), Centre d'études nucléaires, Service de documentation du Commissariat à l'énergie atomique, 1967.- 27 cm, 1Q3 P., (Thèse. Se. phys. Paris. Centre d'Orsay. 1967. No 221.).* 1967. (Cited on page 43.)
- [Cornara *et al.* 2012] S. Cornara, F. Pirondini, A. Caramagno, M. Price, J. González del Amo and B. Carnicero-Domínguez. *Analyses of Remote Sensing Mission Scenarios with Electric Propulsion.* In 56th International Astronautical Congress, 2012. (Cited on page 2.)
- [Cusson *et al.* 2018] S. E. Cusson, M. P. Georjgin, H. C. Dragnea, E. T. Dale, V. Dhaliwal, I. D. Boyd and A. D. Gallimore. *On channel interactions in*

- nested Hall thrusters*. Journal of Applied Physics, vol. 123, no. 13, page 133303, 2018. (Cited on page 3.)
- [Dannenmayer & Mazouffre 2011] Käthe Dannenmayer and Stéphane Mazouffre. *Elementary Scaling Relations for Hall Effect Thrusters*. Journal of Propulsion and Power, vol. 27, no. 1, pages 236–245, 2011. (Cited on page 4.)
- [Dannenmayer & Mazouffre 2013] K Dannenmayer and Stéphane Mazouffre. *Electron flow properties in the far-field plume of a Hall thruster*. Plasma Sources Science and Technology, vol. 22, no. 3, page 035004, 2013. (Cited on pages 97, 140 and 143.)
- [Dannenmayer *et al.* 2014] K Dannenmayer, S Mazouffre, P Kudrna and M Tichý. *The time-varying electron energy distribution function in the plume of a Hall thruster*. Plasma Sources Science and Technology, vol. 23, no. 6, page 065001, 2014. (Cited on pages 97 and 140.)
- [Darwin 1963] H. W. Darwin. *Atomic cross-sections for inelastic electronic collisions*. Technical report Report, EUR-CEA-FC, 1963. (Cited on page 33.)
- [Domínguez Vázquez 2019] Adrián Domínguez Vázquez. *Axisymmetric simulation codes for hall effect thrusters and plasma plumes*. Phd thesis, University Carlos III, 2019. (Cited on pages 146, 158 and 168.)
- [Dressler *et al.* 2009] Rainer A Dressler, Yu-hui Chiu, Oleg Zatsarinny, Klaus Bartschat, Rajesh Srivastava and Lalita Sharma. *Near-infrared collisional radiative model for Xe plasma electrostatic thrusters: the role of metastable atoms*. J. Phys. D: Appl. Phys., vol. 42, no. 18, page 185203, 2009. (Cited on pages xvii, 37, 81, 82, 83 and 226.)
- [Felt'san 1967] P.V. Felt'san. *Experimental study of the excitation cross sections of 2p levels of atoms of inert gases (Russian): Thesis for the degree of Candidate of Physical and Mathematical Sciences*. 1967. (Cited on pages 31 and 221.)
- [Filipović *et al.* 1988] D. Filipović, B. Marinković, V. Pejcev and And L. Vusković. *Electron-impact excitation of xenon at incident energies between 15 and 80 eV*. Phys. Rev. A, vol. 37, no. 2, pages 356–364, 1988. (Cited on pages 32 and 221.)
- [Fine *et al.* 2020] Jonathan A. Fine, Anand A. Rajasekar, Krupal P. Jethava and Gaurav Chopra. *Spectral deep learning for prediction and prospective validation of functional groups*. Chemical Science, vol. 11, no. 18, pages 4618–4630, 2020. (Cited on page 174.)
- [Fons & Lin 1998] John T. Fons and Chun C. Lin. *Measurement of the cross sections for electron-impact excitation into the $5p^56p$ levels of xenon*. Phys. Rev. A, vol. 58, no. 6, pages 4603–4615, 1998. (Cited on pages 32, 33, 34, 35, 37, 42 and 80.)

- [Frias *et al.* 2012] Winston Frias, Andrei I. Smolyakov, Igor D. Kaganovich and Yevgeny Raitses. *Long wavelength gradient drift instability in Hall plasma devices. I. Fluid theory*. *Physics of Plasmas*, vol. 19, no. 7, page 072112, 2012. (Cited on page 10.)
- [Froula *et al.* 2011] Dustin H. Froula, Siegfried H. Glenzer, Neville C. Luhmann and John Sheffield. *Chapter 2 and Chapter 5*. In *Plasma Scattering of Electromagnetic Radiation (Second Edition)*, pages 103–142. Academic Press, second edition édition, 2011. (Cited on page 15.)
- [Garrigues *et al.* 2008] Laurent Garrigues, Gerjan J. M. Hagelaar, Jean Pierre Boeuf, Yevgeny Raitses, Artem Smirnov and Nathaniel J. Fisch. *Simulations of a Miniaturized Cylindrical Hall Thruster*. *IEEE Transactions on Plasma Science*, vol. 36, no. 5, pages 2034–2042, 2008. (Cited on page 4.)
- [Garrigues *et al.* 2019] L. Garrigues, S. Santhosh, L. Grimaud and S. Mazouffre. *Operation of a low-power Hall thruster: comparison between magnetically unshielded and shielded configuration*. *Plasma Sources Science and Technology*, vol. 28, no. 3, page 034003, 2019. (Cited on page 3.)
- [Gascon *et al.* 2003] N. Gascon, M. Dudeck and S. Barral. *Wall material effects in stationary plasma thrusters. I. Parametric studies of an SPT-100*. *Physics of Plasmas*, vol. 10, no. 10, pages 4123–4136, 2003. (Cited on pages 130, 131 and 132.)
- [Ghosh *et al.* 2019] Kunal Ghosh, Annika Stuke, Milica Todorović, Peter Bjørn Jørgensen, Mikkel N. Schmidt, Aki Vehtari and Patrick Rinke. *Deep Learning Spectroscopy: Neural Networks for Molecular Excitation Spectra*. *Advanced Science*, vol. 6, no. 9, page 1801367, 2019. (Cited on pages 174 and 180.)
- [Giannetti *et al.* 2020] V. Giannetti, M. M. Saravia and T. Andreussi. *Measurement of the breathing mode oscillations in Hall thruster plasmas with a fast-diving triple Langmuir probe*. *Physics of Plasmas*, vol. 27, no. 12, page 123502, 2020. (Cited on page 126.)
- [Godyak & Demidov 2011] V. Godyak and V. I. Demidov. *Probe measurements of electron-energy distributions in plasmas: what can we measure and how can we achieve reliable results?* *Journal of Physics D: Applied Physics*, vol. 44, no. 23, page 233001, 2011. (Cited on page 135.)
- [Godyak 2021] V. Godyak. *RF discharge diagnostics: Some problems and their resolution*. *Journal of Applied Physics*, vol. 129, no. 4, page 041101, 2021. (Cited on page 135.)
- [Goebel & Katz 2008] D.M. Goebel and I. Katz. *Fundamentals of Electric Propulsion: Ion and Hall Thrusters*. 2008. (Cited on pages 142 and 166.)

- [Golubovskii *et al.* 2013] Y. Golubovskii, S. Gorchakov and D. Uhrlandt. *Transport mechanisms of metastable and resonance atoms in a gas discharge plasma*. Plasma Sources Science and Technology, vol. 22, no. 2, page 023001, 2013. (Cited on page 44.)
- [Gonzales *et al.* 2014] Ashley E. Gonzales, Justin W. Koo and William A. Hargus. *Comparison of Numerical and Experimental Time-Resolved Near-Field Hall Thruster Plasma Properties*. IEEE Transactions on Plasma Science, vol. 42, no. 3, pages 806–812, 2014. (Cited on pages 102, 116, 117 and 120.)
- [Grimaud & Mazouffre 2017] L. Grimaud and S. Mazouffre. *Ion behavior in low-power magnetically shielded and unshielded Hall thrusters*. Plasma Sources Science and Technology, vol. 26, no. 5, page 055020, 2017. (Cited on page 3.)
- [Géron 2019] Aurélien Géron. Hands-on machine learning with Scikit-Learn, Keras, and TensorFlow: concepts, tools, and techniques to build intelligent systems. Second edition édition, 2019. (Cited on pages 180 and 181.)
- [Hairer & Wanner 1996a] Ernst Hairer and Gerhard Wanner. *Convergence for Linear Problems*. In Ernst Hairer and Gerhard Wanner, editors, Solving Ordinary Differential Equations II: Stiff and Differential-Algebraic Problems, Springer Series in Computational Mathematics, pages 321–338. 1996. (Cited on page 48.)
- [Hairer & Wanner 1996b] Ernst Hairer and Gerhard Wanner. *Generalized Multistep Methods*. In Ernst Hairer and Gerhard Wanner, editors, Solving Ordinary Differential Equations II: Stiff and Differential-Algebraic Problems, Springer Series in Computational Mathematics, pages 261–278. 1996. (Cited on page 48.)
- [Hairer & Wanner 1996c] Ernst Hairer and Gerhard Wanner. *Stability of Multistep Methods*. In Ernst Hairer and Gerhard Wanner, editors, Solving Ordinary Differential Equations II: Stiff and Differential-Algebraic Problems, Springer Series in Computational Mathematics, pages 240–249. 1996. (Cited on page 48.)
- [Hara & D.Boyed 2013] Kentaro Hara and Iain D.Boyed. *Low Frequency Oscillation Analysis of a Hall Thruster Using a One-Dimensional Hybrid-Direct Kinetic Simulation*. In the 33rd International Electric Propulsion Conference., 2013. (Cited on page 195.)
- [Hara 2019] Kentaro Hara. *An overview of discharge plasma modeling for Hall effect thrusters*. Plasma Sources Science and Technology, vol. 28, no. 4, page 044001, 2019. (Cited on pages 10 and 11.)
- [Hargus & Charles 2010] William A. Hargus and Christopher S. Charles. *Near-Plume Laser-Induced Fluorescence Velocity Measurements of a Medium*

- Power Hall Thruster*. Journal of Propulsion and Power, vol. 26, no. 1, pages 135–141, 2010. (Cited on page 126.)
- [Hartgers *et al.* 2001] A. Hartgers, J. van Dijk, J. Jonkers and J. A. M. van der Mullen. *CRModel: A general collisional radiative modeling code*. Computer Physics Communications, vol. 135, no. 2, pages 199–218, 2001. (Cited on page 42.)
- [Hayashi 2003] Makato Hayashi. *Bibliography of electron and photon cross sections with atoms and molecules published in the 20th century*. NIFS-DATA-079 1 NIFS Series, 2003. (Cited on page 33.)
- [Hearn 1963] A. G. Hearn. *Radiative Transfer of Doppler Broadened Resonance Lines*. Proceedings of the Physical Society, vol. 81, no. 4, pages 648–662, 1963. (Cited on page 43.)
- [Heddle & Gallagher 1989] D. W. O. Heddle and Jean W. Gallagher. *Measurements of electron impact optical excitation functions*. Rev. Mod. Phys., vol. 61, no. 2, pages 221–278, 1989. (Cited on page 32.)
- [Hofer *et al.* 2008] Richard R. Hofer, Lee K. Johnson, Dan M. Goebel and Richard E. Wirz. *Effects of Internally Mounted Cathodes on Hall Thruster Plume Properties*. IEEE Transactions on Plasma Science, vol. 36, no. 5, pages 2004–2014, 2008. (Cited on page 132.)
- [Holstein 1947] T. Holstein. *Imprisonment of Resonance Radiation in Gases*. Physical Review, vol. 72, no. 12, pages 1212–1233, 1947. (Cited on page 43.)
- [Holzhauer & Massig 1978] E. Holzhauer and J. H. Massig. *An analysis of optical mixing in plasma scattering experiments*. Plasma Physics, vol. 20, no. 9, pages 867–877, 1978. (Cited on page 15.)
- [Honoré *et al.* 2011] C. Honoré, S. Tsikata, D. Grésillon, A. Héron, N. Lemoine and J. Cavalier. *Hall Thruster small scale plasma fluctuations: Qualifying 2D PIC Simulations against Collective Scattering Experimental Data*. In The 32nd International Electric Propulsion Conference., 2011. (Cited on pages 7, 10 and 19.)
- [Hutchinson 2002] I. H. Hutchinson. Principles of plasma diagnostics. Cambridge University Press, 2nd ed édition, 2002. (Cited on page 37.)
- [Irons 1979] F. E. Irons. *The escape factor in plasma spectroscopy—I. The escape factor defined and evaluated*. Journal of Quantitative Spectroscopy and Radiative Transfer, vol. 22, no. 1, pages 1–20, 1979. (Cited on page 43.)
- [Jackson *et al.* 2018] Jerry Jackson, Joseph Cassady, May Allen, Roger Myers, Todd Tofil, Dan Herman and Eric Pencil. *Development of high power hall thruster systems to enable the NASA exploration vision*. In Space Propulsion conference, 2018. (Cited on page 2.)

- [Jahn & Choueiri 2003] Robert G. Jahn and Edgar Y. Choueiri. *Electric Propulsion*. In Encyclopedia of Physical Science and Technology (Third Edition), pages 125–141. Academic Press, third edition édition, 2003. (Cited on page 2.)
- [Jing & Lang 2015] Xingjian Jing and Ziqiang Lang. Frequency Domain Analysis and Design of Nonlinear Systems based on Volterra Series Expansion: A Parametric Characteristic Approach. Understanding Complex Systems. 2015. (Cited on page 117.)
- [Joung *et al.* 2021] Joonyoung F. Joung, Minhi Han, Jinhyo Hwang, Minseok Jeong, Dong Hoon Choi and Sungnam Park. *Deep Learning Optical Spectroscopy Based on Experimental Database: Potential Applications to Molecular Design*. JACS Au, vol. 1, no. 4, pages 427–438, 2021. (Cited on pages 174 and 181.)
- [Jr & Clark 1990] C. A. DeJoseph Jr and J. D. Clark. *Electron impact infrared excitation functions from the 5d levels of xenon*. J. Phys. B: At. Mol. Opt. Phys., vol. 23, no. 11, page 1879, 1990. (Cited on page 32.)
- [Jung *et al.* 2005] R. Jung, John Boffard, L. Anderson and Chun Lin. *Electron-impact excitation cross sections from the xenon $J=2$ metastable level*. Phys. Rev. A, vol. 72, 2005. (Cited on pages 32, 33, 35 and 224.)
- [Jung *et al.* 2009] R. O. Jung, John B. Boffard, L. W. Anderson and Chun C. Lin. *Excitation into $5p^57p$ levels from the ground level and the $J=2$ metastable level of Xe*. Phys. Rev. A, vol. 80, no. 6, page 062708, 2009. (Cited on pages 32, 33 and 35.)
- [Kaganovich *et al.* 2020] Igor D. Kaganovich, Andrei Smolyakov, Yevgeny Raitses, Eduardo Ahedo, Ioannis G. Mikellides, Benjamin Jorns, Francesco Tacogna, Renaud Gueroult, Sedina Tsikata, Anne Bourdon, Jean-Pierre Boeuf, Michael Keidar, Andrew Tasman Powis, Mario Merino, Mark Cappelli, Kentaro Hara, Johan A. Carlsson, Nathaniel J. Fisch, Pascal Chabert, Irina Schweigert, Trevor Laffleur, Konstantin Matyash, Alexander V. Khrabrov, Rod W. Boswell and Amnon Fruchtman. *Physics of $\mathbf{E} \times \mathbf{B}$ discharges relevant to plasma propulsion and similar technologies*. Physics of Plasmas, vol. 27, no. 12, page 120601, 2020. (Cited on pages 5 and 10.)
- [Kang *et al.* 2014] Jun Kang, Wenjun Meng, Ajith Abraham and Hongbo Liu. *An adaptive PID neural network for complex nonlinear system control*. Neurocomputing, vol. 135, pages 79–85, 2014. (Cited on page 202.)
- [Kanik *et al.* 2001] I Kanik, P V Johnson and G K James. *Electron-impact-induced emission and excitation cross sections of xenon at low energies*. Journal of Physics B: Atomic, Molecular and Optical Physics, vol. 34, no. 9, page 1685, 2001. (Cited on page 32.)

- [Karabadzhak *et al.* 1997] George Karabadzhak, Flur Gabdullin, Anatoli Korsun, Yuri Plastinin and Ekaterina Tverdokhlebova. *Optical Emission of a Hall Thruster Plume in Space Condition*. 1997. (Cited on page 36.)
- [Karabadzhak *et al.* 2006] George F. Karabadzhak, Yu-hui Chiu and Rainer A. Dressler. *Passive optical diagnostic of Xe propelled Hall thrusters. II. Collisional-radiative model*. *Journal of Applied Physics*, vol. 99, no. 11, page 113305, 2006. (Cited on pages xvii, xxix, 6, 36, 43, 62, 78, 79, 81, 82, 83, 90, 126, 154, 191, 209 and 224.)
- [Kaur *et al.* 1998] Savinder Kaur, R. Srivastava, R. P. McEachran and A. D. Stauffer. *Electron impact excitation of the states of Ar, Kr and Xe atoms*. *J. Phys. B: At. Mol. Opt. Phys.*, vol. 31, no. 21, page 4833, 1998. (Cited on page 32.)
- [Khayms & Martinez-Sanchez 1996] V. Khayms and M. Martinez-Sanchez. *Design of a miniaturized Hall thruster for microsatellites*. In 32nd Joint Propulsion Conference and Exhibit, Joint Propulsion Conferences. 1996. (Cited on page 4.)
- [Kim *et al.* 2022] Jinwoo Kim, Dongho Lee, Guentae Doh, Sanghoo Park, Holak Kim and Wonho Choe. *Three-dimensional tomographically reconstructed optical emission profiles of Hall thruster plasmas*. *Plasma Sources Science and Technology*, vol. 31, no. 1, page 015013, 2022. (Cited on page 117.)
- [Kingma & Ba 2015] Diederik P. Kingma and Jimmy Ba. *Adam: A Method for Stochastic Optimization*. In the 3rd International Conference for Learning Representations, 2015. (Cited on page 179.)
- [Konopliv *et al.* 2021] Mary Konopliv, Lee K. Johnson, Vernon H. Chaplin, Robert B. Lobbia, Anirudh Thuppul, Timothy Simka and Richard E. Wirz. *Collisional-Radiative Models of Neutral and Singly-Ionized Xenon in Hall Thrusters: Experimental Validation and Model Investigations*. In AIAA Propulsion and Energy 2021 Forum, 2021. (Cited on pages 120, 126 and 171.)
- [Koo *et al.* 2017] Junmo Koo, Daegeun Ha, Damdae Park, Hyun-Joon Roh, Sangwon Ryu, Gon-Ho Kim, Kye Hyun Baek and Chonghun Han. *Design of optical emission spectroscopy based plasma parameter controller for real-time advanced equipment control*. *Computers & Chemical Engineering*, vol. 100, pages 38–47, 2017. (Cited on page 174.)
- [Koppel *et al.* 2004] Christophe Koppel, Frédéric Marchandise, Denis Estublier and Laurent Jolivet. *The Smart-1 Electric Propulsion Subsystem In Flight Experience*. In 40th AIAA/ASME/SAE/ASEE Joint Propulsion Conference and Exhibit, 2004. (Cited on page 2.)
- [Korotkov *et al.* 1988] A.I. Korotkov, L.K. Mitryukhin, N.I. Petrov and G.M. Sorokin. *Electron-impact measurement of excitation functions of lower*

- metastable states of Xe I atom*. Opt. Spectrosc. (Engl. Transl.), vol. 64:2, 1988. (Cited on page 32.)
- [Kramida & Ralchenko 1999] Alexander Kramida and Yuri Ralchenko. *NIST Atomic Spectra Database, NIST Standard Reference Database 78*, 1999. (Cited on pages 31, 34 and 228.)
- [Kramida *et al.* 2019] A. Kramida, Yu. Ralchenko, J. Reader and NIST ASD Team. NIST Atomic Spectra Database (ver. 5.7.1), [Online]. Available: <https://physics.nist.gov/asd> [2020, January 13]. National Institute of Standards and Technology, Gaithersburg, MD., 2019. (Cited on page 83.)
- [Kraskov *et al.* 2004] Alexander Kraskov, Harald Stögbauer and Peter Grassberger. *Estimating mutual information*. Phys. Rev. E, vol. 69, page 066138, 2004. (Cited on page 190.)
- [Lafleur *et al.* 2017] T Lafleur, S D Baalrud and P Chabert. *Characteristics and transport effects of the electron drift instability in Hall-effect thrusters*. Plasma Sources Science and Technology, vol. 26, no. 2, page 024008, 2017. (Cited on pages 5, 10, 11 and 13.)
- [Lafleur *et al.* 2018] T. Lafleur, R. Martorelli, P. Chabert and A. Bourdon. *Anomalous electron transport in Hall-effect thrusters: Comparison between quasi-linear kinetic theory and particle-in-cell simulations*. Physics of Plasmas, vol. 25, no. 6, page 061202, 2018. (Cited on pages 10, 11, 13 and 14.)
- [Lazurenko *et al.* 2005a] A. Lazurenko, V. Vial, M. Prioul and A. Bouchoule. *Experimental investigation of high-frequency drifting perturbations in Hall thrusters*. Physics of Plasmas, vol. 12, no. 1, pages 013501–013501–9, 2005. (Cited on page 10.)
- [Lazurenko *et al.* 2005b] A. Lazurenko, V. Vial, M. Prioul and A. Bouchoule. *Experimental investigation of high-frequency drifting perturbations in Hall thrusters*. Physics of Plasmas, vol. 12, no. 1, pages 013501–013501–9, 2005. (Cited on page 126.)
- [Lazurenko *et al.* 2007a] A. Lazurenko, T. Dudok de Wit, C. Cavoit, V. Krasnoselskikh, A. Bouchoule and M. Dudeck. *Determination of the electron anomalous mobility through measurements of turbulent magnetic field in Hall thrusters*. Physics of Plasmas, vol. 14, no. 3, page 033504, 2007. (Cited on pages 5 and 10.)
- [Lazurenko *et al.* 2007b] A. Lazurenko, T. Dudok de Wit, C. Cavoit, V. Krasnoselskikh, A. Bouchoule and M. Dudeck. *Determination of the electron anomalous mobility through measurements of turbulent magnetic field in Hall thrusters*. Physics of Plasmas, vol. 14, no. 3, page 033504, 2007. (Cited on page 126.)

- [Lee *et al.* 2021] H.C. Lee, C.H. Lim, Y.T. Lau and O.H. Chin. *Triple Langmuir probe measurements in a low-energy tongue-flared configuration plasma thruster*. *Vacuum*, vol. 187, page 110135, 2021. (Cited on page 126.)
- [Leray & Bretagne 1997] Philippe Leray and Jean Bretagne. *Étude de la Physique Interne d'un Propulseur à Plasmas Stationnaire Par Spectrométrie Optique d'Émission*. PhD thesis, Université d'Orsay, 1997. (Cited on pages 146 and 171.)
- [Leray *et al.* 1997] Philippe Leray, Jean Bonnet and Daniel Pigache. *Spatially Resolved Emission Spectroscopy Along a SPT Channel*. In 2nd Euro. Space. Prop. Conf., ESA SP-398 (Noordwijk), 1997. (Cited on page 36.)
- [Levchenko *et al.* 2020] I. Levchenko, S. Xu, S. Mazouffre, D. Lev, D. Pedrini, D. Goebel, L. Garrigues, F. Taccogna and K. Bazaka. *Perspectives, frontiers, and new horizons for plasma-based space electric propulsion*. *Physics of Plasmas*, vol. 27, no. 2, page 020601, 2020. (Cited on page 3.)
- [Lin *et al.* 2023] Keren Lin, Atsushi Nezu and Hiroshi Akatsuka. *Development of diagnostics of electron density and temperature for atmospheric-pressure helium plasma based on optical emission spectroscopy analysis and a collisional-radiative model*. *Jpn. J. Appl. Phys.*, vol. 62, no. SL, page SL1005, 2023. (Cited on page 36.)
- [Madison & Shelton 1973] D. H. Madison and W. N. Shelton. *Distorted-Wave Approximation and Its Application to the Differential and Integrated Cross Sections for Electron-Impact Excitation of the 2^1P State of Helium*. *Phys. Rev. A*, vol. 7, pages 499–513, 1973. (Cited on page 33.)
- [Makato 2022] Hayashi Makato. *HAYASHI Database*, www.lxcat.net. 2022. (Cited on page 33.)
- [Manzella 1993] David H Manzella. *Stationary Plasma Thruster Plume Emissions*. In the 23rd International Electric Propulsion Conference, 1993. (Cited on page 36.)
- [Mazouffre *et al.* 2014] S. Mazouffre, S. Tsikata and J. Vaudolon. *Development and experimental characterization of a wall-less Hall thruster*. *Journal of Applied Physics*, vol. 116, no. 24, page 243302, 2014. (Cited on page 3.)
- [Mazouffre 2012] Stéphane Mazouffre. *Laser-induced fluorescence diagnostics of the cross-field discharge of Hall thrusters*. vol. 22, no. 1, page 013001, 2012. (Cited on page 126.)
- [Mazouffre 2016] Stéphane Mazouffre. *Electric propulsion for satellites and spacecraft: established technologies and novel approaches*. *Plasma Sources Science and Technology*, vol. 25, no. 3, page 033002, 2016. (Cited on page 2.)

- [Meiden 2011] van der Meiden H.J. *Thomson scattering on low and high temperature plasmas*. Phd Thesis, Technische Universiteit Eindhoven, 2011. (Cited on page 15.)
- [Mewe 1967] R. Mewe. *Relative intensity of helium spectral lines as a function of electron temperature and density*. British Journal of Applied Physics, vol. 18, no. 1, page 107, 1967. (Cited on pages 37 and 43.)
- [Miller & Woellert 2020] Mike Miller and Kirk Woellert. *Nanosatellites: Space and ground technologies, operations and economics*. 2020. (Cited on page 1.)
- [Mityureva & Smirnov 1994] A. A. Mityureva and V. V. Smirnov. *Excitation of heavy rare gases to metastable states by electron impact*. J. Phys. B: At. Mol. Opt. Phys., vol. 27, no. 9, page 1869, 1994. (Cited on page 32.)
- [Moisan *et al.* 2021] Michel Moisan, Danielle Kéroack and Luc Stafford. *Physique atomique et spectroscopie optique*. 2021. (Cited on pages 28 and 30.)
- [Moiseiwitsch & Smith 1968] B. L. Moiseiwitsch and S. J. Smith. *Electron Impact Excitation of Atoms*. Rev. Mod. Phys., vol. 40, no. 2, pages 238–353, 1968. (Cited on page 33.)
- [Molisch & Oehry 1998] Andreas F. Molisch and Bernhard P. Oehry. *Radiation trapping in atomic vapours*. Oxford science publications. 1998. (Cited on page 43.)
- [Nakazaki *et al.* 1997] S. Nakazaki, K. A. Berrington, W. B. Eissner and Y. Itikawa. *Excitation of xenon by electron impact*. J. Phys. B: At. Mol. Opt. Phys., vol. 30, no. 24, page 5805, 1997. (Cited on page 32.)
- [Nakles & Matlo 2019] Michael R. Nakles and Taylor S. Matlo. *Hall Thruster Near-Field Plume Characterization Through Optical Emission Spectroscopy*. In Proceedings of 36th International Electric Propulsion Conference, 2019. (Cited on page 117.)
- [Orlikovskii & Rudenko 2001] A. A. Orlikovskii and K. V. Rudenko. *In situ Diagnostics of Plasma Processes in Microelectronics: The Current Status and Immediate Prospects. Part I*. Russian Microelectronics, vol. 30, no. 2, pages 69–87, 2001. (Cited on page 174.)
- [O'Reilly *et al.* 2021] Dillon O'Reilly, Georg Herdrich and Darren F. Kavanagh. *Electric Propulsion Methods for Small Satellites: A Review*. Aerospace, vol. 8, no. 1, 2021. (Cited on page 2.)
- [Pagnon *et al.* 2004] D. Pagnon, P. Lasgorceix and M. Touzeau. *Control of the Ceramic Erosion by Optical Emission Spectroscopy: Results of PPS1350-G Measurements*. In 4th International Spacecraft Propulsion Conference, volume 555 of *ESA Special Publication*, page 23.1, October 2004. (Cited on page 36.)

- [Parks & Katz] D. Parks and I. Katz. *A preliminary model of ion beam neutralization*. In 14th International Electric Propulsion Conference. (Cited on page 142.)
- [Pedregosa *et al.* 2011] F. Pedregosa, G. Varoquaux, A. Gramfort, V. Michel, B. Thirion, O. Grisel, M. Blondel, P. Prettenhofer, R. Weiss, V. Dubourg, J. Vanderplas, A. Passos, D. Cournapeau, M. Brucher, M. Perrot and E. Duchesnay. *Scikit-learn: Machine Learning in Python*. Journal of Machine Learning Research, vol. 12, pages 2825–2830, 2011. (Cited on page 180.)
- [Perez-Luna *et al.* 2007] J. Perez-Luna, G. J. M. Hagelaar, L. Garrigues and J. P. Boeuf. *Model analysis of a double-stage Hall effect thruster with double-peaked magnetic field and intermediate electrode*. Physics of Plasmas, vol. 14, no. 11, page 113502, 2007. (Cited on page 3.)
- [Petronio *et al.* 2023a] Federico Petronio, Thomas Charoy, Alejandro Alvarez Laguna, Anne Bourdon and Pascal Chabert. *Two-dimensional effects on electrostatic instabilities in Hall thrusters. I. Insights from particle-in-cell simulations and two-point power spectral density reconstruction techniques*. Physics of Plasmas, vol. 30, no. 1, page 012103, 2023. (Cited on pages xiv, 10, 39, 90 and 92.)
- [Petronio *et al.* 2023b] Federico Petronio, Thomas Charoy, Alejandro Alvarez Laguna, Anne Bourdon and Pascal Chabert. *Two-dimensional effects on electrostatic instabilities in Hall thrusters. II. Comparison of particle-in-cell simulation results with linear theory dispersion relations*. Physics of Plasmas, vol. 30, no. 1, page 012104, 2023. (Cited on pages 90 and 115.)
- [Petronio 2023] Federico Petronio. *Plasmas Instabilities in Hall Thrusters: a Theoretical and Numerical Study*. PhD dissertation, Institut Polytechnique de Paris (IPP), 2023. (Cited on pages 6, 90, 91, 92, 95, 159 and 168.)
- [Pilania *et al.* 2016] G. Pilania, A. Mannodi-Kanakkithodi, B. P. Uberuaga, R. Ramprasad, J. E. Gubernatis and T. Lookman. *Machine learning bandgaps of double perovskites*. Scientific Reports, vol. 6, no. 1, page 19375, 2016. (Cited on page 174.)
- [Potrivitu *et al.* 2019] G.-C. Potrivitu, S. Mazouffre, L. Grimaud and R. Jussot. *Anode geometry influence on LaB6 cathode discharge characteristics*. Physics of Plasmas, vol. 26, no. 11, page 113506, 2019. (Cited on page 144.)
- [Powis & Shneider 2018] Andrew T. Powis and Mikhail N. Shneider. *Particle-in-cell modeling of laser Thomson scattering in low-density plasmas at elevated laser intensities*. Physics of Plasmas, vol. 25, no. 5, page 053513, 2018. (Cited on page 11.)

- [Priti *et al.* 2019a] Priti, R. K. Gangwar and R. Srivastava. *Collisional-radiative model of xenon plasma with calculated electron-impact fine-structure excitation cross-sections*. Plasma Sources Sci. Technol., vol. 28, no. 2, page 025003, 2019. (Cited on pages 6, 33, 35, 37, 42, 126 and 228.)
- [Priti *et al.* 2019b] Priti, R. K. Gangwar and Rajesh Srivastava. *Electron Excitation Cross Sections of Fine-Structure $5p^56s \sim 5p^56p$ Transitions in Xenon*. In P. C. Deshmukh, E. Krishnakumar, Stephan Fritzsche, M. Krishnamurthy and Sonjoy Majumder, editors, Quantum Collisions and Confinement of Atomic and Molecular Species, and Photons, Springer Proceedings in Physics, pages 172–179, 2019. (Cited on pages 32 and 35.)
- [Puech & Mizzi 1991] V Puech and S Mizzi. *Collision cross sections and transport parameters in neon and xenon*. Journal of Physics D: Applied Physics, vol. 24, no. 11, page 1974, 1991. (Cited on page 33.)
- [Puech 2022] V Puech. *PUECH Database, www.lxcat.net*. 2022. (Cited on page 33.)
- [Raccuglia *et al.* 2016] Paul Raccuglia, Katherine C. Elbert, Philip D. F. Adler, Casey Falk, Malia B. Wenny, Aurelio Mollo, Matthias Zeller, Sorelle A. Friedler, Joshua Schrier and Alexander J. Norquist. *Machine-learning-assisted materials discovery using failed experiments*. Nature, vol. 533, no. 7601, pages 73–76, 2016. (Cited on page 174.)
- [Raitses *et al.* 2009] Y. Raitses, A. Smirnov and N. J. Fisch. *Effects of enhanced cathode electron emission on Hall thruster operation*. Physics of Plasmas, vol. 16, no. 5, page 057106, 2009. (Cited on page 132.)
- [Raitses *et al.* 2011] Yevgeny Raitses, Igor D. Kaganovich, Alexander Khrabrov, Dmytro Sydorenko, Nathaniel J. Fisch and Andrei Smolyakov. *Effect of Secondary Electron Emission on Electron Cross-Field Current in $\mathbf{E} \times \mathbf{B}$ Discharges*. IEEE Transactions on Plasma Science, vol. 39, no. 4, pages 995–1006, 2011. (Cited on page 10.)
- [Ralchenko 2016] Yuri Ralchenko. Modern Methods in Collisional-Radiative Modeling of Plasmas, volume 90 of *Springer Series on Atomic, Optical, and Plasma Physics*. 2016. (Cited on pages 36, 55 and 86.)
- [Raptor 2003] Raptor. *UW Atomic Collisions Web Site*, 2003. (Cited on pages xiv and 30.)
- [Ross 2014] Brian C. Ross. *Mutual Information between Discrete and Continuous Data Sets*. PLoS ONE, vol. 9, no. 2, page e87357, 2014. (Cited on page 190.)
- [Rutten 2003] Robert J. Rutten. Radiative Transfer in Stellar Atmospheres. 2003. (Cited on pages xxx and 237.)

- [Sadeghi & Sabbagh 1977] N. Sadeghi and J. Sabbagh. *Collisional transfer between the $6s'[\frac{1}{2}]_{0,1}$ and $6p[\frac{1}{2}]_1$ xenon levels*. Phys. Rev. A, vol. 16, no. 6, pages 2336–2345, 1977. (Cited on page 32.)
- [Schiller *et al.* 1982] S. Schiller, U. Heisig, K. Steinfelder, J. Strümpfel, R. Voigt, R. Fendler and G. Teschner. *On the investigation of d.c. plasmatron discharges by optical emission spectrometry*. Thin Solid Films, vol. 96, no. 3, pages 235–240, 1982. (Cited on page 174.)
- [Shabshelowitz *et al.* 2014] Adam Shabshelowitz, Alec D. Gallimore and Peter Y. Peterson. *Performance of a Helicon Hall Thruster Operating with Xenon, Argon, and Nitrogen*. Journal of Propulsion and Power, vol. 30, no. 3, pages 664–671, 2014. (Cited on page 3.)
- [Smirnov *et al.* 2002] A. Smirnov, Y. Raitses and N. J. Fisch. *Parametric investigation of miniaturized cylindrical and annular Hall thrusters*. Journal of Applied Physics, vol. 92, no. 10, pages 5673–5679, 2002. (Cited on page 4.)
- [Smirnov *et al.* 2006] A.N. Smirnov, Y. Raitses and N.J. Fisch. *Electron cross-field transport in a miniaturized cylindrical Hall thruster*. IEEE Transactions on Plasma Science, vol. 34, no. 2, pages 132–141, 2006. (Cited on page 4.)
- [Smirnov *et al.* 2007] Artem Smirnov, Yegeny Raitses and Nathaniel J. Fisch. *Experimental and theoretical studies of cylindrical Hall thrusters*. Physics of Plasmas, vol. 14, no. 5, page 057106, 2007. (Cited on page 4.)
- [Smirnov *et al.* 2008] A. Smirnov, Y. Raitses and N. J. Fisch. *Controlling the Plasma Flow in the Miniaturized Cylindrical Hall Thruster*. IEEE Transactions on Plasma Science, vol. 36, no. 5, pages 1998–2003, 2008. (Cited on page 4.)
- [Snyder *et al.* 2020] John S. Snyder, Vernon H. Chaplin, Dan M. Goebel, Richard R. Hofer, Alejandro Lopez Ortega, Ioannis G. Mikellides, Taylor Kerl, Giovanni Lenguito, Faraz Aghazadeh and Ian Johnson. *Electric propulsion for the psyche mission: Development activities and status*. 2020. (Cited on page 2.)
- [Sobel'man *et al.* 1995] Igor I. Sobel'man, Leonid Vainshtein and Evgenii A. Yukov. *Excitation of Atoms and Broadening of Spectral Lines*. Springer Series on Atomic, Optical, and Plasma Physics. 2 édition, 1995. (Cited on page 42.)
- [Sommerville 2006] Jason D. Sommerville. *Emission cross sections for neutral xenon impacted by Xe^+ and Xe^{2+}* . Master of Science in Mechanical Engineering, Michigan Technological University, 2006. (Cited on pages 81 and 83.)
- [Song & Mazumder 2012] Lijun Song and Jyoti Mazumder. *Real Time Cr Measurement Using Optical Emission Spectroscopy During Direct Metal Deposition Process*. IEEE Sensors Journal, vol. 12, no. 5, pages 958–964, 2012. (Cited on page 174.)

- [Song *et al.* 2012] Lijun Song, Cunshan Wang and Jyoti Mazumder. *Identification of phase transformation using optical emission spectroscopy for direct metal deposition process*. In High Power Laser Materials Processing: Lasers, Beam Delivery, Diagnostics, and Applications, volume 8239, pages 120–128, 2012. (Cited on page 174.)
- [Stone 1974] M. Stone. *Cross-Validatory Choice and Assessment of Statistical Predictions*. Journal of the Royal Statistical Society: Series B, vol. 36, no. 2, pages 111–133, 1974. (Cited on page 179.)
- [Szabo *et al.* 2013] James Szabo, Bruce Pote, Surjeet Paintal, Mike Robin, Adam Hillier, Richard D. Branam and Richard E. Huffmann. *Performance Evaluation of an Iodine-Vapor Hall Thruster*. Journal of Propulsion and Power, 2013. (Cited on page 3.)
- [Szabo *et al.* 2017] James Szabo, Mike Robin and Vlad Hurby. *Bismuth Vapor Hall Effect Thruster Performance and Plume Experiments*. In 35th International Electric Propulsion Conference, 2017. (Cited on page 3.)
- [Taccogna & Minelli 2018] Francesco Taccogna and Pierpaolo Minelli. *Three-dimensional particle-in-cell model of Hall thruster: The discharge channel*. Physics of Plasmas, vol. 25, no. 6, page 061208, 2018. (Cited on page 10.)
- [Taccogna *et al.* 2009] Francesco Taccogna, Savino Longo, Mario Capitelli and Ralf Schneider. *Anomalous transport induced by sheath instability in Hall effect thrusters*. Applied Physics Letters, vol. 94, no. 25, page 251502, 2009. (Cited on page 10.)
- [Tavant *et al.* 2018] Antoine Tavant, Vivien Croes, Romain Lucken, Trevor Lafleur, Anne Bourdon and Pascal Chabert. *The effects of secondary electron emission on plasma sheath characteristics and electron transport in an discharge via kinetic simulations*. Plasma Sources Science and Technology, vol. 27, no. 12, page 124001, 2018. (Cited on page 168.)
- [Tavant 2019] Antoine Tavant. *Study of the plasma/wall interaction and erosion on a plasma thruster of low power*. These de doctorat, Université Paris-Saclay (ComUE), 2019. (Cited on pages 6 and 11.)
- [Tejeda & Knoll 2023] J. M. Tejeda and A. Knoll. *An oxygen-fuelled Hall Effect Thruster: Channel length, ceramic walls and anode material experimental analyses*. Acta Astronautica, vol. 203, pages 268–279, 2023. (Cited on page 3.)
- [Tilinin 1977] G. N. Tilinin. *High-frequency plasma waves in a Hall accelerator with an extended acceleration zone*. Soviet Physics Technical Physics, vol. 22, pages 974–978, 1977. (Cited on page 130.)

- [Tsikata & Hara 2019] S. Tsikata and Kentaro Hara. *Plasma instabilities in cross-field configuration: an analysis of the relevance of different modes for electron transport*. In the 36th International Electric Propulsion Conference., 2019. (Cited on page 11.)
- [Tsikata *et al.* 2009] S. Tsikata, N. Lemoine, V. Pisarev and D. M. Grésillon. *Dispersion relations of electron density fluctuations in a Hall thruster plasma, observed by collective light scattering*. *Physics of Plasmas*, vol. 16, no. 3, page 033506, 2009. (Cited on pages 5, 10 and 21.)
- [Tsikata *et al.* 2010] S. Tsikata, C. Honoré, N. Lemoine and D. M. Grésillon. *Three-dimensional structure of electron density fluctuations in the Hall thruster plasma: $\mathbf{E} \times \mathbf{B}$ mode*. *Physics of Plasmas*, vol. 17, no. 11, page 112110, 2010. (Cited on pages 5, 10 and 21.)
- [Tsikata *et al.* 2013] S Tsikata, C Honoré and D Grésillon. *Collective Thomson scattering for studying plasma instabilities in electric thrusters*. *Journal of Instrumentation*, vol. 8, no. 10, pages C10012–C10012, 2013. (Cited on pages 5, 10 and 126.)
- [Tsikata *et al.* 2014] S. Tsikata, J. Cavalier, A. Héron, C. Honoré, N. Lemoine, D. Grésillon and D. Coulette. *An axially propagating two-stream instability in the Hall thruster plasma*. *Physics of Plasmas*, vol. 21, no. 7, page 072116, 2014. (Cited on pages 5 and 10.)
- [Tsikata *et al.* 2017] S. Tsikata, A. Héron and C. Honoré. *Hall thruster microturbulence under conditions of modified electron wall emission*. *Physics of Plasmas*, vol. 24, no. 5, page 053519, 2017. (Cited on pages 10 and 24.)
- [van der Burgt *et al.* 1989] P. J. M. van der Burgt, W. B. Westerveld and J. S. Risley. *Photoemission Cross Sections for Atomic Transitions in the Extreme Ultraviolet due to Electron Collisions with Atoms and Molecules*. *Journal of Physical and Chemical Reference Data*, vol. 18, no. 4, pages 1757–1805, 1989. (Cited on page 32.)
- [van der Mullen 1990] J. A. M. van der Mullen. *Excitation equilibria in plasmas; a classification*. *Physics Reports*, vol. 191, pages 109–220, 1990. (Cited on page 26.)
- [Vicek & Pelikan 1990] J. Vicek and V. Pelikan. *A collisional-radiative model applicable to argon discharges over a wide range of conditions. III. Application to atmospheric and subatmospheric pressure arcs*. *J. Phys. D: Appl. Phys.*, vol. 23, no. 5, page 526, 1990. (Cited on page 36.)
- [Villafana *et al.* 2021] W Villafana, F Petronio, A C Denig, M J Jimenez, D Eremin, L Garrigues, F Taccogna, A Alvarez-Laguna, J P Boeuf, A Bourdon, P Chabert, T Charoy, B Cuenot, K Hara, F Pechereau, A Smolyakov,

- D Sydorenko, A t and O Vermorel. *2D radial-azimuthal particle-in-cell benchmark for $E \times B$ discharges*. Plasma Sources Science and Technology, vol. 30, no. 7, page 075002, 2021. (Cited on page 6.)
- [Villafana *et al.* 2023] W. Villafana, B. Cuenot and O. Vermorel. *3D particle-in-cell study of the electron drift instability in a Hall Thruster using unstructured grids*. Physics of Plasmas, vol. 30, no. 3, page 033503, 2023. (Cited on page 10.)
- [Wales & Doye 1997] David J. Wales and Jonathan P. K. Doye. *Global Optimization by Basin-Hopping and the Lowest Energy Structures of Lennard-Jones Clusters Containing up to 110 Atoms*. The Journal of Physical Chemistry A, vol. 101, no. 28, pages 5111–5116, 1997. (Cited on page 155.)
- [Walhout *et al.* 1994] M. Walhout, A. Witte and S. L. Rolston. *Precision measurement of the metastable $6s [3/2]_2$ lifetime in xenon*. Phys. Rev. Lett., vol. 72, pages 2843–2846, 1994. (Cited on page 31.)
- [Wang *et al.* 2019] Yang Wang, Yan-Fei Wang, Xi-Ming Zhu, Oleg Zatsarinny and Klaus Bartschat. *A xenon collisional-radiative model applicable to electric propulsion devices: I. Calculations of electron-impact cross sections for xenon ions by the Dirac B-spline R-matrix method*. Plasma Sources Sci. Technol., vol. 28, no. 10, page 105004, 2019. (Cited on page 37.)
- [Ward *et al.* 2016] Logan Ward, Ankit Agrawal, Alok Choudhary and Christopher Wolverton. *A general-purpose machine learning framework for predicting properties of inorganic materials*. npj Computational Materials, vol. 2, no. 1, pages 1–7, 2016. (Cited on page 174.)
- [Warner 2007] Noah Zachary Warner. *Theoretical and Experimental Investigation of Hall Thruster Miniaturization*. Phd thesis, Massachusetts Institute of Technology, 2007. (Cited on page 4.)
- [Xue *et al.* 2016] Dezhen Xue, Prasanna V. Balachandran, John Hogden, James Theiler, Deqing Xue and Turab Lookman. *Accelerated search for materials with targeted properties by adaptive design*. Nature Communications, vol. 7, no. 1, page 11241, 2016. (Cited on page 174.)
- [Yang *et al.* 2010] Juan Yang, Shigeru Yokota, Ryotaro Kaneko and Kimiya Komurasaki. *Diagnosing on plasma plume from xenon Hall thruster with collisional-radiative model*. Physics of Plasmas, vol. 17, no. 10, page 103504, 2010. (Cited on page 37.)
- [Young *et al.* 2018] C V Young, A Lucca Fabris, N A MacDonald-Tenenbaum, W A Hargus and M A Cappelli. *Time-resolved laser-induced fluorescence diagnostics for electric propulsion and their application to breathing mode dynamics*. vol. 27, no. 9, page 094004, 2018. (Cited on page 126.)

- [Yu *et al.* 2000] D. H. Yu, P. A. Hayes, J. F. Williams, V. Zeman and K. Bartschat. *Internal spin-orbit coupling and electron exchange in the excitation of $np^5(n+1)p$ states of neon, krypton and xenon atoms by polarized electrons*. J. Phys. B: At. Mol. Opt. Phys., vol. 33, no. 10, page 1881, 2000. (Cited on page 33.)
- [Zatsarinny & Bartschat 2009] Oleg Zatsarinny and Klaus Bartschat. *B-spline calculations of oscillator strengths in noble gases*. Phys. Scr., vol. 2009, no. T134, page 014020, 2009. (Cited on page 228.)
- [Zatsarinny & Bartschat 2010] Oleg Zatsarinny and Klaus Bartschat. *Benchmark calculations for near-threshold electron-impact excitation of krypton and xenon atoms*. J. Phys. B: At. Mol. Opt. Phys., vol. 43, no. 7, page 074031, 2010. (Cited on pages 32, 33 and 35.)
- [Zatsarinny & Bartschat 2013] Oleg Zatsarinny and Klaus Bartschat. *The B-spline R-matrix method for atomic processes: application to atomic structure, electron collisions and photoionization*. J. Phys. B: At. Mol. Opt. Phys., vol. 46, no. 11, page 112001, 2013. (Cited on pages 32, 33 and 42.)
- [Zhang *et al.* 2015] Yunchao Zhang, Christine Charles and Rod Boswell. *Principle of radial transport in low temperature annular plasmas*. Physics of Plasmas, vol. 22, no. 7, page 073510, 2015. (Cited on page 168.)
- [Zhong *et al.* 2020] Linlin Zhong, Anthony B Murphy, Xiaohua Wang and Mingzhe Rong. *Calculation of two-temperature plasma composition: I. Mass action law methods and extremum searching methods*. J. Phys. D: Appl. Phys., vol. 53, no. 6, page 065202, 2020. (Cited on page 36.)
- [Zhu & Pu 2010] Xi-Ming Zhu and Yi-Kang Pu. *Optical emission spectroscopy in low-temperature plasmas containing argon and nitrogen: determination of the electron temperature and density by the line-ratio method*. J. Phys. D: Appl. Phys., vol. 43, no. 40, page 403001, 2010. (Cited on page 36.)
- [Zhu *et al.* 2009] Xi-Ming Zhu, Wen-Cong Chen, Jiang Li and Yi-Kang Pu. *Determining the electron temperature and the electron density by a simple collisional-radiative model of argon and xenon in low-pressure discharges*. J. Phys. D: Appl. Phys., vol. 42, no. 2, page 025203, 2009. (Cited on page 36.)
- [Zhu *et al.* 2012] Xi-Ming Zhu, Yi-Kang Pu, Yusuf Celik, Sarah Siepa, Edmund Schüngel, Dirk Luggenhölscher and Uwe Czarnetzki. *Possibilities of determining non-Maxwellian EEDFs from the OES line-ratios in low-pressure capacitive and inductive plasmas containing argon and krypton*. Plasma Sources Sci. Technol., vol. 21, no. 2, page 024003, 2012. (Cited on page 36.)
- [Zhu *et al.* 2015] Xi-Ming Zhu, Tsanko Vaskov Tsankov, Dirk Luggenhölscher and Uwe Czarnetzki. *2D collisional-radiative model for non-uniform argon plasmas: with or without ‘escape factor’*. Journal of Physics D: Applied Physics, vol. 48, no. 8, page 085201, 2015. (Cited on pages 43 and 44.)

- [Zhu *et al.* 2016] Xi-Ming Zhu, Zhi-Wen Cheng, Yi-Kang Pu and Uwe Czarnetzki. *Escape factors for Paschen 2p–1s emission lines in low-temperature Ar, Kr, and Xe plasmas*. *Journal of Physics D: Applied Physics*, vol. 49, no. 22, page 225204, 2016. (Cited on page 44.)
- [Zhu *et al.* 2019] Xi-Ming Zhu, Yan-Fei Wang, Yang Wang, Da-Ren Yu, Oleg Zatsarinny, Klaus Bartschat, Tsanko Vaskov Tsankov and Uwe Czarnetzki. *A xenon collisional-radiative model applicable to electric propulsion devices: II. Kinetics of the 6s, 6p, and 5d states of atoms and ions in Hall thrusters*. *Plasma Sources Sci. Technol.*, vol. 28, no. 10, page 105005, 2019. (Cited on pages xxix, 6, 35, 37, 43, 76, 77, 78, 79, 86, 90, 126, 154 and 168.)
- [Ziegler & Nichols 1942] J G Ziegler and N B Nichols. *Optimum Settings for Automatic Controllers*. 1942. (Cited on pages 198 and 199.)
- [Åström & Hägglund 1984] Karl Johan Åström and Tore Hägglund. *Automatic Tuning of Simple Regulators*. Technical Reports TFRT-7269, 1984. (Cited on page 198.)

Titre : Étude de l'Émission Optique des Propulseurs à Effet Hall à l'aide d'un Modèle Collisionnel Radiatif, des Simulations PIC et du Machine Learning

Mots clés : Propulsion électrique, Propulseur à effet Hall, Spectroscopie, Modèle collisionnel radiatif, Simulation PIC, Machine Learning

Résumé : Ce travail propose une analyse de l'émission optique des propulseurs à effet Hall dans le contexte actuel de l'industrie aérospatiale visant à réduire les coûts d'exploitation spatiale. S'appuyant sur le code PIC LPPic, cette thèse explore la plume du propulseur en couplant les résultats de simulations à des diagnostics virtuels, en particulier la diffusion Thomson Collective et la spectroscopie d'émission. La thèse est structurée en huit chapitres couvrant la méthodologie des diagnostics virtuels de diffusion Thomson Collective, le modèle collisionnel radiatif HET0D pour le xénon neutre et aussi le cadre pour générer des spectres d'émission optique à partir des simulations. Les résultats soulignent l'importance de tenir compte des gradients spatiaux dans la plume du propulseur lors de l'extraction des paramètres plasma à partir de l'émission optique, tout en proposant des bonnes pratiques sur le choix des ratios de raie et des paramètres à considérer. Le couplage PIC/HET0D valide également les hypothèses des modèles collisionnels radiatifs consistant à négliger le transport des métastables et à supposer une fonction de distribution d'énergie des

électrons maxwellienne dans la plume du propulseur. Le couplage a également mis en évidence les limitations de bande passante spécifiques aux raies d'émission spontanée pour la mise en œuvre de la spectroscopie d'émission optique pour l'étude des instabilités à haute fréquence. Le passage vers les expériences "réelles" valide l'intérêt des diagnostics virtuels et confirme l'adéquation de l'émission optique et des modèles collisionnels radiatifs pour le suivi et le contrôle des propulseurs à effet Hall. Enfin, ce travail présente aussi une implémentation innovante des réseaux de neurones avec la spectroscopie d'émission, améliorant la performance des modèles collisionnels radiatifs et de la spectroscopie d'émission pour des applications pratiques : en accélérant le processus d'extraction des paramètres plasma à partir des spectres d'émission, en réduisant le matériel nécessaire en orbite et en permettant le contrôle optique des paramètres de fonctionnement. Dans l'ensemble, ce travail propose une nouvelle approche au propulseur à effet Hall qui combine les simulations numériques, les diagnostics virtuels, les données expérimentales et les réseaux de neurones.

Title : Investigation of the Optical Emission of Hall Effect Thrusters using a Collisional Radiative Model, Particle-In-Cell Simulations, and Machine Learning

Keywords : Electric propulsion, Hall effect thruster, Spectroscopy, Collisional radiative modelling, PIC simulation, Machine Learning

Abstract : This thesis offers an analysis of Hall Effect thruster optical emissions within the context of micro reusable launchers and ride-share satellite programs, aiming to reduce space operation costs. It builds on the LPPic Particle-In-Cell code, exploring plasma dynamics and interactions via simulation results coupled with virtual diagnostics: virtual collective Thomson scattering and optical emission spectroscopy. The thesis is structured into eight chapters, covering topics such as virtual collective Thomson scattering diagnostics, the HET0D collisional radiative model for neutral xenon, and a framework to generate optical emission spectra from Particle-In-Cell simulations of Hall thruster. It emphasizes the importance of accounting for spatial gradients in the thruster plume when extracting plasma parameters from optical emission. It also validates assumptions in collisional radiative models of neglecting the metastable transport and assuming

a Maxwellian EEDF in the plume. It also highlighted line-specific bandwidth limitations for the implementation of optical emission spectroscopy to study high-frequency instabilities. Experiments validate virtual diagnostic analysis, confirming the adequacy of optical emission and collisional radiative models for monitoring Hall Effect thrusters. Additionally, the thesis presents an innovative integration of artificial neural networks, enhancing the scope of use of collisional radiative models and optical emission spectroscopy by speeding up the extraction process of plasma parameters from emission spectra, reducing the needed hardware in-orbit, and allowing the optical control of the operating parameters. All in all, this research contributes to electric propulsion by combining numerical simulations, virtual diagnostics, experimental data, and neural networks to deepen understanding of Hall Effect thrusters.